Hypersonic Boundary Layer Instability Measurements at Low and High Angles of Attack



Sebastien Wylie

St John's College

University of Oxford

A thesis submitted for the degree of

Doctor of Philosophy

Trinity 2019

This thesis is dedicated to
Mamie Colette
Je t'adore, merci pour tout ce que tu as fait pour tes enfants et petits-enfants

Acknowledgements

I would firstly like to thank my supervisor, Dr. Matthew McGilvray, for his endless support and guidance throughout this research. He has truly been the best supervisor that I could have ever asked for. It has been an awesome journey from Petrograd to Stockholm, thank you.

I would like to express my gratitude to everyone in the Oxford Hypersonics Group. In particular, I would like to thank Dr. Luke Doherty for operating the HDT, and most importantly, for always finding the time to help. Thanks to Rowland Penty-Geraets, for helping with the heat transfer measurements, to Tobias Hermann, for spending time on the Focused Schlieren setup, to Philipp Kerth, for all your work with the most recent freestream disturbance campaign, to Matt Satchell, for working on the PCB132 calibrations, to Chris Hambidge, for also operating the HDT, and to Oliver Paxton, for taking over multiple engineering tasks and helping with the Cheng correlation code. To the rest of the hypersonics group, thanks for all the good times and unconditional support. It is an awesome group.

This work would not have been possible without multiple technicians in the Osney ThermoFluids Institute. Gregory "Lil' Red" King, thank you for providing endless guidance, both in the instrumentation of the cone models and making sure that my Cockney slang was up to scratch. You have bailed me out on many occasions, and I am very grateful. To Brian "Doc" Bunce, you did an exceptional job machining both cone models, thank you. To James Carter and Duncan "Priest" Blake, thanks for all the good times & helpful discussions. For any future students reading this: if in doubt, ask James.

I am grateful to Dr. Joseph Jewell for providing the STABL2D PSE-Chem stability computations used in this research, for always being willing to discuss the results, and for reviewing parts of this thesis. The comparisons to stability computations have been incredibly insightful, and would otherwise not have been possible. Thanks to Dr. Tom Juliano and Dr. Sebastian Willems for helpful discussions when comparing the HDT dataset to the post-flight experiments in H2K. I would also like to express my gratitude to Prof. David Mee and Dr. Sreekanth

Raghunath for many helpful conversations and guidance in the T4 experiments and subsequent analysis of results, particularly for making comparisons to Howarth's approximation. Finally, thanks are extended to Dr. Russ Cummings, Dr. Steven Schneider, and Dr. Roger Kimmel, for always being available to provide advice and suggestions throughout the project. I am grateful to the European Office Aerospace Research & Development (EOARD) for funding the research.

I am extremely fortunate to have an amazing group of friends in Oxford, all of whom have made my time here so special and unforgettable. Between teaching Pigeon how to play trains, weekly games of squash against Kirbs, paddling with Shrike up the Cherwell, or doing all of the above with Pig, it has been incredible. In no particular order, I would like to thank Pigeon, Katie, Shrike, Panda, Kirbs, Clag, Fist, Hayriye, Ida, Sweeper, EE, HR, Spoons, Ump, Eugie, The Warden, Brick, Big Will, Ribsy, Aurelie, MJ, CP, The Villager, Maddie, Burga, Stenner, Kizza, Lily, The Apprentice, Ellis, Carl, Ainslie, Catherine, Tarts, Fotes, Gadge, Woody, and Flounder. To Celine, Merlin, Ru & Ladd at Oli's... you're awesome, thanks for having me. Thanks to Claire, Teg, Ryu and Bella at Skogen. A huge thanks are also extended to Pizza Pilgrims for supporting me as a professional pizza taster.

To Eva & Jeremy Davies, I can't thank you enough for always being so kind, generous, and welcoming me into your home and family. Jez, your insight into nozzles and cutting edge flying vehicles has proven invaluable. The kindness shown by Eva, Jez, Arthur, Cato, Scoob, and Lucy has meant the world. I am very grateful.

To Mum and Dad, you have always been there for me and have always been incredibly supportive. I love you both so much, and am very grateful for everything that you have done for all of us kids. We are incredibly lucky, thank you. Speaking of which, thanks to Jo, Eva & Alex, for being such great siblings, and to Nanna and Pop, for being such great grandparents. Cheers also, to Beth. It has been so nice to spend time with all of you whenever we can coordinate holidays together. I can't wait to see you all at Christmas.

Finally, thanks most of all to Audrey "Pig" Davies[1] for making the last few years so special. You are an incredible person, and I love you very much. I can't wait to see what our next chapter will bring.

[1]I didn't come up with her nickname, I promise. I'll claim most of the other ones though.

Abstract

This research experimentally investigated the effects of angle of attack, wall-to-total temperature ratio, and freestream disturbance levels on hypersonic boundary layer instabilities at Mach 7. The motivation was to improve the understanding of hypersonic boundary layer instabilities and inform numerical transition models so that transition can be predicted in flight. Although many studies exist on this topic, there is little high resolution data available on instabilities for high angles of attack. The study used a 7° half angle cone with small nose bluntness, and included a heater cartridge to test multiple wall-temperature distributions. Measurements are presented using two experimental facilities with varying wall-to-total temperature ratio: the low total enthalpy Oxford High Density Tunnel (HDT) and the high total enthalpy T4 Stalker Tunnel at The University of Queensland. Models were heavily instrumented with high-frequency PCB132 pressure sensors, to investigate the development of instabilities on the cone surface.

This research contained the first commissioning shots and flow property determination for the Oxford High Density Tunnel facility. Boundary layer instabilities and post-shock freestream pressure fluctuation levels were characterised during different periods of quasi-steady flow. Flow characterisation from 1 kHz - 1000 kHz had a post-shock RMS noise value of $\approx 0.44\%$ to 1.49%. This magnitude is lower than most of the published conventional tunnel results, though is still an order of magnitude above flight and quiet tunnels. To qualify the newly-commissioned HDT facility and developed post-processing codes for boundary layer transition studies, instability measurements were compared to a dataset from DLR's H2K facility. The second mode instability was observed one sensor upstream in the HDT at $\alpha = 0°$, and the transition front was similar at high angles of attack. The second mode disturbance frequency was accurately predicted at $\alpha = 0°$ using the PSE-Chem stability code and analytically using Howarth's boundary layer thickness approximation. The excellent agreement between instability measurements in both facilities and stability computations indicated that the HDT could be trusted for boundary layer transition studies.

The effect of an increase in freestream disturbance levels and angle of attack were independently investigated in the Oxford HDT at $M_\infty = 7$, $Re_{unit,\infty} = 12.3 \times 10^6$

/m, and $T_w/T_0 = 0.6$. At an angle of attack of zero, the second mode was the most dominant instability. The second mode disturbance frequency and growth rate were accurately predicted by PSE-Chem at all freestream disturbance levels. A decrease in freestream fluctuations resulted in a delay in the breakdown of the second mode (A_{max} observed at $Re_x = 4.8 \times 10^6$ to $Re_x = 6.6 \times 10^6$), an increase in the critical N factor ($N_{crit} = 7.2$ to 9.4), and it allowed the second mode to reach larger amplitudes before decaying ($A_{max} = 17\%$ - 19% to 23% - 30%).

A more detailed study of boundary layer instabilities was performed at high angles of attack in HDT to improve the understanding of transition where large pressure gradients exist in flight. Leeward transition was observed upstream of the HIFiRE-1 flight test, most likely due to the higher freestream disturbances in conventional tunnels. The windward boundary layer was more stable in the HDT. This is believed to be due to the destabilization of the second mode at the lower T_w/T_0 experienced in flight. At $\alpha = 8°$, a suspected travelling crossflow instability was detected at low frequencies ($f \approx 20 - 45$ kHz) and results suggested that it is able to coexist with a high-frequency disturbance ($f \approx 250 - 500$ kHz). The increase in freestream disturbance fluctuations caused the baseline low frequency laminar PSD to increase in amplitude. The suspected travelling crossflow instability and the high frequency disturbance were both destabilized at the higher freestream disturbance levels.

To investigate the destabilizing role of wall-to-total temperature ratio on the second mode, boundary layer instabilities were measured at $\alpha = 0°$ in the T4 Stalker Tunnel. The results presented were the first attempt to measure boundary layer instabilities in the facility. The nominal condition was $M_\infty = 7.1$, $Re_{unit,\infty} = 11.4 \times 10^6$ /m, $T_w/T_0 = 0.13$, $H_0 = 2.3$ MJkg^{-1}. A peak in the PSD was observed at the two most downstream gauges, $Re_x = 2.6 - 3.0 \times 10^6$, at a frequency of $f \approx 725 - 790$ kHz. A maximum disturbance amplitude of 8% was measured, however decay to turbulence was not observed due to the short model (maximum $Re_x = 3.0 \times 10^6$) and the stabilizing effect of nose bluntness ($R_N = 1.6$ mm). The disturbance frequency for the final two sensors agreed with estimates using Howarth's approximation, though a discrepancy was observed when comparing to PSE-Chem.

Contents

List of Figures **xiii**

List of Tables **xxv**

Nomenclature **xxvii**

1 Introduction **1**
1.1 Hypersonic Boundary Layer Transition 1
1.2 Research Objectives 5
1.3 Organisation of thesis 8

2 Literature Review **11**
2.1 Paths to Transition 11
2.2 Linear Stability Theory and the Parabolized Stability Equations . . 14
2.3 The e^N method and PSE-Chem solver 16
2.3.1 e^N method 16
2.3.2 STABL: PSE-Chem 17
2.4 Instability Mechanisms 19
2.5 Second Mode Instability 20
2.5.1 Second mode characteristics 20
2.5.2 Estimation of the second mode frequency using Howarth's approximation 23
2.5.3 Measurement techniques 24
2.5.4 Analysis of second mode amplitudes: Marineau's method . . 25
2.5.5 Measurements in conventional wind tunnels 28
2.6 Crossflow Instability 31
2.6.1 Formation of crossflow 31
2.6.2 Stationary crossflow waves 33
2.6.3 Travelling crossflow waves 35
2.6.4 Instability measurements: co-existing stationary modes, travelling modes, and second Mack mode 36
2.7 Parametric Effects, with a focus on Slender Body Experiments . . . 38
2.7.1 Freestream Turbulence Levels 38

2.7.2 Unit Reynolds Number 39
2.7.3 Nose bluntness 39
2.7.4 Angle of attack 42
2.7.5 Wall-cooling effects 47

3 Experimental Setup 51
3.1 Hypersonic Wind Tunnels 51
3.2 The Oxford High Density Tunnel 53
3.2.1 History of the High Density Tunnel 53
3.2.2 Details of operation 54
3.3 The University of Queensland's T4 Stalker Tunnel 59
3.4 Oxford 7° cone models 61
3.4.1 The HDT 7° Cone Model 62
3.4.2 The RST 7° Cone Model 64
3.5 Wall-temperature distributions using a heated nosepiece 66
3.5.1 Heated nosepiece design 66
3.5.2 Wall temperature distribution results 67
3.6 Instrumentation 68
3.6.1 Piezoresistive pressure sensors 68
3.6.2 Heat transfer gauges 70
3.6.3 Piezoelectric pressure sensors 72
3.7 PCB132 processing methods 75
3.7.1 Fast Fourier Transform: Power spectral density (PSD) using Welch's method 75
3.7.2 Continuous wavelet analysis 77

4 Freestream Characterisation of the Oxford High Density Tunnel 83
4.1 Characterization of flow conditions in the HDT 83
4.1.1 Mach number characterisation 84
4.1.2 Total temperature characterization 85
4.1.3 Viscosity model 86
4.1.4 Reynolds number 87
4.2 The Oxford Pitot Rake 89
4.2.1 Spatial Uniformity 92
4.3 Freestream disturbance characterisation: Post-shock PSD rebuild . 93
4.3.1 Individual HDT shot result 95
4.3.2 Effect of HDT facility plateaus 99
4.3.3 Effect of distance from nozzle centreline 101

5 Verification of Boundary Layer Instability Results in the Oxford High Density Tunnel 103
5.1 DLR's Post-HIFiRE-1 Experiments in H2K . . . 104
5.2 HDT conditions: matching H2K experiments . . . 105
5.2.1 Viscosity model . . . 105
5.2.2 Wall-to-total temperature ratio (T_w/T_0) . . . 106
5.2.3 PCB132 correction . . . 106
5.2.4 Summary of conditions . . . 107
5.3 Microalignment of the HDT 7° model . . . 109
5.4 Results at $\alpha = 0°$ . . . 111
5.4.1 Comparison to STABL2D PSE-Chem computations . . . 113
5.5 Results at $\alpha = 6°$ . . . 118
5.6 Results at $\alpha = 9°$ . . . 122
5.7 Comparison of PCB-detected Transition Fronts . . . 123
5.8 Sources of discrepancies . . . 125
5.9 Summary . . . 125

6 Boundary layer instabilities at $\alpha = 0°$ 127
6.1 Static Cone Pressure . . . 128
6.2 The Oxford HDT: high T_w/T_0, $\alpha = 0°$ . . . 129
6.2.1 HDT Plateau #1: $T_w/T_0 = 0.58$, Noise = 1.49 % . . . 130
6.2.2 HDT Plateau #3: $T_w/T_0 = 0.64$, Noise = 0.44% . . . 135
6.2.3 Comparison to STABL2D PSE-Chem Computations . . . 138
6.2.4 HDT comparison to HWT-8, NASA LaRC-20inch and HLB 143
6.2.5 Maximum second mode amplitudes . . . 145
6.3 T4 Stalker tunnel: low T_w/T_0, $\alpha = 0°$ . . . 147
6.3.1 T4 Nominal condition: $Re_{unit} = 11 \times 10^6$ /m, T_w/T_0 const. . 148
6.3.2 Effect of T_w/T_0 distributions . . . 153
6.3.3 Effect of Re_{unit} . . . 157
6.3.4 T4 comparison to HEG and HIEST shock tunnels . . . 159
6.3.5 T4 comparison to HDT . . . 160
6.4 Non-dimensional frequency comparison . . . 162

7 Boundary layer instabilities at angle of attack 165
7.1 HIFiRE-1 flight test . . . 166
7.1.1 Flight test overview . . . 168
7.1.2 Instrumentation . . . 169
7.1.3 Pressure fluctuation transition onset criterion . . . 170
7.2 HDT conditions overview . . . 171
7.3 Static cone pressures at angle of attack . . . 172

7.4 Pressure fluctuation transition onset criterion 174
7.4.1 Comparison to HIFiRE-1 criterion: similarities and discrepancies 175
7.5 HIFiRE-1 descent: sweep in Re_{unit} & angle of attack in the Oxford HDT 177
7.5.1 General observations 177
7.5.2 Comparisons to HIFiRE-1 flight observations 180
7.6 HDT Condition 3: $Re_{unit,\infty} = 12.3 \times 10^6$ /m, $\alpha = 8°$ 181
7.6.1 $Re_x - \phi$ map and transition front 182
7.6.2 Disturbance characteristics 182
7.6.3 Effect of higher freestream disturbance levels: comparison to HDT plateau #1 188

8 Conclusions and Future Work 193
8.1 Conclusions 194
8.1.1 Commissioning of the Oxford HDT 194
8.1.2 Transition at $\alpha = 0°$ 195
8.1.3 Transition at high angles of attack 197
8.2 Future work 200

Appendices

A Oxford 7° Cone Models: instrumentation locations and roughness characterization 205
A.1 HDT 7° Cone Model 205
A.2 RST 7° Cone Model 209

B HDT P_{fill} calculation: pressure loss across the plug valve 213

C Freestream Disturbance Characterization: Frequency-dependent PSD ratio between probes 215
C.1 HDT cap geometry PSD rebuild & R results 217
C.2 Low frequency results: 1 kHz $\leq$ f $<$ 100 kHz 218
C.3 High frequency results: $f \geq 100$ kHz 221

D HDT boundary layer instability measurements at each azimuth: $Re_{unit,\infty} = 12.3 \times 10^6$ /m, $\alpha = 8°$ 225

References 229

List of Figures

1.1 Surface heat transfer on the Re-Entry F ballistic vehicle [14], taken from Figure 1a) in Ref. [6]. The flight vehicle is a 4m beryllium cone with a half-angle of 5, re-entering at an angle of attack (α) near zero, a Mach number of 20 and a total enthalpy of $\approx$ 18 MJ / kg [14]. . . 3

1.2 Illustration of a boundary layer development: laminar, transitional, and turbulent boundary layer over a flat plate [24]. 4

2.1 Paths to turbulence in boundary-layer flows. Figure taken from Fedorov [18], with paths originally devised by Morkovin et al. [45] . 12

2.2 Schematic of the acoustic mode in a high-speed boundary layer, in the body-fixed frame of reference [18]. 22

2.3 Temporal amplification rate for the first four Mack modes with $\psi = 0°$ (2D waves) [17]. 22

2.4 Temporal amplification rate for the most unstable first and second mode (3D) [17]. 22

2.5 A comparison of experimental N factors to linear PSE-Chem computations using Marineau's method, for conventional tunnels at $M_\infty = 6$. Figure reproduced using data from Figure 10 e) and f) in Ref. [54] . 27

2.6 Maximum second mode amplitudes for various wind tunnels and flow conditions. Reproduced using the data from Figure 9 in Ref. [54] and Figure 6 in Ref. [95]. 29

2.7 Marineau's amplitude and N factor results for Mach 14, $Re_{unit,\infty} = 1.7 - 11.9 \times 10^6$ /m in AEDC's Tunnel 9. Reproduced from Fig. 6 a) and Fig. 10 a) in Ref. [54]. $Re_{x,tr}$ indicates the heat transfer detected transition onset. 31

2.8 A typical crossflow profile. Taken from Figure 1 in Ref. [98] 32

2.9 Comparison of the primary and secondary instability amplitude developments in Purdue's BAM6QT Quiet Tunnel, taken from Figure 11 in Edelman et al. [99]. Experiments completed in quiet flow at $M_\infty = 6$, $Re_{unit,\infty} = 7.5 - 11.9 \times 10^6$ /m, $T_w/T_0 = 0.7$. 35

2.10 Effect of freestream turbulence levels on transition locations for multiple geometries and experiments. Figure originally plotted by Stainback [128], and adapted by Schneider [125]. Taken from Figure 3 in Ref. [125] 40
2.11 Effect of Unit Reynolds number on transition locations. Figure plotted by Schneider [5], using data from Table I in ref. [132]. Taken from Figure 17 in Ref. [5]. 40
2.12 Effect of nose radius on transition location. Stetson's experiments in the AFRL High Reynolds-number facility at Mach 6 using an 8° half angle cone. Figure plotted using data and format from Figure 1a. in Paredes et al. [136]. Original data is from Stetson [94]. 41
2.13 Effect of nose radius on measured fluctuations from Stetson experiments at Mach 6 using a 5° half angle cone [89, 65]. 42
2.14 Transition results for the windward and the leeward ray at angle of attack using a sharp cone. The data is from Refs. [131, 145, 143, 146, 147, 134, 148]. α is the angle of attack, and θ_c is the cone half angle. The results have been annotated to show a potential T_w/T_0 and M_∞ trend. 43
2.15 Stetson's transition results at angle of attack with a sharp cone, taken from Figure 7 in Ref. [143]. α is the angle of attack, and θ_c is the cone half angle. 44
2.16 IR thermography result from the H2K post HIFIRE-1 campaign, taken from Figure 11a in Ref. [35]. Side view of the 7° cone at $\alpha = 9°$. $M_\infty = 7$, $Re_{unit,\infty} = 9.1 \times 10^6$ /m, $T_w/T_0 = 0.56$, $R_N = 1.6$ mm. . . 44
2.17 HIFiRE-1 Descent Transition map, compared to results from H2K's post-flight campaign. Taken from Figure 25 in [32]. PHBW1 - PHBW3 are measurements from high-frequency Kulite pressure transducers in flight. HT3 is a high-frequency Vatell heat transfer gauge, and the dot-dashed line given by Re_{tr} is the low-frequency transition measured by a Medtherm coaxial gauge in flight. The H2K $\alpha = 6°, 12°$ results are PCB132-detected transition fronts from the post-flight H2K campaign [36]. 46
2.18 Effect of wall-cooling on the ratio of maximum temporal amplification rate for the first and second mode instability. Results are calculated using linear stability theory for an insulated-wall flat plate at multiple Mach numbers, and the most unstable wave angle for each mode. . 48
2.19 Effect of wall-cooling on the transition Reynolds number. Results are collated by Everhart et al., presented in Figure 7b of Ref. [156]. Transition was detected using heat transfer deviation from laminar trends. 49

2.20 Effect of wall-cooling on the second mode amplitude, as measured by Stetson et al. [151]. Taken from Figure 4 in Ref. [151]. 50

3.1 The scope of hypersonic experimental facilities as a function of velocity and test time [158]. Adapted by Wise, taken from Figure 2.7b in Ref. [159] 52
3.2 An annotated CAD section view of the HDT Ludwieg Tube, fast-acting plug valve, and contoured convergent-divergent nozzle (Mach 7 nozzle shown). 54
3.3 An example of multiple stagnation pressure profiles in the Oxford HDT, to satisfy individual experiment objectives. The different profiles are achieved by modifying the fast-acting plug valve timings. 55
3.4 An annotated schematic of the Quadratec traverse equipment. . . . 56
3.5 An annotated schematic of the Oxford High Density Tunnel (HDT) [160] 57
3.6 The Oxford T6 Stalker Tunnel on the left, and the Oxford High Density Tunnel (HDT) on the right 57
3.7 A CAD schematic of the Oxford High Density Tunnel, along with a detailed view of the HDT 7° cone model at the experiment location. 58
3.8 T4 Free-Piston Reflected Shock Tunnel [163] 59
3.9 Distance-time diagram showing the main processes of the T4 reflected shock tunnel [163, 165, 166]. Taken from Figure 3.2 in Ref. [163] . . 60
3.10 Schematic to illustrate the coordinate system used for the 7° Cone Models. 62
3.11 Isometric and cross-sectional view of the HDT 7° Cone Model. . . . 63
3.12 Isometric and cross-sectional view of the RST 7° Cone Model. The orange element illustrates the nosetip heater cartridge, as detailed in Section 3.5. 65
3.13 Heated nosetip used for the RST 7° Cone Model. Shown with the $R_N = 0.89$ mm nosetip. 67
3.14 Wall-temperature distributions as a function of heater cartridge power, measured using K-Type thermocouples. The dashed lines are spline fits of the thermocouple data. 68
3.15 Figure of the Kulite piezoresistive sensors used in this research. . . 69
3.16 Schematic of the thin film heat transfer gauge [171], along with the PEEK sleeve used to house the gauge for the 7° Cone Models. . . . 71
3.17 PCB method for determining frequency response and factory calibration values for PCB 132 sensors [179]. Taken from Figure 5 in Ort et al. [179] 74

3.18 A comparison of PCB gain profiles for the RTV mounting method, and the Neoprene 60A housing. Results have been reproduced using data from Figure 15 and Figure 16 in Ref. [179]. 74
3.19 An example of processing a PCB132 signals using the fast Fourier transform to obtain the PSD, and integrated power spectra to summarize individual disturbances. 77
3.20 The complex-valued Morlet wavelet used for this research. γ_c is the center frequency, and γ_b is the bandwidth. The Morlet wavelet is defined by Equation 3.2. 79
3.21 An illustration of the cone of influence for a CWT scalogram, plotted as the white dashed line. It shows areas where the scalogram may be affected by edge effects. The CWT result is for the same pressure signal that was processed in Figure 3.19. The HDT facility conditions are: Mach 7, $Re_{unit,\infty} = 12.3 \times 10^6$ /m, and $T_w/T_0 = 0.64$, Noise = 0.44%. 80
3.22 A comparison of power spectral density calculations using the fast Fourier transform and the continuous wavelet transform. The comparison is made on two datasets; one for a 17ms test time in HDT and the other for a 1.5 ms test time in the T4 Stalker Tunnel. The HDT conditions are at $M_\infty = 7.0$, $Re_{unit,\infty} = 12.3 \times 10^6$ /m, $T_w/T_0 = 0.64$, Noise = 0.44%, $Re_x = 6.3 \times 10^6$ (results are presented in Section 6.2). The T4 conditions are at $M_\infty = 7.1$, $Re_{unit,\infty} = 11.4 \times 10^6$ /m, $T_w/T_0 = 0.13$, $Re_x = 3.0 \times 10^6$ (results are presented in Section 6.3). 81
3.23 Using the CWT scalograms to identify and remove non flow representative transient events. This example is from experiments undertaken in the T4 Stalker Tunnel at $M_\infty = 7.1$, $Re_{unit,\infty} = 11.4 \times 10^6$ /m, $T_w/T_0 = 0.13$, $Re_x = 1.3 \times 10^6$. 82

4.1 HDT facility Pitot-to-supply pressure ratio as a function of various supply pressures. The dashed line is the linear relationship used for the Mach 7 nozzle ($T_{fill} = 537$ K). 85
4.2 HDT facility conditions using the Mach 7 nozzle and Keyes' viscosity model. The fill conditions are: $P_{fill} = 2485$ kPa, $T_{fill} = 537$ K. The quasi-steady plateau test times are illustrated by the grey shaded area. 88
4.3 The HDT Pitot rake with multiple Pitot probe geometries. Flow conditions for Schlieren results are at: $M_\infty = 7$, $Re_{\text{unit},,\infty} = 12.1 \cdot 10^6$/m, $T_w/T_0 = 0.64$. 91
4.4 Mach 7 Pitot Survey Results at $P_0 = 1790$ kPa, $T_{fill} = 537$ K. The axial distance downstream from the nozzle exit is shown in the legend, neglecting any recoil of the facility. The shot number is given in brackets. The error bars indicate one standard deviation of the variation during the test time. 92

4.5 Power spectral density rebuilds of freestream Pitot pressure fluctuations measured in multiple high-speed facilities. Re-plotted from Figure 2 in Ref. [120] 94
4.6 Post-shock PSD rebuild example for HDT shot 594. Conditions are at Mach 7, $Re_{unit,\infty} = 12.1 \times 10^6$ /m, using HDT plateau 3. 98
4.7 Calculated noise values for HDT shot 594 (Mach 7, $Re_{unit,\infty} = 12.1 \times 10^6$ /m, plateau 3). Noise values are plotted as a function of the distance from the nozzle centreline, using two methods (time domain and PSD integration). 98
4.8 Effect of HDT facility plateau on post-shock pressure fluctuations for the HDT Mach 7 nozzle. PSD rebuilds are shown for the Pitot probes on the nozzle centreline. Pitot geometry is without caps, (i.e. "small"). The rake location is $x = 68$ mm from the nozzle-exit. . . . 100
4.9 Effect of Pitot probe distance from nozzle centreline on post-shock pressure fluctuations for the HDT Mach 7 nozzle. Results are shown for HDT facility plateau #1 and #3, using the small Pitot geometry. The rake location is $x = 68$ mm from the nozzle-exit. Due to the rake configuration, only Kulite results are presented for $r \geq 120$ mm. 102

5.1 An image of the H2K model inside the test section. Taken from Figure 2 and Figure 3 in Ref. [36] 104
5.2 HDT facility profile and chosen test time used for the verification campaign. 107
5.3 Normalized surface pressure power spectra with traverse set to α_{trav} = 0°, β_{trav} = 0°. Cone model is misaligned. 109
5.4 Normalized surface pressure power spectra with traverse set to α_{trav} = -0.4°, β_{trav} = 0.2°. Cone model is aligned. 110
5.5 Comparison of pressure fluctuation PSD using PCB132 sensors at α = 0°. Conditions are: M = 7, $Re_{unit,\infty} = 9.2 \times 10^6$ /m, and $T_w/T_0 = 0.56$. Both datasets have been processed using Welch's FFT method. 112
5.6 Comparison of second mode amplitude results. 113
5.7 Comparison of PSE-Chem computed N factors. The H2K envelope has been extracted from Figure 15 in Ref. [37]. 114
5.8 H2K N factors for each gauge, and the frequencies of the most amplified disturbances. Reproduced using data from Figure 17 in Ref. [37]. 115

5.9 Comparison of the most amplified disturbance frequencies to those predicted using: (a) PSE-Chem, and (b) Howarth's approximation for the laminar boundary layer thickness [84] (described in Section 2.5.2). The HDT disturbance frequencies are extracted from the PSD presented in Figure 5.5. Results for H2K are generated using data from Figure 5 and Figure 17 in Ref. [37]. 116
5.10 Second mode amplitude and N factor comparison to PSE-Chem computations. Parameters are calculated using the method described by Marineau et al. [54], with more details in Section 2.5.4 and Section 6.2.3. 117
5.11 Comparison of PCB132 surface pressure power spectra results at $\alpha = 6°$. PSD results shown for $\phi = 0°$, 90°, and 180°. 120
5.12 Comparison of integrated PSD results using PCB132 sensors at $\alpha = 6°$. 121
5.13 Comparison of integrated PSD results using PCB132 sensors at $\alpha = 9°$. 122
5.14 PCB-detected transition front. A comparison between HDT and H2K. $M_\infty \approx 7$, $Re_{unit} = 9.2$ x 10^6 /m (H2K) - 9.2 x 10^6 /m (HDT), $r_N = 1.6$ mm, $T_w/T_0 = 0.56$. 124

6.1 Cone surface pressure as a function of axial location. Kulite pressures are compared to those calculated using Cheng's correlation [202, 203], Taylor-Maccoll computations, and an Eilmer4 axisymmetric blunted cone simulation. The HDT condition is at: $M_\infty = 7.0$, $Re_{unit,\infty} = 12.3 \times 10^6$ /m, $T_w/T_0 = 0.64$, $\alpha = 0°$. 128
6.2 HDT facility profile for $\alpha = 0°$ results. P_0 and T_0 values for each test-time are provided in Table 6.1 129
6.3 Power scalograms using the continuous wavelet transform for HDT plateau #1 at $\alpha = 0°$. The scalograms bounds are consistent, ranging from 0 to 0.3. 131
6.4 Surface pressure fluctuation power spectral density using the continuous wavelet transform and fast Fourier transforms (FFT), for HDT plateau #1 at $\alpha = 0°$. 132
6.5 Integrated PSD and heat flux results for HDT plateau #1 at $\alpha = 0°$ The grey area shows the standard deviation of results over the five shots. The turbulent wall heat fluxes are estimated from van Driest [154], whereas the laminar wall heat fluxes are approximated using the adapted Blasius solution (described in [24]). 132
6.6 Transition Reynolds number plotted against the Reynolds number based on nosetip radius. The Stetson results are from Ref. [94], using an 8° cone at Mach 6 and various $Re_{unit,\infty}$ and R_N. The HDT result is at Mach 7, $Re_{unit,\infty} = 12.3 \times 10^6$ /m, $T_w/T_0 = 0.59$, Noise = 1.49%, $R_N = 1.25$ mm. 134

6.7 Power scalograms using the continuous wavelet transform for HDT plateau #3 at $\alpha = 0°$. The scalograms bounds are consistent, ranging from 0 to 0.3. 136
6.8 Surface pressure fluctuation power spectral density using the continuous wavelet transform and fast Fourier transforms, for HDT plateau #3 at $\alpha = 0°$. 137
6.9 Integrated PSD and heat flux results for HDT plateau #3 at $\alpha = 0°$. The grey area shows the standard deviation of results over the five shots. The turbulent wall heat fluxes are estimated from van Driest [154], whereas the laminar wall heat fluxes are approximated using the adapted Blasius solution (described in [24]). 137
6.10 PSE-computed critical N-factor envelope for HDT plateau #1 and #3. 138
6.11 PSE-computed disturbance frequencies compared to second mode frequencies measured in HDT for plateau #1 and #3. The predicted frequencies using Howarth's boundary layer thickness approximation is also included [84]. 140
6.12 Comparison of the HDT experiment growth rate fit (d) and the PSE-computed growth rate (α) for both HDT plateaus. 141
6.13 Comparison of the HDT experimental N factor and the PSE-computed N-factor for both HDT plateaus. 142
6.14 Comparison of N factors between HDT, NASA Langley Research Center's 20inch Wind Tunnel (NASA LaRC), the Hypersonic Ludwieg Tube Braunschweig (HLB) and the Sandia National Laboratories Hypersonic Wind Tunnel (HWT-8). Annotations have been included to show key features. The LaRC, HLB, and HWT-8 results are using a sharp nosepiece, with each dataset extracted from Ref. [54]. The yellow and grey arrows show the HT-detected transition locations for HDT plateau #1 and #3 , respectively. 144
6.15 Comparison of the stability Reynolds number (R_0) to conventional wind tunnel results presented by Marineau et al. [54]. 144
6.16 Comparison of the HDT maximum second mode amplitude to conventional wind tunnel results collated by Marineau et al. [54] and Fedorov [95]. 146
6.17 Power scalograms using the continuous wavelet transform for the T4 Nominal condition: $M_\infty = 7.1$, $Re_{unit,\infty} = 11.9 \times 10^6$ /m, $T_w/T_0 = 0.13$, $\alpha = 0°$, $R_N = 1.55$ mm. The scalograms bounds are consistent, ranging from 0 to 0.1. 149

6.18 Surface pressure fluctuation power spectral density using the continuous wavelet transform and fast Fourier transforms, for the T4 nominal condition: $M_\infty = 7.1$, $Re_{unit,\infty} = 11.9 \times 10^6$ /m, $T_w/T_0 = 0.13$, $\alpha = 0°$, $R_N = 1.55$ mm. The Welch PSD is calculated using the fluctuation data for four repeated shots. 150
6.19 Mean integrated PSD amplitude for the T4 nominal condition: $M_\infty = 7.1$, $Re_{unit,\infty} = 11.9 \times 10^6$ /m, $T_w/T_0 = 0.13$, $\alpha = 0°$, $R_N = 1.55$ mm. 151
6.20 PSE-computed disturbance frequencies compared to Howarth's approximation [84] and the peak PSD frequencies measured in HDT. . 152
6.21 Effect of T_w/T_0 distribution on wavelet scalograms: $M_\infty = 7.1$, $Re_{unit,\infty} = 11.0 \times 10^6$ /m, $T_w/T_0 = 0.13 - 0.19$, $Re_x = 3.0 \times 10^6$, $\alpha = 0°$, $R_N = 1.55$ mm. 154
6.22 Effect of T_w/T_0 distribution on power spectral density (calculated using Welch's method): $M_\infty = 7.1$, $Re_{unit,\infty} = 11.0 \times 10^6$ /m, $T_w/T_0 = 0.13 - 0.19$, $\alpha = 0°$, $R_N = 1.55$ mm. 154
6.23 Effect of T_w/T_0 distribution on integrated PSD amplitude: $M_\infty = 7.1$, $Re_{unit,\infty} = 11.0 \times 10^6$ /m, $T_w/T_0 = 0.13 - 0.19$, $\alpha = 0°$, $R_N = 1.55$ mm. The circle markers indicate sensors where no peak was observed in the PSD ($f_c = 850$ kHz assumed). 155
6.24 Wall temperature distribution for $P = 15$ W, including the location of the first observed peak in the PSD. $M_\infty = 7.1$, $Re_{unit,\infty} = 11.0 \times 10^6$ /m, $T_w/T_0 = 0.13 - 0.19$, $\alpha = 0°$, $R_N = 1.55$ mm. 156
6.25 PSE-computed critical N-factor envelope for T4 nominal condition using multiple wall-temperature distributions. $M_\infty = 7.1$, $Re_{unit,\infty} = 11.9 \times 10^6$ /m, $T_w/T_0 = 0.14 - 0.19$, $R_N = 1.55$ mm. 156
6.26 Effect of $Re_{unit,\infty}$ on wavelet scalograms: $M_\infty = 7.1$, $Re_{unit,\infty} = 5.2 - 11.9 \times 10^6$ /m, $T_w/T_0 = 0.13$, $\alpha = 0°$, $R_N = 1.55$ mm. 158
6.27 Effect of $Re_{unit,\infty}$ on power spectral density (calculated using Welch's method): $M_\infty = 7.1$, $Re_{unit,\infty} = 5.2 - 11.9 \times 10^6$ /m, $T_w/T_0 = 0.13$, $\alpha = 0°$, $R_N = 1.55$ mm. The gold markers illustrate the peak frequency predicted by Howarth's approximation [84]. 158
6.28 Effect of $Re_{unit,\infty}$ on integrated PSD amplitude: $M_\infty = 7.1$, $Re_{unit,\infty} = 5.2 - 11.9 \times 10^6$ /m, $T_w/T_0 = 0.13$, $\alpha = 0°$, $R_N = 1.55$ mm. The circle markers indicate sensors where no peak in the power spectra was observed ($f_c = 850$ kHz assumed). 159
6.29 Comparison of the integrated PSD amplitudes between T4 and HEG and HIEST [54]. 160

6.30 Comparison of the power spectral density results for similar gauges in T4 and HDT. The T4 condition is: $M_\infty = 7.1$, $Re_{unit,\infty} = 11.4 \times 10^6$ /m, $T_w/T_0 = 0.13$. The HDT condition is: $M_\infty = 7.0$, $Re_{unit,\infty} = 8.4 \times 10^6$ /m, $T_w/T_0 = 0.56$. The PSD for the HDT condition is plotted up to 450 kHz, as higher frequencies are affected by the noise floor. 161

6.31 Comparison of the non-dimensional frequency, F. Measurements in HDT and T4 are compared to PSE-Chem computations, the estimated frequency using the Howarth boundary layer thickness approximation, and the result presented by Marineau et al. for the HWT-8 facility using a sharp cone [54]. 163

7.1 HIFiRE-1 descent transition map. Data is extracted from Figure 25 in [32]. PHBW1 - PHBW3 are measurements from high frequency Kulite pressure transducers in flight. HT3 is a high frequency Vatell heat transfer gauge, and the dot-dashed line given by Re_{tr} is the low-frequency transition measured by a Medtherm coaxial gauge in flight. 167

7.2 Contour maps of rms pressure fluctuations from a high frequency Kulite pressure transducer as measured in flight (PHBW1). Taken from Figure 18 in Ref. [32]. The black line shows the transition front as measured using PHBW sensors. The transition onset is defined by the initial rise in normalized high frequency rms. Red diamonds show the transition locations measured using the Vatell thin-film thermopile heat transfer gauges. [31, 32] 170

7.3 Illustration of HDT test conditions, when compared to the HIFiRE-1 flight descent trajectory [26, 31, 32] 171

7.4 Cone surface pressure as a function of azimuth for HDT Conditions 1, 2, and 3. Kulite pressures are compared to those calculated using Cheng's correlation [202, 203]. 173

7.5 HDT criterion for PCB detected transition onset. The criterion is applied to the result at HDT condition 3 for the model at $\alpha = 8°$. . 175

7.6 Integrated surface power spectra for HIFiRE-1 descent conditions, sweeping through both $Re_{unit,\infty}$ (i.e. time) and the uncertainty in angle of attack, α. The power spectra has been calculating using Welch's FFT method, and integrated between f = 100 - 600 kHz. . . 178

7.7 Transition onset lines for HDT condition #3 over the sweep in angles of attack: $5° \leq \alpha \leq 10°$. The figure has been annotated to show key features, including the HIFiRE-1 windward transition observed at $Re_{x,tr} = 4.7 \times 10^6$. The onset criteria is described in Section 7.4. . . 179

7.8 Contour plots of rms surface pressure fluctuation for two frequency bands, corresponding to a suspected travelling crossflow instability and a stationary crossflow / second mode instability. The pink dashed line corresponds to the PCB-detected transition front. The frequency bands are $f = 11 - 80$ kHz and $f = 100 - 500$ kHz. The green diamonds correspond to the thin-film gauge heat transfer detected onset. The green arrow at $\phi = 0°$ indicates that all sensors lied on the laminar baseline along the windward ray. 183
7.9 Transition front comparison between HDT and HIFiRE-1 flight. The green arrow indicates that HT-detected transition onset was not observed along the windward ray in HDT. 183
7.10 Locations of sensors that showed clear low frequency or high frequency peaks in the PSD. The marker colours are used to identify the frequency at each particular location. The red dashed line shows the PCB-detected transition front, extracted from the rms contours. . . 184
7.11 Examples of power spectral density and RMS amplitudes of pressure fluctuations. Results are presented for sensors along the $\phi = 90°$ array. The figure is annotated to illustrate the various stages of disturbance growth, as described in the text. 186
7.12 Comparison of rms pressure fluctuation contours for HDT plateau #1 and HDT plateau #3, with results presented for both frequency bands. The HDT plateau #1 condition is: $Re_{unit,\infty} = 12.3$, $M_\infty = 7.0$, $T_w/T_0 \approx 0.58$, noise $\approx 1.49\%$. The HDT plateau #3 condition is: $Re_{unit,\infty} = 12.3$, $M_\infty = 7.0$, $T_w/T_0 \approx 0.64$, noise $\approx 0.44\%$. 188
7.13 Effect of increased freestream disturbances on the PCB-detected transition onset. Results from HDT plateau #1 (noise $\approx 1.49\%$) are compared to HDT plateau #3 (noise $\approx 0.44\%$), with the Reynolds number and Mach number otherwise matched. 189
7.14 Effect of increased freestream disturbances on multiple sensors along the $\phi = 90°$ array. Results from HDT plateau #1 (noise $\approx 1.49\%$) are compared to HDT plateau #3 (noise $\approx 0.44\%$), with the Reynolds number and Mach number otherwise matched. 190
7.15 Effect of HDT facility plateau on laminar pressure fluctuation PSD. The sensor is at $Re_x = 2.6 \times 10^6$, $\phi = 45°$, as illustrated by the hexagram markers in the accompanying rms magnitude contours (both for low frequency band). 191

8.1 Computed streamlines around a sharp cone at $\alpha = 8°$. Parameters computed using Cheng's correlations [202, 203] for the nominal condition: $M_\infty = 7.0$, $Re_{unit,\infty} = 12.3 \times 10^6$ /m, $T_w/T_0 = 0.64$. . . . 202

A.1 Roughness characterisation for the junction between the front segment and the nosepiece. 208
A.2 Roughness characterisation for an artificial PCB132 sensor inside the HDT 7° cone model. 208
A.3 Roughness characterisation for a PCB132 sensor housed inside neoprene tubing for the RST 7° cone model. 211

B.1 HDT facility required P_{fill} as a function of targeted supply pressures over multiple facility plateaus. The dashed line is the linear relationship used for the Mach 7 nozzle ($T_{fill} \approx 500$ K), as described in Equations B.1 - B.4. 214

C.1 Comparison of Purdue measured PSD ratio and Chaudhry's DNS computations. Taken from Figure 10d in Ref. [197]. Geometries are: $r_{\text{Purdue,large}} = 3.60$ mm, and $r_{\text{Purdue,small}} = 1.50$ mm. 216
C.2 Effect of Pitot probe geometry on post-shock pressure fluctuations for the HDT Mach 7 nozzle plateau #1. Results are shown for Pitot probe located on the nozzle centreline. 218
C.3 Comparison of PSD ratio R to DNS simulations from Chaudhry et al. (for the Purdue probe geometry and flow conditions, taken from Fig 9d in Ref. [197]). HDT conditions are $M_\infty = 7.0$, $Re_{unit,\infty} = 10.7 \times 10^6$ /m. Gauge location is on centreline, $r_{large} = 6.36$ mm and $r_{small} = 3.18$ mm. 219
C.4 Transfer function for the BAM6QT probe, $M_\infty = 6$, $T_0 = 500$ K. Taken from Figure 7 in Ref. [215]. The dashed lines correspond to integer multiples of the standoff frequency, f_Δ. 221
C.5 PSD rebuild and ratio results ($R_{L,S}$ and $R_{M,S}$) with a focus on the higher frequency PCB132 measurements. Results are for the centreline Pitot probe. 223

List of Tables

2.1 Examples of second mode disturbance speeds in conventional wind tunnels over varying conditions. 21

2.2 A summary of hypersonic facilities used to collate measurements of the second mode instability by Marineau et al. [54] and Fedorov et al. [95]. For further details, consult Table 1 in Ref. [54], and Table 1 in Ref. [95] 28

3.1 Summary of anticipated test times and number of PCB132 data points from each facility: HDT, T4, and T6. 75

4.1 Variation in HDT facility conditions using the Mach 7 nozzle for multiple plateaus. This variation is calculated for the $P_{fill} = 2485$ kPa and $T_{fill} = 537$ K condition, with facility profiles shown in Figure 4.2 89

4.2 Sensor locations for various rake lateral positions. Cells are colour-coded to illustrate the radial locations where measurements are taken over the entire frequency range (1 kHz $\leq f <$ 1000 kHz). One probe is marked N/A, as the Kulite in this probe was damaged throughout the entire campaign. 90

4.3 Percentage noise results as a function of HDT facility plateau, using the time domain (RMS_{time}) and frequency domain (RMS_{PSD}) methods. The cap geometry is "small", and it is located on the nozzle centreline. 100

4.4 Percentage noise results as a function of distance from nozzle centreline, using the frequency domain (RMS_{PSD}) method. The cap geometry is "small". Results are shown for facility plateaus #1 and #3. 102

5.1 Summary of conditions used in the HDT instability verification experiments. Conditions and model features are compared to those obtained in H2K [35, 36]. 108

6.1 HDT condition for $\alpha = 0°$ results. The condition is scaled from HIFiRE-1 flight based on the nose radius used ($R_N = 1.25$ mm). The plateau #1 values for T_0, Re_{unit}, and T_w/T_0 are the average quantities over test time. The variation is less than $\pm 5\%$ for each parameter. 129
6.2 T4 condition for $\alpha = 0°$ results. The quoted facility values are the average of all shots at each condition. 147

7.1 HDT facility nominal conditions for mapping the time, angle of attack, and $Re_{unit,\infty}$ during the HIFiRE-1 descent transition phase of flight. The scaled conditions are for the HDT 7° cone model with its $R_N = 1.25$ mm nosepiece. 172
7.2 Effect of angle of attack on disturbance amplitude for HDT Condition 3. The PSD integration bounds are $f = 100 - 600$ kHz. Re_x values correspond to the onset of the increase in disturbance amplitudes above laminar baseline levels, as described in Section 7.4. 179
7.3 Combinations of traverse α and β used to get instability and heat transfer data at a finer resolution of azimuths. 182

A.1 Instrumentation locations in the HDT 7° Cone Model. 'x' is the axial distance from the apex of a theoretically-sharp nosepiece to the gauge. 206
A.2 HDT 7° Cone Model roughness information. R_a is the average roughness of the profile, and R_q is the rms roughness of the profile. The mean and standard deviation (std) of multiple profiles are presented. Only one profile was taken for the PCB sensor, so no standard deviation is calculated. 207
A.3 Instrumentation locations in the RST 7° Cone Model. 'x' is the axial distance from the apex of a theoretically-sharp nosepiece to the gauge. 210
A.4 HDT 7° Cone Model roughness information. R_a is the average roughness of the profile, and R_q is the rms roughness of the profile. The mean and standard deviation (std) of multiple profiles are presented. Only one profile was taken for the PCB sensor roughness and the Neoprene sleeve roughness. 210

C.1 Pitot probe details for multiple cap sizes. The probe geometry is consistent for PCB and Kulite sensors. 217

Nomenclature

A	Disturbance amplitude at specified location
A_0	Initial amplitude at the beginning of disturbance growth.
C_f	Skin friction coefficient
d	Growth rate calculated using experimental measurements
f	Frequency
F	Non-dimensional frequency, $F = \frac{2\pi f}{u_\infty Re_{unit,\infty}}$
H	Enthalpy
L	Length
M	Mach number
N	N factor used for the e^N method
Noise %	The post-shock RMS pressure fluctuations over frequencies 1 kHz $\leq f \leq$ 1000 kHz, as measured using a Kulite and PCB132
P	Pressure, kPa
P	Power, W
r	Distance from nozzle centreline
R	Stability Reynolds number, $\sqrt{Re_x}$
Re	Reynolds number
t	Time
T	Temperature, K
T_w/T_0	Wall-to-total temperature ratio
u	Velocity
x	Axial component of Cartesian coordinate system

Greek symbols

α . . . . . Angle of attack, °

α . . . . . Growth rate, calculated using PSE-Chem

β . . . . . Angle of yaw, °

δ . . . . . Boundary layer thickness

θ_c . . . . . Cone half-angle

λ . . . . . Wavelength

μ . . . . . Viscosity

σ . . . . . Integrated growth rate from the Parabolized Stability Equations

ϕ . . . . . Azimuthal location. $\phi = 0°$ corresponds to the windward ray.

ϕ . . . . . Diameter

φ . . . . . Wind-fixed azimuthal location

χ . . . . . Transfer function for freestream disturbances

Subscripts and superscripts

0 . . . . . Stagnation conditions

∞ . . . . . Freestream condition

c . . . . . Cone surface condition

c . . . . . Centered disturbance frequency

crit . . . . . Critical, used to define the initial deviation of the N factor

e . . . . . Boundary layer edge

max . . . . . Maximum

N . . . . . Nosetip of the cone

t . . . . . Transducer face

tr . . . . . Transition location

unit . . . . . Facility unit Reynolds number, /m

w . . . . . Wall

x . . . . . x-location

Acronyms

AEDC	Arnold Engineering Development Complex
AFRL	Air Force Research Laboratory
BAM6QT	Purdue University's Boeing/U.S. Air Force Office of Scientific Research Mach 6 Quiet Tunnel
BLT	Boundary layer transition
CWT	Continuous wavelet transform
DLR	German Aerospace Center
DHTG	Diamond heat transfer gauge
DNS	Direct Numerical Simulation
DSTO	Australian Defence Science and Technology Organisation
FFT	Fast Fourier Transform
HDT	The Oxford High Density Tunnel
HEG	DLR German Aerospace Center High Enthalpy Shock-Tunnel Göttingen
HIEST	Japan Aerospace Exploration Agency's High Enthalpy Shock Tunnel
HIFiRE	Hypersonic International Flight Research Experimentation
HLB	Technical University of Braunschweig's Mach 6 Hypersonic Ludwieg Tube Braunschweig
HT	Heat transfer
LaRC	NASA Langley Research Center
LST	Linear Stability Theory
PHBW	High Bandwidth Pressure Transducer, from HIFiRE-1 flight
PSD	Power spectral density
PSE	Parabolized Stability Equations
RMS	Root-mean-squared
RST	Reflected shock tunnel
RV	Re-entry vehicle
STABL2D	Stability and Transition Analysis for hypersonic Boundary Layers
SNL HWT	Sandia National Laboratories Hypersonic Wind Tunnel
TFG	Thin film gauge
VKI	von Karman Institute for Fluid Dynamics

xxx

1 Introduction

1.1 Hypersonic Boundary Layer Transition

Boundary layer transition (BLT) is a field that is of high importance when considering the performance and survivability of hypersonic vehicles. The vehicle drag, surface heat transfer rate and skin friction all increase significantly when the boundary layer transitions from a laminar to a turbulent state [1, 2, 3, 4, 5, 6]. In some cases, unexpected asymmetric transition can also negatively impact the vehicle flight dynamics and aerostability, resulting in BLT-induced dynamic motions that cause the vehicle to depart from its intended trajectory [6, 7].

There is frequently a desire to delay transition to maintain the laminar aerodynamic heating loads and increase fuel efficiency [7]. In other cases, however, it is important to trip the boundary layer to enhance mixing or avoid boundary layer separation (e.g. at the inlet of a scramjet engine) [7, 8, 9]. Reed [7] states:

> The most effective strategy for control is to capitalized on the flow physics, to identify the relevant instability mechanisms and what affects them, and modulate the most unstable disturbances as they are just beginning to grow. A fundamental understanding of the laminar-turbulent transition process will lead to efficient control strategies.

The physics of the transition process is complex and currently not adequately understood for predictive purposes in hypersonic flows [6]. Most predictive methods rely on engineering correlations (such as Re_θ/M_e [10]) or linear semi-empirical approaches (such as the e^N method [11, 12, 13]), many of which do not capture important parts of the transition process and are limited to particular geometries or flight trajectories [7].

The Re-Entry F flight test of a ballistic re-entry vehicle (RV) provides an example of the sharp increase in aeroheating caused by the onset of BLT, and the inability to accurately predict its location. The surface heat transfer is shown in Figure 1.1 [14, 6]. As the flow transitions from a laminar to a turbulent state, the aeroheating rises by a factor of 3 - 8, and there is frequently an overshoot on the predicted turbulent heat flux before relaxing [5]. There is quite good agreement in heat transfer rates for both the laminar and turbulent regions, once the transition location is known [5]. However, empirical correlations for calculating the onset and extent of transition are uncertain by a factor of three or more [5]. Predicting the transition location therefore dominates the uncertainty when estimating the overall heat transfer to a vehicle.

The uncertainty in predicting the transition location frequently results in ultra-conservative designs, leading to a reduction in mission capacity for hypersonic vehicles. This is highlighted in a report from the Defence Science Review Board on the National Aerospace Plane (NASP) in 1988 [15]:

> Estimates [of transition] range from 20% to 80% along the body... The estimate made for the point of transition can affect the design vehicle gross take-off weight by a factor of two or more.

Other applications hindered by this lack of understanding include ballistic and lifting re-entry vehicles (RVs), air-breathing cruise vehicles, high-speed missiles, and high-speed reconnaissance aircraft [5].

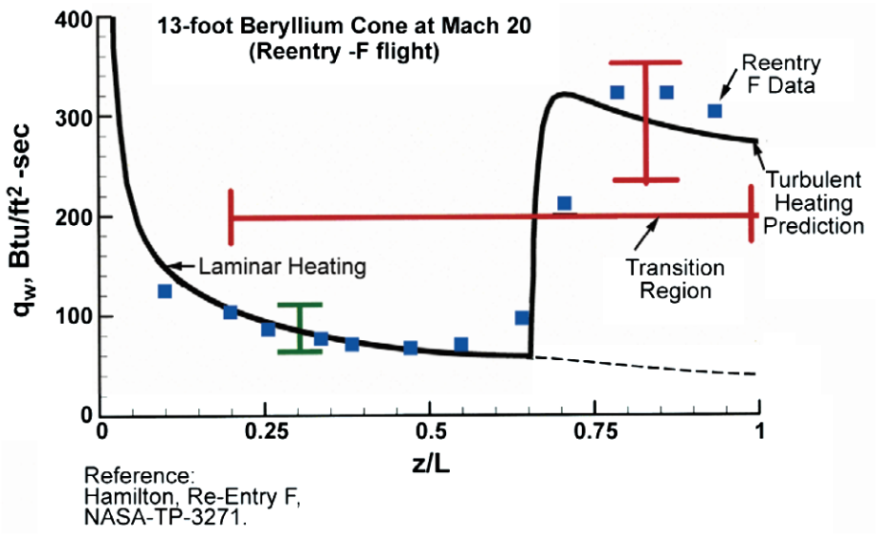


Figure 1.1: Surface heat transfer on the Re-Entry F ballistic vehicle [14], taken from Figure 1a) in Ref. [6]. The flight vehicle is a 4m beryllium cone with a half-angle of 5, re-entering at an angle of attack (α) near zero, a Mach number of 20 and a total enthalpy of $\approx$ 18 MJ / kg [14].

Classical attempts to correlate the transition 'point' with individual parameters have been limited in accuracy and reliability [5]. To adequately understand the transition problem for location-prediction purposes, controlled measurements are being taken of the instabilities that lead to transition. The dominant mechanism is dependent on the geometry, boundary layer mean flow properties, and external disturbances. For example, the streamwise acoustic Mack mode instabilities are expected in two-dimensional boundary layers in hypersonic flows [16, 17, 18], crossflow instabilities are observed in three-dimensional boundary layers where large pressure gradients exist [19, 20, 21, 22], and Görtler instabilities are associated with centrifugal effects on concave surfaces [23, 5, 7].

An illustration of a transitional flow with relatively low disturbance levels is provided in Figure 1.2, in the form of a steady flow over a flat plate (taken from Figure 5-28 in Ref. [24]). The process of receptivity determines the initial amplitudes of the external disturbances once they enter the boundary layer. Depending on the instabilities and the state of the boundary layer in question, some disturbances will grow whilst others will decay. Once a disturbance has grown significantly, or if

the initial amplitude is large enough, the growth becomes non-linear and the wave breaks down to turbulence. There is then a finite transitional region containing turbulent spots with locally intense fluctuations. Finally, the turbulence spots coalesce to form a fully turbulent flow.

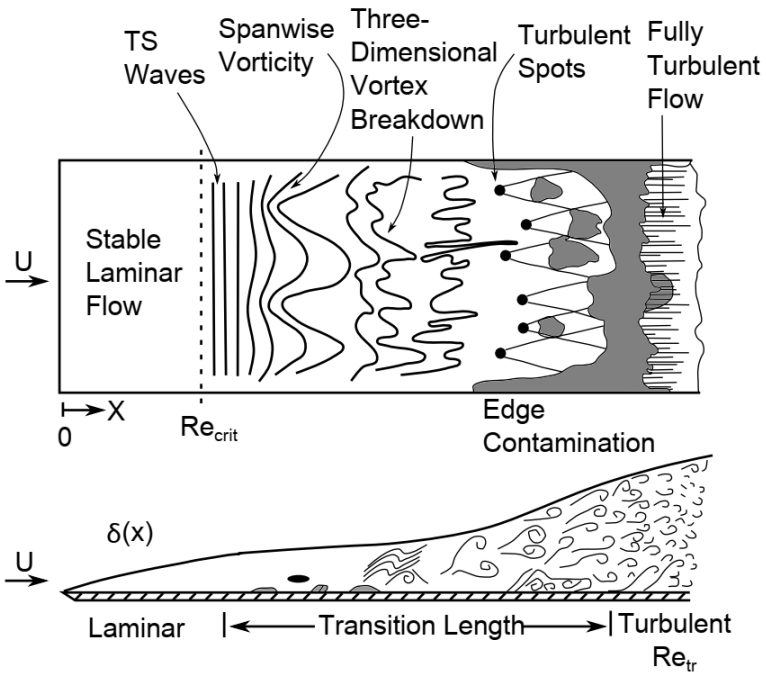


Figure 1.2: Illustration of a boundary layer development: laminar, transitional, and turbulent boundary layer over a flat plate [24].

After the boundary layer has transitioned to turbulence, it is not possible to identify the instability mechanism that led to the breakdown of the laminar boundary layer. The complexities of the transition process also make it difficult to characterize the breakdown by identifying an individual transition 'point'. This highlights the need to understand the receptivity of the boundary layer and the instabilities that develop thereafter.

Ground facilities are used extensively worldwide to conduct boundary layer transition research at flight-representative conditions. One of the main benefits is that it is significantly cheaper to operate a wind tunnel than it is to conduct a flight

test [25]. An additional benefit is that it is often possible to take measurements using instrumentation and optics which would otherwise not be accessible in flight [25]. A major drawback, however, is that no individual facility can capture all conditions experienced in flight. Typically, this means that the freestream disturbance environment, Reynolds number, Mach number, wall-to-total temperature ratio, and total enthalpy are not all matched. Thus, a range of facilities are often used to match the parameters that are critical to the phenomena being studied, and errors are inevitably introduced when extrapolating ground test observations to flight.

1.2 Research Objectives

The primary objective for this research is to improve the understanding of hypersonic boundary layer instabilities, so that measurements from ground facilities can be more effectively used to inform physics based numerical transition models to aid in high-speed vehicle design. In particular, this work aims to provide high resolution data of instabilities at high angle of attack, and to provide additional insight into the role of freestream disturbances on the second mode instability at an angle of attack of 0°.

To achieve this, this work commissioned the Oxford HDT and was also the first experimental campaign in the facility. To enable meaningful instability measurements, this required a characterisation of the HDT freestream, and to establish confidence in the facility and processing methods for boundary layer instability measurements. The primary objective is then split into two separate transition problems of increasing complexity:

1. Second mode dominated transition

The aim is to investigate the role of freestream disturbance environments and wall-to-total temperature ratio on second mode dominated transition. Boundary layer instabilities are considered on a slender axisymmetric cone with small nose

bluntness, at an angle of attack of zero degrees. An example application is a missile re-entering the atmosphere without any pitch or yaw, where the second mode instability is expected to dominate transition at high Mach numbers.

The Oxford HDT is a Ludwieg Tube that is able to replicate the Mach numbers (M_∞) and Reynolds numbers ($Re_{unit,\infty}$) experienced in flight, though has higher wall-to-total temperature ratios (T_w/T_0) and freestream disturbance levels (noise %). This research aims to investigate the second mode instability at multiple quasi-steady test times with differing freestream disturbance levels, whilst keeping T_w/T_0 constant. The hope is that trends observed at varying freestream disturbance environments can eventually be extrapolated to flight, if the transition mechanisms remain unchanged.

The University of Queensland's T4 Stalker Tunnel is able to replicate the Mach numbers (M_∞), Reynolds numbers ($Re_{unit,\infty}$), and enthalpies (H_0) experienced in flight, though has higher freestream disturbance levels (noise %) and shorter test time. The objective of the T4 experiments is to investigate second mode growth at flight-representative wall-to-total temperature ratios, and to compare results with the higher T_w/T_0 HDT results. A secondary objective is to investigate the effect of wall temperature distributions, using a nosetip heater cartridge to replicate the front-end heating that is observed in flight.

2. Three-dimensional instabilities at high angles of attack

The second transition problem investigates the three-dimensional boundary layer that exists in regions containing strong circumferential pressure gradients. These gradients are observed on swept wings or when vehicles re-enter the atmosphere with pitch or yaw. For example, the HIFiRE-1 geometry was a 7° half-angle axisymmetric cone with small nose bluntness. The descent phase of the flight test provided a wealth of transition data at Mach 7 and high angles of attack: $\alpha \approx 6°$

- 13° [26, 27, 28, 29, 30, 31, 32, 33, 34]. The observed transition front was highly three-dimensional, and contained multiple discrepancies when compared to the only post-flight experiments conducted in DLR's H2K facility [35, 36, 37].

A key objective of the current research is to compare transition observations to the HIFiRE-1 flight dataset, so that ground experiments can be more effectively compared to flight. This expands on the H2K tests, incorporating much higher sensor resolution and conditions. Boundary layer instabilities are measured in the Oxford HDT using a 50% scale model, at the angles of attack and Reynolds numbers observed in flight. Particular care must also be given to the transition onset criterion, so that like-for-like comparisons can be made.

The current understanding of high-speed crossflow instabilities is limited when compared to the incompressible literature [22]. An additional objective is therefore to improve our understanding of the high-speed crossflow instability at various azimuths around the cone surface. The stationary and travelling crossflow instabilities are expected to play a role in the transition process at azimuths around the cone, along with the second mode instability. This research intends to investigate the characteristics of these disturbances, and examine how they change over multiple quasi-steady test times with differing freestream disturbance levels.

1.3 Organisation of thesis

Chapter 2: Literature review

This chapter aims to provide a summary of the literature relevant to this research. The various paths to transition are described, and details are provided about the instabilities that are expected to dominate at low and high angles of attack. The chapter concludes with a brief summary of parametric effects, focusing on slender body experiments.

Chapter 3: Experimental setup

Chapter 3 details the experimental setup and various processing methodologies. The Oxford High Density Tunnel (HDT) and The University of Queensland's T4 Stalker Tunnel are described, along with the two axisymmetric cone models. Information is then provided about the various instrumentation and processing methods used throughout the research.

Chapter 4: Freestream characterisation of the Oxford High Density Tunnel

This research represents the commissioning and first measurements in the Oxford HDT. Chapter 4 describes the freestream determination method for the facility, and characterises the post-shock freestream disturbance levels for multiple quasi-steady test times using the Mach 7 nozzle.

Chapter 5: Verification of boundary layer instability results in the Oxford High Density Tunnel

The objective of Chapter 5 is to verify the HDT facility, and the various processing methods, for boundary layer instability measurements. Boundary layer instability measurements are compared to a similar dataset obtained in DLR's H2K facility, and PSE-Chem stability computations. The HDT conditions are matched to the H2K campaign, and results are compared at low and high angles of attack.

Chapter 6: Boundary layer instabilities at $\alpha = 0°$

Results are presented at $\alpha = 0°$ in the Oxford HDT and The University of Queensland's T4 Stalker Tunnel. The effect of freestream disturbances is investigated in the HDT results, whereas the T4 measurements investigate the effects of wall temperature distributions and facility Reynolds number. Results from both facilities are compared to stability computations and similar conventional tunnels.

Chapter 7: Boundary layer instabilities at angle of attack

Chapter 7 investigates the transition front and boundary layer instabilities at high angles of attack. Results are compared to the HIFiRE-1 flight test wherever possible. The three-dimensional boundary layer instabilities are scrutinized at various azimuths around the cone.

2
Literature Review

This chapter reviews some of the literature that is most relevant to this research. The various paths to transition are described. Details are provided about the second mode instability and the crossflow instabilities, as these are expected to be the dominant instability mechanisms in this research. Finally, the parameters that impact boundary layer transition in the current work are discussed, with a focus on slender-body experiments. An overview of hypersonic ground facilities is provided in Chapter 3, along with details about the Oxford HDT and The University of Queensland's T4 Stalker Tunnel.

2.1 Paths to Transition

High speed boundary layer transition processes are dependent on numerous parameters in the mean flow, as well as the type of disturbances that are present [18]. The understanding of the transition process has evolved over several decades, particularly with recent progress in transient growth mechanisms [38, 39, 40, 41, 42, 43, 44]. The most recent road map is shown in Figure 2.1 [18]. This illustrates the various paths to turbulence for boundary-layer flows, as a function of increasing

disturbance level.

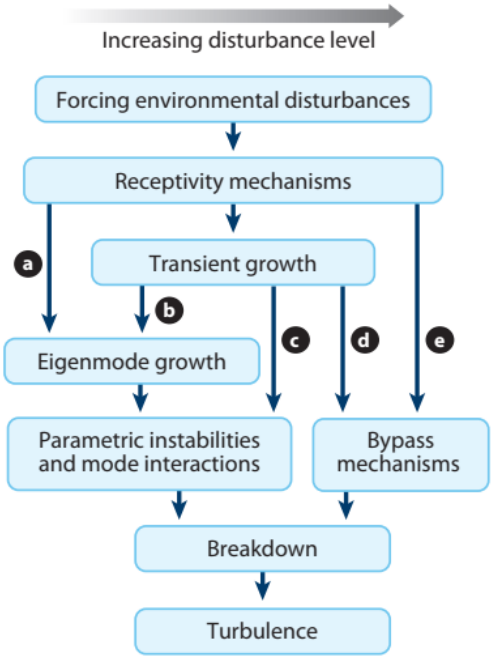


Figure 2.1: Paths to turbulence in boundary-layer flows. Figure taken from Fedorov [18], with paths originally devised by Morkovin et al. [45]

The transition process is initiated by a growth of disturbances, which originate on the body or in the freestream. Disturbances originating on the body may come in the form of roughness, joints in components, and surface waviness, whilst some of the freestream disturbances include vorticity, acoustic waves, entropy, and particles [5]. The receptivity mechanisms outline the way that environmental disturbances interact with the boundary layer and the surface of the body[1]. The interaction between the disturbances and the instability waves then dictates whether the waves will grow or decay [47]. The instabilities are affected by the mean boundary layer flow, and are therefore heavily dependent on the flow properties and surface geometry. Depending on the initial amplitude, frequency and phase of these initial boundary layer disturbances, different paths to transition may follow.

[1] A review of boundary-layer receptivity to external acoustic and vortical disturbances is given by Saric et al. [46]

Path a): Eigenmode growth (natural transition)

Path a) is the traditional natural transition path to turbulence for low-disturbance environments where modal growth is dominant. It is associated with boundary layer instabilities such as the first and second modes, crossflow instability, and Görtler vortices [18]. The initial growth of these disturbances is described by linear stability theory (LST) of primary modes [46]. This growth is relatively slow, and can be quite accurately predicted using the e^N LST method. As the amplitude grows, three-dimensional and non-linear interactions occur in the form of secondary instabilities, and cause the boundary layer to breakdown.

Paths b), c), and d): Transient growth

Paths b) - d) are affected by transient growth, and are defined separately using transient growth theory. Transient growth occurs when two stable modes interact, undergo algebraic growth, and then decay exponentially [48, 39, 46]. Reshotko suggests that the largest effects come from non-orthogonal superposition of two slightly damped, highly oblique (nearly streamwise) T-S and Squire modes [39].

- Path b) is the case that transient growth provides a higher amplitude to the eigenmode growth described by path a) [39]. These modes then continue to grow linearly, before three-dimensional and non-linear interactions cause the boundary layer to breakdown.
- Path c) has continually higher amplitudes at the end of transient growth. It is the case where eigenmode growth is bypassed, or that the transient growth is large enough to directly excite secondary instabilities and interactions between modes [39].
- In Path d), the transient growth associated with large environmental disturbances results in a full spectrum of disturbances in the boundary layer, completely bypassing the linear eigenmode growth [39].

Transient growth theory has emerged as a possible cause for laminar-turbulent transition in multiple cases, particularly where modal amplification is weak. An example of this is the "blunt body paradox", where a transition reversal is observed for geometries such as circular cones when the nose-tip bluntness is progressively increased.

Path e): Bypass mechanisms

Bypass transition has been used to define transition paths that cannot be explained via modal amplification of small-amplitude disturbances or transient growth theory [45]. It typically occurs when forcing disturbances are so strong that the modal growth of linear disturbances is bypassed completely [47, 46]. Linear stability theory and transient growth theory fail to predict the transition location, as turbulent spots occur and the boundary layer quickly becomes fully turbulent. Examples of large external disturbances include high freestream turbulence levels, and significant surface roughness [49, 50, 39, 46].

2.2 Linear Stability Theory and the Parabolized Stability Equations

Linear Stability Theory

Linear stability theory (LST) is used to investigate whether a sinusoidal disturbance becomes amplified or damped when it enters a given laminar flow [17]. It predicts disturbance growth throughout the first stage of eigenmode development (Path A in Figure 2.1), though does not capture any of the non-linear breakdown processes or the transition location. The theory predicts the wave number, Reynolds number, phase velocity, as well as the amplification and damping rates of disturbances[2].

The linear stability theory approach is to decompose a laminar flow into the sum of a steady mean flow and an unsteady small perturbation, which is assumed to be a sine wave. The Navier-Stokes equations are linearized and rewritten using this decomposition, with terms that include products of perturbations assumed to

[2]Extensive reviews of linear stability theory can be found in references [51, 17]

be negligible. The perturbations are assumed to propagate within the boundary layer independently of each other. They are referred to as "modes", and are described according to Eq. 2.1, where: $q(y)$ refers to the amplitude function of the specified flow quantity, x, y and z correspond to the coordinate system used, and the variables t, α, β,and ω denote time, wavenumbers in x and z direction, and angular frequency respectively [17].

$$q'(x, y, z, t) = q(y)e^{i(\alpha x+\beta z-\omega t)} \tag{2.1}$$

The solution to the eigenvalue problem determines whether these perturbations grow or decay. It can be solved using temporal theory (where α, β are real, ω is complex and the amplitude varies with time) or the spatial theory (where α, β are complex, ω is real, and the amplitude varies with space) [17]. For most practical applications a spatial stability analysis is of interest. When considering eq. 2.1, if $-\alpha_i > 0$ the wave will be amplified due to an unbounded exponential growth. $-\alpha_i = 0$ indicates that the wave is neutral, whilst $-\alpha_i < 0$ suggests that the wave is damped.

Parabolized Stability Equations

Unlike linear stability theory (LST), the parabolized stability equations (PSE) incorporate the history of the disturbance and the streamwise variation of the basic flow [52]. The disturbance equations are parabolized using the method proposed by Herbert [52]. The equations partially account for nonparallelism, and the initial boundary value is suitable for analysing exponential as well as transient growth of disturbances [52]. Linearization of the parabolized stability equations allows individual non-interacting disturbance modes to be considered [53]. Solving the linear PSE equations instead of linear stability theory therefore makes it possible to track disturbances as they move through and interact with the boundary layer.

2.3 The e^N method and PSE-Chem solver

2.3.1 e^N method

One method for predicting transition is by using the semi-empirical e^N method to correlate calculated disturbance growth rates with experimentally measured transition locations [11, 12, 13]. The N-factor for the most amplified wave angles is calculated by integrating the growth rates (σ) between two separate streamwise locations. The disturbance growth rate is computed from the local streamwise wavenumber (α) and the disturbance kinetic energy (E):

$$\sigma = \alpha_i + \frac{1}{2E}\frac{dE}{dS} \tag{2.2}$$

The N factor can then be calculated as

$$N = \ln\left(\frac{A}{A_0}\right) = \int_{s_0}^{s} -\sigma dx \tag{2.3}$$

where A is the amplitude at a given streamwise location (s), and A_0 is the initial amplitude at the beginning of disturbance growth.

The critical N factor (N_{crit}) must be correlated for each experimental facility. Lower N-factors are expected in environments with higher freestream disturbances. This is due to larger initial amplitudes (A_0), resulting in a smaller growth before boundary layer destabilization occurs [13]. For example, the conventional tunnel results collated by Marineau et al. observed a N_{crit} range of $\approx 3 - 7.5$ [54]. These results calculated the initial disturbance (A_0) according to Marineau's method and have assigned N_{crit} as the first deviation from the PSE-Chem calculated envelope [54] (see Section 2.5.4). The critical N factors in quiet tunnels and flight are expected to be larger, in the order of $N_{crit} \approx 8 - 11$ [55, 56].

The e^N method has multiple limitations. It does not include any of the physics of the transition process, and it does not account for the receptivity of the boundary layer. It also cannot be used to predict transition in scenarios involving transient growth of bypass mechanisms. Lastly, it does not calculate the amplitude of the initial disturbance[3]. Despite these limitations, the e^N method is considered to be the most reliable and practical method for estimating transition location in wind tunnels. For further reviews on the background of the e^N method, along with its application to high-speed compressible boundary layers, consult Refs. [13, 52].

2.3.2 STABL: PSE-Chem

The PSE-Chem/STABL software is used for the stability analysis of boundary layer instability measurements. Comparisons are made to results obtained in the Oxford High Density Tunnel (HDT) and The University of Queensland's T4 Stalker Tunnel. The stability computations used in this research were completed by Dr. Joseph Jewell[4]. The PSE-Chem setup are adaptations of previous stability work that has been undertaken by Jewell et al. in Refs. [57, 58].

PSE-Chem performs the stability analysis as part of the University of Minnesota's STABL (Stability and Transition Analysis for hypersonic Boundary Layers) software suite [53]. It solves the reacting, two-dimensional, axisymmetric, linear parabolized stability equations to predict the amplification of disturbances as they interact with the boundary-layer [52]. The mean flow over the cone is computed by the reacting, axisymmetric Navier-Stokes equations with a structured grid, using a version of the NASA Data Parallel-Line Relaxation (DPLR) code [59] which is included as part of the STABL-2D software suite, as described by Johnson [60] and Johnson et al. [61]. This flow solver is based on the finite-volume formulation. The use of

[3]Marineau et al. propose a method to calculate A_0, using a combination of experimental results and parameters from PSE-Chem computations. This method is detailed in Section 2.5.4, and used in this research.

[4]Dr. Joseph Jewell is currently an Assistant Professor at Purdue University's School of Aeronautics and Astronautics.

an excluded volume equation of state is not necessary because the static pressure over the cone is assumed to be sufficiently low that the gas can be treated as ideal. The mean flow is computed on a single-block, structured grid with dimensions of 361 cells by 359 cells in the streamwise and wall-normal directions, respectively. The inflow gas composition in the cold flow cases is air with 0.233 O_2 and 0.767 N_2 mass fractions. For the reflected shock tunnel cases, the inflow gas composition was determined using The University of Queensland's ESTCj program and library [62]. All PSE-Chem computations include chemistry, however the impact of chemical reactions is negligible for the cold-flow cases.

Grids for the 7-degree half angle sharp cone and different bluntness conditions were generated using STABL's built-in grid generator, and mean flow solutions examined to ensure that at least 100 points normal to the cone surface were placed in the boundary layer for each stagnation pressure. The boundary layer profiles and edge properties are extracted from the mean flow solutions during post-processing. The wall-normal extent of the grid increases down the length of the cone, from 0.25 mm at the tip to 50 mm at the base, allowing for the shock to be fully contained within the grid for all cases tested. The grid is clustered at the wall as well as at the nose in order to capture the gradients in these locations. The non-dimensional wall distance y^+ for the grid, extracted from the DPLR solution for each case, is everywhere less than 1, where y^+ is used as a measure of local grid quality at the wall in the wall-normal direction.

When progressing downstream, a disturbance is initially stable and damped: $\sigma < 0$. After the neutral stability position is reached, the disturbance become unstable ($\sigma > 0$) and grows. It reaches a maximum amplitude, after which it again becomes stable and damped. This results in the succession of peaks, which are used to generate the maximum N factor envelope. The maximum N factor value increases with x, due to the longer distance available for positive growth. The disturbance frequency (f_c) also shifts to smaller values as the boundary layer thickens when

progressing downstream.

2.4 Instability Mechanisms

For the high-speed boundary layers and model geometries considered in this research, the two instabilities that are expected to dominate transition are the second "Mack" mode waves, and the three-dimensional crossflow instabilities. For this reason, both instabilities will be detailed in Section 2.5 and Section 2.6 respectively, along with some key results from the high-speed literature to date.

A note on other instabilities

There are several other instability mechanisms that are capable of destabilizing a boundary layer, some of which are briefly mentioned here. In subsonic and early supersonic flows, the dominant two-dimensional instabilities are Tollmien-Schlichting (T-S) waves. For three dimensional boundary layers, such as over a swept wing or cone at angle of attack, the crossflow instability becomes important. For shear flows passing over concave surfaces, the Görtler instability may also play a significant role in transition [23].

An entropy layer forms in high-speed flows when a strong shock curves in front of a blunt body, causing high pressure gradients outside the boundary layer. Instabilities within the entropy layer are able to impact the stability of the boundary layer, and are believed to be a potential cause for transition reversal on blunted geometries [63, 64, 65, 66, 67]. In hypervelocity flows, the vorticity magnitude grows with the density ratio across the shock [68]. Evidence suggests that the resulting shock layer instabilities destabilize the shear layer [68]. Computations by Hornung [68] show that two distinct non-linear growth mechanisms can occur under these conditions.

2.5 Second Mode Instability

2.5.1 Second mode characteristics

The second mode instability is expected to be the dominant instability for 2D geometries in high-speed flows, such as flat plates or cones at low angles of attack. These were discovered in Mack's computations, where he used linear stability theory to calculate temporal disturbance frequencies and growth rates of inviscid instabilities in a compressible boundary layer over an adiabatic flat plate [51, 17]. For Mach numbers greater than one, the inviscid stability equation becomes hyperbolic and contains an infinite discrete set of eigenvalues that satisfy the boundary conditions [17, 69].

The higher modes are trapped acoustic waves which present as rope-like structures within the boundary layer [70, 71]. Physically, it was determined that they exist whenever there is a region of local supersonic flow relative to the phase speed of the instability wave [51, 72, 73, 74, 17, 75]. The local convective Mach number, M_c, must therefore be supersonic for a small region above the wall [75]. The waves continuously reflect back and forth between the wall and the sonic line ($y = y_a$), which is sonic relative to the disturbance phase velocity [18]. This is illustrated in Figure 2.2 for the body-fixed frame of reference, where $U(y)$ is the mean-flow profile, $p(y)$ is the pressure disturbance profile, and the sonic line acts as an acoustic waveguide [18].

The maximum amplification rate of the various modes is given in Figure 2.3 as a function of Mach number [17]. It is clear that the second mode is the most unstable 2D mode when the Mach number is greater than two[5]. Computations with 3D viscous disturbances showed that the first mode can be most unstable for wave angles greater than zero (where $\varphi = 0°$ is 2D). The higher acoustic modes are always most unstable when they are 2D, as the thickness of the supersonic flow

[5]This calculation was undertaken on an adiabatic flat plate boundary layer, however the same result was observed for 2D waves in all boundary layers that Mack investigated [17].

region is at its maximum [17]. Figure 2.4 illustrates the comparison between the 3D first mode and second mode temporal amplification rates (R = 1500, adiabatic flat plate) [17].

The second mode propagates at a speed close to the boundary-layer edge velocity (u_e), and the fluctuation wavelength is approximately twice the boundary-layer thickness ($\lambda \approx 2\delta$) [69, 76]. The frequency of the second mode disturbances can then be estimated in the first case according to

$$f_c \approx \kappa \frac{u_e}{2\delta} \tag{2.4}$$

where κ has been measured in the range $\approx 0.7 - 1.0$ [16, 77, 78, 79, 80, 81].

Table 2.1 reviews some of the disturbance speeds (u_c) that have been measured in multiple conventional wind tunnels, as a fraction of the computed edge velocity (u_e). Depending on facility conditions and nosetip bluntness, the disturbance frequencies range from 100 kHz to over 1 MHz [76].

Ref.	Facility	Condition and geometry	Method	u_c/u_e
[81]	AEDC Tunnel B	$M_\infty = 7.9$, $Re_{unit,\infty} = 1.6 - 6.6$ R_N sharp, $\theta_c = 7°$	Hot wire probes	0.95 - 1.0
[80]	HEG	$M_\infty = 8$, $Re_{unit,\infty} = 2.4$ $R_N = 2.5$ mm, $\theta_c = 7°$	PCB132 sensors	0.85
[78]	VKI Longshot	$M_\infty = 9.4 - 10.8$ $Re_{unit,\infty} = 3.4 - 5.8$ $R_N = 1.75$ mm, $\theta_c = 7°$	PCB132 sensors	0.93
[82]	AFRL Ludwieg Tube	$M_\infty = 6.14$ $Re_{unit,\infty} = 4.9 - 9.3$ R_N = sharp, $\theta_c = 7°$	Calibrated Schlieren	0.94 - 0.97

Table 2.1: Examples of second mode disturbance speeds in conventional wind tunnels over varying conditions.

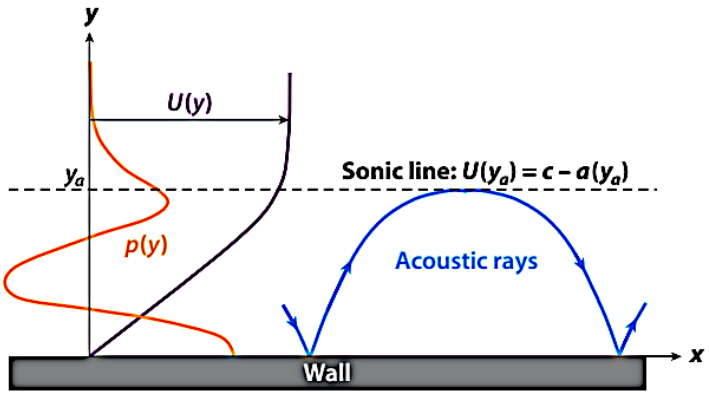


Figure 2.2: Schematic of the acoustic mode in a high-speed boundary layer, in the body-fixed frame of reference [18].

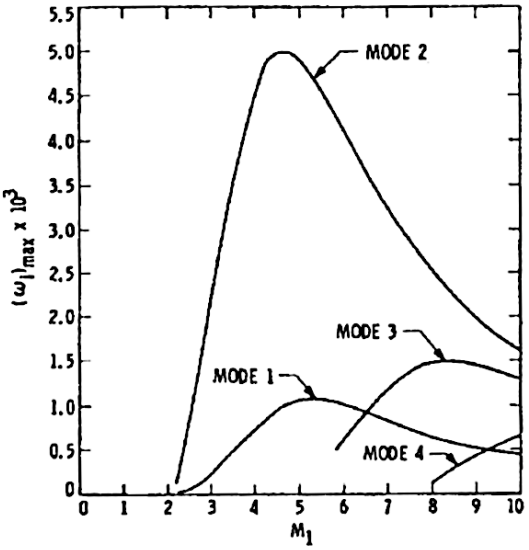


Figure 2.3: Temporal amplification rate for the first four Mack modes with $\psi = 0°$ (2D waves) [17].

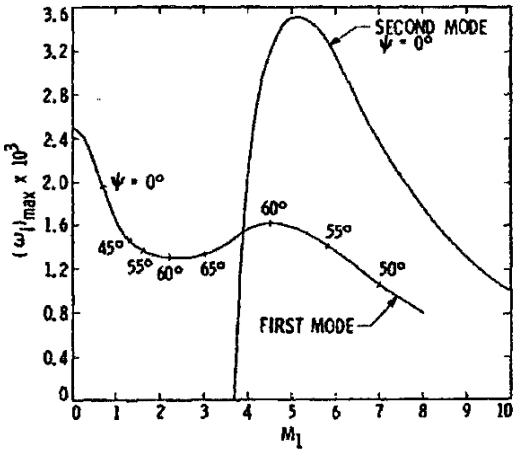


Figure 2.4: Temporal amplification rate for the most unstable first and second mode (3D) [17].

2.5.2 Estimation of the second mode frequency using Howarth's approximation

A semi-empirical model is used to obtain a rough estimate of the frequencies of the second mode instabilities [83]. Howarth describes the theory of compressible flow in a flat plate laminar boundary layer, for the case when the viscosity is proportional to the absolute temperature ($\mu \propto T$) and the Prandtl number is unity [84]. This assumption effectively overestimates the effects of viscosity, though allows Howarth to reduce the number of particular solutions required to evaluate the effect of compressibility on laminar boundary layers.

With the edge of the boundary layer defined as $\frac{u}{u_e} = 0.999$, Howarth relates the compressible boundary layer (δ) to its incompressible counterpart (δ_i), as:

$$\begin{aligned} \frac{\delta - \delta_i}{\delta_i} &= 0.1987(\gamma - 1)M_e^2 \\ &= 0.0795M_e^2 \end{aligned} \tag{2.5}$$

where M_e is the edge Mach number. The Blasius flat plate laminar boundary layer solution is substituted into Equation 2.5, and the Mangler transformation [24] is used to convert the flat plate solution to that of a sharp cone ($\delta_{cone} = \frac{\delta_{plate}}{\sqrt{3}}$). The following equation can subsequently be used to roughly estimate the compressible boundary layer thickness over a cone,

$$\delta = \frac{5\sqrt{x}(1 + 0.08M_e^2)}{\sqrt{Re_{unit,e}}} \tag{2.6}$$

where $Re_{unit,e}$ is the unit Reynolds number evaluated at boundary layer edge conditions, and x represents the axial location.

Substituting this boundary layer thickness into $f_c = u_e/(2\delta)$ gives

$$f_c = \frac{0.173u_e\sqrt{Re_{unit,e}}}{\sqrt{x}(1 + 0.08M_e^2)} \tag{2.7}$$

Sreekanth and Mee compared predicted frequencies (using Equation 2.7) to second mode frequencies observed in fifteen hypersonic facilities, including the Oxford HDT[6] [83]. The range of flow conditions included $Re_{unit,e} = 2.6 - 17.4 \times 10^6$ /m, $M_e = 4.5 - 7.8$, and $T_w/T_0 = 0.1 - 0.9$, using cone half angles ranging from $\theta_c = 4°$ - $7°$ and with nose radii less than 3 mm. The edge conditions were calculated using the Taylor-Maccoll solutions [85]. Sreekanth and Mee find that estimates of second mode frequencies match the experimental measurements to within ±10% [83].

The Howarth approximation also provided a more accurate estimate of the laminar boundary layer thickness than the analytical expressions of White [24, 86] (see Ref. [77] or Ref. [24]) and Mallinson [87]. Equation 2.7 is therefore used to provide an estimate of the second mode disturbance frequency in this research, with results also compared to the STABL2D PSE-Chem findings wherever possible.

2.5.3 Measurement techniques

Second mode instability measurements have historically been taken using hot-wire anemometers [88, 89]. Hot-wires are unable to survive in harsh environments, meaning that their use was limited to moderate Mach numbers ($M_\infty \leq 8$), Reynolds numbers ($Re_{unit,\infty}$), and the low enthalpies (H_0) that exist in cold flow tunnels. Figure 2.13 shows an example of second mode fluctuations using a constant current hot-wire anemometer, as measured by Stetson [89, 65].

In 2006, Fujii used piezoelectric pressure sensors to investigate the role of two-dimensional roughness on second mode instabilities [90]. The PCB132 model sensors are flush-mounted, and therefore allow multiple measurements to be taken along a single array. They have a sufficiently high resonance frequency for most conditions ($\geq$ 1 MHz), a pressure resolution of 7 Pa, and most importantly they are more robust to flows at higher M_∞, $Re_{unit,\infty}$ and H_0. Despite issues with the sensor calibration

[6]The compared measurements from Ref. [83] are the boundary layer instability measurements presented in Chapter 5.

(see Section 3.6.3), these piezoelectric sensors have been the most common method used to measure second mode instabilities over the past decade, and are the focus of this research.

Significant progress has also been made using multiple optical techniques. Optical techniques have the advantage of being completely non-intrusive, and being able to resolve the higher second mode frequencies that are expected in some high enthalpy facilities ($f_c \geq 1$ MHz). Techniques such as Focused Laser Differential Interferometry (FLDI) [91] and calibrated Schlieren [92] have been able to quantitatively characterize second mode instabilities.

2.5.4 Analysis of second mode amplitudes: Marineau's method

The analysis of second mode amplitudes implemented in this research follows the methodology proposed by Marineau et al. [93, 54]. The methodology makes use of experimental data and PSE-Chem computations to compare the N-factors and growth rates. It is briefly described below, however more discussion and several validity tests can be found in Refs. [93, 54].

The stability Reynolds number, R, and the dimensionless frequency scaling from Stetson [94], F, are introduced as Eq. 2.8 and Eq. 2.9 respectively.

$$R = \sqrt{Re_x} \tag{2.8}$$

$$F = \frac{2\pi f}{u_\infty Re_{unit,\infty}} \tag{2.9}$$

where Re_x is the axial Reynolds number, f is the frequency, and u_∞ the freestream velocity. The PSE-computed maximum N factor envelope is then expressed as a linear function of growth rate,

$$N = \alpha R + b \tag{2.10}$$

where α is the PSE-computed growth rate, and b is a constant. The stability Reynolds number at the neutral point can then be calculated for the case where N = 0 in Eq. 2.10

$$R_0 = \frac{-b}{\alpha} \tag{2.11}$$

The second mode amplitudes at each sensor location are calculated by integrating the pressure fluctuation power spectral density[7] over the second mode peak. The integrated frequency band is $f_c \pm 100$ kHz, however the size of this band has a small effect on computed amplitudes due to the energy concentration at the peak second mode frequency [54]. The second mode disturbances exhibit an exponential growth, such that

$$A = ce^{dR} \tag{2.12}$$

where c and d are constants. If the second mode disturbance growth is well-predicted by PSE-Chem, then $d \approx \alpha$. Using the definition of the N factor (Eq. 2.3) and the linear expression for the PSE N-factor envelope (Eq. 2.10),

$$A = A_0 e^N = A_0 e^{\alpha R + b} \tag{2.13}$$

The initial amplitude can then be estimated by combining Eq. 2.12 and Eq. 2.13,

$$A_0 = ce^{-b} \tag{2.14}$$

where c is calculated from the fit of measured second mode amplitudes, and b is the PSE-calculated N factor value when $R = 0$. Marineau states that: "A_0 can be interpreted as a mean initial amplitude for the unstable frequencies over the range of fitted amplitudes" [54]. It is acknowledged that this is an approximation, because the

[7]The PSD is calculated using Welch's method, normalising by the Taylor-Maccoll conical-flow solution. Further information can be found in Section 3.7.1

initial amplitudes are expected to vary with frequency, and because the experimental growth rate d must be similar to the PSE-calculated α. The experimentally determined N factors can then be calculated using Eq. 2.14 and Eq. 2.3,

$$N(s) = \ln\left(\frac{A(s)e^b}{c}\right) \tag{2.15}$$

An example of the experimental N factor comparison to PSE-Chem for conventional tunnels at $M_\infty = 6$ is provided in Figure 2.5. This has been reproduced from Figure 10 e) and f) from Marineau et al. [54], using data from the NASA LaRC 20inM6 tunnel and the Technical University of Braunschweig (TUB) Hypersonic Ludwieg Tube (HLB).

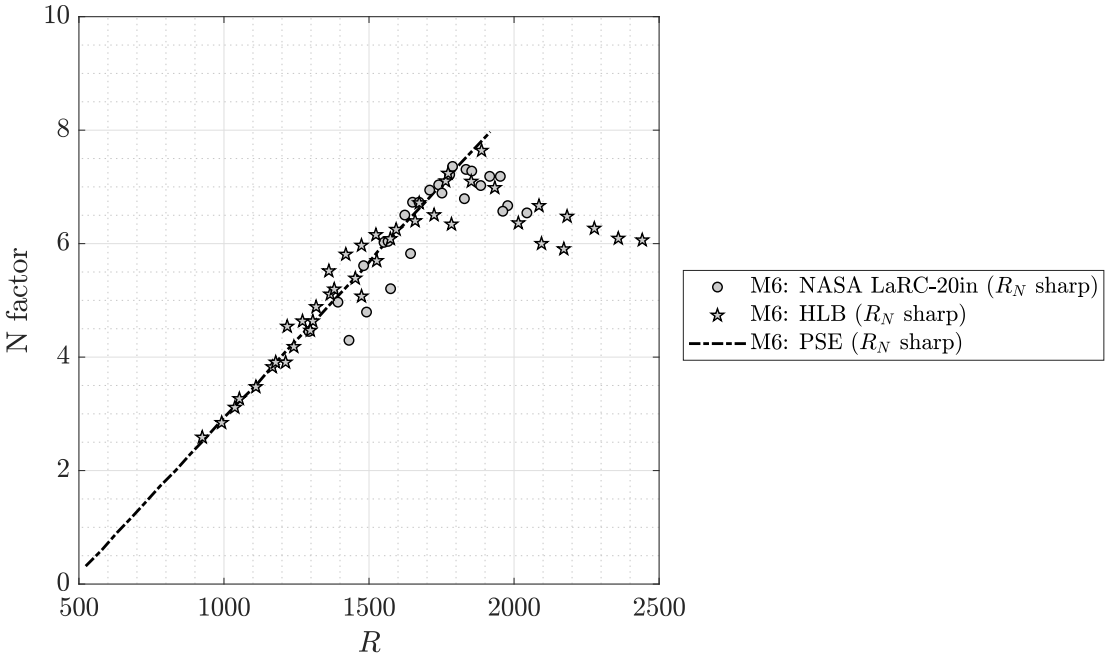


Figure 2.5: A comparison of experimental N factors to linear PSE-Chem computations using Marineau's method, for conventional tunnels at $M_\infty = 6$. Figure reproduced using data from Figure 10 e) and f) in Ref. [54]

2.5.5 Measurements in conventional wind tunnels

Marineau et al. compared second mode amplitudes to PSE-Chem for sharp slender cones in 11 hypersonic wind tunnels as part of the NATO AVT-240 research effort [54]. The individual freestream Mach number and Reynolds number for each facility are presented in Table 2.2, with further details also available in Table 1 in Ref. [54], and Table 1 in Ref. [95]. Measurements were obtained at $M_\infty = 5 - 14$, $Re_{unit,\infty} = 1.5 - 16 \times 10^6$ /m, and $T_w/T_0 = 0.1 - 0.8$. Nearly all models were 7° half-angle sharp cones, of varying length. The HIEST and HEG models had a small nose bluntness ($R_N = 2.5$ mm), whilst the BAM6QT cone had a smaller half-angle ($\theta_c = 2.5$ and 3). Some of their key findings are discussed in the subsections below.

Organisation	Tunnel name	Mach Number M_∞	Reynolds number $Re_{unit,\infty}$ [$\times 10^6$ /m]
Sandia National Laboraties (SNL)	HWT-5	5	10 - 12.8
	HWT-8	8	4.1 - 13
Purdue University	BAM6QT	6	6.4 - 12
NASA Langley Research Center	LaRC 20-in	6	6.8 - 13
	LaRC 31-in	10	1.7 - 6.6
Technical University of Braunschweig	HLB	6	5 - 16
DLR, German Aerospace Center	HEG	8	1.5 - 2.4
Japan Aerospace Exploration Agency	HIEST	8	3.3 - 4.8
von Karman Institute for Fluid Dynamics	Longshot	10	3.3 - 12
Arnold Engineering Development Complex	Tunnel 9	10	2.0 - 15
		14	1.7 - 12

Table 2.2: A summary of hypersonic facilities used to collate measurements of the second mode instability by Marineau et al. [54] and Fedorov et al. [95]. For further details, consult Table 1 in Ref. [54], and Table 1 in Ref. [95]

1. Maximum second mode amplitude (A_{max})

The maximum second mode amplitude stayed relatively constant for edge Mach numbers (M_e) greater than ≈ 5.8, and decreased significantly for lower M_e [54]. This result is shown in Figure 2.6, which is reproduced using the data from Figure 9 in Ref. [54]. No measurements at Mach 7 are included in this result, however the trend indicates that the maximum amplitude should lie in the region $A_{max} = 20\% - 30\%$.

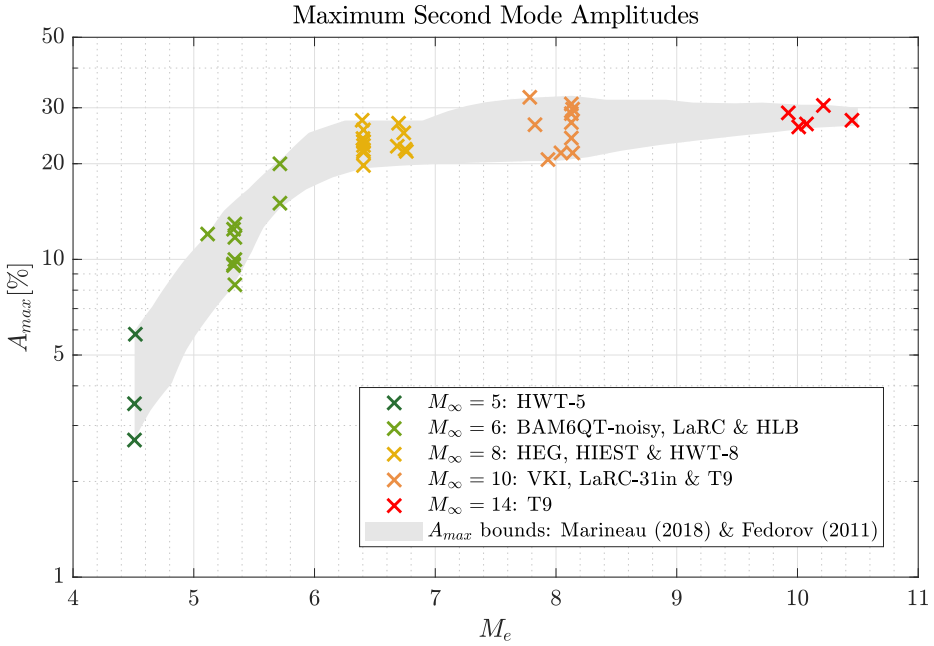


Figure 2.6: Maximum second mode amplitudes for various wind tunnels and flow conditions. Reproduced using the data from Figure 9 in Ref. [54] and Figure 6 in Ref. [95].

2. Amplitude and N-factor observations

Second mode measurements were compared to PSE-Chem computations over the wide range of conditions. Some of Marineau's observations are listed below [54]. Figure 2.7 shows some results at Mach 14 in the AEDC Tunnel 9 facility[8]. The figure has been reproduced from Figure 6 a) and Figure 10 a) in Ref. [54]. Annotations have been included to illustrate Marineau's observations, where possible.

[8]The high Mach number results are chosen as they also included the heat-transfer detected transition location

1. A_{max} did not clearly vary with $Re_{unit,\infty}$

2. A_{max} occurs slightly downstream of the heat-transfer detected transition location[9], $Re_{x,tr}$.

3. In most results, the experimental growth rate ($d = dA/dR$) did not vary with $Re_{unit,\infty}$, and agreed quite well with the PSE-computed growth rate (α).

4. For a given R, the amplitude increased when the facility Reynolds number ($Re_{unit,\infty}$) was reduced. This was the case in most facilities, and suggests that the boundary layer is stabilized when $Re_{unit,\infty}$ increases.

5. The initial disturbance, A_0, decreased with increasing facility Reynolds number. The relationship $A_0 \sim (Re_{unit,\infty} \cdot L_{\text{nozzle}})^{-1}$ agreed with the data quite well, and the trend is expected to be due to a decrease in acoustic wave radiation from the nozzle wall boundary layer at higher $Re_{unit,\infty}$.

6. The critical N factor increased as a function of $Re_{unit,\infty}$. This can be reasoned as: A_{max} stayed constant with $Re_{unit,\infty}$ whilst A_0 decreased.

[9]This corresponds to the first deviation from theoretical laminar baseline levels.

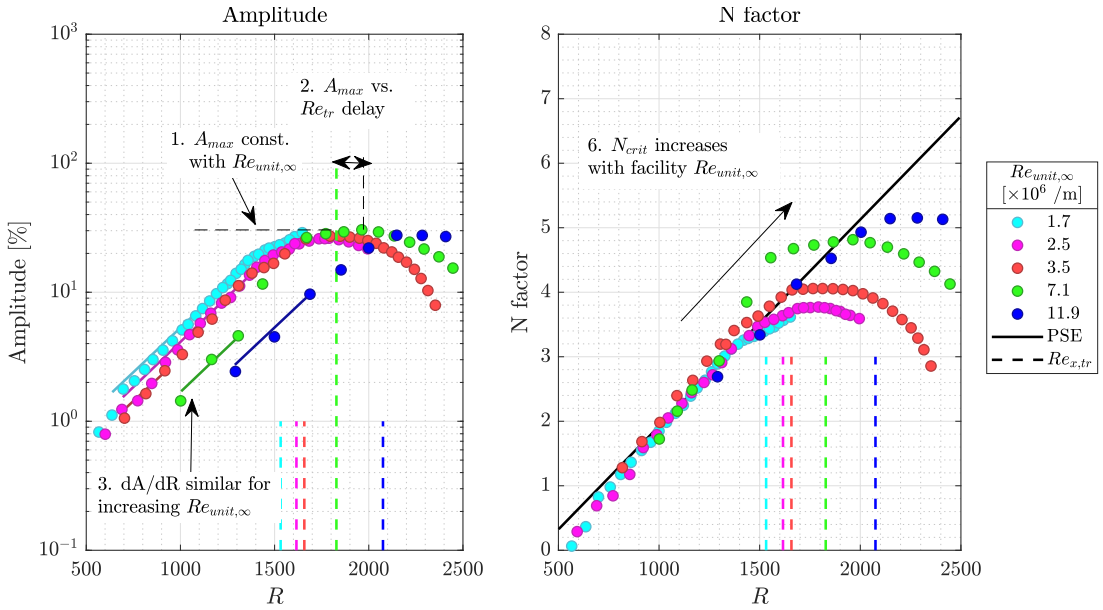


Figure 2.7: Marineau's amplitude and N factor results for Mach 14, $Re_{unit,\infty} = 1.7 - 11.9 \times 10^6$ /m in AEDC's Tunnel 9. Reproduced from Fig. 6 a) and Fig. 10 a) in Ref. [54]. $Re_{x,tr}$ indicates the heat transfer detected transition onset.

2.6 Crossflow Instability

The crossflow instability is a three-dimensional instability mechanism that is expected to play a significant role in transition for cones at high angles of attack and in low-disturbance environments such as flight. It exists in regions of pressure gradient on swept surfaces, such as cones at angle of attack [20]. The majority of crossflow research has been undertaken at low speeds, however most findings are expected to extend to higher Mach numbers [21, 96]. Further to this, the majority of crossflow research has also focused on the stationary modes, as it is believed that the stationary mode is more prominent in the low-noise flight environment. A comprehensive review of low-speed crossflow research (pre-2003) can be found in Ref. [20, 97, 19]. An overview of recent progress in high-speed crossflow research (both stationary and travelling) can then be found in Ref. [22, 98, 99, 100].

2.6.1 Formation of crossflow

A cone at angle of attack experiences a stronger shock along its windward ray, resulting in higher post-shock pressures. A pressure gradient acts laterally around

the cone, driving fluid from the windward to the leeward side and causing the streamlines to be curved at the boundary-layer edge [19]. The streamwise velocity is reduced for the flow inside the boundary layer, but the circumferential pressure gradient remains constant [19, 20]. This results in a secondary flow in the boundary layer called crossflow, which is perpendicular to the local inviscid-flow velocity vector inside the boundary layer [19, 20]. A typical crossflow profile is shown in Figure 2.8, taken from Craig and Saric [98]. For a cone at angle of attack, the crossflow is expected to reach a maximum about 2/3 of the way from the wind to the lee ray ($\phi = 120°$) [5, 20].

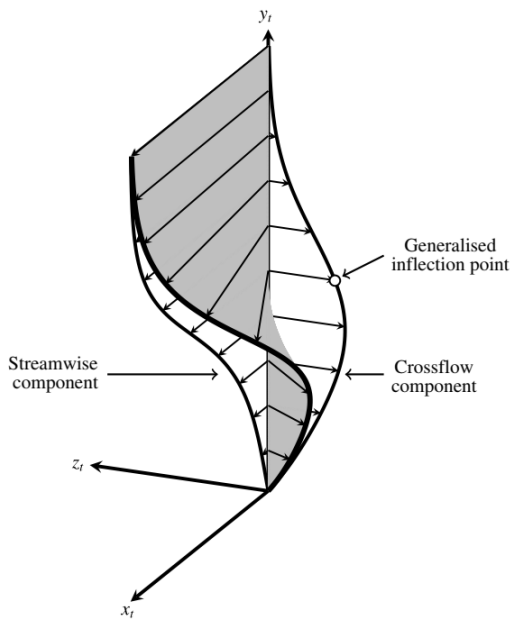


Figure 2.8: A typical crossflow profile. Taken from Figure 1 in Ref. [98]

A generalized inflection point exists between the maximum velocity of the low-momentum fluid near the wall and the boundary layer edge. The inflection point is a necessary condition for inviscid instability[10] [101]. The primary crossflow instabilities are present either as stationary or travelling vortices, which follow the streamlines moving through the generalized inflection point in the boundary layer [102]. In low speed flows, the stationary modes are more dominant in low

[10]This is the compressible counterpart to Rayleigh's criterion in subsonic flows [17]

noise environments such as flight, whereas the travelling modes typically dominate in conventional tunnels [97, 20]. This is not necessarily the case for crossflow dominated transition in high-speed flows.

2.6.2 Stationary crossflow waves

The initial amplitude of the stationary crossflow waves is determined by roughness height, diameter, and spacing [103, 104, 105]. The stationary waves produce weak velocity disturbances, causing a distortion of the mean flow. The distorted mean flow actually stabilizes the primary disturbance, and causes the crossflow vortices to saturate [20, 106, 98]. Transition is then observed downstream of the saturation point. It is for this reason that the semi-empirical e^N factor approach is not well-suited to measurements of the stationary wave amplitudes [107].

The breakdown of the saturated crossflow waves have been attributed to high-frequency secondary instabilities that develop in the modified mean flow [98, 22, 108]. An N-factor approach is better suited to the secondary instabilities, as they grow quickly after the primary vortices have saturated and before the boundary layer has transitioned. The secondary instabilities are typically classified as type-I modes or type-II modes [109]. The type-I modes are produced by spanwise or azimuthal gradients of the streamwise mean flow ($\partial U/\partial z$ or $\partial U/\partial \theta$), whereas the type-II modes are produced by wall-normal gradients ($\partial U/\partial r$) [110, 109]. Craig and Saric [111] suggest that the frequency of each mode can be estimated in the first case by

$$f_I \approx \frac{u_e}{2\delta} \tag{2.16}$$

$$f_{II} \approx \frac{u_e}{\delta} \tag{2.17}$$

The estimated frequency for type-I secondary instabilities is similar to the second mode instability (Eq. 2.4). It is worth noting that surface pressure measurements are unable to distinguish between the second mode instability and the type-I

secondary instability. Recent work has also suggested that the second mode may be modulated and destabilized by the stationary crossflow vortices, which complicates the transition process even further [100].

Isolated stationary crossflow measurements: 7° half angle cone at $\alpha = 6°$ in the Purdue BAM6QT Quiet Tunnel

The Purdue 7° cone research has isolated the growth of individual crossflow waves, by using a variety of discrete roughness elements to generate stationary vortices. Ward and Henderson made the first measurements of a high-frequency secondary instability using PCB132 sensors [112, 113, 114, 115]. The sensors were distributed in a high density over a relatively small azimuthal region ($\phi = 110° - 160°$) to isolate the growth and breakdown of secondary instabilities for individual stationary crossflow vortices [116, 99].

Figure 2.9 shows a comparison of the primary and secondary instability amplitudes, as measured in the Purdue BAM6QT quiet tunnel by Edelman et al. [99]. The schematic has been taken from Figure 11 in Ref. [99], with more details also available in Ref. [116]. The high density of sensors and use of IR thermography made it possible to: (I) capture the growth and saturation of the vortex, (II) the linear growth of the secondary instability, (III) the beginning of turbulent intermittency, (IV) the peak amplitude of the secondary instability, and (V) a fully turbulent boundary layer [116, 99, 22]. The measured frequencies also identified the presence of multiple secondary instability modes, and these compared quite well to estimated frequencies based on edge velocity and boundary layer thickness [117].

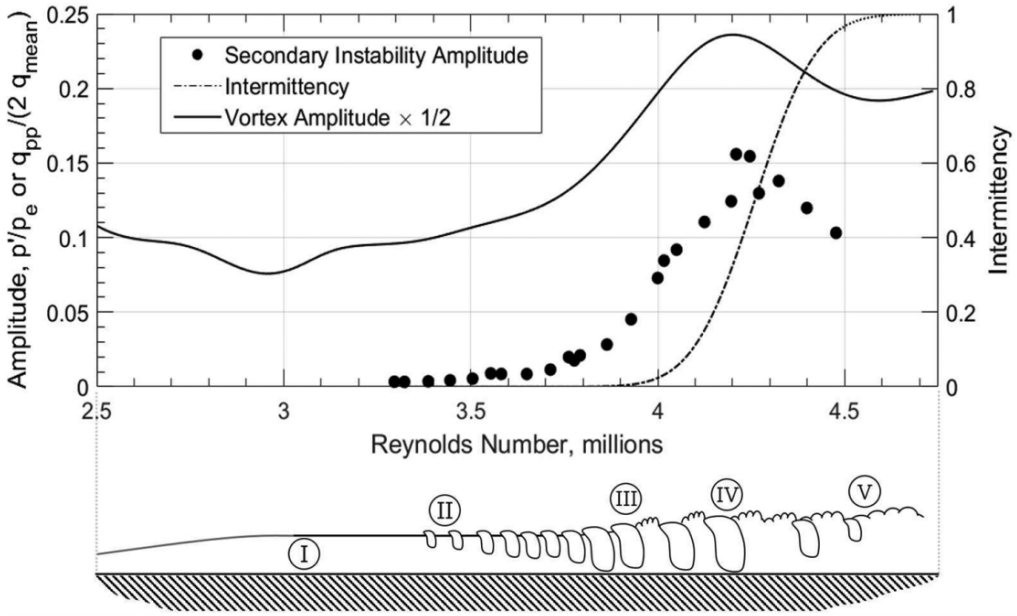


Figure 2.9: Comparison of the primary and secondary instability amplitude developments in Purdue's BAM6QT Quiet Tunnel, taken from Figure 11 in Edelman et al. [99]. Experiments completed in quiet flow at $M_\infty = 6$, $Re_{unit,\infty} = 7.5 - 11.9 \times 10^6$ /m, $T_w/T_0 = 0.7$.

2.6.3 Travelling crossflow waves

Considerably less research has been done on the travelling mode than its stationary counterpart. Travelling crossflow modes in the low-speed environment have been excited by the vortical content of freestream turbulence [118]. The same is often assumed for hypersonic flow, however this may not be the case. Travelling crossflow waves were measured by Borg et al. [119] on the HIFiRE-5 elliptic cone in the Purdue BAM6QT tunnel. Their measurements identified the instability at $f \approx 45$ kHz under quiet flow, however no disturbance was observed under noisy flow. The travelling mode frequency does coincide with the region of maximum freestream disturbance content [120], however this interaction is still unclear. More attention is now being given to the travelling modes, and particularly to their non-linear interactions with the stationary crossflow modes and the second Mack mode.

2.6.4 Instability measurements: co-existing stationary modes, travelling modes, and second Mack mode

Measurements have shown travelling and stationary crossflow modes coexisting in multiple conventional and quiet wind tunnels. Some of these experiments and their findings are outlined briefly below. Corke et al. investigated passive discrete roughness for transition control on a sharp 7° half-angle cone at $\alpha = 6°$ in the Air Force Academy (AFA) Mach 6 Ludwieg Tube Facility [121]. They had off-wall azimuthal profiles of mean and fluctuating total pressure at multiple axial locations. The experiments revealed evidence of a non-linear interaction between stationary and travelling crossflow modes, which may indicate a mechanism of early transition in conventional hypersonic tunnels [121].

Munoz et al. took surface pressure fluctuation measurements using a sharp 7° half angle cone at $\alpha = 6°$ in the Hypersonic Ludwieg Tube Braunschweig at Mach 6 [122]. They used infrared images to identify the location, direction, and growth of stationary crossflow instabilities. Munoz et al. observed two clear peaks in their surface pressure spectra. A high-frequency peak ($f \approx 200 - 500$ kHz) was attributed to the second mode or stationary crossflow waves, whilst a low-frequency peak ($f \approx 20 - 50$ kHz) was assumed to be a first mode disturbance that grew concurrently [122]. Craig et al. suggest that it is more likely that the low frequency peak represents travelling crossflow waves [98], and that this argument is supported with computations by Kuehl et al. [123] and Oliviero et al. [102].

The Texas A&M experiments used a 7° half-angle cone at $\alpha = 5.6°$ in their Mach 6 Quiet Tunnel [98]. Measurements were made using a constant-temperature hot-wire anemometer system with a frequency response up to 180 kHz. Modal growth was investigated by separating the results into individual frequency bands, where a travelling wave ($f \approx 35$ kHz) was observed to coexist with the stationary wave [98]. Stationary crossflow waves were also observed to grow and saturate. A type-I secondary instability was seen, centered on a frequency of 110 kHz. Transition to

turbulence or type-II secondary instabilities were not measured, due to limited model length and frequency limitations of the hot-wire anemometer system respectively [98].

Ward [124] studied the interaction between stationary and travelling crossflow vortices on a 7° half angle cone at $\alpha = 6°$ in the BAM6QT quiet tunnel. This work has been continued by Edelman et al. [100], where they investigated the effect of roughness on the non-linear breakdown mechanisms. A discrete roughness resulted in the modulated second mode being the most dominant mechanism, without any evidence of the travelling crossflow in the surface pressure power spectra. This is contrasted with the use of a random roughness, which showed a travelling crossflow wave coexisting with a higher-frequency peak, assumed to be a type-I secondary instability of the stationary vortices.

2.7 Parametric Effects, with a focus on Slender Body Experiments

The breakdown of a hypersonic boundary layer is clearly a complex process that is influenced by many parameters. Some of the influencing parameters relevant to this research include the Mach number, Unit Reynolds number, nose bluntness, wall-to-total temperature ratio, freestream turbulence, real-gas effects and angle of attack (α). A brief overview of general transition-location and instability trends is provided, with focus on similar slender body experiments. Only parameters that are directly related or varied in this research are addressed, despite the fact that many more contribute to the transition process (e.g. Mach number, surface ablation, surface roughness, chemistry, and so forth). Further reviews can be found in Refs. [16, 5].

2.7.1 Freestream Turbulence Levels

Conventional wind tunnels have freestream fluctuation levels that are significantly higher than flight [125, 126]. These freestream fluctuations come mostly in the form of acoustic waves which are radiated from turbulent boundary layers along the nozzle walls [127, 126]. The higher freestream turbulence levels provide an additional disturbance to the boundary layer, and therefore contribute to the breakdown process. More information about methods used to characterize freestream turbulence levels is given in Section 4.3, and in Ref. [120].

Conventional tunnel results have shown an increase in transitional Reynolds number when the freestream turbulence levels are lower, for a given geometry and flow condition. This is illustrated in Figure 2.10, where Stainback compared transition Reynolds number data as a function of measured disturbance levels for multiple geometries [128] (replotted by Schneider in [125]). The results obtained in conventional wind tunnels therefore represent a conservative transition scenario

when compared to flight, assuming that the same instability mechanisms and path to turbulence is followed.

2.7.2 Unit Reynolds Number

Most experimental results obtained in conventional wind tunnels have shown that the transition Reynolds number increases with the freestream unit Reynolds number [125, 5, 129, 130, 131]. An example of this is shown in Figure 2.11, plotted from Table I in Ref. [132] by Schneider [5]. Results are presented for the end of transition on a 5° half-angle sharp cone at $\alpha = 0°$, measured in the NASA Ames and Langley conventional wind tunnels at an edge Mach number of 6.8 [133, 125]. The measurements show a clear increase in transitional Reynolds number with unit Reynolds number.

It should be noted that multiple conventional tunnel datasets do not agree with this trend, such as the Ludwieg tube at Göttingen [134], however these are a minority. Quiet tunnels measurements have also consistently shown that there is no unit Reynolds number dependence on transition [135, 125]. Pate suggested that the trend observed in conventional wind tunnels can be largely attributed to a decrease in environmental disturbances as the unit Reynolds number increases [127, 125]. This is expected to be due to lower acoustic wave radiation from the thinner nozzle wall boundary layer when the facility Reynolds number increases.

2.7.3 Nose bluntness

The nose bluntness has a significant impact on local boundary layer properties, and therefore its stability. This is largely due to its effect on the formation of the entropy layer, which flows downstream from the apex of the cone and subsequently impacts the mean flow properties. As the nose bluntness initially increases, the swallowing distance becomes larger and the boundary layer is stabilized over a

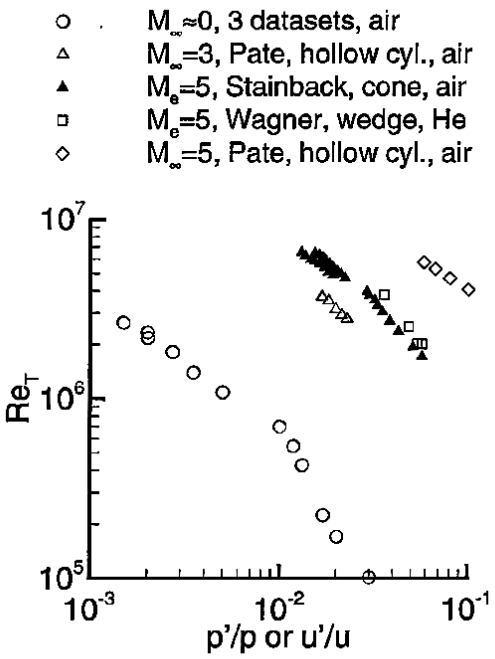


Figure 2.10: Effect of freestream turbulence levels on transition locations for multiple geometries and experiments. Figure originally plotted by Stainback [128], and adapted by Schneider [125]. Taken from Figure 3 in Ref. [125]

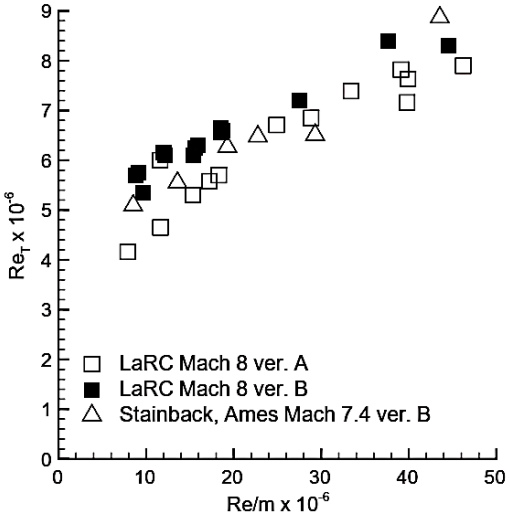


Figure 2.11: Effect of Unit Reynolds number on transition locations. Figure plotted by Schneider [5], using data from Table I in ref. [132]. Taken from Figure 17 in Ref. [5].

larger portion of the cone.

The role of nose-tip bluntness on boundary-layer transition is frequently illustrated by plotting the transitional Reynolds number ($Re_{x,tr}$) against the Reynolds number based on the nosetip radius (Re_{R_N}). Results from Stetson's experiments in the AFRL High Reynolds-number facility at Mach 6 using an 8° half angle cone are shown in Figure 2.12 [94, 136]. The figure has been replotted from the data presented in Figure 1a of ref. [136]. The transition onset location is determined by the initial deviation of the heat-transfer coefficient or the Stanton number from the laminar trend.

The Stetson result has been annotated to show two clear regions. Firstly, for small nose bluntness, the transition location moves downstream with increased bluntness.

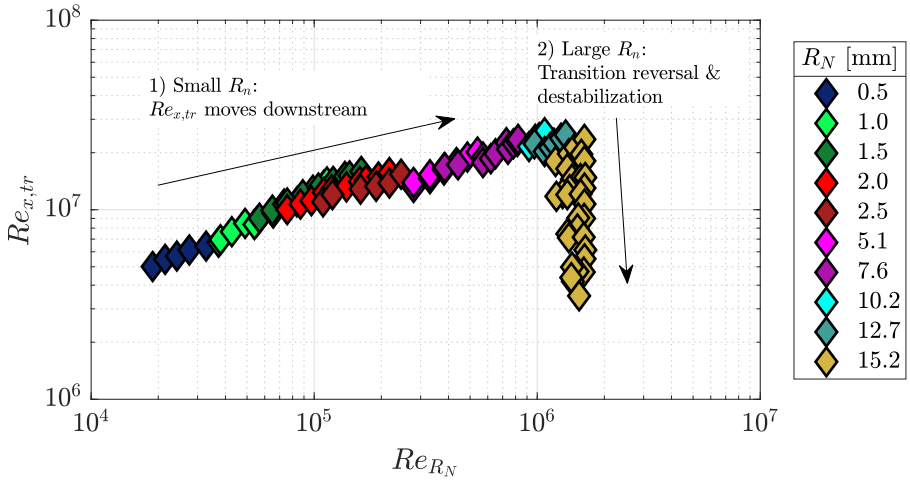


Figure 2.12: Effect of nose radius on transition location. Stetson's experiments in the AFRL High Reynolds-number facility at Mach 6 using an 8° half angle cone. Figure plotted using data and format from Figure 1a. in Paredes et al. [136]. Original data is from Stetson [94].

Stabilization continues until the swallowing length is equal to the transition location [94, 65]. When the nose radius is further increased, transition occurs within the entropy layer and the boundary layer is destabilized. This transition reversal is known as the "blunt body paradox", and has been the focus of significant research [63, 64, 65, 66, 67, 136]. Many measurements have shown a similar transition reversal after reaching a critical nosetip Reynolds number. Examples include measurements taken by Softley et al. at Mach 10, T_w/T_0 of 0.26 [137, 130], as well as Marineau et al, in the U.S. Air Force AEDC Hypervelocity Wind Tunnel Number 9 (Tunnel 9) at Mach 10 and T_w/T_0 of approximately 0.3 [131]. For the small bluntness' used in this research, the results are expected to lie within the initial stabilization region (this comparison is made in Section 6.2.1).

The stabilizing effect on the second mode growth can also be visualised in the fluctuation spectra results. Stetson took measurements using a hot-wire for a cone with a "sharp" tip and a cone with a nose radius of 3.81 mm, as shown in Figure 2.13 [89, 65]. A stabilization is clearly observed at the peak second mode frequency, when a small amount of bluntness is introduced to the "sharp" cone geometry.

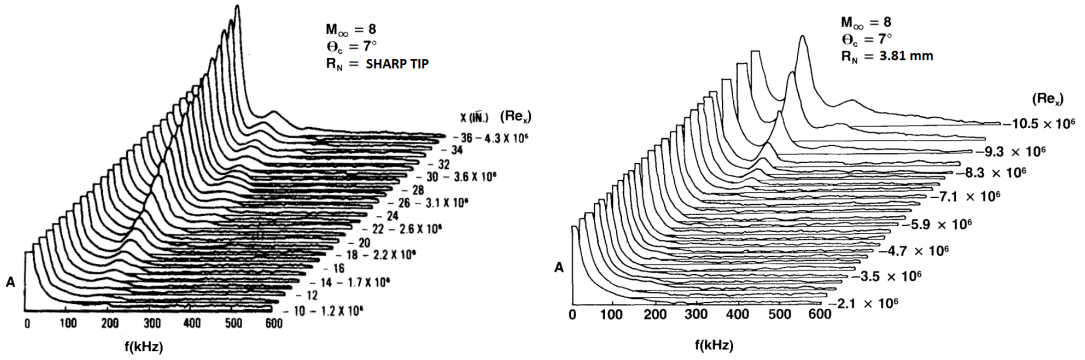


Figure 2.13: Effect of nose radius on measured fluctuations from Stetson experiments at Mach 6 using a 5° half angle cone [89, 65].

2.7.4 Angle of attack

Boundary layer transition changes significantly at high angles of attack, and is largely dependent on the cone bluntness, freestream Reynolds number, freestream turbulence levels, and surface roughness. A review of the instabilities that are expected at high angles of attack was provided in Section 2.6. A reversal in trends has been observed for larger nosetip bluntness' and freestream Reynolds numbers[11] [138, 139, 131, 140]. Only results for sharp cones or cones with small bluntness will be reviewed here. For more information about the bluntness reversal problem, consult Refs. [141, 142, 143, 5, 138, 139, 131, 140].

Windward and leeward transition

Windward transition remains two-dimensional at high angles of attack, so is expected to be dominated by second mode growth. Results in the literature have shown that the transition location moves forward on the leeward side, and moves aft on the windward side [144, 139, 141, 145, 143, 146, 138, 35, 36, 37, 131, 140]. Some of these measurements have been summarised in Figure 2.14, using data from Refs. [131, 145, 143, 146, 147, 134, 148]. Results are normalised by the transition location at $\alpha = 0°$, so that the boundary layer is stabilized if $Re_{x,tr}/(Re_{x,tr})_{\alpha=0°} > 1$. The

[11] The windward transition starts to move forward and the leeward transition moves aft.

abscissa axis normalises the angle of attack by the cone half-angle (θ_c).

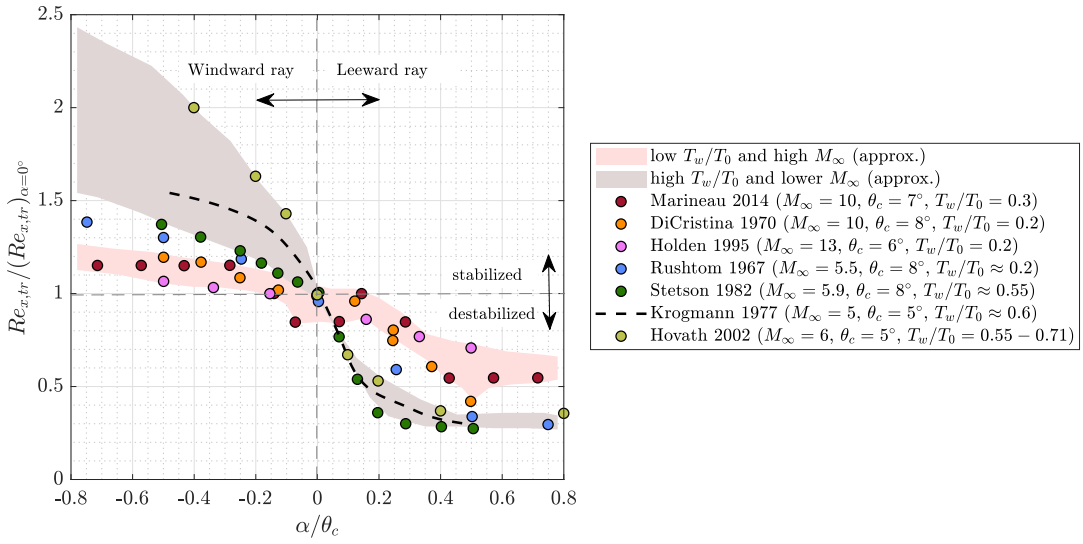


Figure 2.14: Transition results for the windward and the leeward ray at angle of attack using a sharp cone. The data is from Refs. [131, 145, 143, 146, 147, 134, 148]. α is the angle of attack, and θ_c is the cone half angle. The results have been annotated to show a potential T_w/T_0 and M_∞ trend.

The results show a variety of transition displacements along the windward ray and the leeward ray. The reasons for this is not clear. Marineau noted that the rearward transition displacement seems to increase when the Mach number decreases, and/or T_w/T_0 increases [131]. Measurements must isolate the effect of T_w/T_0 and M_∞ independently to identify their role at high angles of attack.

Transition front for cold flow tunnels (high T_w/T_0)

For experiments in cold-flow facilities, transition occurs latest on the windward ray and the boundary layer is continuously destabilized when progressing to the leeward ray [142, 36, 37, 138]. It may therefore be assumed that the crossflow contributes to the destabilization of the boundary layer. This is nicely summarised by Stetson using an 8° half angle cone at Mach 6 in the Flight Dynamics Laboratory (FDL)

Mach 6 wind tunnel[12], as shown in Figure 2.15 [143]. Juliano et al. took boundary layer instability measurements and measured transition at higher angles of attack, with results suggesting that this trend holds for $\alpha \leq 15°$ [36, 35, 37]. Figure 2.16 shows an IR thermography result obtained by H2K at $M_\infty = 7$, $Re_{unit,\infty} = 9.1 \times 10^6$ /m, $T_w/T_0 = 0.56$, $R_N = 1.6$ mm, and $\alpha = 9°$. A clear destabilization is observed from the windward to the leeward ray, even at the higher angle of attack.

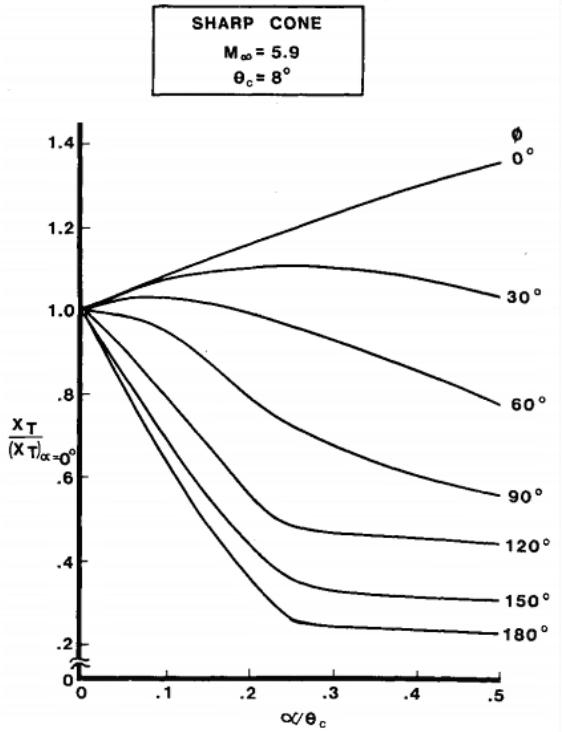


Figure 2.15: Stetson's transition results at angle of attack with a sharp cone, taken from Figure 7 in Ref. [143]. α is the angle of attack, and θ_c is the cone half angle.

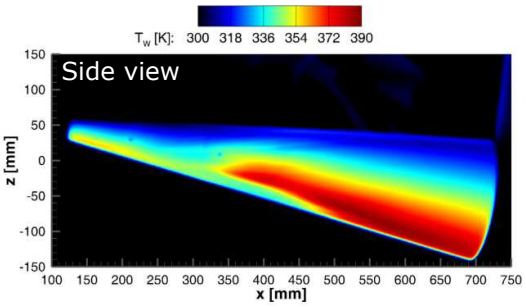


Figure 2.16: IR thermography result from the H2K post HIFIRE-1 campaign, taken from Figure 11a in Ref. [35]. Side view of the 7° cone at $\alpha = 9°$. $M_\infty = 7$, $Re_{unit,\infty} = 9.1 \times 10^6$ /m, $T_w/T_0 = 0.56$, $R_N = 1.6$ mm.

Transition front for tunnels with low T_w/T_0

A discrepancy in transition front shape exists when comparing cold-flow results to flight and facilities with low T_w/T_0. There are multiple datasets where the highest transition Reynolds number does not occur on the windward ray itself, but instead

[12]The Stetson Mach 6 conditions were: $Re_{unit,\infty} = 3.0 - 9.2 \times 10^6$ /m, $T_w/T_0 \approx 0.52 - 0.58$, $\alpha \leq 4°$

occurs on the shoulder of the cone [145, 141, 131, 140, 33, 34]. This feature is commonly referred to as a stable indented front. Both DiCristina [145] and Holden et al. [141] observed transition furthest downstream on the 90° azimuth, using a sharp 8° half-angle cone[13]. In both experiments, transition was measured at discrete locations with 45° azimuth intervals, so they would not have been able to resolve between $45° \leq \phi \leq 90°$ or $90° \leq \phi \leq 135°$ [145, 141].

Marineau et al. took measurements on a 7-degree half angle cone in the AEDC Tunnel 9 at Mach 11, $T_w/T_0 \approx 0.3$ [131]. A finer resolution of azimuths were measured using Temperature Sensitive Paint (TSP). The transition front results presented in Ref. [131] used a nosetip radius of $R_n = 9.53$ mm, so it is hard to separate which features are due to bluntness. Nevertheless, Marineau identified a stable indented front in the region $110° \leq \phi \leq 150°$, varying with angle-of-attack ($1° \leq \alpha \leq 3°$).

Transition front in HIFiRE-1 flight

The descent phase of the HIFiRE-1 flight provided a wealth of transition data at Mach 7 and high angles of attack ($\alpha \approx 6° - 13°$). Results and reviews of the flight test can be found in [26, 27, 28, 29, 30, 31, 32, 33, 34], with more details also provided in Section 7.1. The earliest transition was observed on the leeward ray ($Re_x = 3.1 \times 10^6$, $\alpha = 13°$), whilst the latest transition was observed at azimuths $\phi = 30°$, 280° ($Re_x = 6.0 \times 10^6$, $\alpha = 5°$) [32]. The transition along the windward ray was observed slightly earlier, at $Re_x = 4.7 \times 10^6$, $\alpha = 9°$, $M = 7$ [32].

Figure 2.17 shows the transition front measured in the descent stage of flight, as detected by high frequency Kulite pressure sensors (PHBW1-3) and a Vatell Corporation thin-film thermopile heat transfer gauge (HT3). The figure has been

[13]The DiCristina flow conditions were $M_\infty = 10$, $T_w/T_0 \approx 0.3$, $Re_{unit,\infty} = 0.5 - 0.64 \times 10^6$ /m, whilst the Holden et al. conditions varied from $M_\infty = 11 - 13$, $T_w/T_0 \approx 0.2$, $Re_{unit,\infty} = 0.3 - 2.0 \times 10^6$ /m.

taken from the HIFiRE-1 flight analysis paper from Stanfield et al. (Figure 25 in [32]), and makes a comparison to the transition front measured by Juliano et al. in DLR's H2K facility [35, 36, 37]. An indented front is clearly observed in the flight results, between $\phi = 20° - 60°$, whereas the DLR results show the typical destabilization when progressing to the leeward ray in a cold flow tunnel.

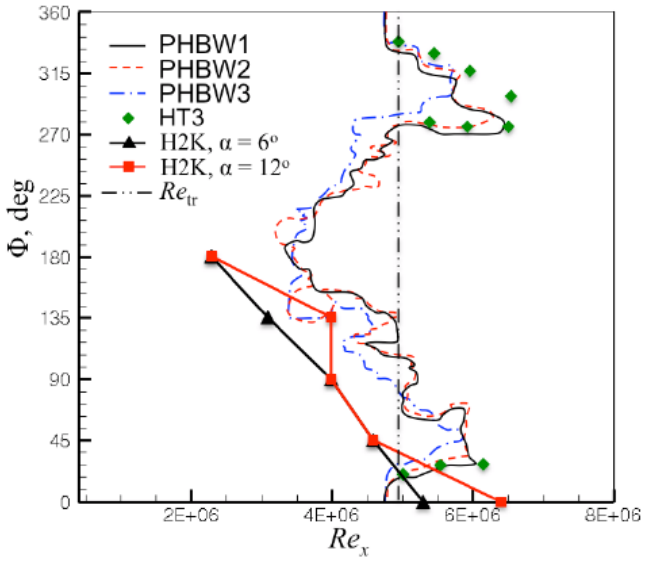


Figure 2.17: HIFiRE-1 Descent Transition map, compared to results from H2K's post-flight campaign. Taken from Figure 25 in [32]. PHBW1 - PHBW3 are measurements from high-frequency Kulite pressure transducers in flight. HT3 is a high-frequency Vatell heat transfer gauge, and the dot-dashed line given by Re_{tr} is the low-frequency transition measured by a Medtherm coaxial gauge in flight. The H2K $\alpha = 6°, 12°$ results are PCB132-detected transition fronts from the post-flight H2K campaign [36].

Summary

The origins of the stable region are still unclear. For the cases that show an indented front, the region of the cone that is more stable than the windward ray also varies. The current hypothesis it that azimuths approaching the windward ray have been destabilized due to wall-cooling effects on the second mode instability [33, 131, 141]. For this reason, it may be more suitable to refer to the transition feature as a sudden windward destabilization rather than a stable indented front. This also provides an explanation for the discrepancy between flight and H2K along the windward ray [36, 34].

2.7.5 Wall-cooling effects

The effect of wall-cooling on boundary layer transition is not clear, and measurements have frequently shown contrasting results. The wall-cooling level has traditionally been quantified using the wall-to-total temperature ratio (T_w/T_0). Many experiments have investigated wall-cooling effects by keeping the model temperature fixed, and changing the tunnel conditions (and therefore the stagnation temperature). This has led to inconsistent results, as the freestream turbulence levels change and are frequently not characterised [5]. Schneider notes that "the movement of transition with wall cooling is controversial; various reversals and re-reversals have been reported" [5]. It is therefore important to eliminate the uncertainty associated with freestream turbulence when investigating wall-cooling, and only change the model wall temperature wherever possible.

Mack's linear stability theory calculations are shown in Figure 2.18, for 2-dimensional waves over a flat plate [17, 149]. Temporal amplification rates are presented for the most unstable wave angle, as a ratio of the cooled to the uncooled cases. First-mode waves are stabilized when the wall is cooled, in agreement with prediction made by Lees [101]. The opposite is observed for second mode waves, as wall cooling destabilizes the boundary layer and accelerates transition at high Mach numbers (e.g. [150, 151, 152, 149]). For the purpose of this research, a focus is given to experimental results at high Mach numbers ($M_\infty \geq 5$), where the second mode instability is expected to dominate transition.

Instability and transition measurements

Multiple experiments have tried to isolate the effect of wall-cooling on boundary layer transition, with mixed results. For results at supersonic Mach numbers, Potter compared various experimental datasets for flat-plate and slender cones [153][14].

[14]It should be noted that this review had multiple limitations. Firstly, the majority of these experiments investigated wall-cooling by changing the flow conditions, and therefore have an additional uncertainty associated with tunnel noise. Datasets were also only shown if they included

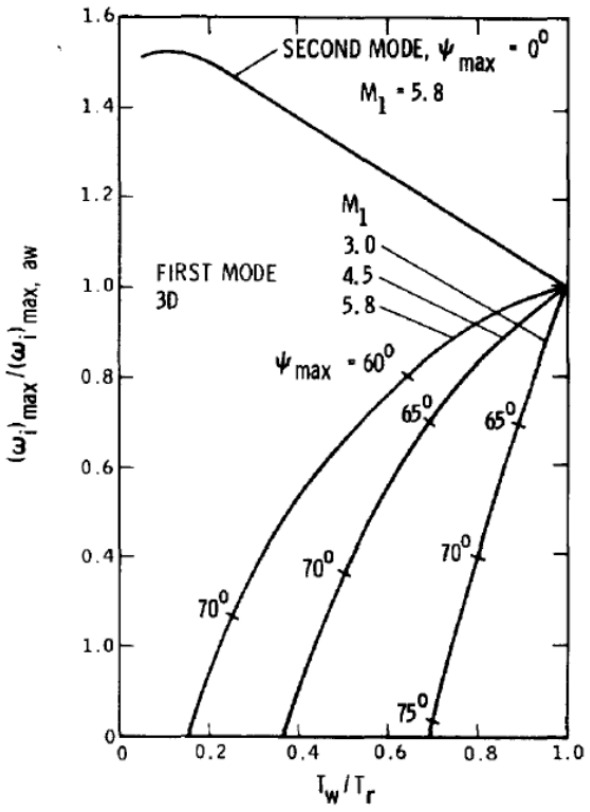


Figure 2.18: Effect of wall-cooling on the ratio of maximum temporal amplification rate for the first and second mode instability. Results are calculated using linear stability theory for an insulated-wall flat plate at multiple Mach numbers, and the most unstable wave angle for each mode.

Van Driest et al. also investigated the effect of wall-cooling at Mach 2.0 - 3.8, in the 12-inch continuous supersonic wind tunnel at the Jet Propulsion Laboratory in CalTech [154]. A transition reversal was attributed to an increased influence of roughness, as the boundary layer becomes thinner when T_w/T_0 decreases (see Figure 20 in Ref. [154]). If this is true, it would be expected that second mode dominated transition could be further destabilized, and no transition reversal would be expected.

Schneider reviewed three experiments that investigated the role of wall cooling by only varying the model wall-temperature, two of which were at hypersonic Mach numbers [5]. Both Sanator et al. [155] and Everhart et al. [156] took measurements

a $T_w = T_{aw}$ condition (due to the use of a normalized Re), which also meant that a lot of the investigations conducted at higher Mach numbers were not presented. Lastly, different methods had been used to determine the transition Reynolds numbers.

using a 5° half-angle cone with internal cooling[15] at Mach 10. Measurements were taken in the Republic Aviation Corporation 36-inch wind tunnel and the Langley continuous-flow hypersonic tunnel, respectively. Combining both datasets, they covered a range of wall-to-total temperature ratios of $0.075 \leq T_w/T_0 \leq 0.63$. Figure 2.19 shows the heat-transfer detected transition results for both experiments, reproduced using data from Figure 7b in Ref. [156]. The result shows no clear effect of wall-cooling, within the range $0.075 \leq T_w/T_0 \leq 0.63$. This is a bit surprising, as linear stability theory predicts that the second mode instability should be destabilized with wall-cooling at these high Mach numbers.

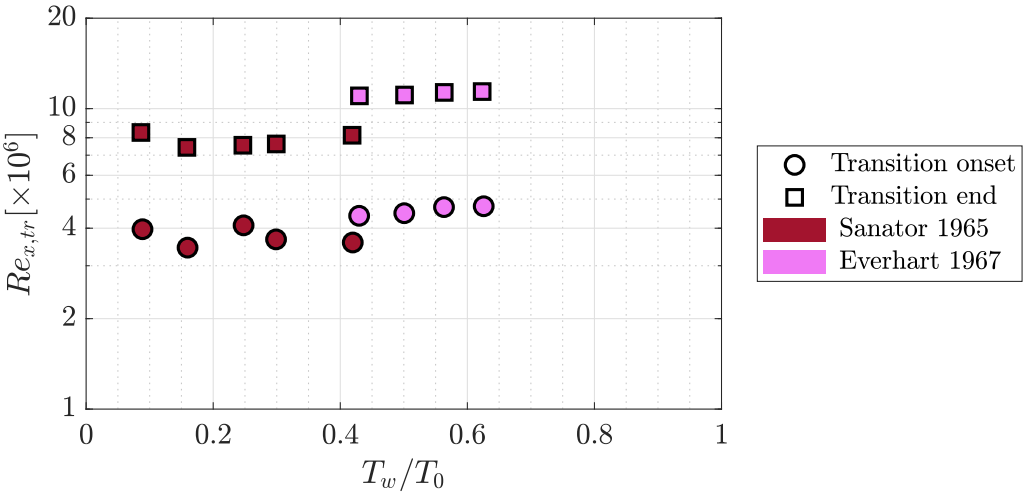


Figure 2.19: Effect of wall-cooling on the transition Reynolds number. Results are collated by Everhart et al., presented in Figure 7b of Ref. [156]. Transition was detected using heat transfer deviation from laminar trends.

Other experiments have observed second mode destabilization with wall-cooling, however this has frequently been achieved by varying facility flow conditions rather than purely model wall temperature. For example, Stetson investigated boundary layer stability on a water-cooled sharp 7° half angle cone at Mach 8 in the AEDC Tunnel B [151]. Disturbances in the cold wall boundary layer grew much faster than those in the boundary layer of the hot wall, as shown in Figure 2.20 (taken

[15]The model used by Sanator et al. [155] also contained a heating unit comprising of multiple electric heating elements.

from Figure 4 in Ref. [151]). Stetson notes that the boundary-layer disturbances are at different frequencies for the cooled and uncooled cases, and these would therefore overlap with different portions of the freestream disturbances (i.e. the A_1 values will slightly differ).

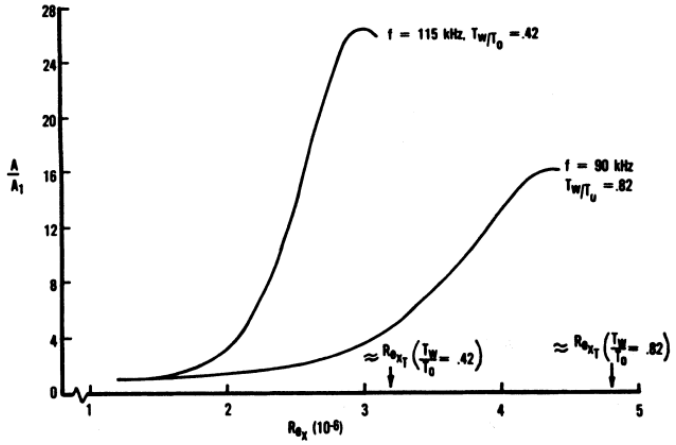


Figure 2.20: Effect of wall-cooling on the second mode amplitude, as measured by Stetson et al. [151]. Taken from Figure 4 in Ref. [151].

Summary

The experimental results are still quite unclear and have not necessarily agreed with the results from linear stability theory [149]. The expectation is still that the second mode waves will be destabilized with wall cooling, and should therefore result in earlier transition when it is the most dominant instability mechanism. It is important for experiments to control variables such as roughness (i.e. frost formation) and freestream disturbances in their investigations.

3 Experimental Setup

3.1 Hypersonic Wind Tunnels

Ground facilities are used extensively worldwide to conduct research at flight-representative conditions. One of the main benefits is that it is significantly cheaper to operate a wind tunnel than it is to conduct a flight test [25]. An additional benefit is that it is often possible to take measurements using instrumentation and optics which would otherwise not be accessible in flight [25]. A major drawback, however, is that no individual hypersonic facility can capture all conditions experienced in flight. This means that a range of facilities are often used to match the parameters that are critical to the phenomena being studied [157].

For boundary layer transition studies, the expectation has traditionally been that the freestream unit Reynolds number and the Mach number must be matched, whilst the temperature and velocity can be relaxed [157]. The Mach number is a measure of the compressibility characteristics of fluid flow. Matching the local Mach number therefore ensures that compressibility effects on the boundary layer are replicated. The unit Reynolds number ($Re_{unit} = \rho u/\mu$) is a parameter used to define the freestream conditions in a wind tunnel or flight. The unit Reynolds number is multiplied by a length scale to ensure that the inertial and viscous forces

are matched at the region of interest. Example length scales for boundary layer transition studies include: nosetip radius, vehicle length, boundary layer thickness.

Blowdown facilities can produce high pressure and high Reynolds number flows for a test time in the order of minutes or seconds, though at the cost of flight-representative enthalpy. Impulse-type wind tunnels typically store thermal, electrical, or chemical energy over a long period of time before allowing it to be rapidly released. This results in instantaneous release rates of energy and produces short test times when compared to the blowdown or continuous techniques. Quiet tunnels are the only facilities that are able to match flight-representative freestream turbulence levels [126], however this is at a cost of Reynolds number and enthalpy.

An overview of the types of wind tunnels and their associated benefits can be found in Refs. [157, 158, 126]. Figure 3.1 shows approximately where each type of facility lies with respect to freestream condition and test time [158, 159].

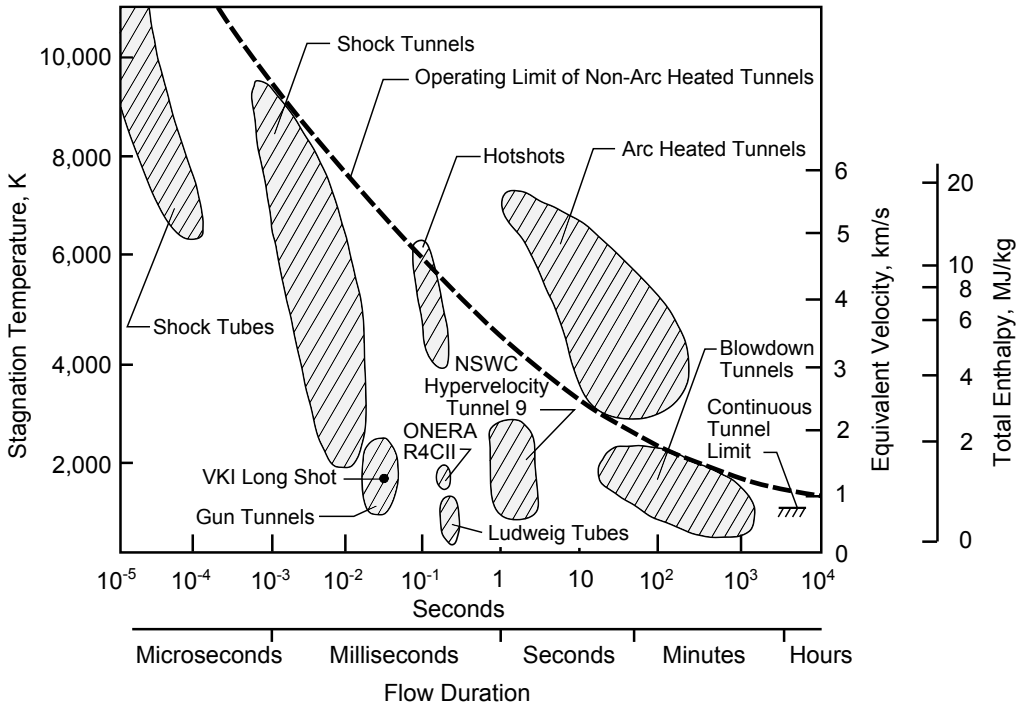


Figure 3.1: The scope of hypersonic experimental facilities as a function of velocity and test time [158]. Adapted by Wise, taken from Figure 2.7b in Ref. [159]

3.2 The Oxford High Density Tunnel

The Oxford HDT is capable of generating relatively long duration flows at high Reynolds number, and is suitable for both steady and unsteady aerothermodynamic testing of hypersonic configurations [160]. This research presents the first experiments in the facility. Thus, these are also the first boundary layer instability measurements and freestream disturbance measurements in the Oxford HDT. A brief history of the HDT is provided below, along with a description of how the facility operates. Chapter 4 details how the freestream conditions are calculated, and characterises the freestream disturbance levels in the facility. Chapter 5 then aims to verify the HDT facility, and the various processing methods, for boundary layer instability measurements. This is accomplished by comparing boundary layer instability results to a similar dataset obtained in DLR's H2K facility [36, 35, 37], and to PSE-Chem stability computations.

3.2.1 History of the High Density Tunnel

The Oxford High Density Tunnel (HDT) was originally developed by the RAE in the United Kingdom in the 1960's. It was initially operated as a cold hydrogen driven shock tube and tunnel [161]. The HDT was acquired by the University of Oxford's Osney Thermo-Fluids Institute in 2012. With the addition of a fast-acting plug valve [161], the HDT added the ability to be operated as a Ludwieg Tube or Light Isentropic Compression Heating (LICH) mode. The facility was commissioned in its Ludwieg Tube mode in June 2016 as part of this thesis work. At the time of writing, over 750 shots have been fired in Ludwieg Tube mode. LICH Tube mode is scheduled to be commissioned in late 2019 / early 2020.

3.2.2 Details of operation

For this research, the Oxford HDT is run using its Ludwieg tube mode. Each experiment begins by filling the barrels with air to the pre-determined fill pressure[1]. External electrical heating of the test gas is used to increase the total temperature, up to a maximum temperature of 573 K. The objective is to heat the test gas enough so that it does not liquefy at the nozzle exit. The Ludwieg tube is attached to a bespoke fast-acting plug valve assembly, which feeds the stagnation plenum of a contoured converging/diverging nozzle. These features are shown in a CAD section view in Figure 3.2. The test time begins when the plug valve is opened, causing the test gas to undergo an unsteady expansion and accelerate through the convergent/divergent nozzle. The facility nozzle exhausts into the test section, and then into a 28 m^3 vacuum tank that is external to the building. The nozzle exit diameter is 350 mm, with a length of 1395 mm between the throat and nozzle exit. The test section has a diameter of 760 mm and a length of 940 mm.

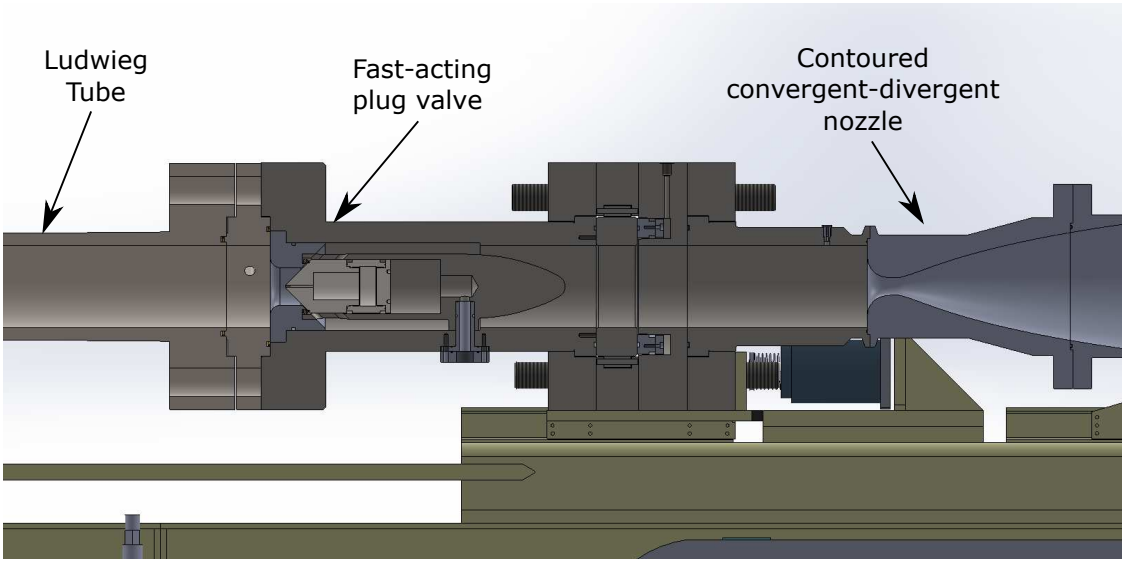


Figure 3.2: An annotated CAD section view of the HDT Ludwieg Tube, fast-acting plug valve, and contoured convergent-divergent nozzle (Mach 7 nozzle shown).

[1]The facility has an overall pressure limit of 275 bar, however, pressures of this order are currently unachievable as the test section must be kept at sub-atmospheric conditions.

A succession of expansion waves propagate into the high pressure region when the plug valve is opened. The initial test time is therefore steady until the expansion wave reflects from the far end of the tube and passes through the nozzle again. This results in multiple quasi-steady flows (referred to as "plateaus") between expansion wave reflections, giving a sweep of conditions for an individual shot. The plug valve timings can be modified to control the amount of flow passing through the facility. This allows the operator to dictate the number of steady test time plateaus that are being captured. Figure 3.3 illustrates the HDT plateaus for two shots where the plug valve timings are significantly different. Shot 330 is an example of a shot which benefits from as much test-time as possible, and can make use of a range of conditions that exist over the various plateaus. Shot 602 is a stagnation pressure profile from a free-flight experiment, where the experimenter wants to limit the amount of test gas passing into the dump tank. Details about the fast-acting plug valve can be found in Ref. [160].

The test section is fitted with a Quadratec traverse mechanism, allowing automatic re-orientation of an experimental model over a range ±15° angle of attack and ±5° angle of yaw. It can be used for microalignment (see Section 5.3), and also allows the experimenter to make changes to the model orientation without

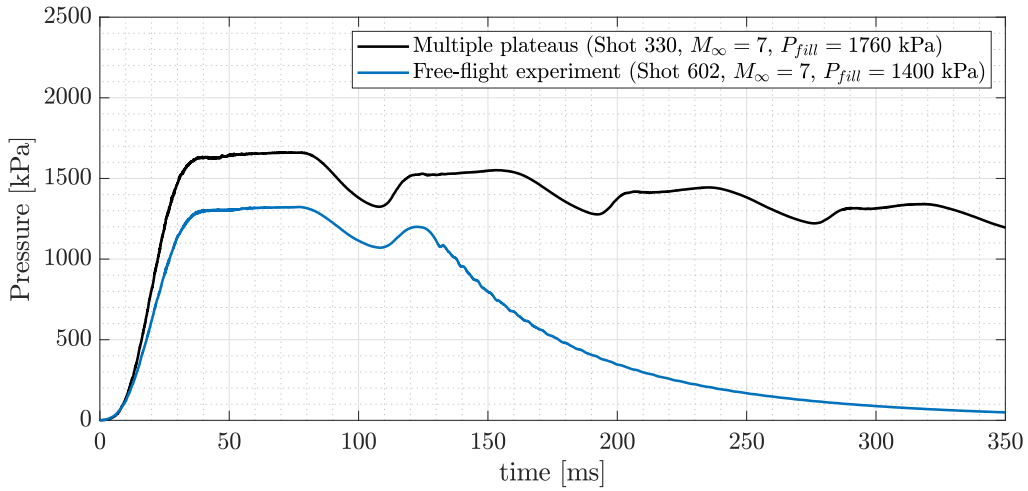


Figure 3.3: An example of multiple stagnation pressure profiles in the Oxford HDT, to satisfy individual experiment objectives. The different profiles are achieved by modifying the fast-acting plug valve timings.

bringing the test section back up to atmospheric pressure, saving time between tests. An annotated schematic of the Quadratec traverse mechanism[2] is shown in Figure 3.4.

Further information concerning the design, operation and installation of the Oxford High Density Tunnel can be found in [160]. A schematic of the Oxford HDT with key components annotated is provided in Figure 3.5, whilst Figure 3.6 is a photograph of the Oxford HDT (on the right), along with the Oxford T6 Stalker Tunnel (on the left). An annotated section view of the HDT facility is provided in Figure **??**, with the HDT 7° Cone model installed at the experiment location. Commissioning has successfully taken place over a range of unit Reynolds numbers ($Re_{unit} \approx 7$ x 10^6 /m to 53 x 10^6 /m) using the Mach 3, 4, 5, 6, and 7 nozzles and a range of wall-to-total temperature ratios ($T_w/T_0 \approx 0.56$ to 1).

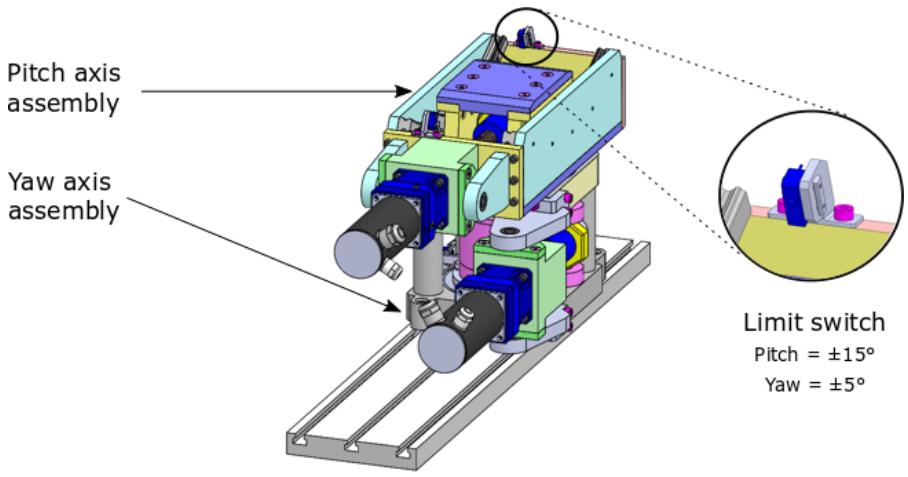


Figure 3.4: An annotated schematic of the Quadratec traverse equipment.

[2]The Quadratec traverse mechanism is referred to as the "traverse" throughout. An identical traverse is used in the T6 Stalker Tunnel.

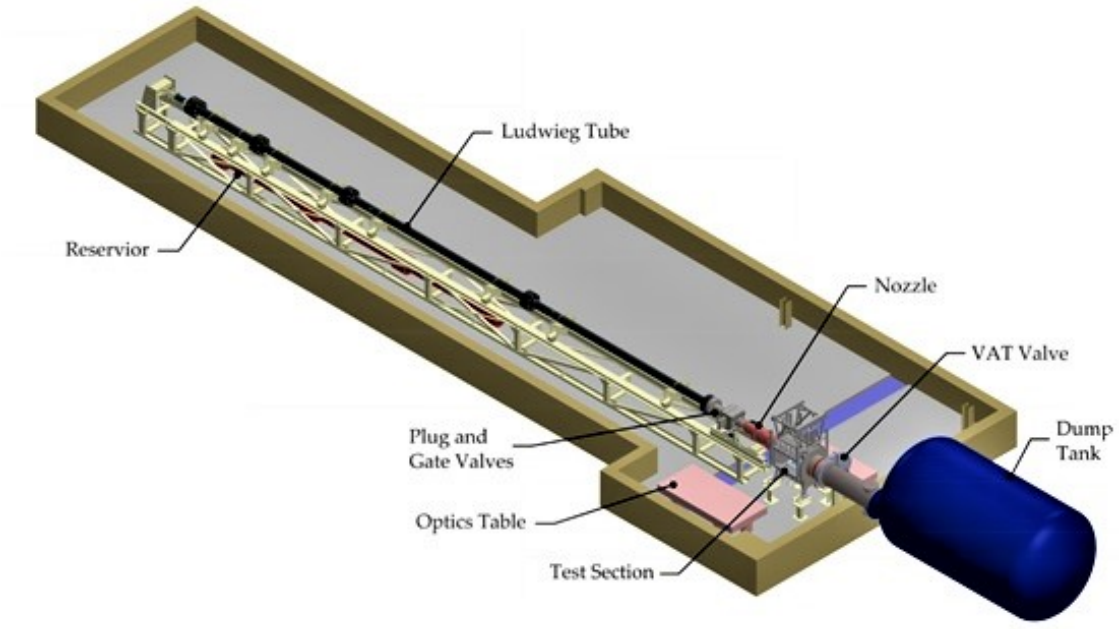


Figure 3.5: An annotated schematic of the Oxford High Density Tunnel (HDT) [160]



Figure 3.6: The Oxford T6 Stalker Tunnel on the left, and the Oxford High Density Tunnel (HDT) on the right

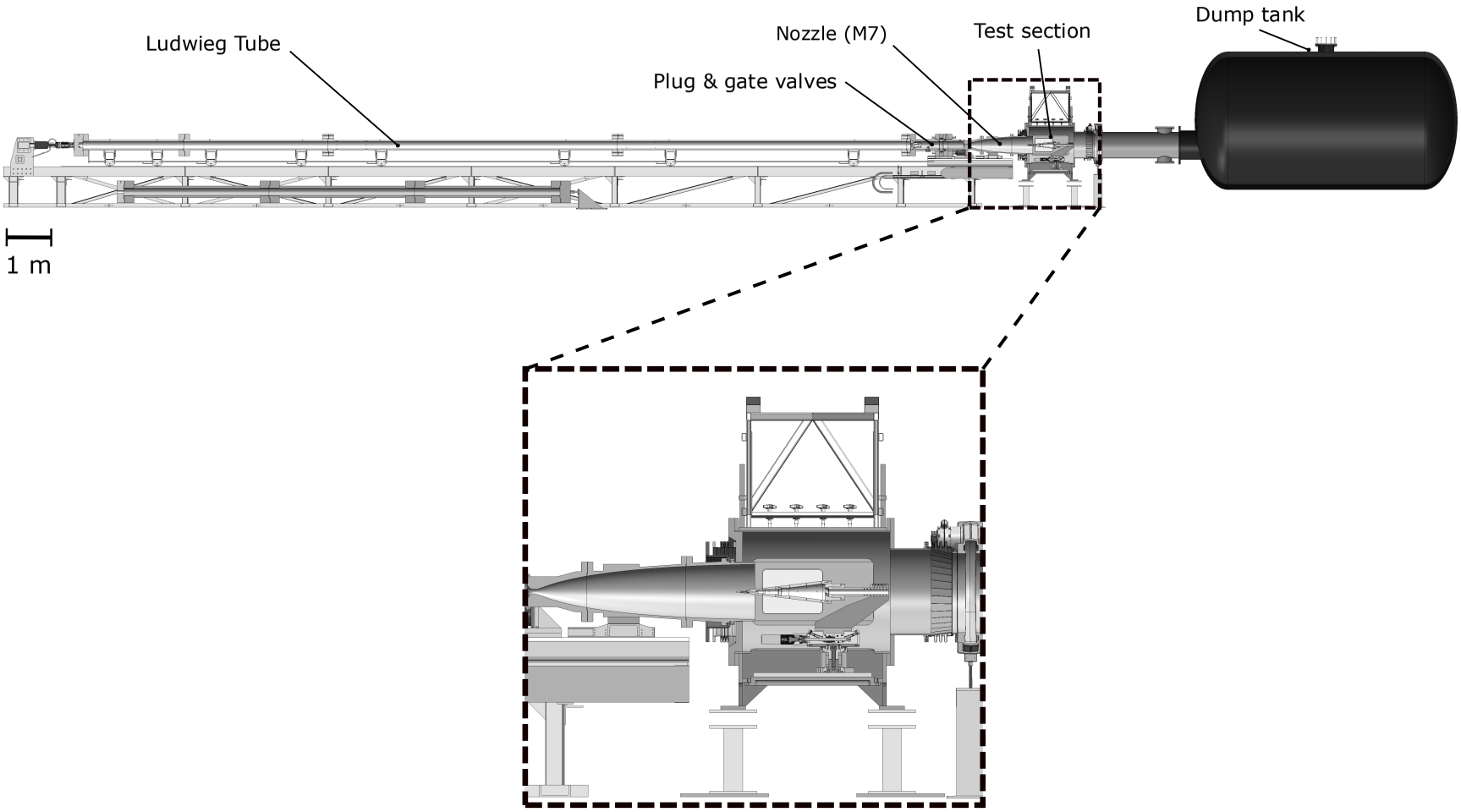


Figure 3.7: A CAD schematic of the Oxford High Density Tunnel, along with a detailed view of the HDT 7° cone model at the experiment location.

3.3 The University of Queensland's T4 Stalker Tunnel

The T4 Free Piston Reflected Shock Tunnel is an impulse type facility, designed to generate high-speed flows with varying Mach number. The facility is composed of five main sections: a reservoir of high pressure air, a compression tube, a shock tube, a nozzle, a test section and a dump tank [162]. An annotated schematic of the T4 Stalker Tunnel is shown in Fig. 3.8.

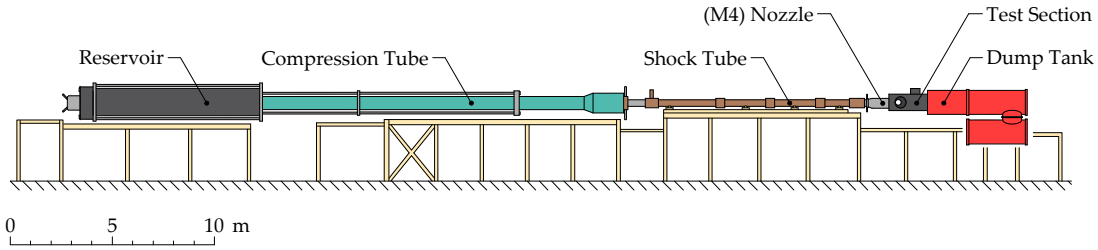


Figure 3.8: T4 Free-Piston Reflected Shock Tunnel [163]

An un-scored brightform steel diaphragm separates the driver from the shocktube, whilst a secondary 0.1 mm thick Mylar diaphragm separates the shocktube from the nozzle [164]. The thickness of the primary diaphragm is varied between two to four millimetres for this research. A reservoir of high pressure air propels the 92 kg steel piston down the compression tube, causing it to adiabatically compress the driver gas[3]. When the pressure in front of the piston reaches the burst pressure of the diaphragm, the diaphragm ruptures and a shock wave travels down the shock tube, compressing, and accelerating the test gas[4] [162]. The shockwave is followed by the contact surface, separating the test gas from the driver gas, along with an unsteady expansion.

As the shockwave passes through the shock tube, it increases the test gas pressure and temperature. The shock wave reflects from the end of the shock tube, re-compressing and stagnating the test gas. The high pressure test gas ruptures

[3] A driver gas mixture of helium and argon is used in this research
[4] The test gas used in this research is air.

the Mylar diaphragm and expands through the nozzle and over the model [162]. After a period of unsteady expansion, the steady test gas flow is established and the test time begins. The end of the test time occurs when either the unsteady expansion reduces the usable mass flow through the nozzle, or the test gas becomes contaminated by the driver gas [164]. In practice, this results in a test time of approximately one to five milliseconds. The distance-time diagram for the processes described above is shown in Figure 3.9 [163, 165, 166]. More information about free-piston driven reflected shock tunnels can be found in Refs. [166, 164, 165, 163].

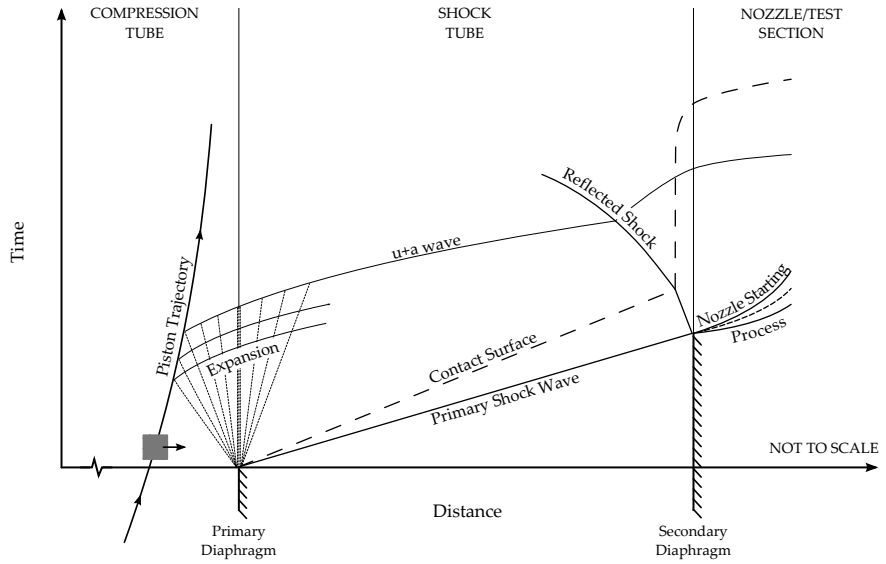


Figure 3.9: Distance-time diagram showing the main processes of the T4 reflected shock tunnel [163, 165, 166]. Taken from Figure 3.2 in Ref. [163]

The freestream disturbances in T4 were not characterised for this campaign. He and Morgan [167] measured Pitot-pressure fluctuations using fast pressure transducers, with response frequencies up to 250 kHz. The rms Pitot pressure was roughly 3% of the mean, though variation between 2% - 8% was observed for the conditions tested. This result indicates that the T4 facility is expected to have freestream disturbance levels that are of a similar order to other conventional tunnels [125].

3.4 Oxford 7° cone models

Two axisymmetric conical models were used for transition experiments. The HDT 7° Cone Model was suitable for longer-duration flows, whilst the RST 7° Cone Model was suited to shock tunnels (T4 & T6). The models differ in their length, pressure sensor instrumentation mounting method, and instrumentation locations. Each model has a 7° half-angle and multiple interchangeable nose radii. The 7° half angle was chosen due to the large number of datasets available in the literature, such as the HIFiRE-1 flight test. It is possible to physically rotate the cone models about their revolution axes in 45° increments, to get a broad coverage of results between the windward and leeward ray. To minimize discontinuities between segments, both cone models were fully assembled before the final surface finishing was done.

For both models, sensors were staggered in the azimuthal direction in 90° intervals. This was beneficial for multiple reasons. Firstly it allowed sensors on diametrically opposing arrays to be used to confirm microalignment of the model in both angle-of-attack and angle-of-yaw. Secondly, it reduced the number of shots required to get full azimuthal coverage (particularly helpful in reflected shock tunnels). Lastly, it reduced the density of sensors for a given flow streamline, with the hope to decrease the potential gauge-induced roughness. A drawback of this approach is that multiple shots were required to obtain measurements at all axial locations for a given azimuth. The following sections provide an overview of the models used (HDT model & RST model), along with the instrumentation and processing methods.

Coordinate system

The axial distance from the apex of the cone nosetip is denoted by x. The azimuthal angle (ϕ) corresponds to the angle about the x-axis, with the windward ray equalling 0° and the leeward ray corresponding to 180°. Figure 3.10 illustrates the coordinate system used. The model-fixed azimuthal angle is denoted by φ.

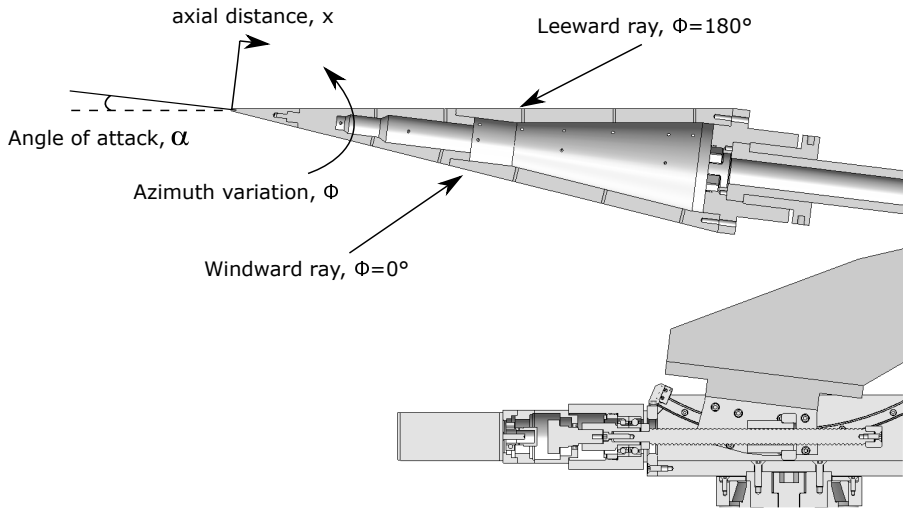


Figure 3.10: Schematic to illustrate the coordinate system used for the 7° Cone Models.

3.4.1 The HDT 7° Cone Model

The HDT 7° Cone Model has a length of 550 mm along its revolution axis, with a corresponding base diameter of 140 mm. This was deemed to be the maximum model size that could confidently fit inside the HDT Mach 7 coreflow, particularly at high angles of attack ($\alpha \leq 14°$). The length corresponds to 50% scale of the HIFiRE-1 flight vehicle. The nosepiece and front segment of the HDT HIFiRE model are made of case hardened EN36B steel, whilst the rear segment is made of Aluminium 7375. Figure 3.11 shows the HDT 7° Cone Model, along with a cross-section view to illustrate the main components. Several interchangeable nosepieces were available, ranging from $0.05 \leq R_N \leq 2.5$ mm. This corresponds to a nose-to-base ratio range of $0.00036 \leq \frac{R_N}{R_B} \leq 0.0179$. The nosetips used in the HDT 7° Cone Model did not

include a heater cartridge.

The HDT 7° Cone Model was instrumented with nineteen high-frequency pressure sensors (PCB132A31), five static pressure sensors (Kulite XTEL-140M), six thin-film heat transfer gauges [168], and two diamond calorimeter gauges [169]. The surface roughness was characterised using an Alicona InfiniteFocus camera. The average roughness (R_a) and root-mean squared roughness (R_q) are measured for each segment (nosetip, front & rear), as well as the steps between segments. The maximum surface roughness was on the front segment: $R_a = 1.8\mu\text{m} \pm 0.1$ (one stdev) and $R_q = 2.3\mu\text{m} \pm 0.1$ (one stdev). The junction between the front & rear segment had a peak-to-peak step in the order of ≈ 30 μm. The individual instrumentation locations and surface roughness characterisation details are provided in Appendix A.

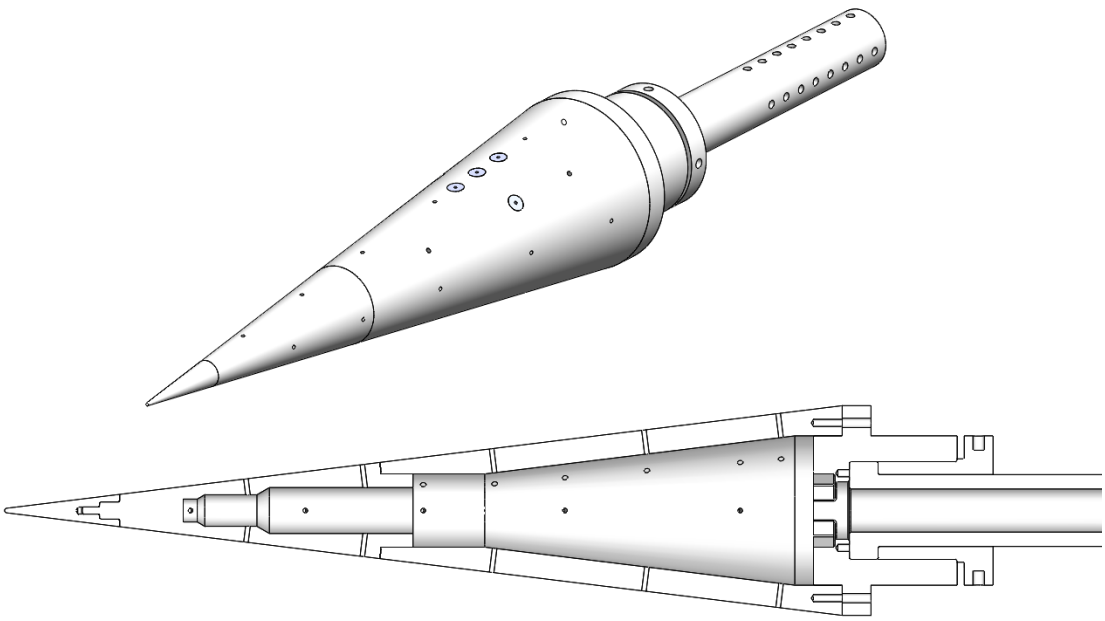


Figure 3.11: Isometric and cross-sectional view of the HDT 7° Cone Model.

3.4.2 The RST 7° Cone Model

The RST 7° Cone Model has a length of 380 mm along its revolution axis, with a corresponding base diameter of 96 mm. This corresponds to a 34% scale model of the HIFiRE-1 flight vehicle. There are multiple reasons why a separate model is required for experiments in Oxford's T6 facility and the University of Queensland's T4 facility. Firstly, model vibrations have the potential to affect the piezoelectric sensors when they are mounted directly to the model using RTV. The PCB132 sensors are mounted within neoprene tubing, in an attempt to damp out these vibrations [170]. Secondly, both T6 and T4 have smaller test sections when compared to the Oxford HDT. To ensure that the model would still be within the coreflow at high angles of attack, a smaller model was also required.

The nosepiece and front segment of the RST 7° Cone Model are made of case hardened EN36B steel, whilst the rear segment is made of EN24T steel. Figure 3.12 shows the T6 7° Cone Model, along with a cross-section view to illustrate the main components. The same set of nosepieces from the HDT 7° Cone Model are compatible for use with the RST 7° Cone Model. The smaller rear segment base diameter results in a nose-to-base ratio range of $0.00052 \leq \frac{R_N}{R_B} \leq 0.026$. Nosetip heater cartridges were used in experiments with the RST 7° Cone Model (detailed in Section 3.5).

The RST 7° Cone Model was instrumented with 16 high-frequency pressure sensors (PCB132A31), two static pressure sensors (Kulite XCEL-152), nine thin-film heat transfer gauges [168], and six diamond calorimeter gauges [169]. The average roughness (R_a) and root-mean squared roughness (R_q) are measured for each segment (nosetip, front & rear), as well as the steps between segments. The maximum surface roughness was observed on the rear segment: $R_a = 1.8\mu\text{m} \pm 0.1$ (one stdev) and $R_q = 2.9\mu\text{m} \pm 0.3$ (one stdev). The roughness profiles were also investigated for the PCB132 sensors installed in the neoprene tubing. The neoprene mounting method resulted in alarmingly large steps between the tubing and the

sensor, with peak-to-peak magnitudes as high as 200 μm. The instrumentation locations and surface roughness characterisation details are provided in Appendix A.

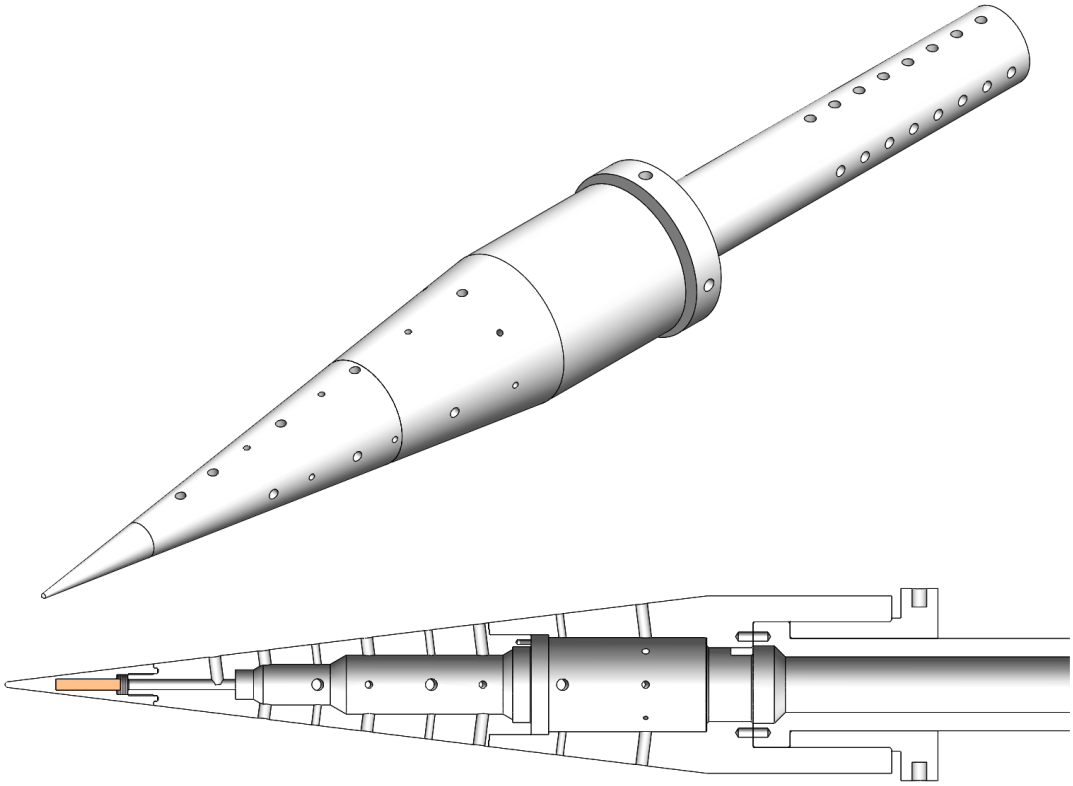


Figure 3.12: Isometric and cross-sectional view of the RST 7° Cone Model. The orange element illustrates the nosetip heater cartridge, as detailed in Section 3.5.

3.5 Wall-temperature distributions using a heated nosepiece

A 40 W DC powered heater cartridge was installed inside the RST 7° Cone Model nosepiece. This made it possible to investigate the effect of small changes in wall-to-total temperature ratio on boundary layer instabilities, whilst keeping tunnel freestream conditions constant. This research opted to heat the nosetip for multiple reasons. Firstly, a heated nosetip allowed further use out of the RST 7° Cone Model. Secondly, internal cooling throughout the entire model would have been difficult to achieve whilst continuing to use PCB132 sensors for instability measurements. This is due to their limited operating temperature range of 255 - 352 K. Heating the nosetip in a controlled manner allows the front part of the cone to be heated to higher temperatures whilst ensuring that the most upstream PCB gauge did not overheat.

3.5.1 Heated nosepiece design

Figure 3.13 shows the installation of the DC powered heater cartridge inside the cone nosepiece. Power is provided to the heater cartridge through the small channel inside the front segment. Three K-Type thermocouples are located within the channel at the same axial location as the most upstream PCB sensor, PCB1. Measurements are taken at the beginning of each test, to confirm that wall-temperatures do not exceed the operating limit for a given heating load. The metallurgy for the K-type thermocouple is maintained throughout all connections within the model, so that the cold junction is measured at the test section wall.

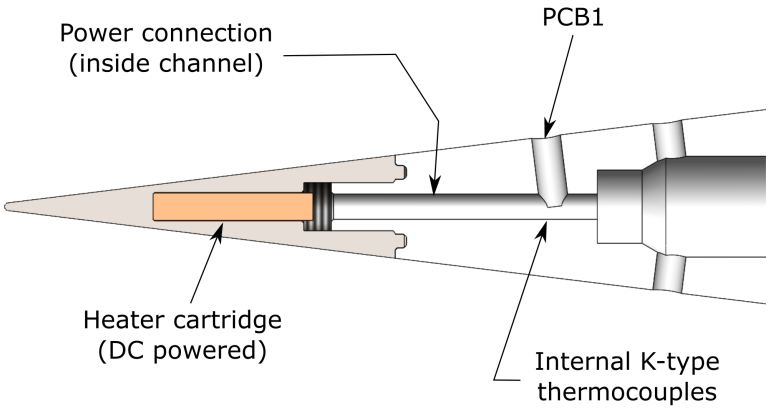


Figure 3.13: Heated nosetip used for the RST 7° Cone Model. Shown with the $R_N = 0.89$ mm nosetip.

3.5.2 Wall temperature distribution results

The wall temperature distribution was characterised for a range of heater cartridge powers under vacuum. To achieve this, the RST 7° Cone Model was installed inside the T6 test section. A series of K-type thermocouples were placed at various axial locations on the $\varphi = 270°$ ray and inside the front segment channel, with the cold junction taken at the test section wall.

Wall temperature distributions were obtained for a range of heater cartridge powers, $P = 5 - 30$ W, with results presented in Figure 3.14. For each case, the model was left to reach a steady-state temperature. A drop-off in wall-temperature is expected at the interface between the nosepiece and the front segment, $x = 85$ mm. The internal K-type thermocouples agree with the thermocouple on the cone surface at the same axial location, with a discrepancy of less than 1 K. These results show that a maximum heater cartridge power of $P = 15$ W is achievable before exceeding the operational temperature at PCB1.

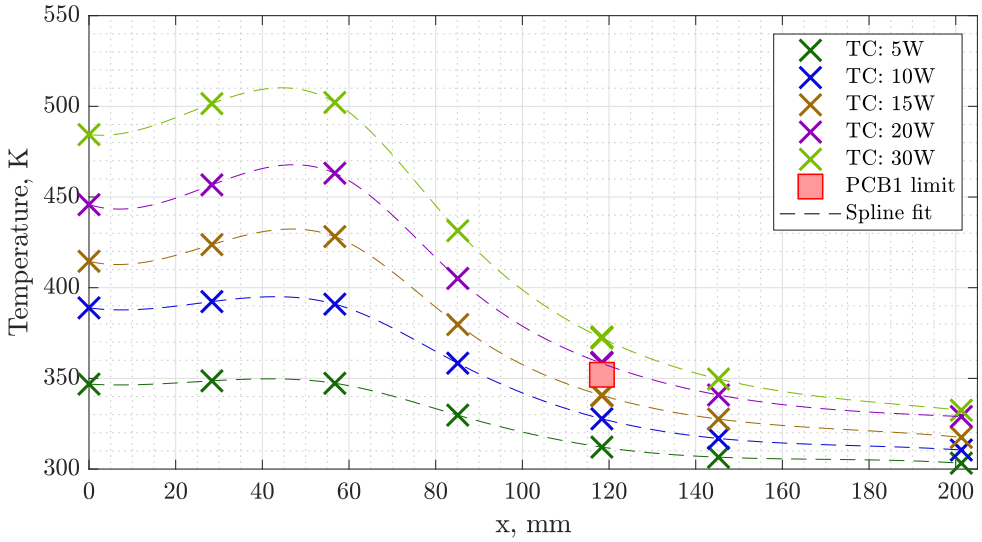


Figure 3.14: Wall-temperature distributions as a function of heater cartridge power, measured using K-Type thermocouples. The dashed lines are spline fits of the thermocouple data.

3.6 Instrumentation

The experimental campaigns make use of piezoresistive pressure sensors, piezoelectric pressure sensors, and thin-film gauges. Each instrumentation is detailed in the subsections that follow, along with information about the data processing methods used. The output of all instrumentation are measured with NI PXIe-6368 Multifunction I/O Modules, operated at 2 megasamples per second per channel in the Oxford HDT.

3.6.1 Piezoresistive pressure sensors

Piezoresistive pressure sensors are used for static pressure measurements along the cone surface. Kulite XTEL-140M sensors are used in the HDT 7° Cone Model, Kulite XCEL-152 sensors are used in the RST 7° Cone Model, and Kulite XCQ-093 sensors are used for freestream characterization studies in a Pitot rake. Figure 3.15 shows an image of each of the sensor models. The XTEL-140M and XCEL-152 sensor models have a pressure range of 35 kPa, and a natural frequency of 175 kHz. This pressure range is sufficient for the small pressures that are expected on the

cone surface. The Kulite XTEL-140M sensors have an external diameter of 2.54 mm and make use of a thread to install the sensor. The Kulite XCEL-152 model has an external diameter of 3.80 mm, and is glued directly into the model using RTV. All piezoresistive sensors are calibrated in the tunnel at the beginning of each day of testing. They are connected to a FYLDE FE-H379-TA high bandwidth transducer amplifier, with a Butterworth 2 pole low pass filter applied at 30 kHz.



(a) XTEL-140(M) **(b)** XCEL-152

Figure 3.15: Figure of the Kulite piezoresistive sensors used in this research.

The primary uses of the piezoresistive sensors is to take static wall pressure measurements and Pitot pressure measurements. The Kulite upper-bound frequency limit is too low to resolve most of the boundary layer instabilities that are expected in this research. That being said, on multiple occasions the power spectra over the low frequency band is processed. One example includes the characterization of post-shock freestream fluctuations over a low-frequency band using Kulite XCQ-093 sensors in a Pitot rake (see section 4.3).

3.6.2 Heat transfer gauges

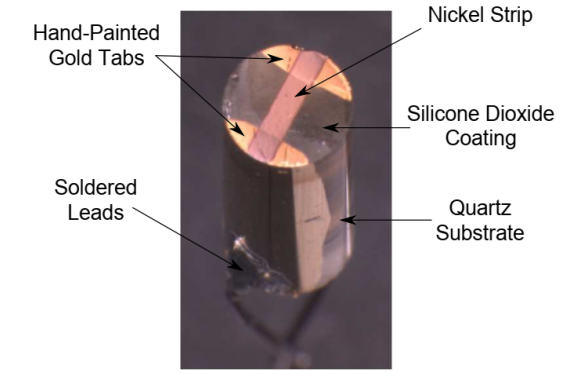
Thin film heat transfer gauges [168, 171] and diamond calorimeter gauges [169] are used to detect transition onset in both 7° Cone Models. Fast response times and robustness are key criteria for taking heat transfer measurements in hypervelocity wind tunnels. In this research, only results from thin film heat transfer gauges are presented. Details about the gauge, data processing, calibration, and signal conditioning are given below.

Thin film heat transfer gauges

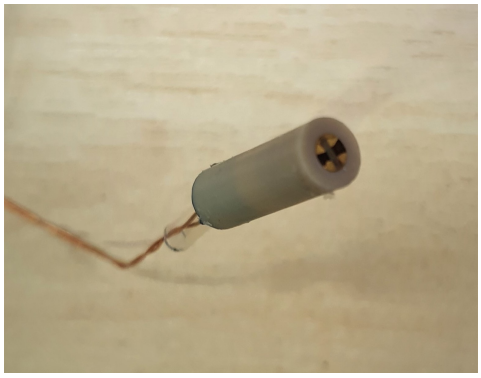
The thin film heat transfer gauges are manufactured at the University of Queensland's Centre for Hypersonics. The sensors work by placing a thin metallic film within the flow. This film acts as a resistance thermometer, making it possible to calculate the temperature history and therefore the heat transfer rate from the signal [171]. Response times in the order of $1 - 2\mu$s are achievable [168, 171]. This is sufficiently low to obtain an accurate history of the heat flux within the short test times in reflected shock tunnels ($\approx$ 1ms). The film is assumed to be sufficiently thin so that its heat capacity is negligible [172, 171]. The substrate is assumed to be sufficiently thick so that it acts as a semi-infinite medium [172]. A detailed description of the theory behind thin-film gauge operation can be found in Schultz and Jones [173].

A 20nm Nickel strip is sputtered onto an optically smooth quartz substrate [171]. The gauge resistances typically range from $20 - 100\Omega$. Nickel is used due to its high temperature coefficient at the anticipated operating conditions, and Quartz is chosen due to its well-documented thermal properties and lack of variation with temperature [173, 172, 171]. A layer of SiO_2 is deposited over the surface of the gauge to increase the gauge durability and eliminate any electrical shortage from ionized flow [171]. Figure 3.16a shows the key features of a thin film gauge. For testing in the 7° Cone Models, it is housed within a PEEK sleeve, as shown in

Figure 3.16b. The external PEEK diameter is 4 mm, and the gauge is glued directly into both models using RTV.



(a) A thin-film heat transfer gauge with annotations to highlight key components. Taken from Ref. [171].



(b) Thin film gauge inside PEEK housing.

Figure 3.16: Schematic of the thin film heat transfer gauge [171], along with the PEEK sleeve used to house the gauge for the 7° Cone Models.

At the University of Oxford, the thin film gauge coefficient of resistance as a function of temperature were found using water bath calibration process as described by Collins [174]. At the University of Queensland, the calibration process is similar though makes use of an oven. All gauges are calibrated both before and after each campaign. Both processes involve raising and lowering the temperature in a controlled manner over multiple steps. During each step, the temperature of the oven or bath is recorded along with the resistance of the gauge. The measured temperature is plotted against the resistance to form points on a straight line,with the gradient of the line of best fit used as the sensitivity of the gauge, α_R.

A constant current of 10mA is supplied to the thin film gauges. An in-house HTA4.5 amplifier was used to amplify the voltage signal. The amplifier has a gain profile which rises with frequency, to reduce digitisation errors and signal to noise issues for high frequency heat flux fluctuations [175]. To account for the frequency dependent HTA4.5 amplifier gain, the inverse impulse response of the amplifier was convolved with the measured signal [176]. The deboosted voltage and coefficient of

resistance are used to calculate the temperature as a function of time. A convolution impulse response was then applied to the de-boosted temperature to calculate the surface heat flux, using the codes developed by Oldfield [176]. For this research, the local surface heat flux was then averaged over the flow test time and compared to theoretical baseline levels.

The heat transfer detected transition onset is defined as the location where heat flux increases above laminar baseline levels. The theoretical turbulent heat flux is estimated from van Driest [177]. The theoretical laminar heat flux is approximated using the Blasius solution and the Reynolds analogy to relate the Stanton number (St) to the skin friction coefficient (C_f). The result is adapted for a compressible flow over an axisymmetric cone ($C_{f,cone} = \sqrt{3}C_{f,plate}$) as described by White [24]. Thin film measurements are compared to theoretical baselines in the HDT results at $\alpha = 0°$. In nearly all cases, the thin-film gauges are at matching locations to the PCB132 sensors, and allow a direct comparison between the transition onset from local heat-flux and the PCB-detected instabilities for a given array.

3.6.3 Piezoelectric pressure sensors

PCB132 fast-response piezoelectric pressure transducers have successfully measured pressure fluctuations at instability frequencies in many hypersonic facilities around the world. The first successful use of the sensors for this purpose was by Fujii using a 5° half angle cone at Mach 7.1 [90]. The PCB132A31 model has a 350 kPa range, a resonant frequency above 1MHz, and a discharge time constant of $\geq 45\mu$s. The discharge time constant causes the gain to tail off below 11 kHz. The sensor diameter is 3.18 mm, however the sensing element is only a square area of 0.762 x 0.762 mm^2. This sensing element is not necessarily located at the centre of the sensor for the PCB 132A31 model[5] [178]. The sensors are connected to PCB 482C

[5]The PCB 132B38 model is the successor to the PCB 132A31 model. This sensor has a circular sensing element of 0.62 mm^2 which is located on the center of the sensor. It also makes use of FEP type cable to output the signal.

Series signal conditioners.

Piezoelectric sensors are used for multiple purposes in this research. Their primary use is to resolve pressure fluctuations at frequencies where boundary layer instabilities are anticipated. A second use for the sensors is to characterise the post-shock freestream turbulence levels in a Pitot rake. The sensors are not used for static pressure measurements, due to the difficulty in deconvolving the signal to recover the signal at frequencies below 11 kHz. Information regarding the sensor calibration is given in Section 3.6.3 below, whilst the various processing methods are detailed in Section 3.7.

Calibration of PCB132 sensors

PCB use a low pressure shock tube calibration system to determine the sensitivity and frequency response of each sensor [179]. The PCB132 sensor is mounted using RTV in a Pitot configuration at the end of the shock tube. A PCB 134A reference sensor is mounted next to the PCB132 sensors, and is used to measure the reflected pressure step. They convert the PCB132 response into the frequency domain, and scale it to the reference pressure from the PCB 134A sensor. An example of this process is shown in Figure 3.17, taken from Figure 5 in Ort et al. [179]. The factory calibration value is then taken to be the flat region centered at 20 kHz (shown as red in Figure 3.17).

Berridge et al. noted that the calibrations are linear over a range of pressures, indicating that the PCB factory calibration should be accurate at the smaller amplitudes expected from second mode waves. Nevertheless, there are multiple concerns when using the PCB132 sensors for power spectral density analysis. Firstly, it is clear from Figure 3.17 that the factory calibration value is only accurate over a small portion of the frequency range ($\approx 10^4 - 10^5$ Hz). The sensitivity varies significantly over the frequencies where instabilities are anticipated in this research

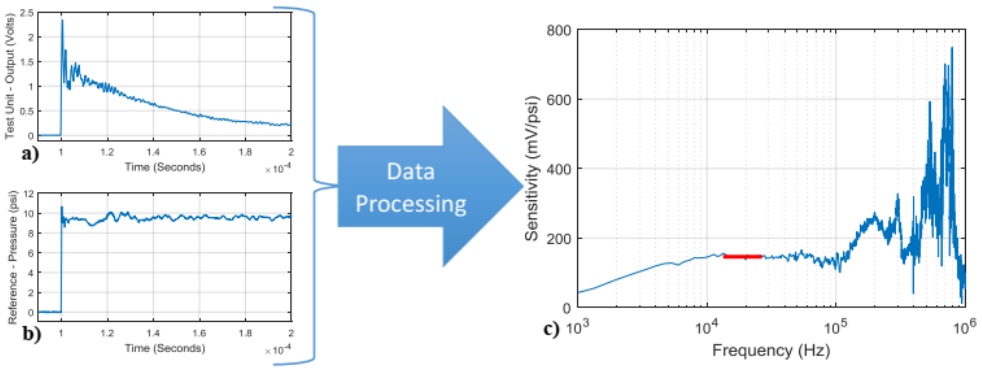


Figure 3.17: PCB method for determining frequency response and factory calibration values for PCB 132 sensors [179]. Taken from Figure 5 in Ort et al. [179]

(200kHz − 700kHz). A second concern is that the frequency response of the sensors is highly dependent on the mounting method used [179].

Figure 3.18 shows the gain profile obtained by PCB when using the Neoprene 60A tubing, and RTV inside a hole of ID 0.128". Both profiles show a flat sensitivity profile for the low-frequency band where travelling crossflow waves may exist at high angles of attack ($f \approx 11 - 80$ kHz). There is a significant sensitivity variation at the frequencies where second mode or stationary crossflow waves are expected. No correction was applied for this research, however this is an area of ongoing work.

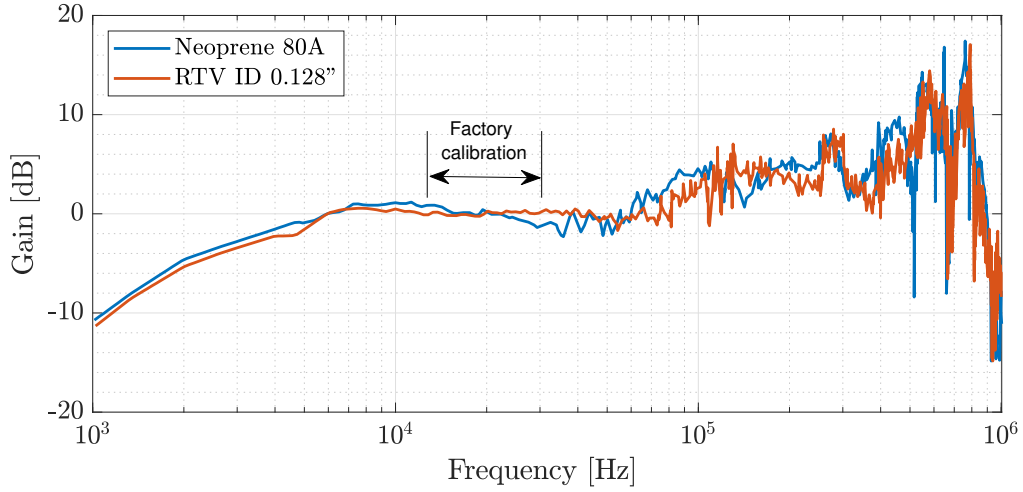


Figure 3.18: A comparison of PCB gain profiles for the RTV mounting method, and the Neoprene 60A housing. Results have been reproduced using data from Figure 15 and Figure 16 in Ref. [179].

3.7 PCB132 processing methods

The PCB132 sensors are processed using multiple techniques. This makes it possible to understand the presence of boundary layer instabilities along the 7° Cone Models both as a function of time, and as a summary for the entire test-time. Table 3.1 summarises the typical test times and corresponding data points for each of the facilities presented in this research. Each processing method is briefly detailed in the subsections that follow.

Facility	Test time (typical, ms)	Data points ($\times 10^3$)	Sampling rate (MHz)	Mounting method	Hole size (ϕ, mm)
Oxford HDT Ludwieg Tube	18	36	2	RTV	3.25
UQ T4 RST Mode	1.5	3	2.5	Neoprene 6705	6.35

Table 3.1: Summary of anticipated test times and number of PCB132 data points from each facility: HDT, T4, and T6.

3.7.1 Fast Fourier Transform: Power spectral density (PSD) using Welch's method

The power spectral density (PSD) is calculated over the stable flow test time using Welch's method [180]. The data is split into blocks containing 500 samples each, with 50% overlap between consecutive blocks. Each block is normalized by the cone static pressure[6] for each test, and then multiplied by the Hann function. The local cone static pressure is expected to change as a function of azimuth at high angles of attack, and this variation is addressed in Section 7.3. The power spectral density is calculated using a fast Fourier transform for each block, and the final result is the arithmetic mean of all blocks.

[6]The high angle of attack results in the HDT verification experiments are an exception to this, presented in Section 5.5. For these tests, the pressure fluctuations are normalised by the calculated freestream static pressure in the test section (assuming an isentropic expansion from stagnation conditions). The reason for this is so that results can be compared directly to those obtained in DLR's H2K facility.

Disturbance amplitudes

To summarize the magnitude of separate disturbances, the PSD is integrated over different frequency ranges of interest. The anticipated disturbance frequencies are dependent on the boundary layer thickness and edge velocity, which in turn vary with model geometry and the total temperature of the flow (among other factors). The frequency bands used to summarise the anticipated disturbances are detailed at the beginning of each of the test campaigns. A high frequency band is expected to correspond to the second mode instability at low angle of attack, and possibly a secondary instability of the stationary crossflow vortices at high angle of attack. In practice, these high frequency disturbances were observed at $f \approx 100 - 500$ kHz in HDT, and possibly at $f \approx 600 - 900$ kHz in T4. A low frequency band corresponds to a low-frequency disturbance that was observed at high angle of attack in the HDT, which may correspond to the travelling crossflow instability ($f \approx 11 - 80$ kHz).

The PSD and disturbance amplitude processing is illustrated in Figure 3.19. The result is for a shot in the Oxford HDT at Mach 7, $Re_{unit,\infty} = 12.3 \times 10^6$ /m, $T_w/T_0 = 0.64$, Noise = 0.44%. The raw pressure and PSD are shown for a PCB132 sensor at x = 510 mm in the HDT 7° Cone Model, with $R_N = 1.25$ mm and $\alpha = 0°$.

$Re_x - \phi$ maps

Contours of the integrated power spectra are presented on a $Re_x - \phi$ map, to visualize the disturbance shape around the cone at high angles of attack and make comparisons to the HIFiRE-1 flight wherever possible. These maps are plotted as a function of the Reynolds number based on axial location ($Re_x = Re_{unit} \times x_{PCB}$) for azimuths around the cone. The colour levels represent the magnitudes of the normalised fluctuations in the frequency band of interest. The maximum contour value corresponds to the maximum normalised fluctuations value that was observed in each campaign. For clarity, this maximum value is specified at the beginning of each campaign.

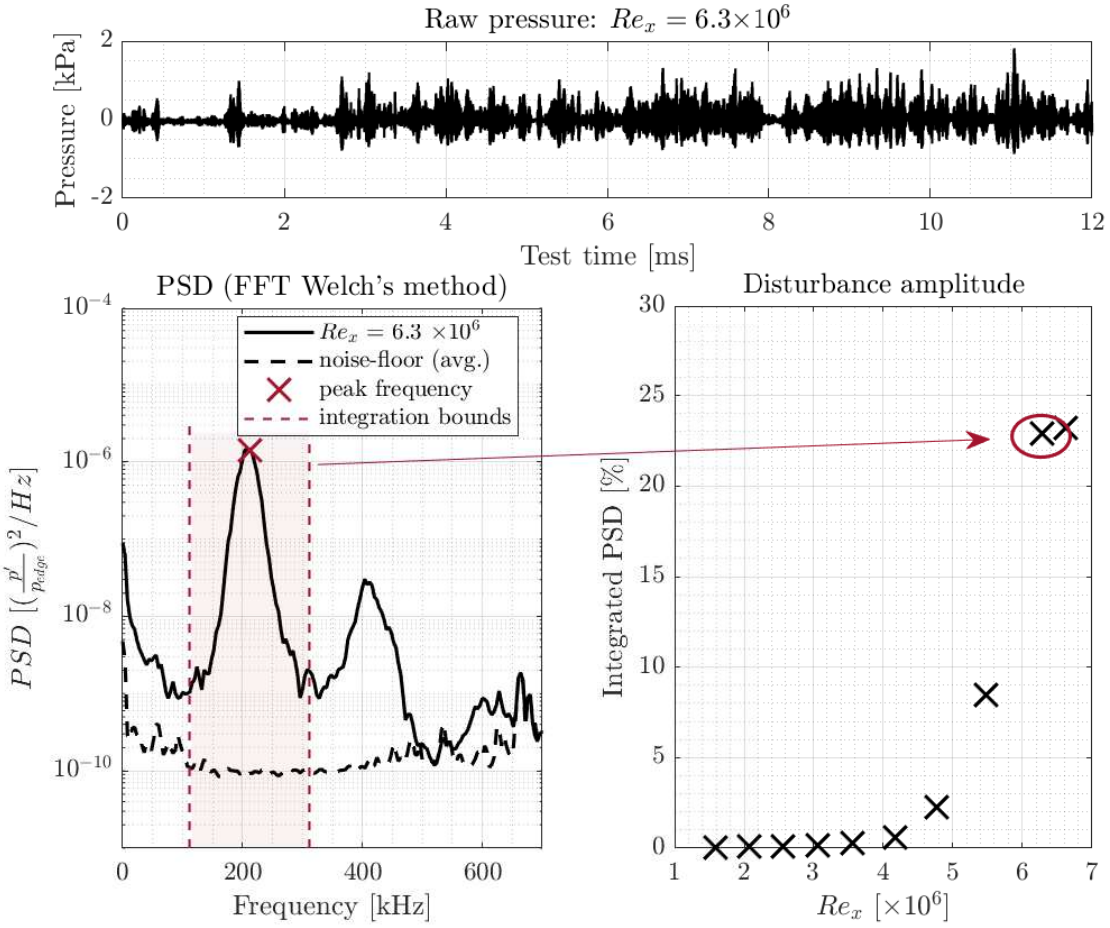


Figure 3.19: An example of processing a PCB132 signals using the fast Fourier transform to obtain the PSD, and integrated power spectra to summarize individual disturbances.

3.7.2 Continuous wavelet analysis

Motivation

The continuous wavelet transform (CWT) is useful for identifying time-frequency characteristics of boundary layer disturbances at a high resolution [181]. This contrasts with the fast Fourier transform approach, which decomposes a signal into sines and cosines of infinite length, and effectively loses all time-localization information. There are multiple examples of scenarios that benefit from the use of CWTs. One example is to identify the second mode wave packets both as a function of time and frequency. For example, Grossir et al. [78, 79] and Wagner et al. [182, 80] used the CWT to characterise the second mode instability in the VKI Longshot

facility and DLR's HEG facility, respectively. A second example is for identifying and removing non-flow-representative transient events that may impact the sensor and corrupt the averaging in a normal PSD calculation.

Whilst Fourier transforms are useful for summarising frequency content over entire time periods[7], an additional benefit of the CWT is that it requires fewer data points to summarise the spectral content of a signal. This is particularly helpful for experiments undertaken in reflected shock tunnels, where the test time can be in the order of $\approx$ 1 ms. For example, Berridge et al. investigated the effect of record length when calculating the power spectra to identify second mode instabilities on a 7° half-angle cone using fast Fourier transforms. For the dataset used by Berridge et al., they observed that record lengths needed to contain more than 15 FFTs to eliminate the noisy spectra that arises from a lack of averaging [183].

Wavelet transform properties

A wavelet is a small concentrated burst of finite energy in the time domain, that also exhibits some oscillation with time [181]. A continuous wavelet transform is then a convolution of a dataset with a scaled and shifted version of a previously-defined wavelet basis function (also called a mother wavelet) [181], as shown in Equation 3.1. It is similar to the Fourier transform, except that the $e^{j\omega t}$ has been replaced by the mother wavelet, $\Psi_{\tau,a}(t)$. The choice of mother wavelet is a key parameter in the analysis, as the shape must resemble the feature of interest in the data. The complex-valued Morlet wavelet is used in this research, due to its similarity to the dominant pressure oscillations in transitional hypersonic boundary layers [184, 79]. The wavelet basis function can generate a family of wavelets by either stretching or translating itself over a range of values [181, 185].

[7]For example, see the comparison of FFT to CWT for the Oxford HDT result in Figure 3.22. Over the same test time, the FFT method is able to clearly resolve the higher harmonic of the second mode, whereas it is not as clear in the CWT result.

$$X(\tau, a) = \int_{-\infty}^{+\infty} x(t)\Psi^*_{\tau,a}(t)dt \tag{3.1}$$

The Morlet wavelet can be expressed in terms of its center frequency, γ_c, and its bandwidth, γ_b, according to Equation 3.2 [181]. For the current application, a center frequency of $\gamma_c = 6$ and a bandwidth of $\gamma_b = 1$ are used. The number of octaves determines the span of frequencies being analyzed, while the number of voices per octave determines the number of samples (frequencies or scales) across this span [186]. Ten voices per octave are used in this research. The complex-valued Morlet wavelet used for this research is shown in Figure 3.20.

$$\Psi_{\text{Morlet}}(t) = \frac{1}{\sqrt{\pi\gamma_b}} \times e^{j2\pi\gamma_c t - (t^2/\gamma_b)} \tag{3.2}$$

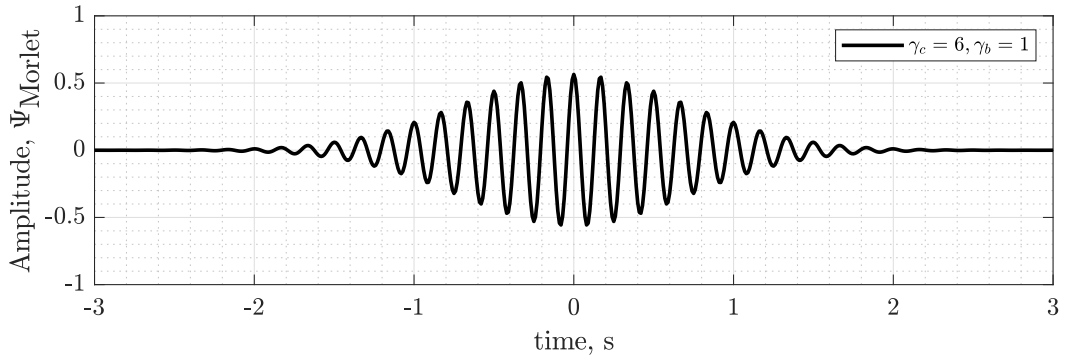


Figure 3.20: The complex-valued Morlet wavelet used for this research. γ_c is the center frequency, and γ_b is the bandwidth. The Morlet wavelet is defined by Equation 3.2.

Result 1: Scalogram

The CWT can be presented as a scalogram, where the contour levels correspond to the complex wavelet coefficients. A higher wavelet coefficient indicates a greater presence of the Morlet wavelet at that particular frequency and moment in time. This makes it possible to trace waves within the time-frequency domain.

Edge effects become important at the start or end of the test time, and at low or high frequencies. These effects originate from stretched wavelets when they

extend beyond the edges of the observation interval. A cone of influence shows areas in the scalogram that may be affected by edge effects. An example is shown in Figure 3.21, for the same pressure signal that was processed in Figure 3.19. The CWT scalograms presented in this research are all in the frequency-time space within the cone of influence, so that uncertainties from edge effects are avoided.

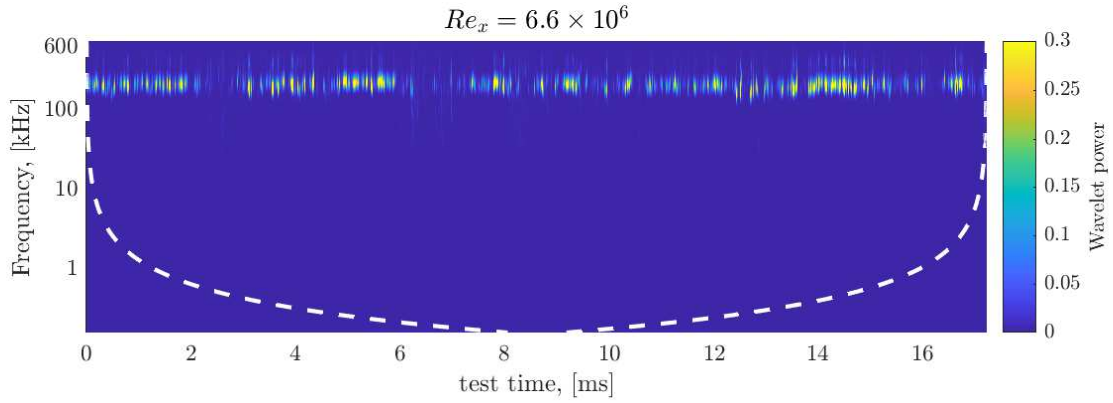


Figure 3.21: An illustration of the cone of influence for a CWT scalogram, plotted as the white dashed line. It shows areas where the scalogram may be affected by edge effects. The CWT result is for the same pressure signal that was processed in Figure 3.19. The HDT facility conditions are: Mach 7, $Re_{unit,\infty} = 12.3 \times 10^6$ /m, and $T_w/T_0 = 0.64$, Noise = 0.44%.

Result 2: Power spectral density (PSD)

The CWT can be used to recover the power spectral density of the signal over the test time. The CWT PSD is calculated by summing the squared complex Morlet wavelet coefficients from the scalogram. The result is then normalized by the number of time samples. Figure 3.22 illustrates a comparison of the PSD when generated using fast Fourier transforms or the continuous wavelet transform. The comparison is made on the same sensor that was used in the previous subsections for the HDT results, as well as for a measurement in the T4 Stalker Tunnel.

Both methods are able to resolve the dominant frequencies in the spectra, however the FFT Welch method is able to capture more of the finer details. The normalising method used for the CWT method also seems to be incorrect, as the

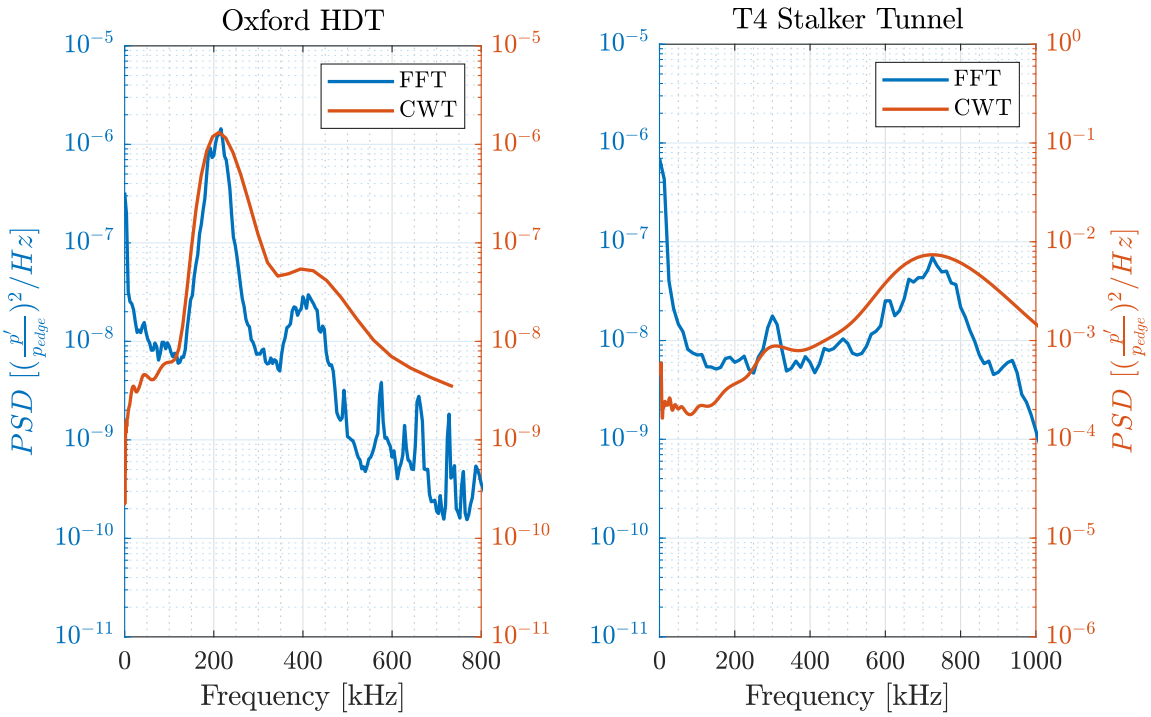


Figure 3.22: A comparison of power spectral density calculations using the fast Fourier transform and the continuous wavelet transform. The comparison is made on two datasets; one for a 17ms test time in HDT and the other for a 1.5 ms test time in the T4 Stalker Tunnel. The HDT conditions are at $M_\infty = 7.0$, $Re_{unit,\infty} = 12.3 \times 10^6$ /m, $T_w/T_0 = 0.64$, Noise = 0.44%, $Re_x = 6.3 \times 10^6$ (results are presented in Section 6.2). The T4 conditions are at $M_\infty = 7.1$, $Re_{unit,\infty} = 11.4 \times 10^6$ /m, $T_w/T_0 = 0.13$, $Re_x = 3.0 \times 10^6$ (results are presented in Section 6.3).

PSD values are dependent on the test-time data size. For this research, the CWT PSD is used to cross-check the frequency features that have been observed using the FFT Welch's method. Disturbance amplitudes presented in the literature have integrated the PSD using the FFT method. For this reason, and due to the incorrect CWT normalisation, the CWT PSD is not integrated to provide amplitudes.

Result 3: Identification and removal of non flow representative transient events

On multiple occasions in the T4 results, the wavelet scalograms in the harsher reflected shock tunnel environments appeared to be corrupted by non flow representative "events". It is not clear what caused these events to occur, though one

possibility is particles impacting the PCB132 sensor. When a non flow representative event was clearly identified, it was not included in the calculation of power spectral density using Welch's method. This process is only done in clear cases, where the power spectral density using Welch's method would otherwise not accurately summarise the test-time content (instead, the FFT averaging would be overwhelmed by the "event"). Figure 3.23 illustrates an example of this process, along with the effect on the power spectral density.

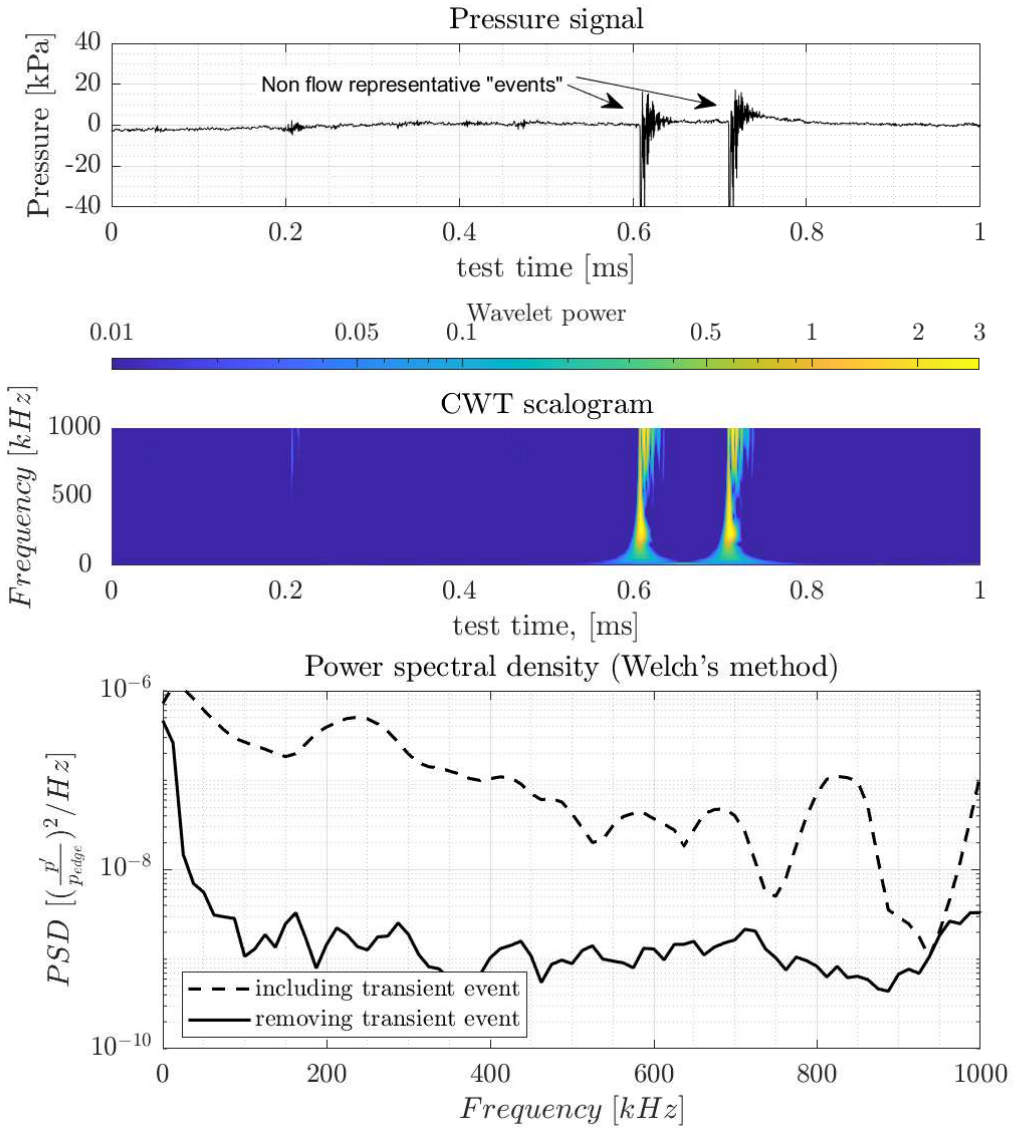


Figure 3.23: Using the CWT scalograms to identify and remove non flow representative transient events. This example is from experiments undertaken in the T4 Stalker Tunnel at $M_\infty = 7.1$, $Re_{unit,\infty} = 11.4 \times 10^6$ /m, $T_w/T_0 = 0.13$, $Re_x = 1.3 \times 10^6$.

4

Freestream Characterisation of the Oxford High Density Tunnel

This chapter aims to provide details about the HDT freestream conditions and disturbance levels. The first sections outline how the Mach number, total temperature (T_0), and facility Reynolds numbers ($Re_{unit,\infty}$) were determined. The chapter then aims to characterise the post-shock freestream disturbance levels in the HDT using its Mach 7 nozzle.

4.1 Characterization of flow conditions in the HDT

A pre-measured Mach number and total temperature history is used alongside the measured supply pressure to calculate the freestream conditions. An isentropic expansion for a perfect gas ($\gamma = 1.4$) is assumed through the nozzle to the test section. The stagnation pressure is measured for each shot using a Kulite XT-190SM located in the nozzle plenum[1]. The static conditions are then calculated using the stagnation properties and Mach number, based on the isentropic relations. The Reynolds number is calculated using these freestream conditions and the chosen

[1]In practice, the barrel fill pressure must be specified for a target stagnation pressure at a particular facility plateau. For this reason, the pressure loss across the plug valve has been characterised as a part of the commissioning of the facility. The Mach 7 results are presented in Appendix B.

viscosity model (see Section 4.1.3). The following subsections provide details about how key variables were calculated using the Mach 7 nozzle.

4.1.1 Mach number characterisation

The Pitot survey characterises the Pitot-to-supply pressure ratios (P_{Pitot}/P_0) for the range of conditions that are targeted in the campaign. The Pitot-to-supply pressure is then used to calculate the Mach number distribution with an iterative scheme, according to Equation 4.1. An example of a Mach number profile is illustrated in Figure 4.2. The facility trace shows that the Mach number stays relatively constant at the design value, even whilst the supply pressure, and therefore Reynolds number, decrease after each plateau.

$$\frac{P_{Pitot}}{P_0} = \left(\frac{M^2(\gamma+1)}{(M^2(\gamma-1)+2)}\right)^{\frac{\gamma}{\gamma-1}} \left(\frac{\gamma+1}{(2\gamma M^2-(\gamma-1))}\right)^{\frac{1}{\gamma-1}} \tag{4.1}$$

The Mach number is expected to vary slightly with supply pressure, P_0. Ideally this variation would be measured using a Pitot probe in situ, however this was not possible due to limited space in the test section. Figure 4.1 shows the spread in P_{Pitot}/P_0, and therefore Mach number, obtained over a range of supply pressures for the Mach 7 nozzle. These results are used to generate a linear relationship for each nozzle, such that $\frac{P_{Pitot}}{P_0} = f(P_0)$. The measured stagnation pressure is then used for each shot to calculate the shot-specific P_{Pitot}/P_0 and the Mach number distribution. The Mach 7 relationship is given by Equation 4.2.

$$\left(\frac{P_{Pitot}}{P_0}\right)_{M_{nozzle}=7} = -5.5734\text{e-}7 \times P_0 + 1.6833\text{e-}2 \tag{4.2}$$

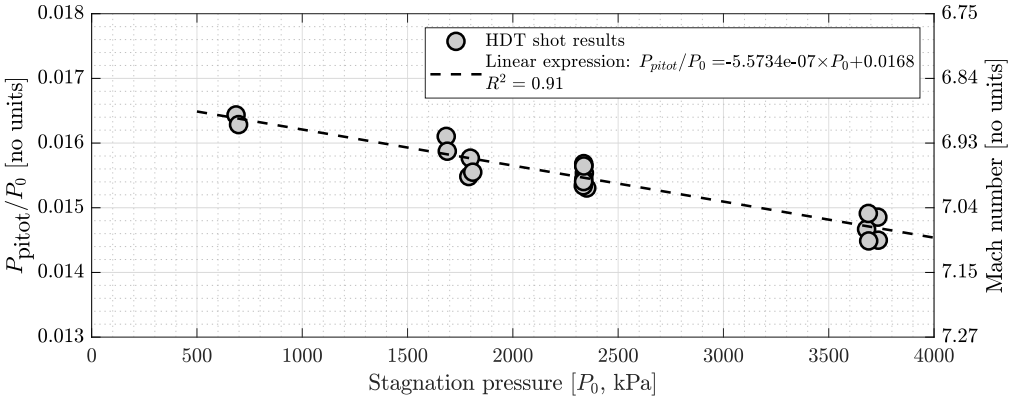


Figure 4.1: HDT facility Pitot-to-supply pressure ratio as a function of various supply pressures. The dashed line is the linear relationship used for the Mach 7 nozzle (T_{fill} = 537 K).

4.1.2 Total temperature characterization

Total temperature measurements are particularly important for freestream characterisation due to its influence on the wall-to-total temperature ratio, viscosity, and the facility unit Reynolds number. The total temperature profile is measured in the HDT using differentially heated thin film heat transfer gauges and heated aspirated thermocouples, both mounted on the surface of a flat faced blunt test model. The aspirated thermocouple measurements are deconvolved using an analytical thermal model [187]. These measurements were led by Dr. Tobias Hermann, with details about the characterization method presented in Ref. [187] alongside total temperature results using the Mach 5 nozzle.

A barrel fill temperature of $T_{fill} \approx 500$ K was used for all Mach 7 results presented in this research. The resultant total temperature profile is presented alongside the other facility conditions in Figure 4.2. The later plateaus are relatively constant at $T_0 = 454 - 457$K, and the timing of each plateau agrees quite well with the supply pressure profile. The total temperature profile did not change as a function of fill pressure [187].

A key feature is the large overshoot in total temperature during the first facility plateau. This originates from an unsteady compression of the test gas into the

settling chamber, causing a short period where the upstream enthalpy is converted into internal energy [187]. This process results in a short period where the total temperature rises above the fill temperature by a factor of the specific heat ratio. As the Mach number decreases and the throat diameter becomes larger, this feature is expected to happen over a shorter period of time. The analysis for the unsteady compression process is shown in Ref. [187].

4.1.3 Viscosity model

The choice of viscosity model (μ) is particularly important for the calculation of the freestream unit Reynolds number ($Re_{unit,\infty} = \frac{\rho_\infty u_\infty}{\mu_\infty}$) [188]. Each viscosity model is only accurate over a finite range of flow conditions (T_{static} in particular) and test gases. For this reason, multiple viscosity models are currently being implemented in experimental facilities around the world. It is important to use a suitable viscosity model for the facility flow environment, and to quote the key variables (P_0, T_0, M_∞) that are being used to calculate the Reynolds number.

Keyes' [189] viscosity model is used in the HDT. Roy [190] suggests that Keyes' viscosity model should be used when $T < 100$ K. Others quote low-temperature limits in the region of $80 \leq T < 120$ K, below which Keyes' viscosity model is best suited. It is described by the following expression:

$$\mu_{\text{Keyes}} = \frac{1.488\text{e-}6 \times \sqrt{T}}{1 + \frac{122.1 \cdot 10^{-5/T}}{T}} \tag{4.3}$$

An alternative viscosity model is used in the HDT verification campaign in Chapter 5. This is to ensure that the freestream conditions are calculated using the same method as DLR's H2K facility [36, 35]. Details of the H2K viscosity model are provided in Section 5.2.1.

4.1.4 Reynolds number

The unit Reynolds number is calculated according to Equation 4.4, where ρ_∞ is the density (assuming perfect gas, $\rho_\infty = \frac{P_\infty}{RT_\infty}$), u_∞ is the velocity ($u_\infty = M_\infty\sqrt{\gamma RT_\infty}$), and μ_∞ is the viscosity from Keyes' model [189]. The static pressure and temperature are calculated from the isentropic relations[2], whilst the measurements of total pressure, temperature, and Mach number have been described above.

$$Re_{\text{unit},\infty} = \frac{\rho_\infty u_\infty}{\mu_\infty} \tag{4.4}$$

Figure 4.2 shows an example of the HDT facility Reynolds number profile using the Mach 7 nozzle. This is plotted alongside the stagnation pressure profile for $P_{fill} = 2485$ kPa, $T_{fill} = 537$ K. The grey area shows the locations of each HDT facility plateau. A clear first plateau is not observed in the Reynolds number profile due to the overshoot in total temperature. Nevertheless, the facility is capable of generating constant conditions in later plateaus for test times in the order of 30-50 ms. Table 4.1 shows the percentage variation in $Re_{unit,\infty}$ for each plateau at the nominal conditions in this research.

Higher freestream disturbance levels are expected throughout the unsteady compression (see Section 4.3.2). The majority of HDT boundary layer instability results are processed using the third plateau, however comparisons are made to results obtained using other plateaus.

[2]Future tests would benefit from use of static pressure probes to measure the freestream static pressure directly, as per [78, 79].

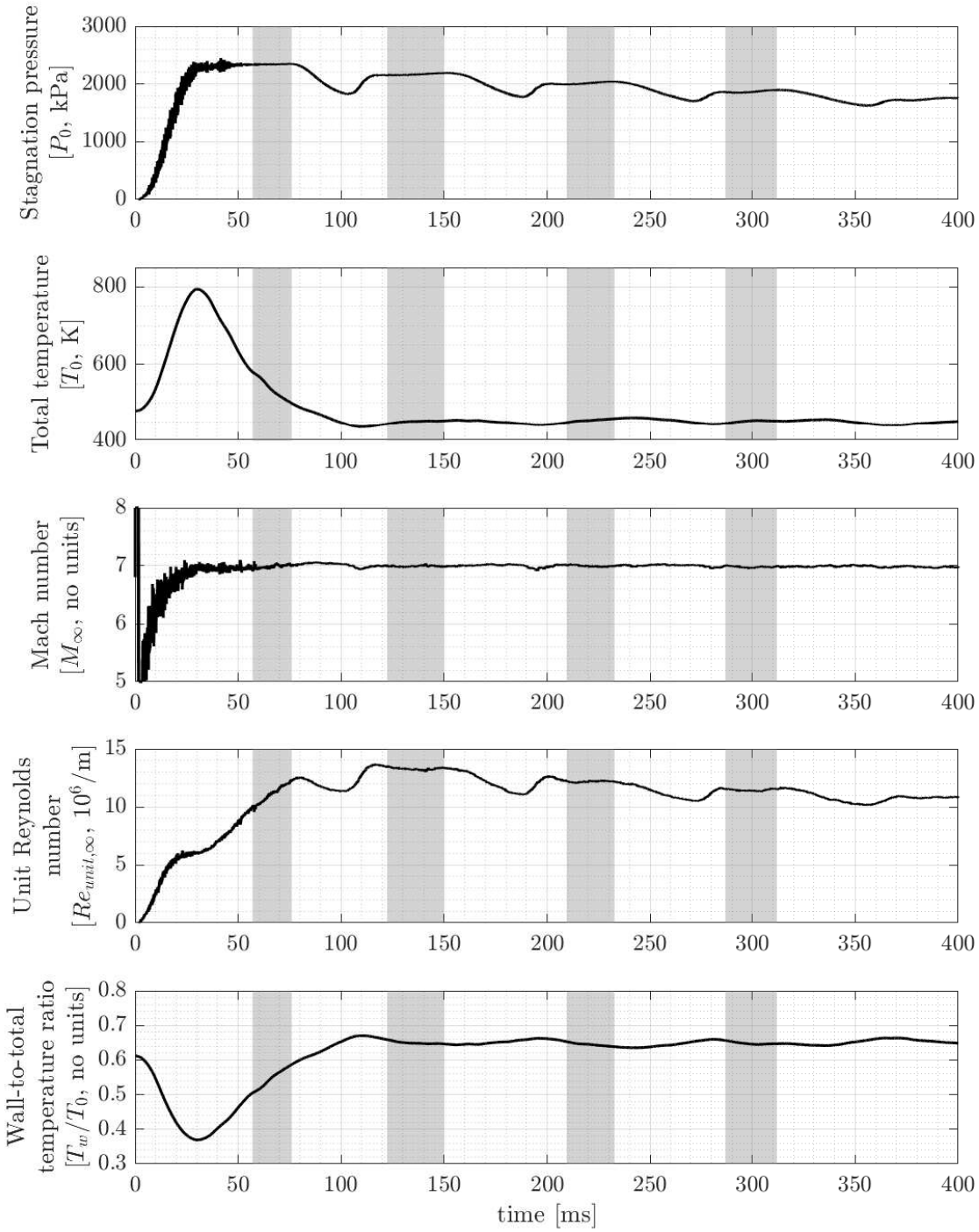


Figure 4.2: HDT facility conditions using the Mach 7 nozzle and Keyes' viscosity model. The fill conditions are: $P_{fill} = 2485$ kPa, $T_{fill} = 537$ K. The quasi-steady plateau test times are illustrated by the grey shaded area.

Parameter	Facility plateau	Mean	Range	Standard deviation
P_0 [kPa]	1	2341	48	7
	2	2167	58	13
	3	2018	60	17
	4	1868	56	16
T_0 [K]	1	508	24	7
	2	451	8	2
	3	455	9	2
	4	452	6	1
$Re_{unit,\infty}$ [10^6 /m]	1	11.9	1.0	0.1
	2	13.3	0.5	0.1
	3	12.2	0.3	0.1
	4	11.5	0.4	0.1

Table 4.1: Variation in HDT facility conditions using the Mach 7 nozzle for multiple plateaus. This variation is calculated for the $P_{fill} = 2485$ kPa and $T_{fill} = 537$ K condition, with facility profiles shown in Figure 4.2

4.2 The Oxford Pitot Rake

A Pitot survey is used to characterise the temporal/spatial uniformity and freestream turbulence levels of the HDT freestream. The Pitot rake contains ten gauges, with a spacing between each gauge equal to 20 mm. Kulite XCQ-093 sensors and PCB132 sensors were installed at various locations over multiple test campaigns. The Kulite XCQ-093 sensors are used for Pitot pressure and low-frequency fluctuation measurements, whilst the PCB132 sensors measure high frequency fluctuations. The Pitot probe has a thread so that multiple cap sizes can be tested. For the results presented in this chapter, the Pitot radius is kept constant at 3.18 mm, with a 1 mm fillet radius.

An image of the Pitot rake with two cap-size combinations is shown in Figure 4.3, along with the associated Schlieren flowfield. The axial rake position for all freestream disturbance measurements was at $x = 68$ mm from the nozzle exit,

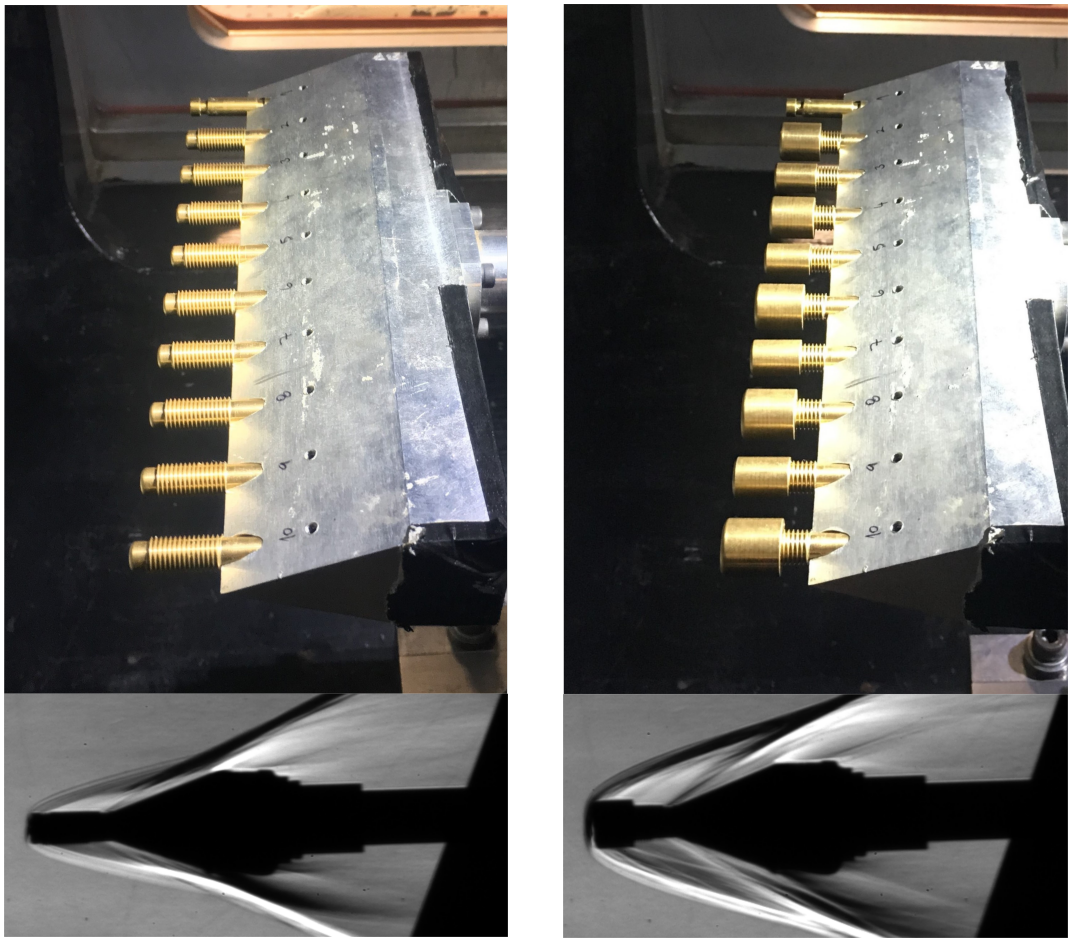
equal to 1463 mm from the nozzle throat.

It is possible to shift the rake location in the lateral direction in 20 mm intervals. The total rake coverage is therefore up to 180 mm from the centreline of the nozzle. Shifting the rake makes it possible to use Kulite and PCB measurements over successive tests, to rebuild post-shock fluctuations over the full frequency range (1 kHz $\leq f <$ 1000 kHz) at a given radial location.

The distribution of PCB132 (PCB) and Kulite XCQ-093 (Kul) sensors are shown in Table 4.2 for the three rake shifted positions. The nozzle centreline is at $r = 0$ mm. Cells are colour-coded to illustrate locations where a full PSD rebuild can be calculated. Measurements are taken using all cap sizes (small, medium, large) at each lateral location. The PSD is calculated using Welch's method, with details described in Section 3.7.1. The Kulite data is split into blocks containing 3000 samples each ($\text{nfft}_K = 3000$), whilst the PCB data is split into blocks with 500 samples ($\text{nfft}_{PCB} = 500$).

Lat. pos.	distance from centreline (mm)											
	180	160	140	120	100	80	60	40	20	0	-20	-40
# 1	-	-	Kul	Kul	Kul	Kul	PCB	N/A	PCB	Kul	PCB	Kul
# 2	-	Kul	Kul	Kul	Kul	PCB	N/A	PCB	Kul	PCB	Kul	-
# 3	Kul	Kul	Kul	Kul	PCB	N/A	PCB	Kul	PCB	Kul	-	-

Table 4.2: Sensor locations for various rake lateral positions. Cells are colour-coded to illustrate the radial locations where measurements are taken over the entire frequency range (1 kHz $\leq f <$ 1000 kHz). One probe is marked N/A, as the Kulite in this probe was damaged throughout the entire campaign.



(a) No caps: all probes are "small"

(b) Alternating "medium" and "large" caps.

Figure 4.3: The HDT Pitot rake with multiple Pitot probe geometries. Flow conditions for Schlieren results are at: $M_\infty = 7$, $Re_{\text{unit},,\infty} = 12.1 \cdot 10^6/\text{m}$, $T_w/T_0 = 0.64$.

4.2.1 Spatial Uniformity

Figure 4.4 illustrates the size of the core flow as a function of sensor location downstream (nozzle exit at x = 0). The coreflow typically has a radius between 140 – 160 mm at the nozzle exit and decreases to a radius of 100 – 120 mm at x = 418 mm downstream. The Pitot-to-supply ratio seems to be constant across the gauges inside the core flow. As an example, for Shot 59 the average Pitot-to-supply ratio is 1.5869×10^{-2}, with a range of $\pm 1.14 \times 10^{-4}$. This result also highlights that the Pitot-to-supply pressure ratio shot-to-shot differences are minimal at a given condition.

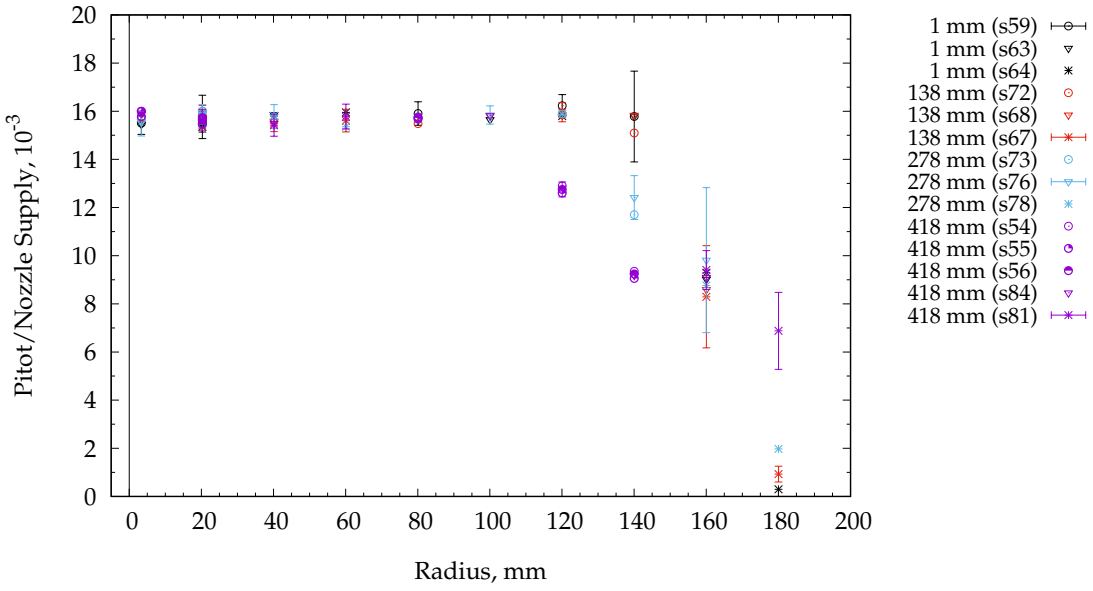


Figure 4.4: Mach 7 Pitot Survey Results at $P_0 = 1790$ kPa, $T_{fill} = 537$ K. The axial distance downstream from the nozzle exit is shown in the legend, neglecting any recoil of the facility. The shot number is given in brackets. The error bars indicate one standard deviation of the variation during the test time.

4.3 Freestream disturbance characterisation: Post-shock PSD rebuild

A characterization of disturbance levels in the freestream is beneficial for boundary-layer transition experiments. Freestream disturbances come mostly in the form of acoustic fluctuations that are radiated from turbulent boundary layers along the nozzle walls [127, 126]. A recent overview of methods currently used to quantify freestream disturbances in conventional hypersonic wind tunnels is provided by Duan et al. [120].

The Kovasznay modal decomposition analysis is used to better characterise the nature and origins of freestream disturbances [191]. Measurements are typically taken using Pitot probes and hot-wires, to decompose wind-tunnel freestream disturbances into three modes of co-varying physical properties: an acoustic mode, an entropy mode, and a vorticity mode [191, 120]. This method has been used in multiple facilities, and some examples can be found in Ref. [192, 193, 194, 195, 78]. Duan et al. [120] review recent work on the combined modal analysis [191, 195], along with the findings from Direct Numerical Simulations of a full-scale facility nozzle [196].

Two methods for characterizing the freestream turbulence levels have been pursued in this research. This chapter will focus on the first method, where the frequency spectra of post-shock pressure fluctuations are quantified using a single Pitot geometry, and results are compared over multiple scenarios (e.g. probe location, facility plateau, and against other facilities). The second method is to normalise the post-shock fluctuations using multiple Pitot probe geometries, and compare the results to DNS. The results obtained using multiple Pitot geometries requires further work, however this method has shown promise and will be pursued in the future. For this reason, initial comparisons to Chaudhry's DNS results [197] are presented in Appendix C, along with a discussion of the results.

Figure 4.5 shows the post-shock PSD rebuild for multiple facilities at various flow conditions, re-plotted from data in Figure 2 in Ref. [120]. Measurements are taken in the Hypersonic Ludwieg Tube Braunschweig (HLB), Purdue Boeing/AFOSR Mach-6 Quiet Tunnel (BAM6QT), the NASA 20-Inch Mach 6 tunnel (NASA 20-in), the Sandia Hypersonic Wind Tunnel at Mach 8 (Sandia), and AEDC Tunnel 9 (AEDC). Flow conditions are at Mach numbers from 6 - 14, and facility Reynolds numbers ranging from 6.3×10^6/m to 13.3×10^6/m. The PSDs are computed from Kulite sensors in the low-frequency range (0.1 kHz $\leq f <$ 20 kHz), and PCB132 sensors in the high-frequency range (11 kHz $\leq f <$ 1000 kHz). For information about the axial and radial locations of each sensor, see the legend of Figure 2 in Ref. [120]. Pitot probe geometry details were not quoted.

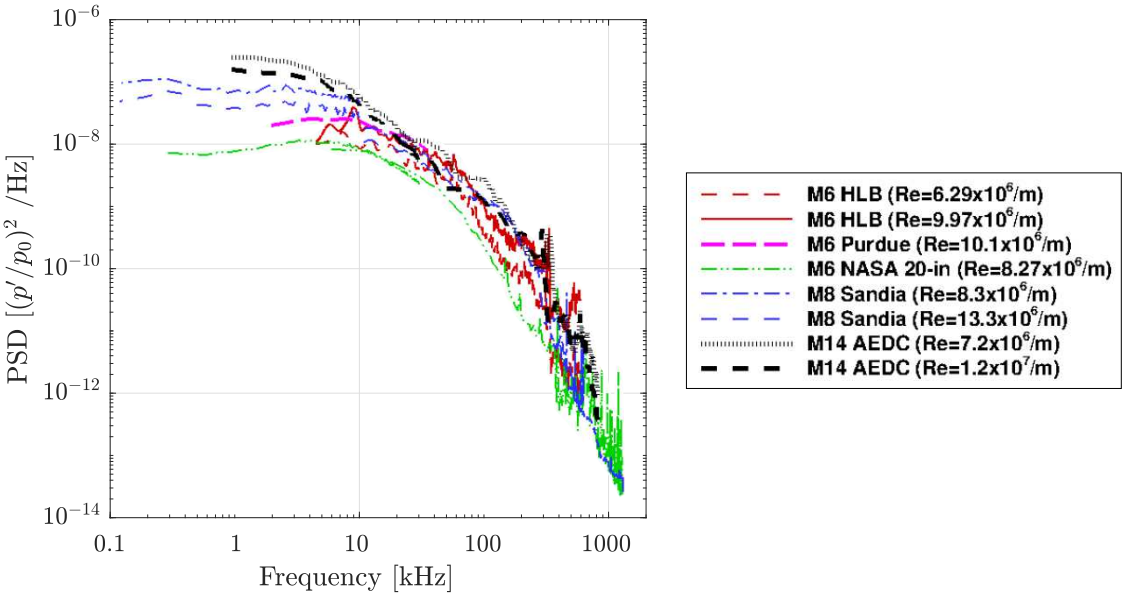


Figure 4.5: Power spectral density rebuilds of freestream Pitot pressure fluctuations measured in multiple high-speed facilities. Re-plotted from Figure 2 in Ref. [120]

These measurements describe the post-shock fluctuations rather than the actual disturbances in the tunnel freestream. A transfer function is able to relate post-shock disturbances to those that are present in the freestream. This relationship is given by Equation C.1, where "t" is the post-shock transducer signal [197]. Information about the transfer function is therefore required to understand the

freestream disturbances. The post-shock pressure fluctuations for the Oxford HDT are compared to the results shown in Figure 4.5. These results should be seen as a comparison to other facilities or an input to computations, rather than a full rebuild of the disturbances in the freestream itself.

$$\chi(f) = \frac{\mathrm{PSD_t}}{\mathrm{PSD}_\infty} \tag{4.5}$$

4.3.1 Individual HDT shot result

The post-shock pressure fluctuations are measured over the full frequency range using Kulite and PCB132 pressure sensors. Kulite and PCB132 results are only used together if they are at the same radial location and with the same cap geometry. Measurements are taken at Mach 7, $Re_{\mathrm{unit},\infty} \approx 10.4 - 13.2 \times 10^6$ /m (varying over facility plateaus[3]), and $T_w/T_0 = 0.53 - 0.65$. The Kulite pressure fluctuations are normalized by the measured Pitot pressure using that particular sensor. The PCB pressure fluctuations are normalised by the Pitot pressure, as measured using the neighbouring Kulite sensor[4].

Percentage noise calculation (Noise %)

A percentage noise value is calculated to summarize the freestream disturbance results. It is equal to the root mean square of the freestream pressure fluctuations (RMS_f) divided by the average Pitot pressure ($P_{\mathrm{Pitot,mean}}$) over the test time:

$$\text{Noise } \% = \frac{\mathrm{RMS}_f}{P_{\mathrm{Pitot,mean}}} \times 100 \tag{4.6}$$

[3]Facility plateaus 1-4 have conditions as follows:
Plateau 1: $M_\infty = 7.0$, $Re_{\mathrm{unit},\infty} \approx 10.4 \times 10^6$ /m, $T_w/T_0 \approx 0.53$
Plateau 2: $M_\infty = 7.0$, $Re_{\mathrm{unit},\infty} \approx 13.2 \times 10^6$ /m, $T_w/T_0 = 0.65$
Plateau 3: $M_\infty = 7.0$, $Re_{\mathrm{unit},\infty} \approx 12.2 \times 10^6$ /m, $T_w/T_0 = 0.65$
Plateau 4: $M_\infty = 7.0$, $Re_{\mathrm{unit},\infty} \approx 11.4 \times 10^6$ /m, $T_w/T_0 = 0.65$

[4]It should be noted that the neighbouring Kulite sensor chosen for normalising the PCB fluctuations was always at a greater distance from the nozzle centreline. This was chosen so that any uncertainties towards the edge of the coreflow would result in an over-predicted freestream noise level.

Two methods are used to calculate the RMS_f for each test time [198]. In the time domain method, a minimum-order bandpass filter is used to reduce the pressure signal to the desired frequencies. The bandpass filter has a stopband attenuation of 60 dB and compensates for the delay introduced by the filter. A bandpass filter steepness of 0.98 is used, to reduce the width of the bandpass filter's transition regions. The root-mean-square of the filtered pressure signal is then calculated. For the frequency domain method, the PSD of pressure fluctuations are integrated over the designated frequency bounds. The RMS is then calculated by taking the square root of the integral, as per Parseval's theorem.

The frequency bounds used for Kulites is 1 kHz $\leq f_{\mathrm{K}} <$ 20 kHz, whilst the range of frequencies calculated for PCB132 sensors is 20 kHz $\leq f_{\mathrm{PCB}} <$ 1000 kHz. The total percentage noise is calculated using the frequency domain method. This is equal to the square root of the integral of the full PSD (1 kHz $\leq f <$ 1000 kHz), and is equivalent to:

$$\text{Total Noise } \% = \sqrt{{\text{Noise}_{\text{Kulite}}}^2 + {\text{Noise}_{\text{PCB}}}^2} \tag{4.7}$$

Figure 4.6 shows PSD results for an individual HDT shot (shot 594), considering only facility plateau #3. For Pitot probes at similar radial locations, the low-frequency Kulite PSD overlaps quite well with the higher-frequency PCB132 measurements. The PSD increases for gauges that approach the edge of the coreflow, as would be expected. The trend is evident for the low-frequency Kulite sensors, as these are located further away from the nozzle centreline. For $f <$ 300 kHz, the coreflow normalized PSD magnitudes are significantly lower than the conventional tunnel data presented in Ref. [120] (shown as grey in Figure 4.6).

The measured signal at the higher-frequency end of the PCB132 measurements ($\approx f >$ 400 kHz) is at the same magnitude as the electrical noise floor. This indicates that the PSD of the flow must be less than or equal to the noise-floor over these frequencies. The true percentage noise values may therefore be smaller

than the values calculated. The high-frequency tail-off observed in similar facilities (expected to be $\approx f^{-3.5}$ [120]) is not captured due to the high electrical noise levels. The electrical noise is not subtracted from the signal, as this would result in an unrealistic "zero" PSD at high frequencies. The noise-floor PSD is plotted in each figure to illustrate at what stage the signal is no longer flow-representative. The post-shock freestream disturbance levels are therefore expected to be below the noise floor at these higher frequencies.

Figure 4.7 shows the calculated percentage noise values for shot 594. Results are presented as a function of probe distance from the nozzle centreline, using two different methods (described in Section 4.3.1). The percentage noise values are constant within the coreflow, and there is quite good agreement between the time domain method and the PSD integral method (as would be expected). The freestream noise increases as the distance reaches the edge of the coreflow region.

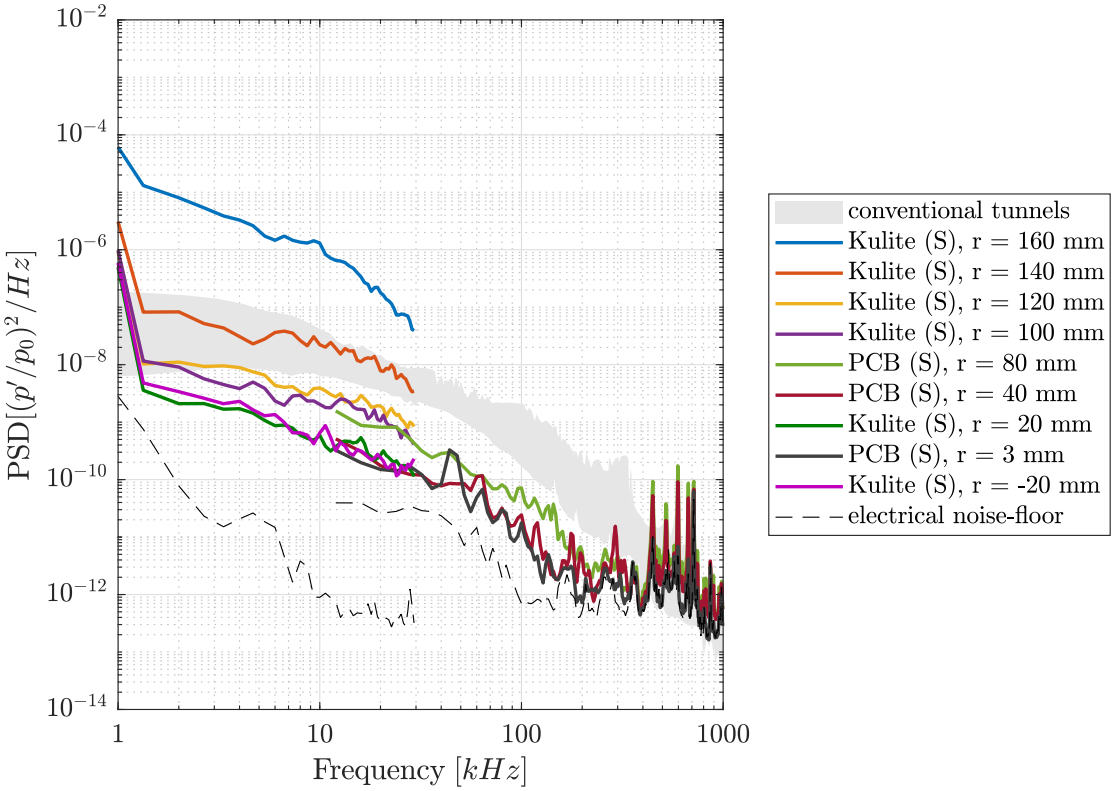


Figure 4.6: Post-shock PSD rebuild example for HDT shot 594. Conditions are at Mach 7, $Re_{unit,\infty} = 12.1 \times 10^6$ /m, using HDT plateau 3.

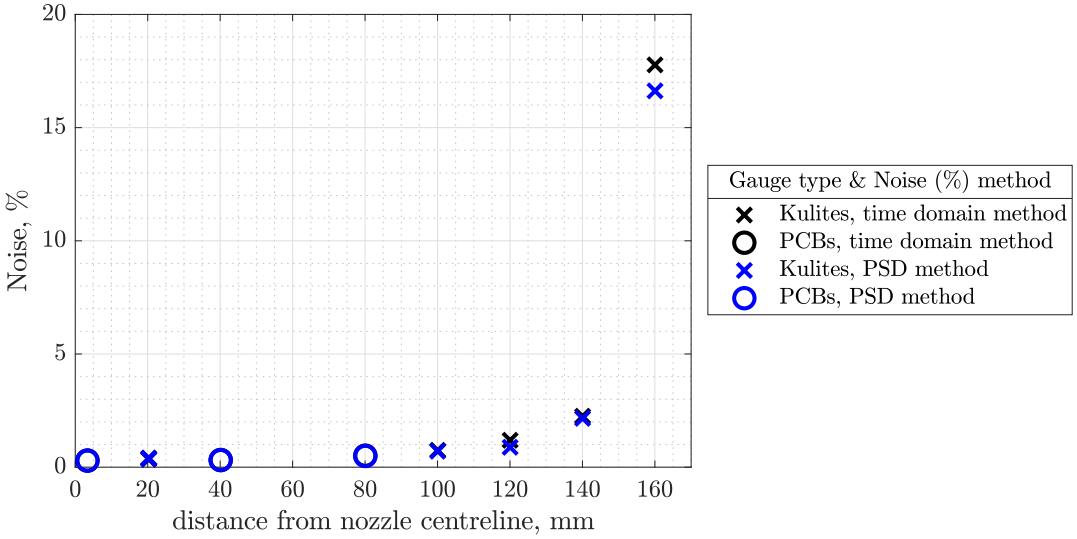


Figure 4.7: Calculated noise values for HDT shot 594 (Mach 7, $Re_{unit,\infty} = 12.1 \times 10^6$ /m, plateau 3). Noise values are plotted as a function of the distance from the nozzle centreline, using two methods (time domain and PSD integration).

4.3.2 Effect of HDT facility plateaus

Figure 4.8 shows the PSD rebuild as a function of HDT facility plateau. This result is presented for the small Pitot probes on the nozzle centreline, however the same trends are observed at each radial location and for each cap geometry. Plateau #1 has significantly higher freestream turbulence levels than all of the later plateaus. This is expected to be due to fluctuations associated with the unsteady compression into the settling chamber (see Section 4.1.2).

Despite the higher fluctuation levels, the PSD of plateau #1 lies within the range of published conventional tunnel results from Ref. [120]. The tail-off seems to agree quite well with $\approx f^{-3.5}$, as has been observed by other facilities. The PSD of plateaus #2 - #4 are at significantly lower magnitudes, and are affected by the noise-floor at higher frequencies ($\approx f > 3 \cdot 10^5$).

Table 4.3 gives the percentage noise as a function of facility plateau using the time domain and the frequency domain method. Results are given only for the small Pitot probe on the centreline. This reiterates that the noise is quite constant for plateaus #2 - #4, with total noise values ranging from 0.42 - 0.47. The total percentage noise of plateau #1 is over three times larger.

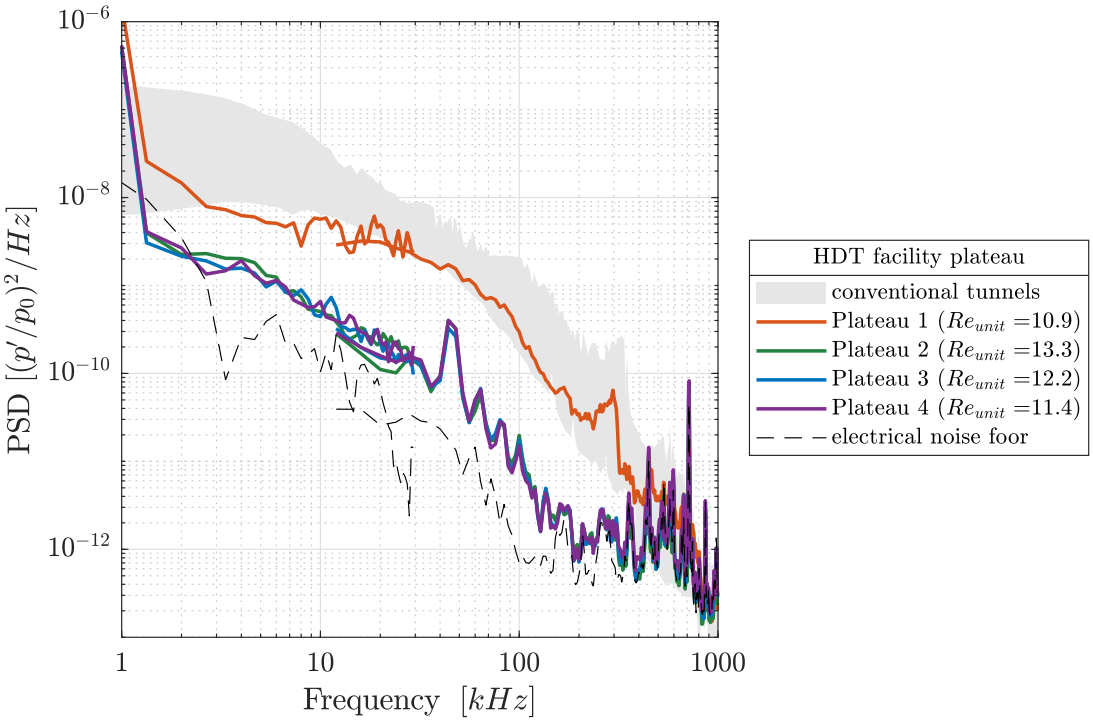


Figure 4.8: Effect of HDT facility plateau on post-shock pressure fluctuations for the HDT Mach 7 nozzle. PSD rebuilds are shown for the Pitot probes on the nozzle centreline. Pitot geometry is without caps, (i.e. "small"). The rake location is $x = 68$ mm from the nozzle-exit.

HDT facility plateau	Kulite Noise (%) (1 kHz - 20 kHz)		PCB Noise (%) (20 kHz - 1000 kHz)		Total (%)
	RMS_{time}	RMS_{PSD}	RMS_{time}	RMS_{PSD}	RMS_{PSD}
#1	1.26	1.09	0.98	1.01	1.49
#2	0.40	0.36	0.22	0.22	0.42
#3	0.36	0.38	0.22	0.23	0.44
#4	0.63	0.41	0.23	0.23	0.47

Table 4.3: Percentage noise results as a function of HDT facility plateau, using the time domain (RMS_{time}) and frequency domain (RMS_{PSD}) methods. The cap geometry is "small", and it is located on the nozzle centreline.

4.3.3 Effect of distance from nozzle centreline

The PSD rebuild is calculated as a function of distance from the nozzle centreline for each cap geometry and facility plateau. Figure 4.9 shows the PSD rebuild for r = 0, 20, 40, 80, and 100 mm. Results are shown for facility plateaus #1 and #3, due to the noteworthy differences in noise levels observed in Section 4.3.2. Results for the small Pitot probe geometry are presented, however the same trends were observed for the medium and large cap geometries.

The PSD rebuild is relatively constant for r = 0 - 40 mm, indicating that the freestream disturbances are uniform inside the Mach 7 coreflow. The PSD rebuild starts to increase at $r = 80$ mm, and is then noticeably larger at $r = 100$ mm as the Pitot probe exits the HDT coreflow. The PCB132 and Kulite results do not overlap for plateau #1 at $r \geq 80$ mm (11 kHz $\leq f <$ 20 kHz). At this condition, the rise in PCB132 PSD suggests that the probe is exiting the coreflow, whilst no rise is observed for the Kulite sensors at low frequencies. There is much better agreement for all distances at plateau #3.

The percentage noise is summarized for each facility plateau in Table 4.4. The calculated percentage noise values tend to increase with distance from the nozzle centreline. The total percentage noise for plateau #3 at $r = 100$ mm (0.75%) is lower than the coreflow value for plateau #1 on the nozzle centreline (1.49%). This result suggests that the choice of HDT facility plateau has a greater impact on freestream disturbance levels than the location within the coreflow (for distances up to r = 100 mm from the nozzle centreline).

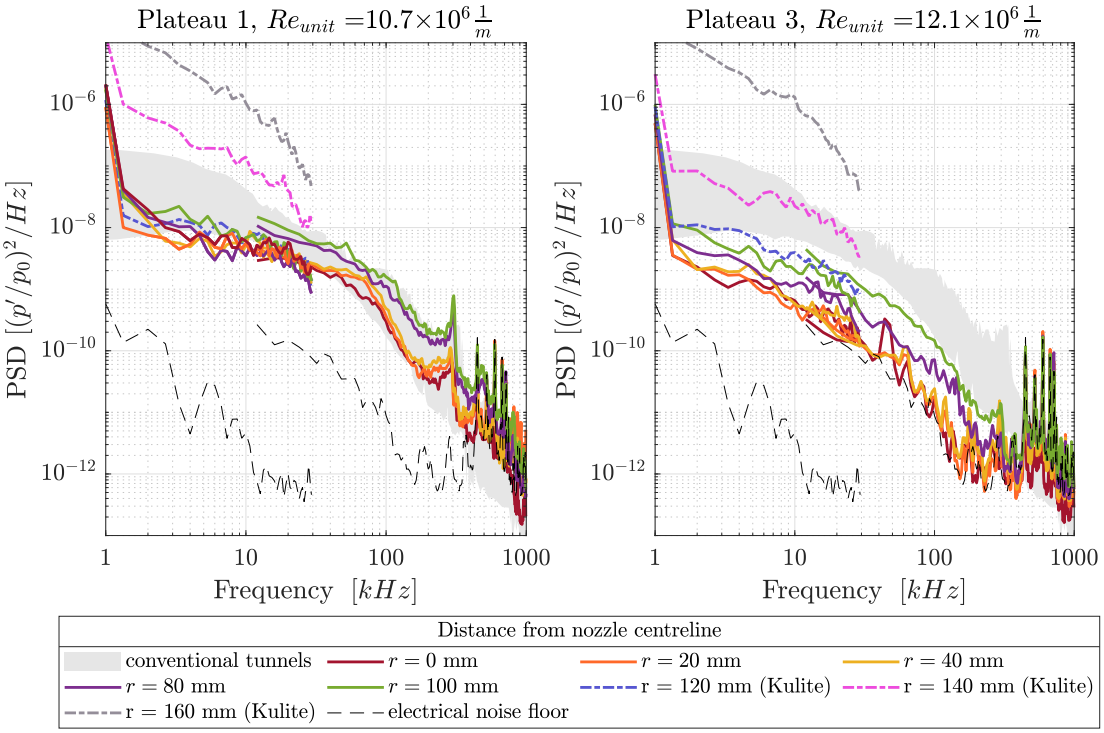


Figure 4.9: Effect of Pitot probe distance from nozzle centreline on post-shock pressure fluctuations for the HDT Mach 7 nozzle. Results are shown for HDT facility plateau #1 and #3, using the small Pitot geometry. The rake location is $x = 68$ mm from the nozzle-exit. Due to the rake configuration, only Kulite results are presented for $r \geq 120$ mm.

r (mm)	Plateau #1			Plateau #3		
	Kulite (%)	PCB (%)	Total (%)	Kulite (%)	PCB (%)	Total (%)
0	1.08	1.01	1.48	0.38	0.23	0.44
20	1.13	1.22	1.67	0.41	0.33	0.53
40	1.40	1.26	1.88	0.40	0.31	0.51
80	0.96	1.81	2.06	0.52	0.42	0.67
100	1.15	2.25	2.53	0.58	0.48	0.75
120	1.19	-	-	0.88	-	-
140	5.21	-	-	2.16	-	-
160	17.53	-	-	16.62	-	-

Table 4.4: Percentage noise results as a function of distance from nozzle centreline, using the frequency domain (RMS_{PSD}) method. The cap geometry is "small". Results are shown for facility plateaus #1 and #3.

5

Verification of Boundary Layer Instability Results in the Oxford High Density Tunnel

The objective of the first HDT test campaign was to establish confidence in the newly-commissioned facility and implemented post-processing techniques for boundary layer transition studies. Freestream conditions were matched to a similar cold-flow facility, so that comparisons could be made to an existing dataset of boundary layer instability measurements. This chapter compares instability measurements from the HDT to results obtained in DLR's H2K facility [35, 36, 37]. The majority of the results from this subsection have been presented at AIAA Aviation 2018, and can be found in Ref. [199].

The automated traverse is used to ensure that the cone model is correctly aligned to the incoming flow before sweeping through angles of attack. This microalignment process is detailed before any instability measurements are compared to H2K. A comparison of boundary layer instability results is then presented at $\alpha = 0°$, $\alpha = 6°$ and $\alpha = 9°$. The $\alpha = 0°$ results are compared to PSE-Chem, and to predicted frequencies using Howarth's approximation.

5.1 DLR's Post-HIFiRE-1 Experiments in H2K

Post-HIFIRE-1 experiments were completed at flight-representative angles of attack and Reynolds numbers in DLR Cologne's H2K facility in 2013 [35, 36, 37]. The H2K experiments used an axisymmetric cone model scaled at 64% to flight. The nominal conditions were: $Re_{unit} \approx 9.2 \times 10^6$ /m, $M = 7.08, r_N = 1.6$ mm, $T_w/T_0 = 0.56$, and $\alpha = 0°$ - $15°$. Their targeted condition corresponds to a flight $Re_{unit} \approx 6.2 \times 10^6$ /m, and matches the largest transition Re_x measured in flight (t = 484.3 seconds).

The thermographic analysis for the post-flight H2K campaign are presented in Ref. [35], whilst the surface pressure fluctuation results are in the companion paper, Ref. [36]. These results are then summarised and compared to linear stability theory in Ref. [37]. Figure 5.1 shows an image of the model in the H2K test section, taken from Figure 2 and Figure 3 in Ref. [36]. The H2K 7° cone model is made out of PEEK material.



Figure 5.1: An image of the H2K model inside the test section. Taken from Figure 2 and Figure 3 in Ref. [36]

5.2 HDT conditions: matching H2K experiments

The HDT model is matched to the model tested in H2K both in terms of its nose radius ($R_N = 1.6$ mm) and sensor axial locations, though is 171 mm shorter due to the smaller HDT coreflow size. Matching the nose radius and sensor locations makes it possible to directly compare the instability results measured in both facilities using PCB132 sensors. The HDT model length is 550 mm, whereas the H2K model length is 721 mm.

The power spectral density results are processed using Welch's FFT method in both facilities, as described in Section 3.7.1. Pressure fluctuations are normalised by the edge pressure for the $\alpha = 0°$ results, and by the test section static pressure (p_∞) for the results at angle of attack[1]. The normalised power spectra is then integrated over the same frequency band (100 kHz $\leq f \leq$ 500 kHz), and the same criteria is used to present the PCB-detected transition front.

5.2.1 Viscosity model

The viscosity model was matched to that used in H2K, to ensure that there were no discrepancies in methods for calculating facility flow conditions. In DLR's H2K facility, Sutherland's viscosity model is typically used with a low-temperature interpolation [200]. If $T > 120$K, $\mu_{H2K} = \mu_{\text{Sutherland}}$, where

$$\mu_{\text{Sutherland}} = \frac{1.458\text{e-}6 \times T^{3/2}}{T + 110.4} \tag{5.1}$$

When the temperature passes below this limit, a linear interpolation is assumed between the value of the viscosity at 120 K and the origin:

$$\begin{aligned} \Delta_{\text{H2K}} &= \frac{\mu_{\text{Sutherland, @ } T=120\text{ K}}}{120} \\ \mu_{\text{H2K}} &= \Delta_{\text{H2K}} \times T \end{aligned} \tag{5.2}$$

[1]This normalisation is chosen to match the processing method applied in Ref. [36] and Ref. [37]

The dynamic viscosities calculated using Keyes' and H2K's viscosity model differ by 10% for the freestream temperature used in HDT ($T_\infty = 49$ K). This difference would be the same for the Reynolds number, meaning that $Re_{unit,\infty} = 8.4 \times 10^6$ /m if Keyes' viscosity model is used instead of $Re_{unit,\infty} = 9.2 \times 10^6$ /m. The discrepancy is not negligible, particularly as the facility Reynolds number is frequently the quoted parameter in boundary layer studies. It should be noted that H2K consistently quote their reservoir conditions, making it possible for other groups to calculate the Reynolds number using their desired viscosity model. For the verification results presented in this chapter, the viscosity model has been matched to the method implemented in H2K's facility.

5.2.2 Wall-to-total temperature ratio (T_w/T_0)

The H2K experiments had a nominal wall-to-total temperature ratio of 0.56. In practice their model had a wall temperature distribution along the cone length, resulting in a range of T_w/T_0 (see Figure 3 in Ref. [35]). For the HDT experiments, measurements are taken using facility plateau #1. This plateau is chosen for the higher total temperatures achieved and the similarity of freestream turbulence levels to other conventional wind tunnels[2]. The HDT test time is chosen so that the average total temperature is equal to 523 K (matching the H2K average T_w/T_0) and the average unit Reynolds number is 9.2×10^6/m. In practice, the total temperature drops from $\approx$ 549 K to 496 K over the test time, whilst the Re_{unit} increases from 8.7 to 9.6 $\times 10^6$ /m. The test time condition variation is $\pm 5\%$ of the target value, and exists due to the unsteady compression into the settling chamber.

5.2.3 PCB132 correction

When comparing the PCB132 power spectra obtained in HDT to those presented in Ref. [36] at high angles of attack, an offset of 100 was observed. This has been

[2]It is assumed that DLR's H2K facility has similar magnitudes of post-shock Pitot pressure fluctuations as the conventional tunnels summarised in Ref. [120]

investigated by collaboration with Dr. Tom Juliano and Dr. Sebastian Willems. The discrepancy is purely due to PCB132 processing methods rather than any differences in measured pressure fluctuations or the uncertainties that arise from uncalibrated PCB132 sensors. The HDT processing method has been compared using the same dataset and matches that used by Willems et al. in H2K [35][200]. Power spectra results from Ref. [36] have therefore been multiplied by 100 when compared to the high angle of attack results in this paper, to bring them in line with the H2K results presented in the companion paper ([35]), and to allow a direct comparison with the HDT power spectra results.

5.2.4 Summary of conditions

The HDT facility profile is shown in Figure 5.2, along with the chosen test time period. Table 5.1 summarises the conditions and model geometry used in each facility.

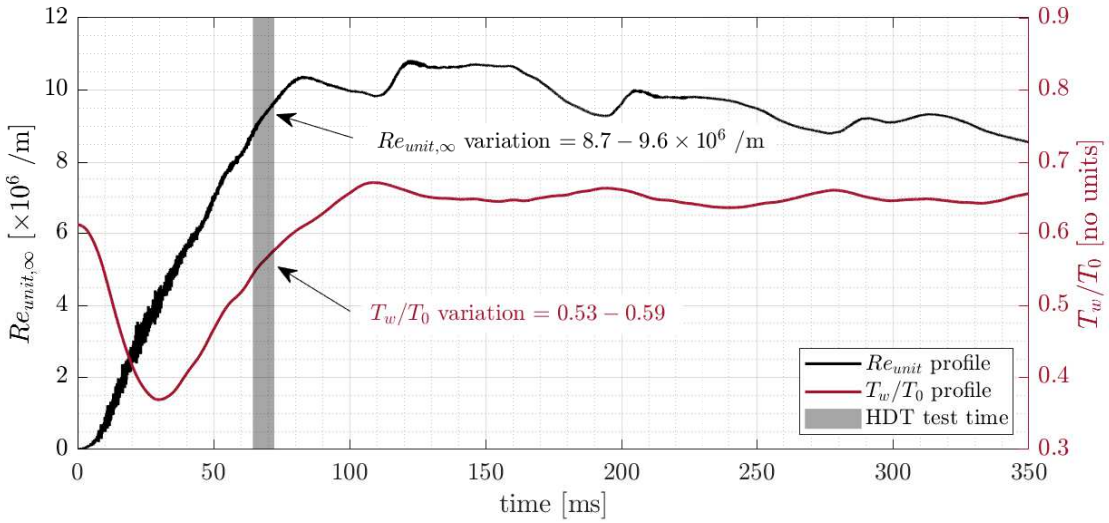


Figure 5.2: HDT facility profile and chosen test time used for the verification campaign.

Parameter	HDT (plateau #1)	H2K
T_0 (K)	523	600
P_0 (kPa)	1660	2300
M_∞	6.94	7.08
$Re_{unit,\infty}(\times 10^6 \frac{1}{m})$	9.2	9.0-9.2
T_w/T_0	0.56	0.56
T_∞ (K)	49	56
P_∞ (Pa)	425	556
α (°)	0, 3, 6, 9, 12	0, 3, 6, 9, 12, 15
Noise (%)	1.49	N/A
R_n(mm)	1.6	1.6
$Re_{x,max}(\times 10^6)$	4.95	6.40
Viscosity model	Sutherland with low temp. correction	
Test time (s)	13×10^{-3}	30

Table 5.1: Summary of conditions used in the HDT instability verification experiments. Conditions and model features are compared to those obtained in H2K [35, 36].

5.3 Microalignment of the HDT 7° model

The automated traverse has been used to ensure the cone model is correctly aligned to the incoming flow. The normalized surface power spectra of high-frequency piezoelectric pressure gauges (PCB132A31) are compared along diametrically opposing arrays. When the disturbance features exist at the same frequency, the boundary layer thickness is matched and the axisymmetric model is well-aligned.

The vertical alignment is confirmed by comparing the results from the windward ray ($\phi = 0°$) and the leeward ray ($\phi = 180°$), whilst the horizontal alignment is verified using the $\phi = 90°$ ray and $\phi = 270°$ ray at $\alpha = 0°$. The alignment is checked at multiple axial locations. The vertical alignment is corrected by adjusting the traverse angle of attack (α_{trav}), whilst the horizontal alignment is corrected by changing the angle of yaw (β_{trav}). Figure 5.3 shows normalized power spectra with the automated traverse set to $\alpha_{trav} = 0°$, $\beta_{trav} = 0°$. When considering the maximum amplitude for the second-mode instabilities, it is clear that the disturbance frequencies do not line up, and the model is therefore poorly aligned.

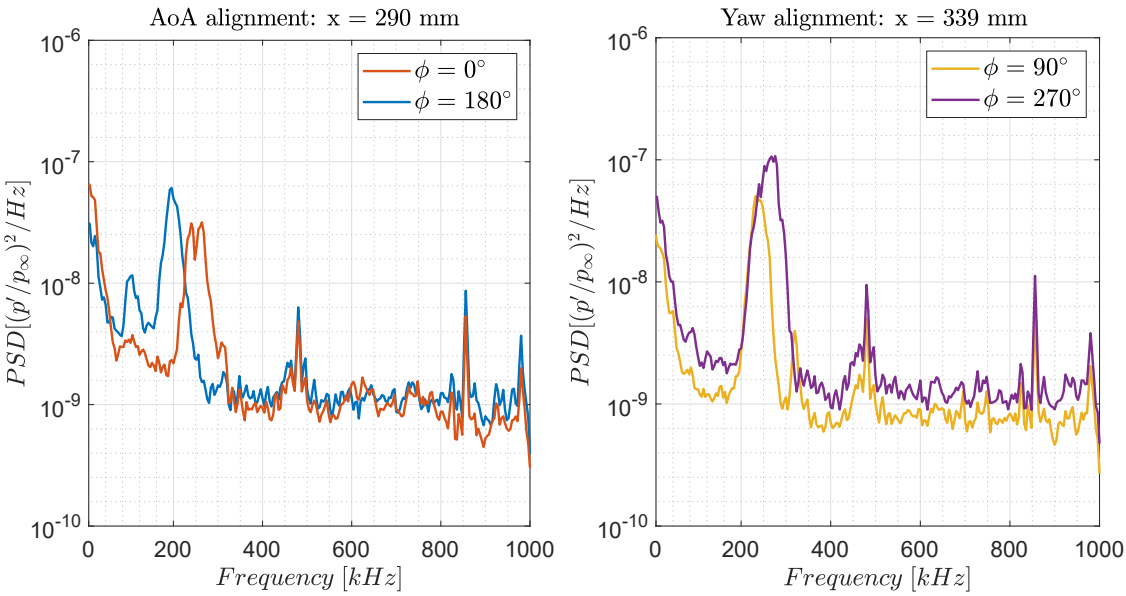


Figure 5.3: Normalized surface pressure power spectra with traverse set to $\alpha_{trav} = 0°$, $\beta_{trav} = 0°$. Cone model is misaligned.

The second mode disturbance is centered on higher frequencies because the acoustic wave is propagating along a thinner boundary layer. For this reason, the traverse angle of attack and angle of yaw are shifted towards the gauge which has the highest second mode instability frequency. This results in a change to the boundary layer thickness along both rays, and ensures that the second mode disturbance frequencies match. Figure 5.4 shows the power spectra results with the automated traverse set to α_{trav} = -0.4° and β_{trav} = 0.2°. With this offset, the second mode frequencies overlap and the model is considered to be well-aligned in both the vertical and horizontal direction. The model microalignment is checked at the beginning of each day of testing and when any modifications to the model are made (e.g. changes to nose radii and azimuthal model rotations).

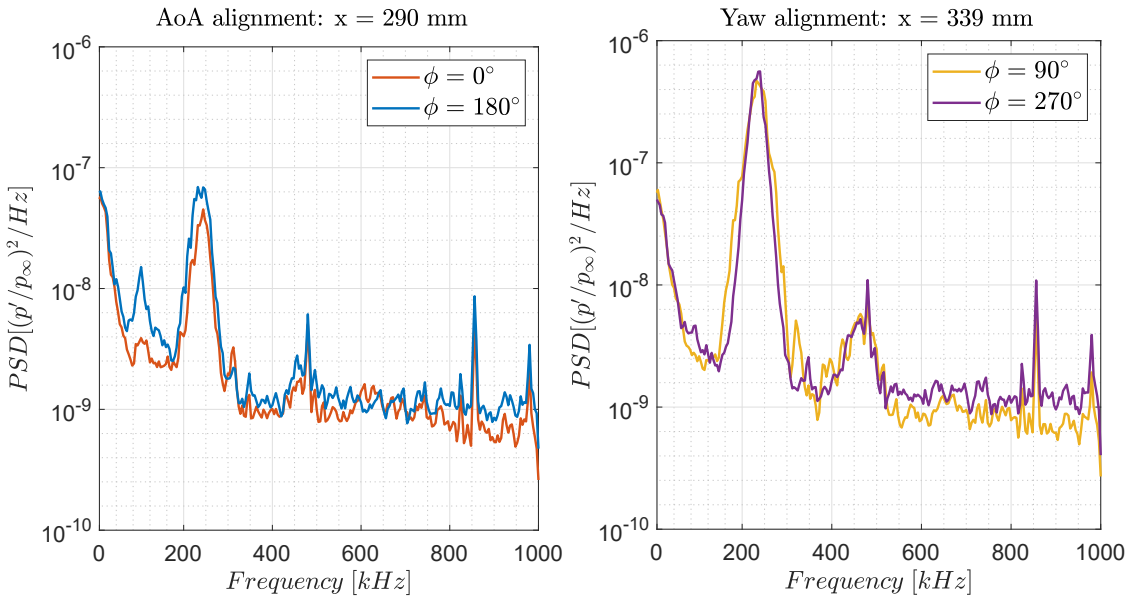


Figure 5.4: Normalized surface pressure power spectra with traverse set to α_{trav} = -0.4°, β_{trav} = 0.2°. Cone model is aligned.

5.4 Results at $\alpha = 0°$

Figure 5.5 shows a comparison of the normalized surface-power spectra for $\alpha = 0°$. The first sign of an amplified disturbance in the HDT results is at $Re_x = 2.3 \times 10^6$, centered at f $\approx$ 260 kHz. The frequency of the second mode disturbance progressively decreases thereafter, as the amplitude increases and the boundary layer thickens downstream. The power spectra starts to broaden over all frequencies at $Re_x = 4.7 \times 10^6$, as the second mode decays to turbulence. A higher harmonic of the second mode is observed from $Re_x = 3.6 \times 10^6$, suggesting that non-linear interactions between modes is occurring. The higher harmonic frequency is double that of the dominant second mode (within 5%).

When comparing both sets of results, there is quite good agreement in the frequencies at which the maximum amplitude occurs. For both facilities, this progressively decreases from f = 250 kHz (HDT) and f = 280 kHz (H2K, [36]) at the first increase in second-mode amplitude, to f = 200 kHz (HDT) and f = 215 kHz (H2K, [36]) at the point of greatest amplitude. There is a clear difference in the location where the maximum amplitude occurs. In the HDT results, the maximum amplitude is observed at $Re_x = 4.1 \times 10^6$, whilst in the H2K facility it is at $Re_x = 4.6 \times 10^6$. This result suggests that the transition process happens one gauge further upstream in the HDT facility.

The PSD can be integrated to give the second mode amplitude, as shown in Figure 5.6. The HDT results are the mean of 10 amplitude measurements at each location, for various cone rotations (i.e. φ rotations). The grey area illustrates the standard deviation of the HDT second mode amplitudes. The H2K results have been reproduced using data from Figure 6 in Ref. [37]. The variation of both datasets is similar. It can be clearly seen that the maximum second mode amplitude occurs at $Re_x = 4.1 \times 10^6$ (x = 445 mm) in the HDT results, whilst it is at $Re_x = 4.7 \times 10^6$ (x = 510 mm) in H2K. These results reiterate that second

mode disturbances are present one gauge further upstream in the HDT facility.

The maximum second mode amplitude before decay is marginally lower in HDT ($A_{max} \approx 18\%$) than H2K ($A_{max} \approx 23\%$). The lower A_{max} value can most likely be attributed to higher freestream disturbance levels in HDT plateau #1, however the values observed by both facilities are within the region of values collated by Marineau et al. [54]. The maximum second mode amplitudes are investigated further in Section 6.2.5.

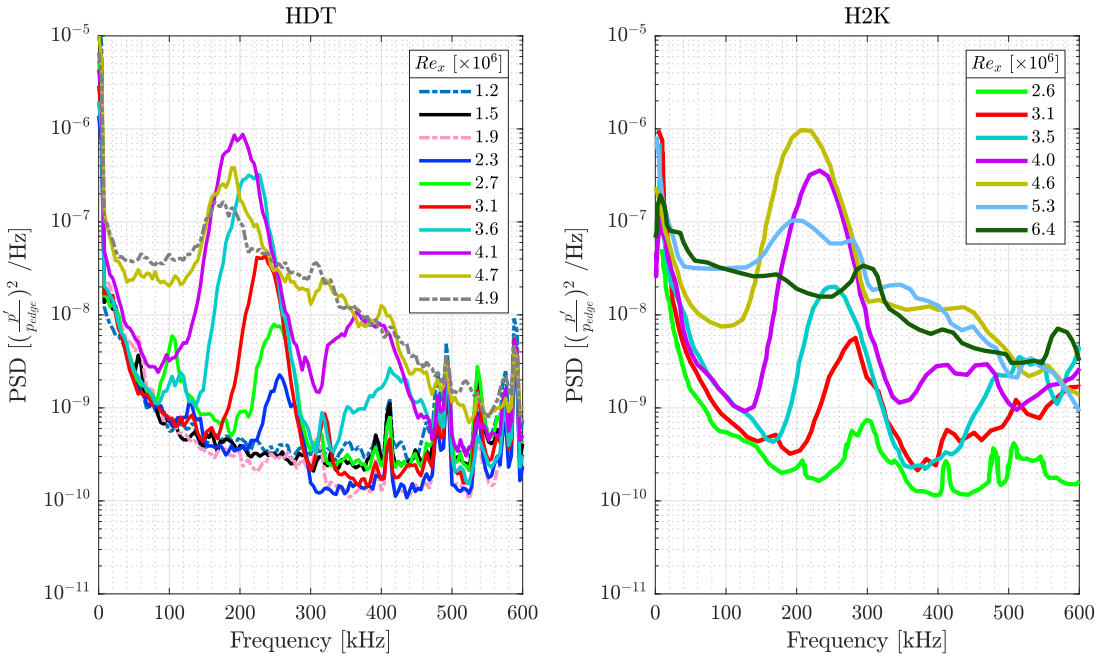


Figure 5.5: Comparison of pressure fluctuation PSD using PCB132 sensors at $\alpha = 0°$. Conditions are: $M = 7$, $Re_{unit,\infty} = 9.2 \times 10^6$ /m, and $T_w/T_0 = 0.56$. Both datasets have been processed using Welch's FFT method.

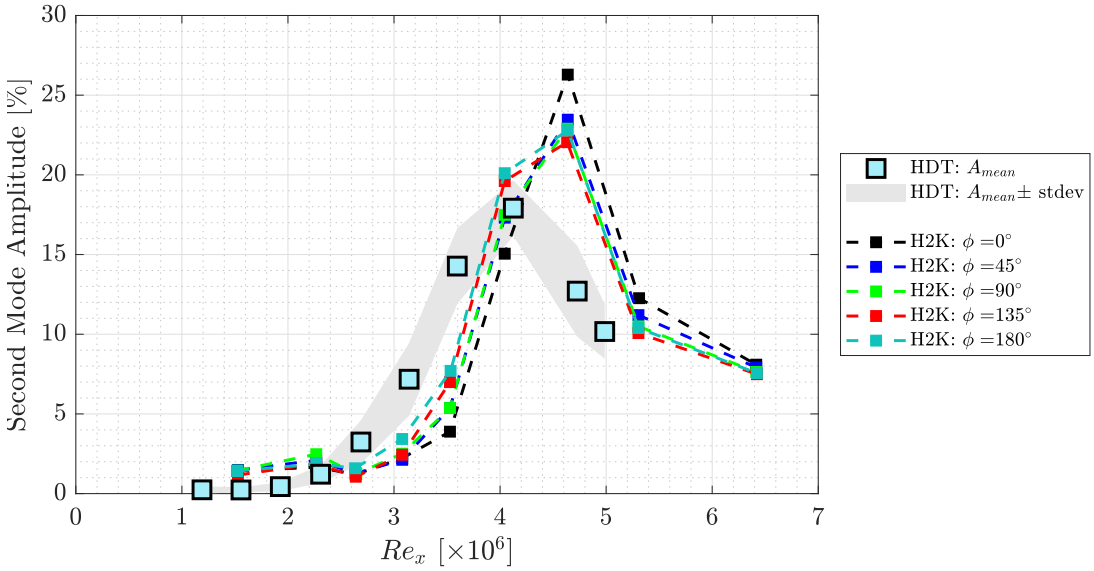


Figure 5.6: Comparison of second mode amplitude results.

5.4.1 Comparison to STABL2D PSE-Chem computations

The HDT instability measurements are compared to STABL2D PSE-Chem stability computations completed by Dr. Joseph Jewell. Section 2.3.2 provides more information about PSE-Chem, along with details about the setup used for this research. Figure 5.7 compares the PSE-Chem computed maximum N factor envelopes for the HDT and H2K conditions and geometries. The H2K envelope has been extracted from Figure 15 in Ref. [37]. It is reassuring that the N factor envelopes agree quite well, seeing as the cone nose radii and the facility flow conditions are matched.

Details about the conditions used in the H2K PSE-Chem computations are provided in Section VI. of Ref. [37]. The H2K measured second mode peaks showed excellent agreement with the PSE-Chem predicted frequencies. The disturbance growth was also accurately predicted by PSE-Chem, when the initial computed power was matched to the experimentally measured value for a sensor upstream

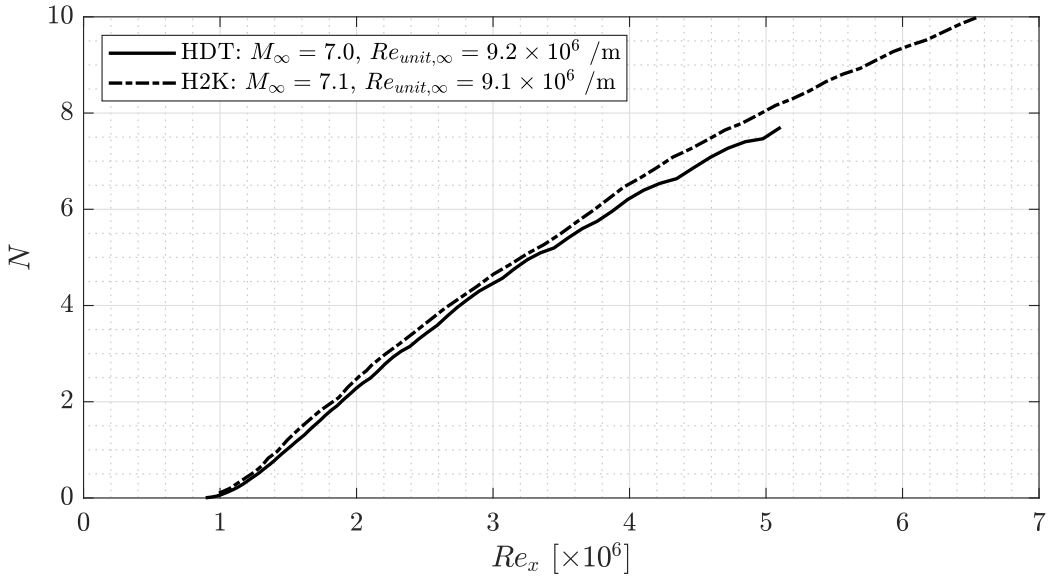


Figure 5.7: Comparison of PSE-Chem computed N factors. The H2K envelope has been extracted from Figure 15 in Ref. [37].

($x = 339$ mm)[3]. A critical N factor of 5.5 - 5.8 was calculated using the heat transfer detected transition onset location, and this agreed well with Alba et al.'s stability analysis results [201].

The frequency of the maximum disturbances for the H2K results was extracted from the PSE-Chem computations presented in Figure 16 of Ref. [37]. Figure 5.8 shows the N factor for each of the H2K sensors. The frequency of the disturbance amplitude decreases as it propagates downstream, as expected. The frequencies of the maximum disturbance amplitudes are denoted by the "X" symbols in the figure. These frequencies are then used to generate the curve shown on the right plot of Figure 5.8 and the dashed line in Figure 5.9a.

[3]This made it possible to track the PSE-Chem computed disturbance power as the second mode propagated from the $x = 339$ mm sensor to the end of the cone.

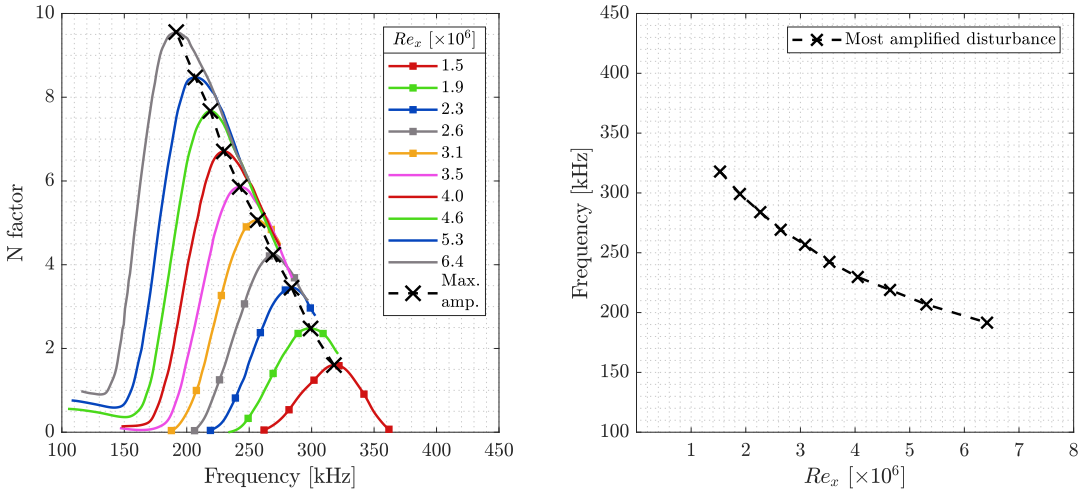
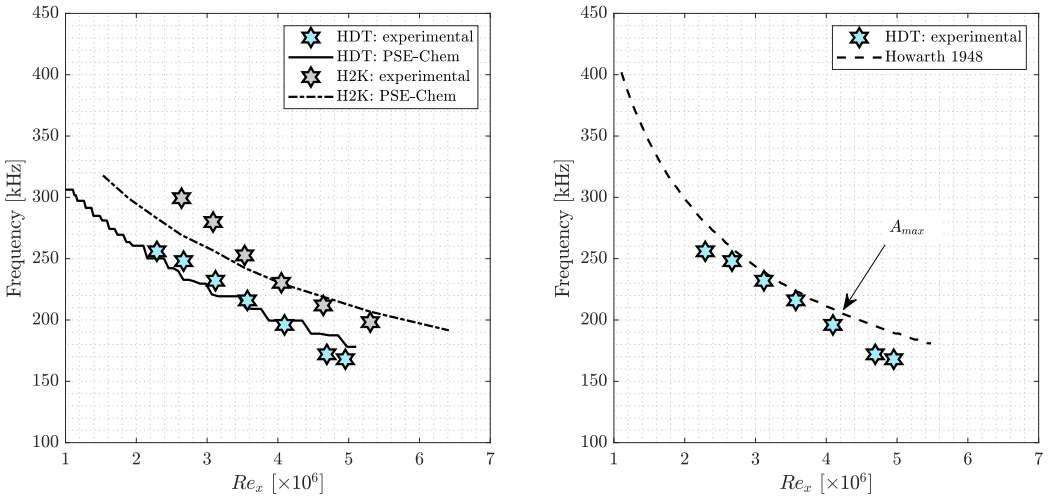


Figure 5.8: H2K N factors for each gauge, and the frequencies of the most amplified disturbances. Reproduced using data from Figure 17 in Ref. [37].

The frequencies of the measured second mode disturbances are compared to PSE-Chem in Figure 5.9a, for both facilities. The experimental results are extracted from the PSD results presented in Figure 5.5. There is good agreement for both datasets with the PSE-Chem computed frequencies. The maximum discrepancy for the HDT disturbance frequencies is 9%, whilst the maximum discrepancy for the H2K frequencies is 11%.

The HDT experiment results are also compared to the estimated disturbance frequency using Howarth's boundary layer thickness approximation [84] in Figure 5.9b (see Section 2.5.2). The estimated frequency uses edge conditions from a Taylor-Maccoll calculation, which assumes a perfectly sharp cone. The sharp cone assumption may be a cause for the slightly over-predicted disturbance frequency using Howarth's approximation. The agreement is still quite good, with discrepancies all less than 13%.



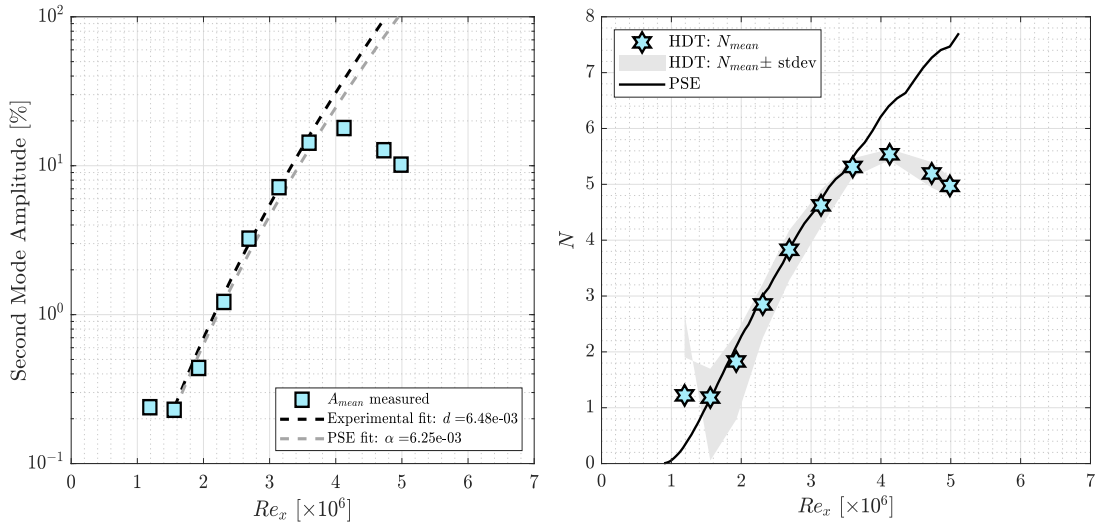
(a) PSE-Chem & H2K measurements **(b)** Howarth's approximation [84]

Figure 5.9: Comparison of the most amplified disturbance frequencies to those predicted using: (a) PSE-Chem, and (b) Howarth's approximation for the laminar boundary layer thickness [84] (described in Section 2.5.2). The HDT disturbance frequencies are extracted from the PSD presented in Figure 5.5. Results for H2K are generated using data from Figure 5 and Figure 17 in Ref. [37].

The HDT second mode amplitudes were processed according to the method described by Marineau et al. [54] (see Section 2.5.4). This provided a means to calculate the experimental N factor and compare these results to PSE-Chem[4]. The second mode amplitude results are shown in Figure 5.10a, along with the experimental growth rate (d) and the PSE-computed growth rate fit (α). The discrepancy between the computed growth rate and the measured growth rate is less than 5%.

The experimental N factor is then presented in Figure 5.10b. The critical N factor is approximately 5.3. This is within the region expected from conventional wind tunnels (typically ≈ 5), and is slightly smaller than the N factor quoted by Juliano et al. in Ref. [37] ($N_{crit} = 5.5 - 5.8$). The smaller critical N factor is likely due to the slightly higher freestream disturbance levels, however a discrepancy may also exist due to the method used to calculated the N factor. H2K computed their critical N

[4]Thin film heat transfer measurements were not obtained for this HDT verification campaign, meaning that a comparison of critical N factor using the heat-transfer detected onset criterion is not possible.



(a) Second mode amplitude and growth rate fits **(b)** N factor

Figure 5.10: Second mode amplitude and N factor comparison to PSE-Chem computations. Parameters are calculated using the method described by Marineau et al. [54], with more details in Section 2.5.4 and Section 6.2.3.

factor using the onset of heat-transfer detected transition, whereas the HDT results have been calculated using Marineau's method for PCB132 measurements [54]. It is reassuring that the critical N factor results are similar nevertheless.

These results illustrate the capabilities of the PSE-Chem software suite to accurately compute the physics of the transition process for the second mode instability. The agreement in frequencies, growth rates, and second mode amplitudes is another indication that the HDT boundary layer instability measurements are as expected, and that the transition results from HDT can be compared to other facilities.

5.5 Results at $\alpha = 6°$

Boundary layer instability measurements are compared at high angles of attack, where different transition mechanisms are expected. Both facilities experience a stabilization of the windward ray and destabilization along the leeward ray as the angle of attack is increased. Figure 5.11 compares the normalized surface-power spectra for both facilities at $\alpha = 6°$, and azimuths: $\phi = 0°$, 90°, and 180°. Figure 5.12 compares the integrated power spectra results and the $Re_x - \phi$ map. H2K results are taken from Ref. [36].

Windward ray ($\phi = 0°$)

Second mode growth is observed along the windward ray in both facilities. The instability exists at a higher frequency than at $\alpha = 0°$ (Figure 5.5), due to the thinner boundary layer present along the windward ray at angle of attack. The disturbance frequencies agree quite well for both datasets, however instabilities are observed upstream in HDT. In both facilities, the disturbance frequency steadily decreases until a peak amplitude is reached at f $\approx$ 400 kHz.

The stabilization of the windward ray at angle of attack is confirmed by the delay in the maximum amplitude of the second mode instability. At $\alpha = 0°$, the maximum instability amplitude was observed at $Re_x = 4.1 \times 10^6$ (Figure 5.5), whilst Figure 5.11 suggests that the maximum amplitude has shifted to downstream of $Re_x = 4.7 \times 10^6$ mm at $\alpha = 6°$. The windward stabilization at angle of attack was also observed in H2K's results, and is common for similar cold flow facilities (see Section 2.7.4).

Progression to the leeward ray ($\phi = 180°$)

The disturbances clearly shift to lower frequencies for azimuths approaching the leeward ray as the boundary layer thickens. The disturbance frequencies show good agreement between both facilities. Crossflow vortices were observed as streaks in the IR thermography results from the H2K campaign at this angle of attack [35]. It is therefore assumed that the secondary instability of stationary crossflow vortices may play a role in the transition process along the shoulder of the cone in both datasets.

The electrical noise levels seem to be higher in the HDT results, making it more difficult to detect the earlier stages of the high frequency disturbance growth. At $\phi = 90°$, the disturbance peaks are more obvious in the HDT results at $f \approx 300-350$ kHz. Along the leeward ray, both facilities show a broadband turbulent PSD profile, with evidence of a disturbance peak only at $Re_x = 2.3 - 2.6 \times 10^6$ mm. The boundary layer is expected to be quite thick along the leeward ray, and may have even separated, which is why the peak is at such low frequencies. The PSD results for the $\phi = 45°$ and $\phi = 135°$ azimuths agree with the observed trends[5].

[5]The PSD spectra for $\phi = 45°$ and $\phi = 135°$ are presented in Figure 12 of Ref. [199].

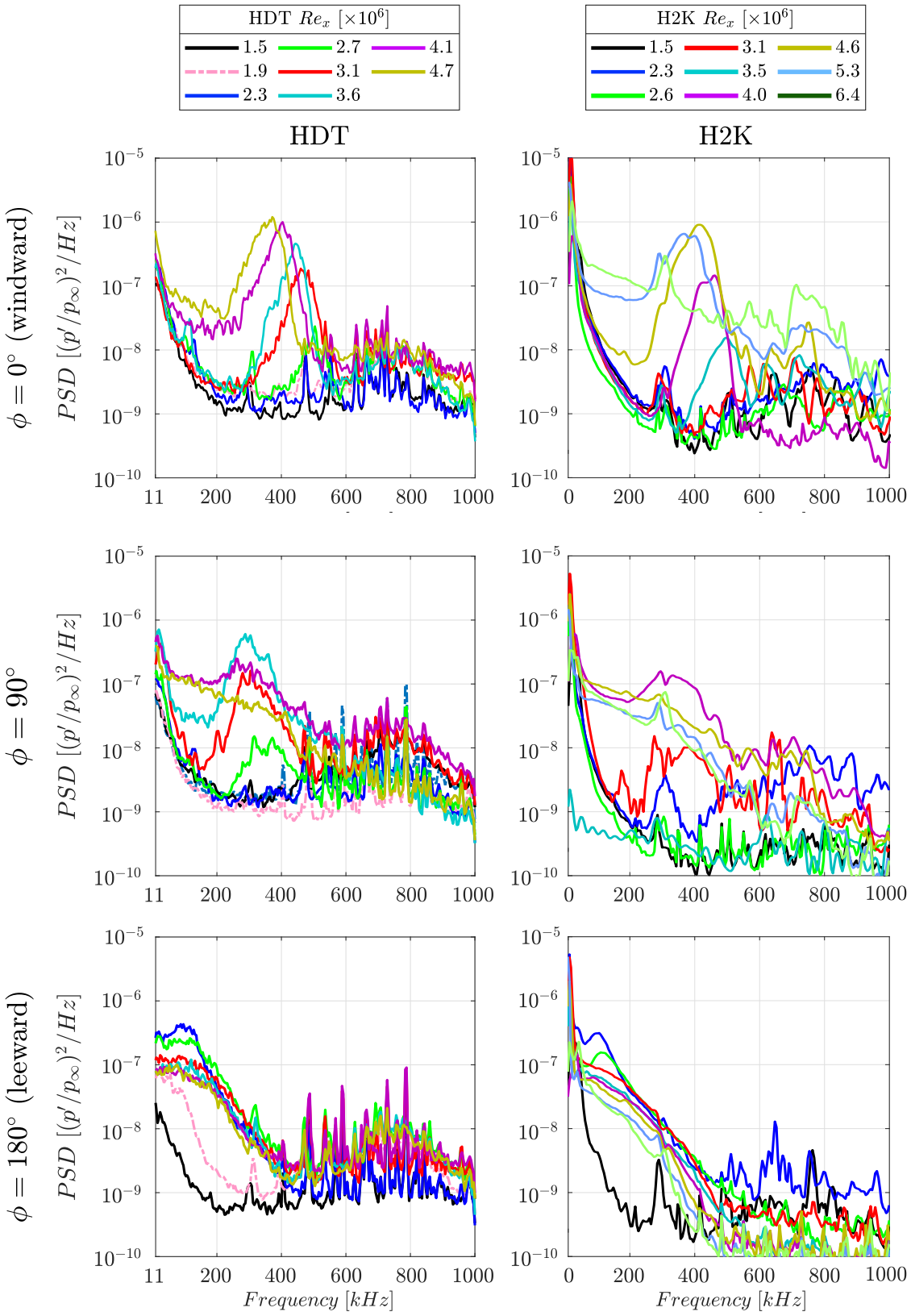


Figure 5.11: Comparison of PCB132 surface pressure power spectra results at $\alpha = 6°$. PSD results shown for $\phi = 0°$, 90°, and 180°.

Disturbance amplitudes

Integrated PSD results show that the maximum normalized pressure fluctuations move upstream and to smaller amplitudes in both facilities. The smaller magnitudes are believed to be due to the higher local mean pressures that exist when approaching the windward ray, as both datasets have normalised fluctuations by the test section pressure rather than the local boundary layer edge pressure. Despite this, both facilities have quite similar maximum fluctuation locations at $\phi = 90°$, 135°, and 180°. The boundary layer is less stable for the windward ray, as was observed in the PSD results in Figure 5.11. This is the reason why the HDT $Re_x - \phi$ map has a smaller gradient than the H2K result.

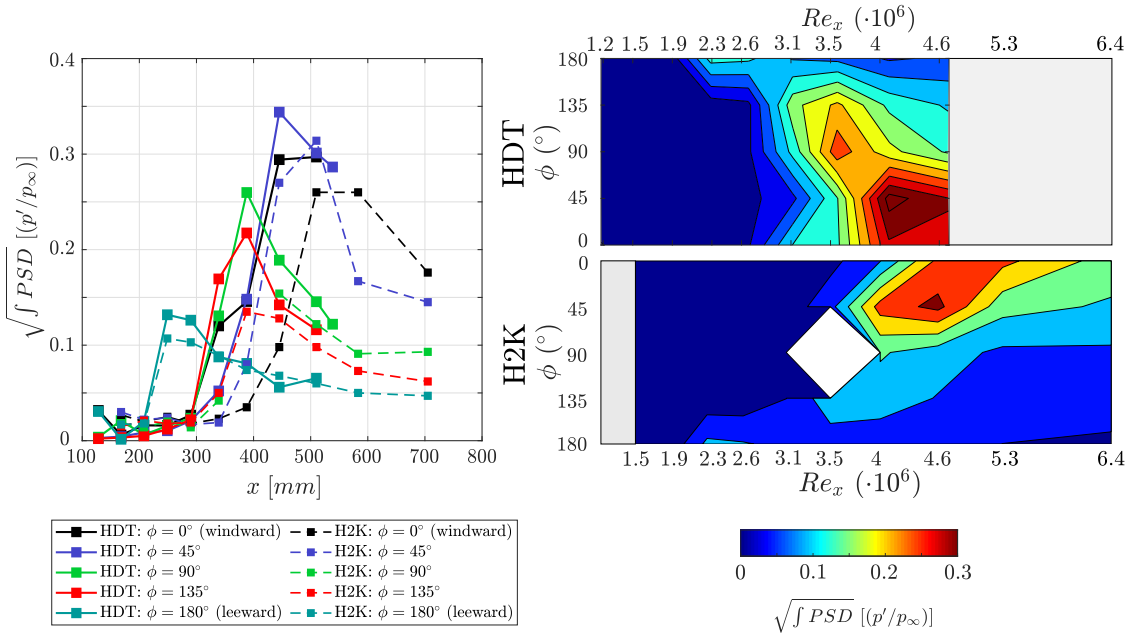


Figure 5.12: Comparison of integrated PSD results using PCB132 sensors at $\alpha = 6°$.

5.6 Results at $\alpha = 9°$

Figure 5.13 compares the integrated power spectra results at $\alpha = 9°$. The trends observed at $\alpha = 6°$ are more prominent as the angle of attack is increased; the windward ray is stabilized further and the leeward ray is continuously destabilized. The windward ray is less stable in the HDT than in H2K, resulting in a smaller disturbance front gradient[6] in the HDT. The maximum pressure fluctuation locations seem to match quite well between both facilities at $\phi = 45°$, 90° and 180°.

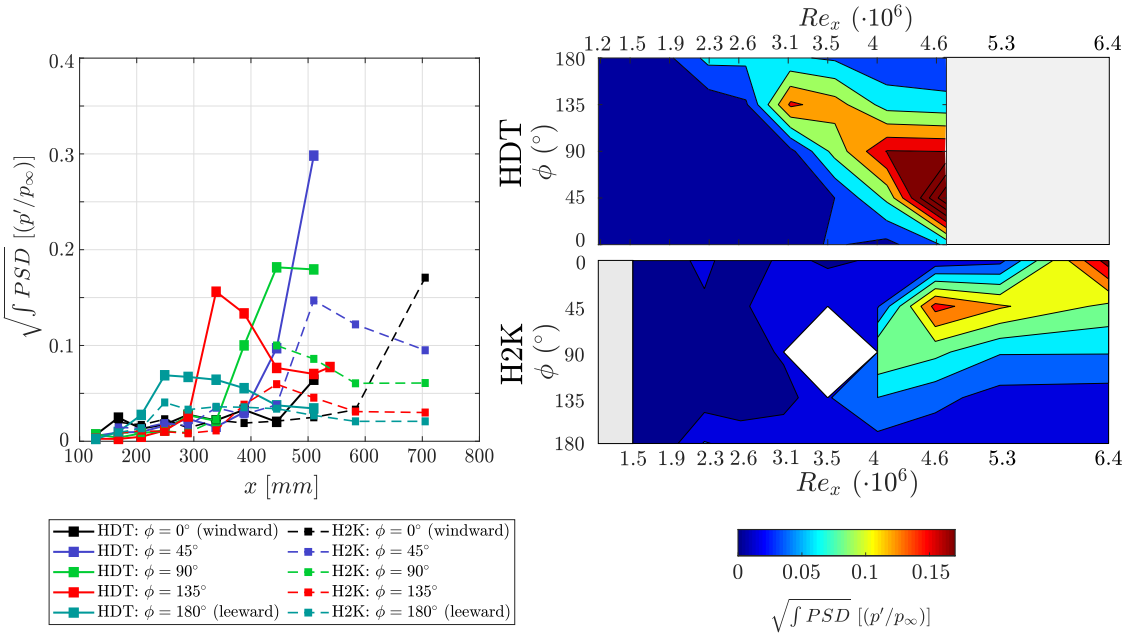


Figure 5.13: Comparison of integrated PSD results using PCB132 sensors at $\alpha = 9°$.

[6]The disturbance front gradient refers to the difference in Re_x, tr between the windward ray and the leeward ray

5.7 Comparison of PCB-detected Transition Fronts

Figure 5.14 shows a comparison in PCB-detected transition onset between both facilities. Values for H2K have been read from Figure 14 in [36]. For both sets of results, the onset location is taken as the first gauge to show broad-frequency increase of pressure fluctuations above laminar levels in the surface pressure spectra. The increase in power spectra must be an order of magnitude at low frequencies ($f \approx 100$ kHz) for it to qualify as onset. The resolution is quite poor due to the spacing between PCB sensors and azimuths (represented by tick spacing on the figure). The map presents the onset transition Reynolds number ($Re_{x,tr}$) as a function of azimuth (ϕ), angle of attack (α) and experimental facility.

The PCB-detected transition fronts for each facilities show similar trends and have quite good agreement, particularly when considering the resolution of PCB132 gauges on the cone. The HDT transition Reynolds number is constant for all azimuths at $\alpha = 0°$, however it is noticeably one-gauge upstream of the results obtained in H2K. This agrees with the integrated power spectra results and the locations where the maximum pressure fluctuations were observed.

The PCB-detected transition onset moves downstream along the windward ray and upstream along the leeward ray as the angle of attack is increased. In both facilities, the stabilization along the windward ray occurs when moving from $\alpha = 6°$ to $\alpha = 9°$. The windward Re_x transition was not detected on the windward ray at $\alpha = 12°$ due to insufficient cone length. This suggests that the windward ray stabilized even further as the angle of attack increased. The increase in $Re_{x,tr}$ detected in H2K along the windward ray is larger, moving from 4.6×10^6 at $\alpha = 6°$, directly to 6.4×10^6 at $\alpha = 9°$ and 12°. H2K did not observe any change in windward $Re_{x,tr}$ when increasing the angle of attack from 9° to 15°. The leeside $Re_{x,tr}$ is consistently one gauge further upstream in the HDT facility, apart from the results obtained at $\alpha = 3°$, where they are matched directly.

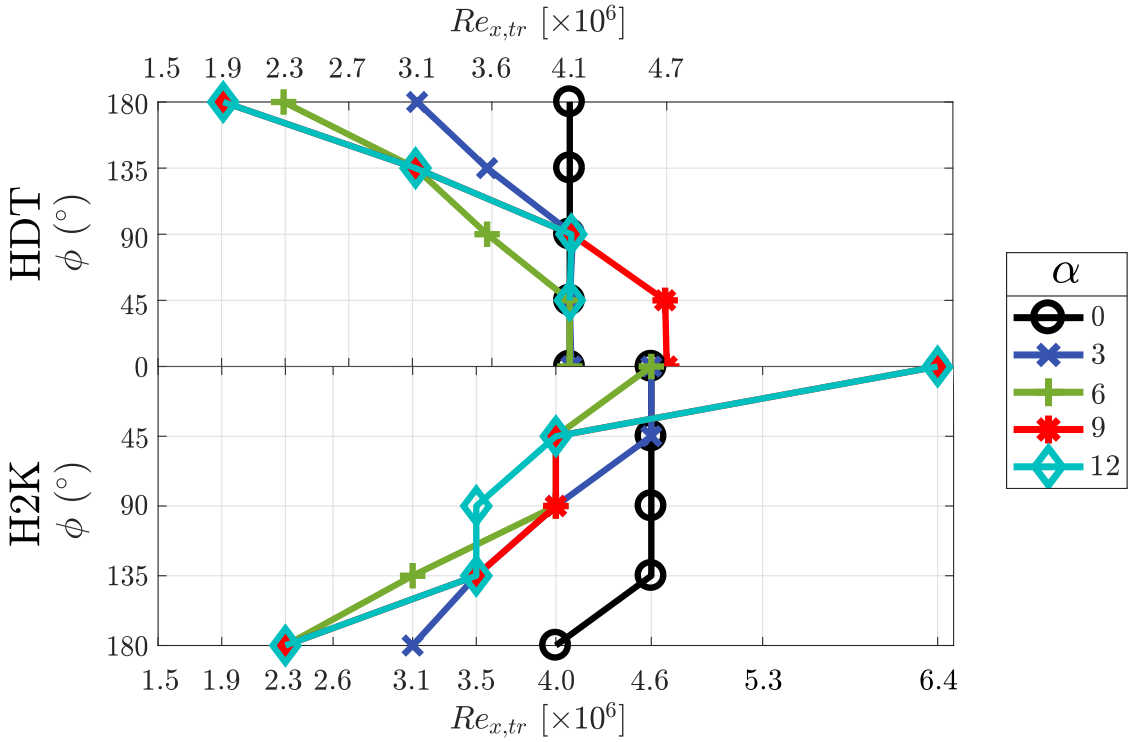


Figure 5.14: PCB-detected transition front. A comparison between HDT and H2K. $M_\infty \approx 7$, Re_{unit} = 9.2 x 10^6 /m (H2K) - 9.2 x 10^6 /m (HDT), r_N = 1.6 mm, T_w/T_0 = 0.56.

5.8 Sources of discrepancies

The small discrepancies in instability location is likely to be due to differences in the experimental setup. Firstly, the wall-to-total temperature ratio is slightly different for both sets of results. The HDT had a slight variation in facility T_w/T_0, whilst the H2K model had a T_w/T_0 distribution along the cone surface. Secondly, there may be differences in freestream turbulence levels between both facilities. The HDT plateau #1 post-shock pressure fluctuations overlapped with conventional tunnels quoted in Ref. [120] (see Section 4.3.2). The H2K nozzle is the larger of the two (600 vs. 350 mm), and may therefore have lower freestream turbulence levels. A third discrepancy may originate from the differences in distributed roughness along the 7° models. The H2K model is made out of PEEK, whilst the HDT model is made using mild steel and aluminium. Each of these factors may contribute to the small discrepancies in the instability locations observed.

5.9 Summary

Boundary layer instability measurements from the Oxford HDT have been compared to a similar dataset from DLR's H2K facility, and to stability computations using the STABL2D PSE-Chem package at $\alpha = 0°$. The second mode instability dominated transition at $\alpha = 0°$ in both facilities, with the measured disturbance frequencies agreeing to computations within 9%. The power spectral density results at high angles of attack indicated that the same three-dimensional transition mechanisms exist in the HDT. A windward stabilization and leeward destabilization was observed in both facilities, when compared to the $\alpha = 0°$ results.

The excellent agreement between instability measurements in both facilities and stability computations indicates that the HDT facility and processing methods can be trusted for boundary layer transition studies.

6

Boundary layer instabilities at $\alpha = 0°$

Boundary layer instability measurements are presented in two facilities at Mach 7 and $\alpha = 0°$. The second mode instability is expected to dominate transition at these conditions, and is therefore the focus of this chapter. Presentation of results is separated according to the facility wall-to-total temperature ratio:

High T_w/T_0 facility: HDT

These subsections investigate the second mode instability properties in a "cold flow" tunnel, where the T_w/T_0 is relatively high (varying from 0.56 - 0.65). The nominal condition is scaled from the final transition Reynolds number observed in HIFiRE-1 flight. Results are presented using multiple facility plateaus, to investigate the effect of an increase in freestream disturbances.

Low T_w/T_0 facility: T4

Instability measurements are obtained in The University of Queensland's T4 Stalker Tunnel at flight-representative enthalpies (i.e. low T_w/T_0). A sweep of facility Reynolds numbers and T_w/T_0 distributions are presented using the front segment of the RST 7° cone model ($Re_x \leq 3 \times 10^6$).

6.1 Static Cone Pressure

The $\alpha = 0°$ pressure fluctuation measurements are normalised by the static cone surface pressure. The static pressure is measured using Kulite XTEL-140(M) sensors at $x = 451$ mm and $x = 480$ mm. Figure 6.1 compares the Kulite pressures to Cheng's correlation [202, 203], a Taylor-Maccoll computation, and an Eilmer4 axisymmetric blunted cone simulation. The agreement between Kulites, Taylor-Maccoll, and the Eilmer4 simulation is all within 1%. The pressure is slightly under-predicted using Cheng's correlation, though still within 5% of the Kulite measurements. The pressure fluctuation results for the following subsections are normalised by the pressure calculated using the Taylor-Maccoll solution [85].

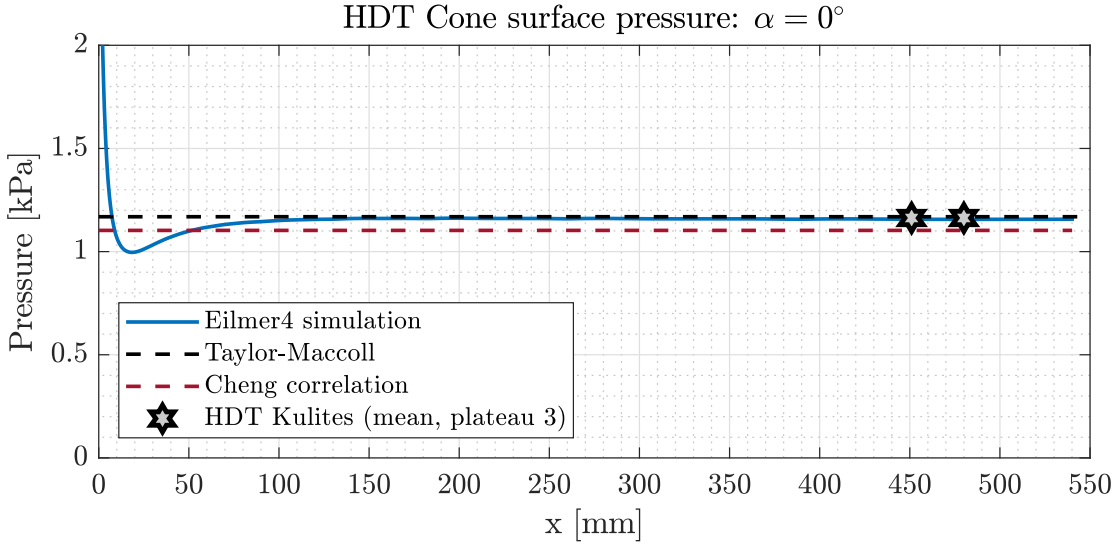


Figure 6.1: Cone surface pressure as a function of axial location. Kulite pressures are compared to those calculated using Cheng's correlation [202, 203], Taylor-Maccoll computations, and an Eilmer4 axisymmetric blunted cone simulation. The HDT condition is at: $M_\infty = 7.0$, $Re_{unit,\infty} = 12.3 \times 10^6$ /m, $T_w/T_0 = 0.64$, $\alpha = 0°$.

6.2 The Oxford HDT: high T_w/T_0, $\alpha = 0°$

Boundary layer instability measurements are presented at the scaled HIFiRE-1 condition using the $R_N = 1.25$ mm nosepiece. Results are compared using HDT facility plateaus #1 and #3, to investigate the role of decreased T_w/T_0 and increased noise levels. A total number of four shots were run at this condition, with the variation in results illustrated by the grey area in the second mode amplitude and heat flux results. The facility condition is provided in Table 6.1 and Figure 6.2.

Parameter	HDT plateau #1	HDT plateau #3
P_0 (kPa)	2344	2023
T_0 (K)	523	455
segment duration (ms)	13	16
Re_{unit} (10^6 /m)	12.3	12.3
M_∞	7.0	7.0
T_w/T_0	0.58	0.64
Noise (total %)	1.49	0.44

Table 6.1: HDT condition for $\alpha = 0°$ results. The condition is scaled from HIFiRE-1 flight based on the nose radius used ($R_N = 1.25$ mm). The plateau #1 values for T_0, Re_{unit}, and T_w/T_0 are the average quantities over test time. The variation is less than $\pm 5\%$ for each parameter.

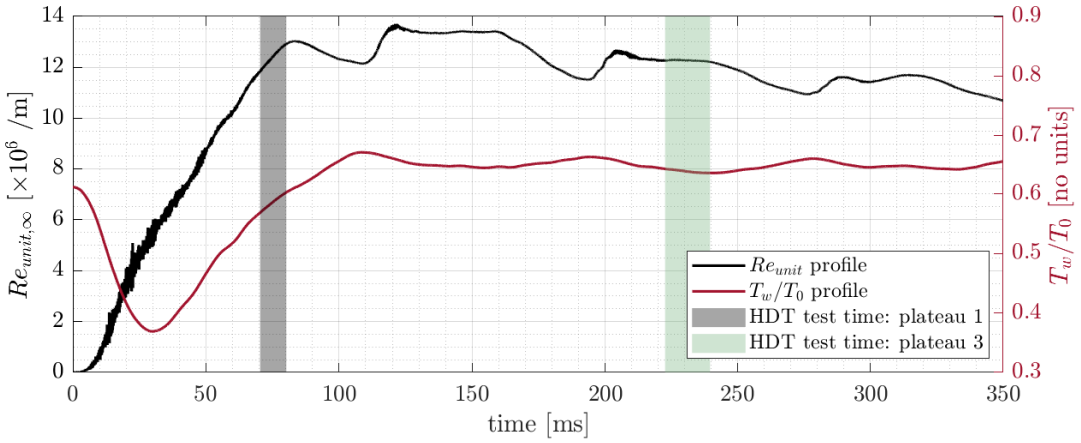


Figure 6.2: HDT facility profile for $\alpha = 0°$ results. P_0 and T_0 values for each test-time are provided in Table 6.1

6.2.1 HDT Plateau #1: $T_w/T_0 = 0.58$, Noise = 1.49 %

Continuous wavelet scalogram results are presented in Figure 6.7, for a succession of PCB132 sensors at $\alpha = 0°$. No wavelets are resolvable at upstream locations ($Re_x < 3.1 \times 10^6$), indicating that the boundary layer is completely stable. Second mode wave packets are then observed over a relatively small frequency band, $f \approx 200 - 300$ kHz. As the disturbances propagate downstream, the wave packets have more power and are observed more frequently throughout the test-time. At the final gauge location, there are not as many wave packets, and the maximum amplitude of the wavelet coefficients has decreased. By this point, the boundary layer has decayed to turbulence and the power exists over a wider range of frequencies.

Power spectral density results are shown in Figure 6.4. These results summarise the fluctuation content over the entire test time, using the continuous wavelet transform and the fast Fourier transform (Welch's method). There is excellent agreement in the disturbance frequency when using both processing methods. The second mode instability is first observed at $Re_x = 3.1 \times 10^6$. The amplitude increases and is centered on lower frequencies thereafter. The maximum second mode amplitude is observed at $Re_x \approx 4.8$, after which the boundary layer clearly breaks down to turbulence.

The second mode amplitudes are summarised along with the thin film gauge heat flux results in Figure 6.5. The results are the mean of eight measurements at the same condition, with the standard deviation shown by the grey area. The figure is annotated to show the heat transfer detected transition onset location, as well as the transition location predicted by Pate's correlation [127].

Pate's correlation relates the normalized free-stream pressure fluctuations between conventional wind tunnels, based on parameters such as the freestream Mach number (M_∞), the nozzle wall mean turbulent skin friction coefficient (C_F), the nozzle wall boundary layer displacement thickness (δ^*), and the length from the

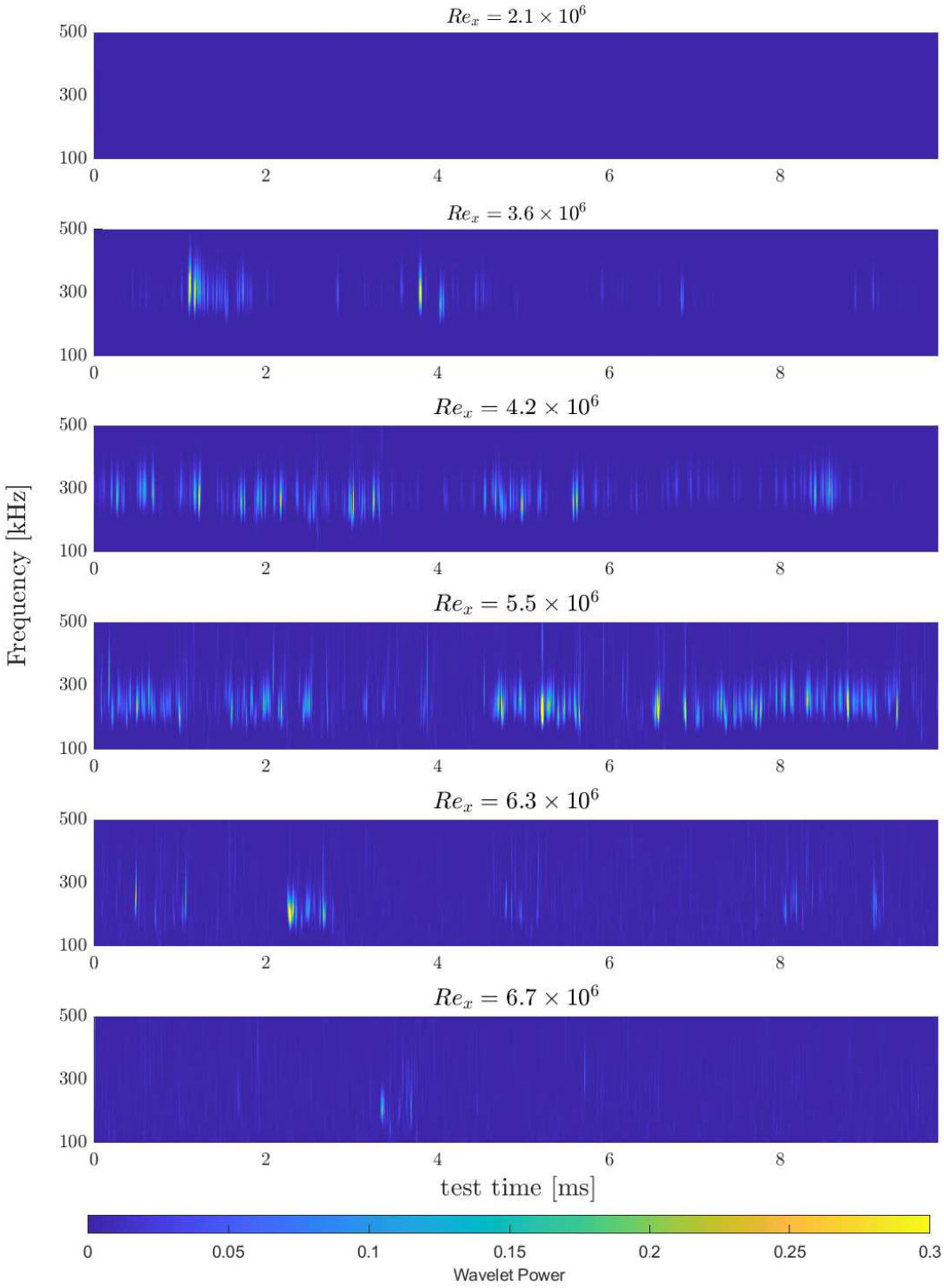


Figure 6.3: Power scalograms using the continuous wavelet transform for HDT plateau #1 at $\alpha = 0°$. The scalograms bounds are consistent, ranging from 0 to 0.3.

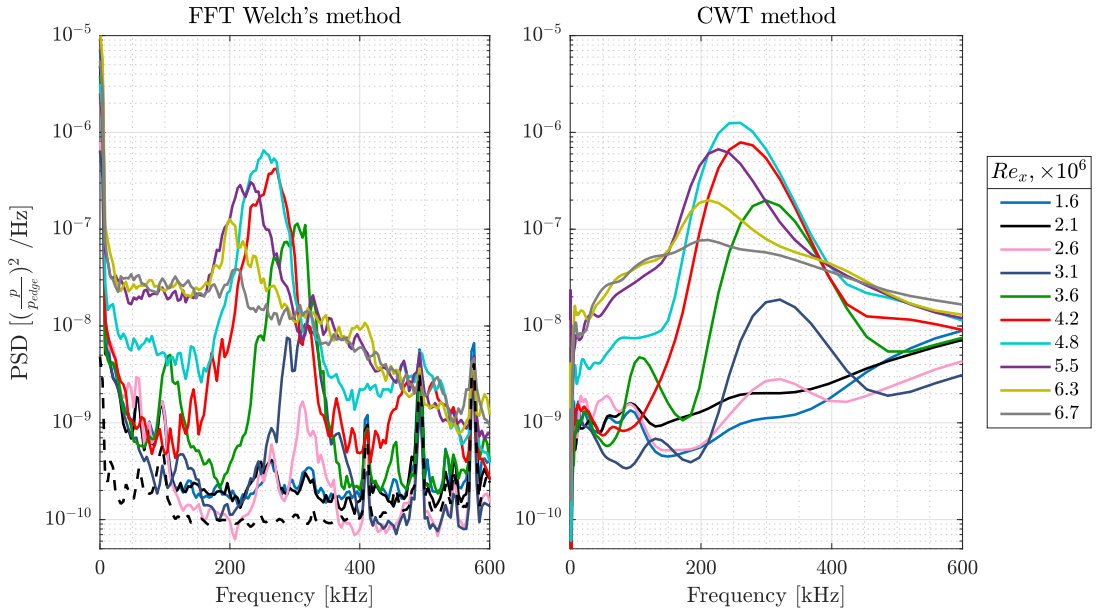


Figure 6.4: Surface pressure fluctuation power spectral density using the continuous wavelet transform and fast Fourier transforms (FFT), for HDT plateau #1 at $\alpha = 0°$.

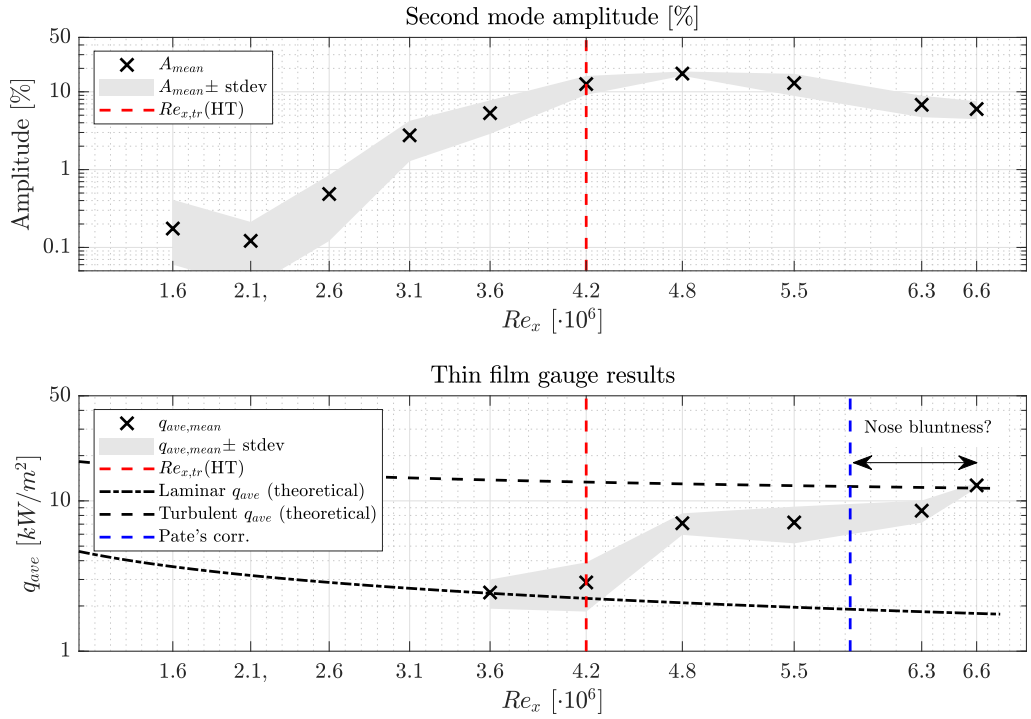


Figure 6.5: Integrated PSD and heat flux results for HDT plateau #1 at $\alpha = 0°$ The grey area shows the standard deviation of results over the five shots. The turbulent wall heat fluxes are estimated from van Driest [154], whereas the laminar wall heat fluxes are approximated using the adapted Blasius solution (described in [24]).

throat to the start of the model (L). Detailed information can be found in Ref. [127]. C_F is computed using the method of Van Driest [154]. δ^* is computed using a correlation developed from nozzle data, which requires the circumference of the wind tunnel (C) as an input. The parameters used in the HDT plateau #1 calculation are: $P_0 = 2344$ kPa, $T_0 = 523$ K, $M_\infty = 6.97$, $C = 2.350$ m, $L = 1.394$ m.

The increase in heat flux occurs at $Re_x \approx 4.2 \times 10^6$, one gauge further upstream than where the maximum second mode instability magnitude is observed ($Re_x \approx 4.8 \times 10^6$). This agrees with the observations presented by Marineau et al. in Refs. [131, 140, 54], and summarised in Section 2.5.5. It should be noted that the third thin film gauge ($Re_x = 4.8 \times 10^6$) showed a delayed response when compared to all other heat transfer gauges. For this reason, it is believed that the q_{ave} shown for TFG3 in Figure 6.5 may be slightly over-predicted for the plateau #1 results.

The transition location predicted by Pate's correlation corresponds to the end of transition, as characterised by the maximum local surface Pitot pressure for sharp cones [127, 78]. This transition location is expected to be similar to the end of the heat-transfer detected transition at high Mach numbers [78]. Figure 6.5 shows the maximum thin film gauge heat flux downstream of the location predicted by Pate's correlation, with a discrepancy of $Re_x \approx 1 \times 10^6$. The freestream disturbance levels in plateau #1 are expected to be similar to the conventional tunnels used by Pate to develop the correlation[1]. For this reason, the delay between the maximum heat flux and the transition location predicted by Pate is expected to be largely due to the stabilizing effect of nose bluntness. Future experiments using a sharp nosetip will provide a direct comparison.

[1]This assumption is based on the post-shock Pitot pressure fluctuations presented in Chapter 4, and the overlap with the data collated by Duan et al. [120].

Nosetip Reynolds number comparison to Stetson [94]

Figure 6.6 shows the HDT transition result superimposed onto the dataset from Stetson at Mach 6 using an 8° half angle cone [94, 136] (described in Section 2.7.3). The HDT result is for the condition used in this chapter: $M_\infty = 7.0$, $Re_{unit,\infty} = 12.3 \times 10^6$ /m, $T_w/T_0 = 0.59$. The result for plateau #1 is presented, due to the similar post-shock pressure fluctuation magnitudes when compared to other conventional wind tunnels [120]. For both sets of experiments, the viscosity models are matched and the transition onset location is determined by the initial deviation of the heat flux or the Stanton number from the laminar trend.

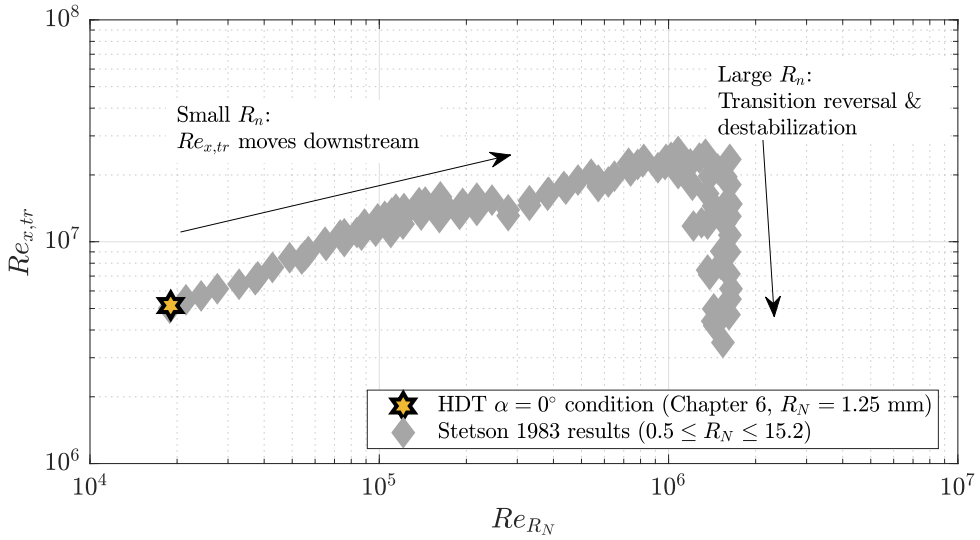


Figure 6.6: Transition Reynolds number plotted against the Reynolds number based on nosetip radius. The Stetson results are from Ref. [94], using an 8° cone at Mach 6 and various $Re_{unit,\infty}$ and R_N. The HDT result is at Mach 7, $Re_{unit,\infty} = 12.3 \times 10^6$ /m, $T_w/T_0 = 0.59$, Noise = 1.49%, $R_N = 1.25$ mm.

The HDT condition clearly lies within the small-bluntness stabilizing regime, before the transition reversal is observed in the Stetson dataset at large bluntness. Even though only one condition is compared to Stetson's dataset, the agreement is excellent (within 5%). This result highlights that even though the small nose-bluntness may cause the boundary layer to be more stable than the sharp cone case, there is no risk of transition reversal.

6.2.2 HDT Plateau #3: $T_w/T_0 = 0.64$, Noise = 0.44%

Figure 6.7 shows continuous wavelet scalogram results for HDT facility plateau #3. The presence of wavelets is delayed when compared to facility plateau #1, as the gauge at the most upstream location ($Re_x = 6.6 \times 10^6$ /m) has not decayed to turbulence. The power spectral density results for the entire test time are shown in Figure 6.4. The first sign of second mode instabilities is at $Re_x = 4.2 \times 10^6$ /m. The maximum second mode amplitude is observed at the most downstream gauges $Re_x \approx 6.3 - 6.6 \times 10^6$ /m, indicating that the boundary layer may break down to turbulence soon after. A higher harmonic of the second mode is observed in the PSD results using FFT Welch's method, for $Re_x \geq 5.5 \times 10^6$ /m.

The pressure fluctuation PSD and the thin film gauge heat flux results are summarized in Figure 6.9. The increase in heat flux occurs at $Re_x \approx 5.5 \times 10^6$, once again one gauge upstream of where the maximum second mode amplitude is observed ($Re_x \approx 6.3 - 6.6 \times 10^6$). The presence of instabilities and the rise in heat flux occur later than in HDT facility plateau #1, due to the lower freestream disturbance levels. The discrepancy between Pate's correlation[2] and the maximum heat flux measurement is larger for plateau #3 (difference in $Re_x > 1 \times 10^6$). The larger discrepancy is expected to be due to the lower post-shock pressure fluctuations measured in HDT plateau #3.

[2]The input's to Pate's correlation for HDT plateau #3 are: $P_0 = 2023$ kPa, $T_0 = 455$ K, $M_\infty = 6.96$, $C = 2.350$ m, $L = 1.394$ m.

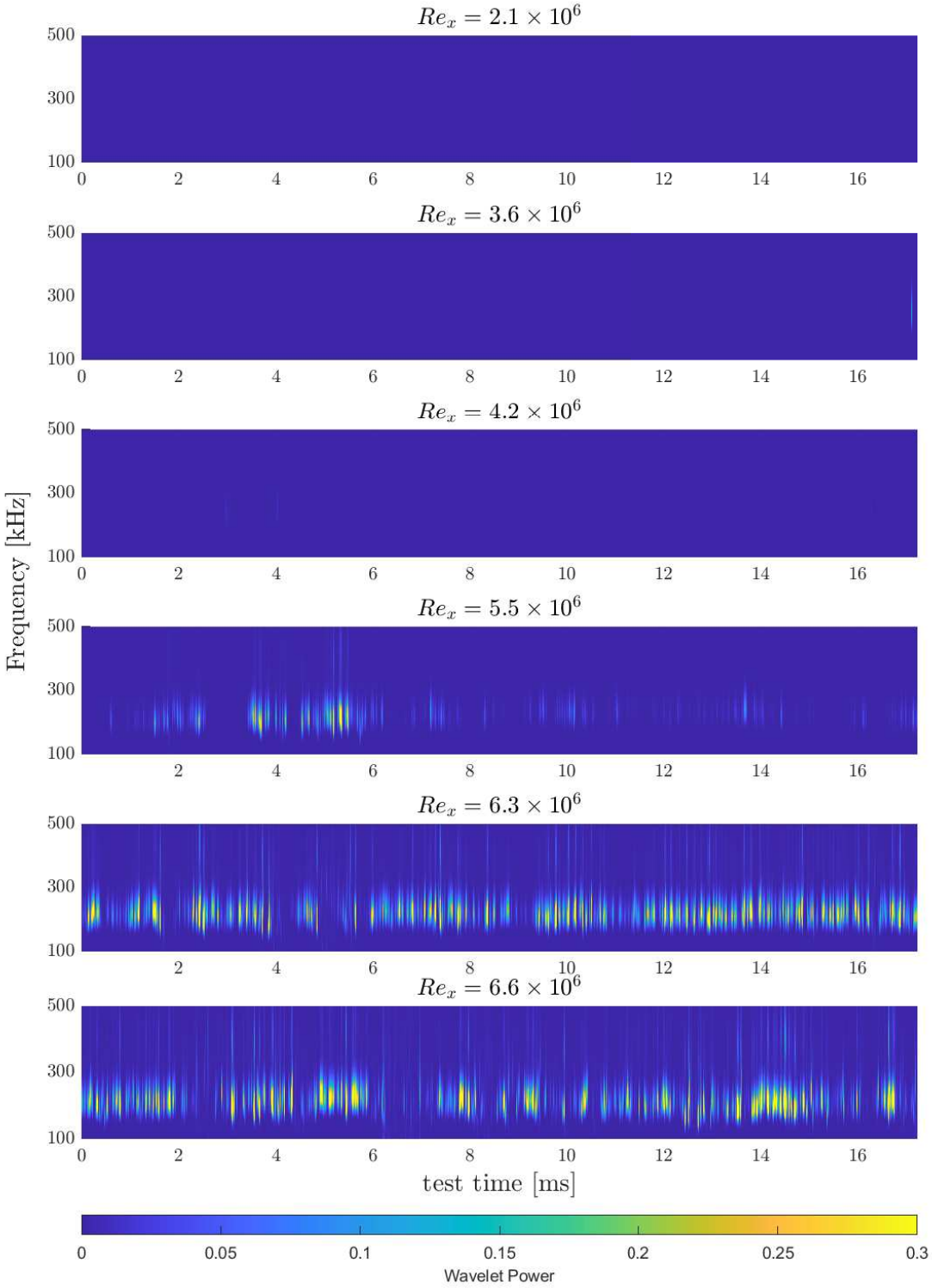


Figure 6.7: Power scalograms using the continuous wavelet transform for HDT plateau #3 at $\alpha = 0°$. The scalograms bounds are consistent, ranging from 0 to 0.3.

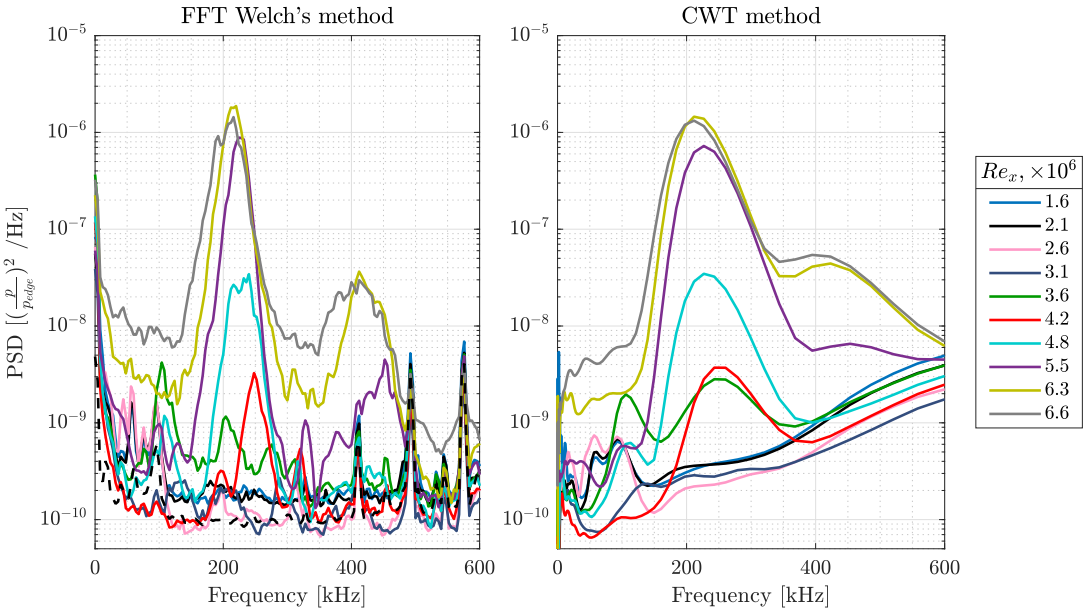


Figure 6.8: Surface pressure fluctuation power spectral density using the continuous wavelet transform and fast Fourier transforms, for HDT plateau #3 at $\alpha = 0°$.

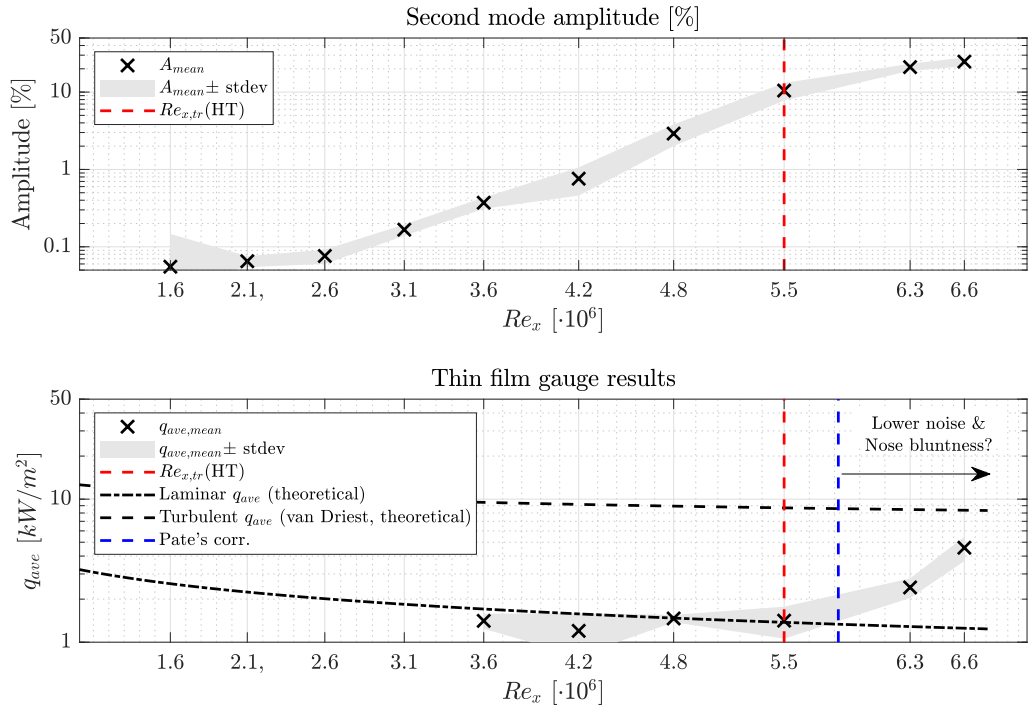


Figure 6.9: Integrated PSD and heat flux results for HDT plateau #3 at $\alpha = 0°$. The grey area shows the standard deviation of results over the five shots. The turbulent wall heat fluxes are estimated from van Driest [154], whereas the laminar wall heat fluxes are approximated using the adapted Blasius solution (described in [24]).

6.2.3 Comparison to STABL2D PSE-Chem Computations

The HDT $\alpha = 0°$ measurements for plateau #1 and #3 are compared to STABL2D PSE-Chem computations [53]. Information about the PSE-Chem setup can be found in Section 2.3.2. It is important to note that the Reynolds number is calculated using Keyes' law, and is therefore consistent with the HDT experiments. The growth rate (α) and N-factor comparisons are made using the method described by Marineau et al. [140, 54], also summarised in Section 2.5.4. Results are compared to different ground facilities in Section 6.2.4.

The PSE-computed critical N-factor envelope for HDT plateau #1 and #3 are shown in Figure 6.10. The differences in total temperatures and total pressures for each plateau do not seem to impact the N-factor envelope, with minor discrepancies only observed at $Re_x \geq 4 \times 10^6$.

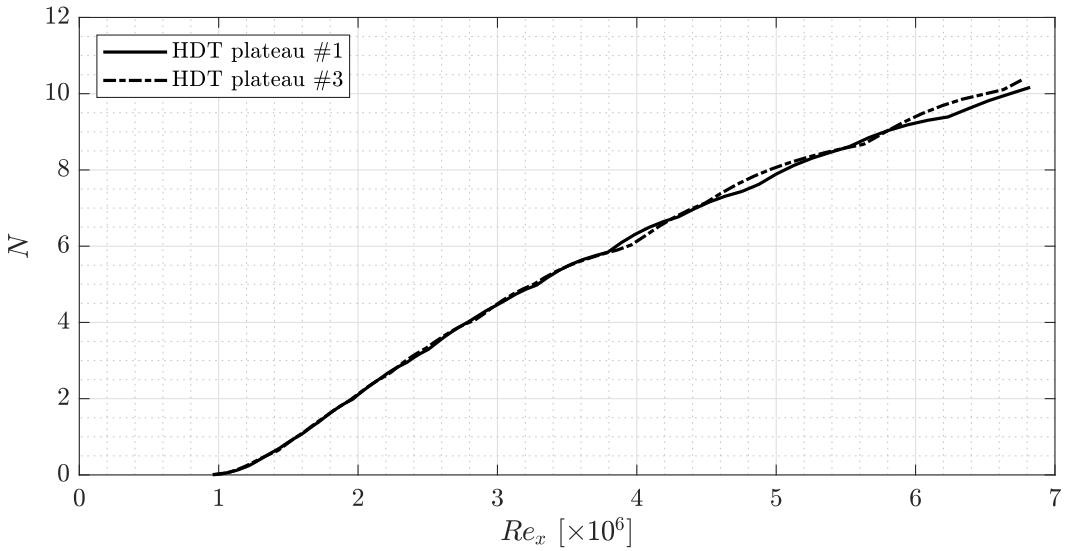


Figure 6.10: PSE-computed critical N-factor envelope for HDT plateau #1 and #3.

Disturbance frequencies

The PSE-predicted disturbance frequencies are compared to the second mode frequencies observed in the HDT experiments. The estimated frequency using Howarth's boundary layer thickness approximation is also included for both plateaus [84], as described in Section 2.5.2. Comparisons are only made for sensor locations where a second mode peak is clearly observed. Results are shown for both HDT facility plateaus in Figure 6.11.

HDT plateau #3 results show excellent agreement with the PSE predicted frequencies, with a discrepancy less than 5%. The CWT and PSD results suggested that the second mode disturbance did not break down to turbulence at the final sensor location. The disturbance frequency agreement between PSE and experiments is therefore reassuring, as the second mode growth is always within the modal growth regime.

HDT plateau #1 shows excellent agreement with the PSE frequencies over $3.5 \leq Re_x \times 10^6 \leq 4.8$, with a discrepancy always less than 4%. The HDT measured disturbance frequencies shift to lower values after the maximum second mode amplitude is reached, at $Re_x \approx 4.8 \times 10^6$. The discrepancy is expected to be due to the non-linear interactions and boundary layer decay that occurs after the maximum second mode amplitude is reached, both of which are not predicted by the linear PSE computations. The frequency estimated using Howarth's method is consistently slightly larger than the PSE-Chem and experimental disturbance frequency. This may be due to the sharp-cone assumptions made in the Taylor-Maccoll computations [84]. Nevertheless, the agreement is still very good, with a discrepancy always within 8% in the modal growth region.

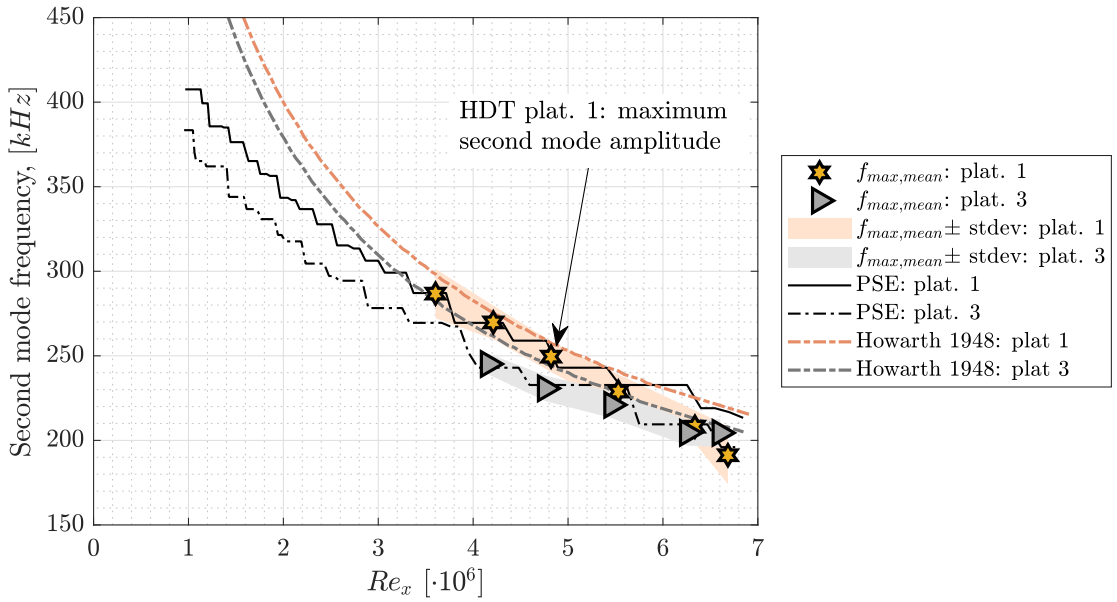


Figure 6.11: PSE-computed disturbance frequencies compared to second mode frequencies measured in HDT for plateau #1 and #3. The predicted frequencies using Howarth's boundary layer thickness approximation is also included [84].

N factors and growth rate

The HDT experiments are compared to PSE-computed N factors using the method outlined in Marineau et al. [140, 54] and Section 2.5.4. Reproduced for convenience, the experimental N factors are calculated according to

$$N(s) = \ln(\mathrm{A}(s)e^b/c) \tag{6.1}$$

Where: b is calculated from the PSE N factor envelope ($N = \alpha R + b$), c is a constant from the experiment-fitted exponential growth equation ($A = ce^{dR}$), and R is the stability Reynolds number ($R = \sqrt{Re_x}$). Results will be plotted as a function of Re_x, for consistency with previous results and because no comparisons are made to other facilities in this subsection.

The PSE calculated growth rate ($\alpha = dN/dR$) is compared to the growth rate from the exponential fit of second mode amplitudes ($d = dA/dR$) in Figure 6.12.

The experimental growth rates are obtained from the line of best fit between $2.1 \leq Re_x \times 10^6 \leq 4.8$ at plateau #1 and $3.6 \leq Re_x \times 10^6 \leq 6.6$ at plateau #3. These ranges are chosen so that only the modal growth of the second mode disturbance is included. There is excellent agreement for both plateaus, with the discrepancy in growth rate being less than 3%. It is clear that both trendlines capture the second mode modal growth region quite well.

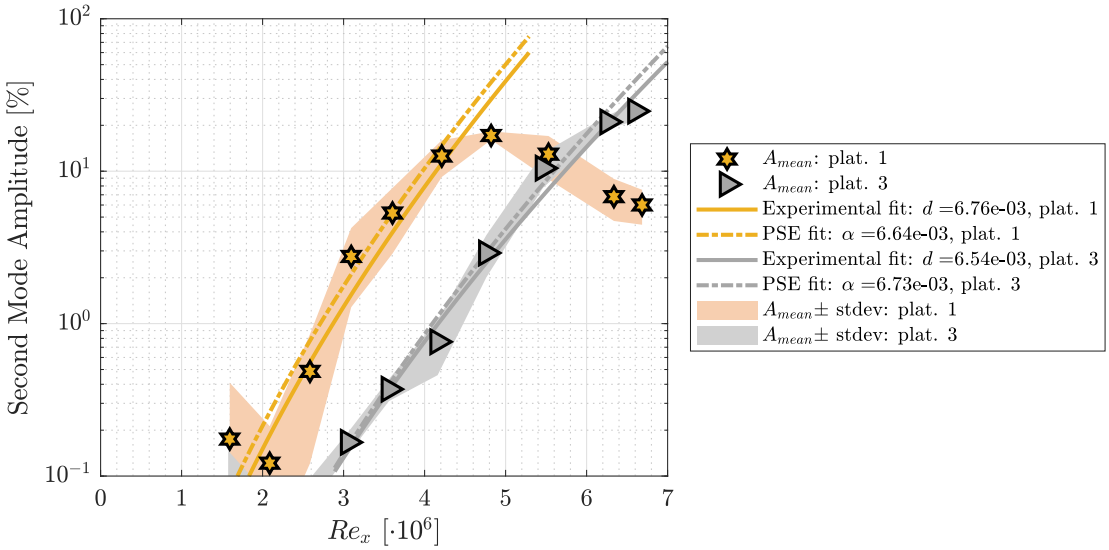


Figure 6.12: Comparison of the HDT experiment growth rate fit (d) and the PSE-computed growth rate (α) for both HDT plateaus.

The HDT experimental N-factors are compared to PSE computations in Figure 6.13. Results for both plateaus show good agreement with the PSE N-factor envelope. The maximum discrepancy is 13% for plateau #1 and 10% for plateau #3, for sensors in the assumed modal growth region. The deviation in the low Re_x limit is expected to be due to the high electrical noise levels. HDT facility plateau #1 reaches a critical N factor of 7.2, at $Re_x = 4.8 \times 10^6$. This occurs one gauge further downstream than the heat-transfer detected transition onset location ($Re_{x,tr} = 4.2 \times 10^6$, $N_{crit,HT} = 6.5$).

The HDT plateau #3 results at the nominal condition ($Re_{unit} = 12.30 \times 10^6$ /m) follow the PSE N-factor envelope closely, however it is not clear if the

final sensor location corresponds to the critical N factor. To capture results further downstream, a shot was processed at a higher Re_{unit} condition. The T_w/T_0, Noise (%), and M_∞ are unchanged from the nominal condition, so the N factor results is expected to complement the results from the nominal condition[3]. The initial amplitude, A_0, was scaled to account for the change in Re_{unit} using the relationship proposed by Marineau et al.[54],

$$A_0 \sim (Re_{unit} L_{nozzle})^{-1} \tag{6.2}$$

The high Reynolds number result is included in Figure 6.13. The extension at higher Re_x suggests that the deviation observed in the nominal plateau #3 results correspond to the critical N factor. The HDT plateau #3 critical N factor is therefore assumed to equal 9.4, occurring at $Re_x = 6.3 \times 10^6$. It is once again observed one sensor downstream of the heat-transfer detected transition onset location ($Re_{x,tr} = 5.5 \times 10^6$).

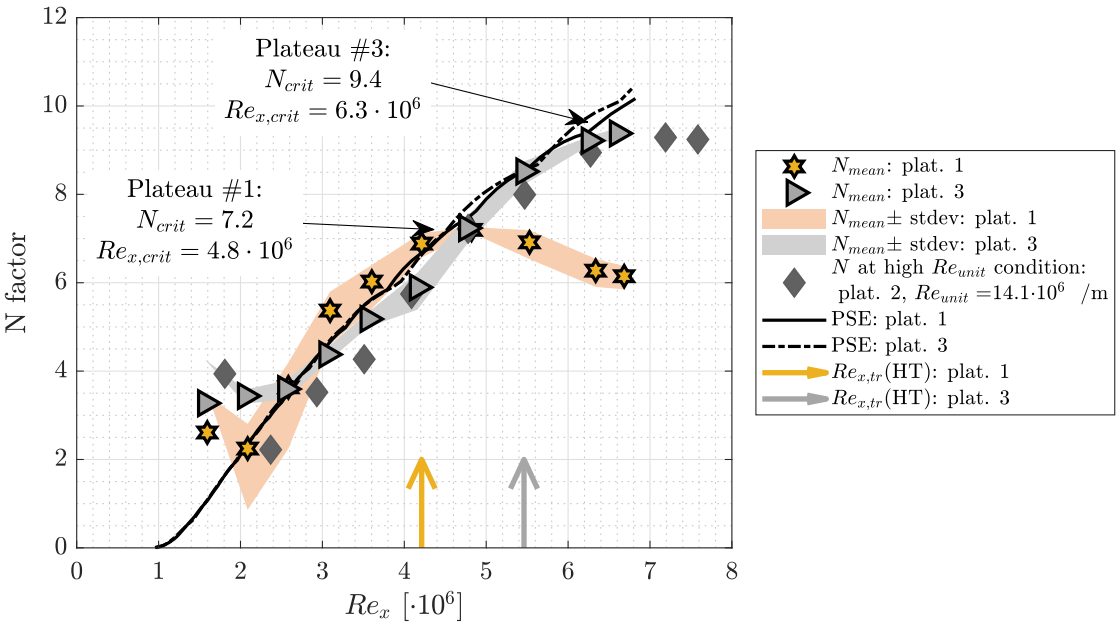


Figure 6.13: Comparison of the HDT experimental N factor and the PSE-computed N-factor for both HDT plateaus.

[3]The conditions for the high Reynolds number shot is: $T_0 = 452$ K, $P_0 = 2292$ kPa, $M_\infty = 7.0$, $Re_{unit} = 14.1 \times 10^6$ /m, Noise = 0.42%.

6.2.4 HDT comparison to HWT-8, NASA LaRC-20inch and HLB

The HDT N factors are compared to results from multiple conventional tunnels at similar Mach numbers in Figure 6.14. This includes the NASA Langley Research Center's 20inch Wind Tunnel ("LaRC-20in", $M_\infty = 6, Re_{unit,\infty} = 6.8 - 13 \times 10^6$ /m, R_N sharp), the Hypersonic Ludwieg Tube Braunschweig ("HLB", $M_\infty = 6, Re_{unit,\infty} = 5 - 16 \times 10^6$ /m, R_N sharp), and the Sandia National Laboratories (SNL) Hypersonic Wind Tunnel ("HWT-8", $M_\infty = 8, Re_{unit,\infty} = 4.1 - 13 \times 10^6$ /m, R_N sharp). Each of the datasets have been extracted from Figure 10 d) - f) in Ref. [54], and were obtained using a sharp nosepiece. The measurements agree quite well with the PSE N factor envelope for each Mach number, and reach a critical N factor in the order $\approx 6 - 8$.

The initial increase in N factor occurs at higher R for the HDT results ($R = \sqrt{Re_x}$), with a delay of $R \approx 500$. This is expected to be due to the larger stability Reynolds number at the neutral point (R_0). The HDT PSE-computed R_0 values ($R_0 = -b/\alpha$) are compared to the dataset collated by Marineau et al. in Figure 6.15. The magnitudes are significantly greater for the HDT cases presented in this research, most likely due to the stabilizing effect of nose bluntness. This suggests that a higher Reynolds number is required in the HDT experiments before disturbances start to be amplified. The resulting delay in the rise of N factor is shown by the annotation in Figure 6.14.

The HDT plateau #1 critical N factor ($N_{crit} = 7.2$) lies within the Mach 6 and Mach 8 conventional tunnel results, all of which are in the order of $N_{crit} \approx 6 - 8$. This is reassuring, as there was good agreement between the HDT plateau #1 post-shock Pitot pressure fluctuation magnitudes and those of HLB, HWT-8, and NASA LaRC-20in (collated by Duan et al. in Ref. [120] and compared in Section 4.3.2). The freestream disturbance magnitudes were significantly lower in HDT plateau #3 (see Figure 4.8). This is expected to be the main cause for the higher critical N

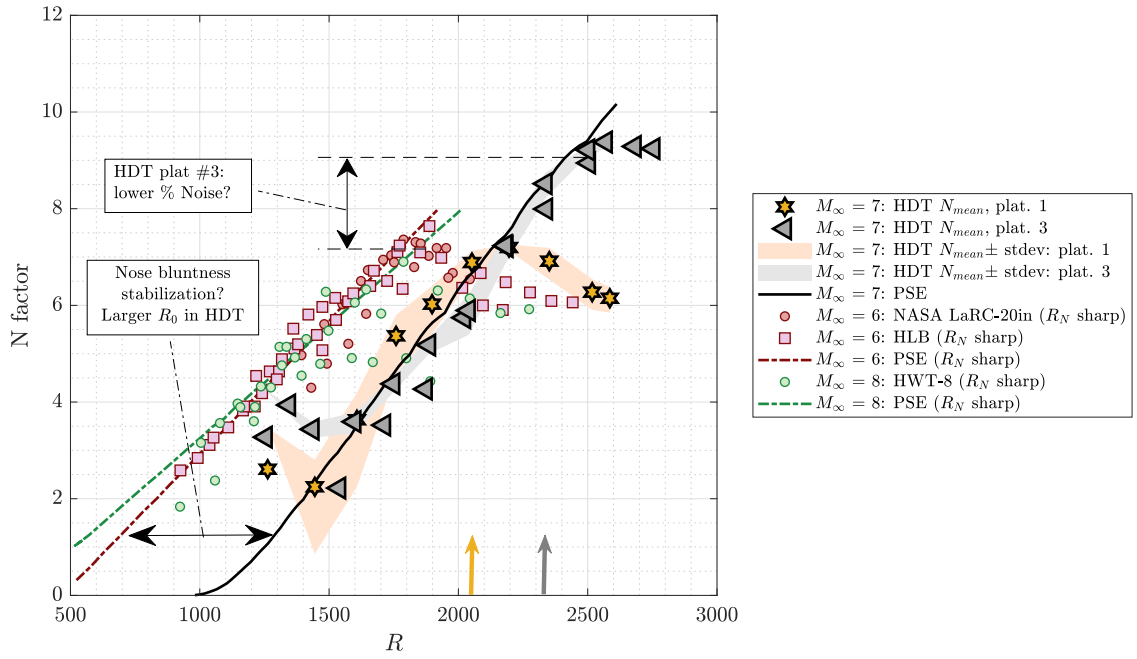


Figure 6.14: Comparison of N factors between HDT, NASA Langley Research Center's 20inch Wind Tunnel (NASA LaRC), the Hypersonic Ludwieg Tube Braunschweig (HLB) and the Sandia National Laboratories Hypersonic Wind Tunnel (HWT-8). Annotations have been included to show key features. The LaRC, HLB, and HWT-8 results are using a sharp nosepiece, with each dataset extracted from Ref. [54]. The yellow and grey arrows show the HT-detected transition locations for HDT plateau #1 and #3 , respectively.

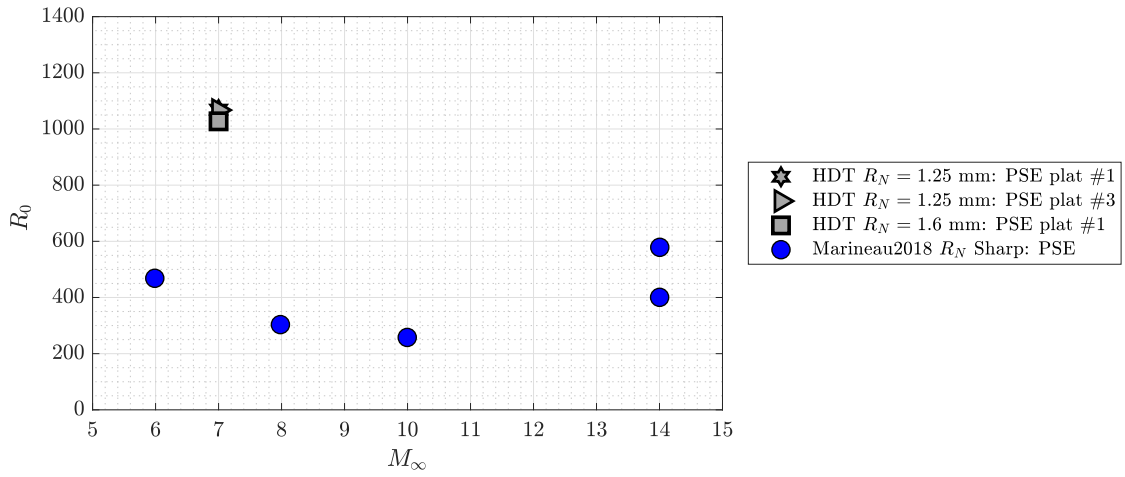


Figure 6.15: Comparison of the stability Reynolds number (R_0) to conventional wind tunnel results presented by Marineau et al. [54].

factor observed ($N_{crit} = 9.4$).

The small bluntness in the HDT 7° cone model is expected to stabilize the boundary layer when compared to the Marineau dataset. This has likely caused the R_0 delay described above, however it is not clear whether the N factor amplitudes are also affected. Future experiments in the HDT will use a sharp nosetip, so that a direct comparison can be made to the Marineau dataset and the effect of nose bluntness can be isolated.

6.2.5 Maximum second mode amplitudes

Figure 6.16 shows the maximum second mode amplitudes from the HDT campaigns superimposed onto the dataset collated by Fedorov [95] and Marineau et al. [54]. The maximum amplitudes measured in the HDT verification campaign ($R_N = 1.6$ mm, Chapter 4) and the H2K experiments from Ref. [37] are also included. The HDT results all agree with the maximum levels observed in conventional tunnels at similar edge Mach numbers (LaRC, HLB, HEG, HIEST, HWT-8 region). The A_{max} values range from 17% - 30% in the HDT, whereas a spline fit of the published conventional tunnel results predicts a range of A_{max} from 17% - 26%.

The maximum amplitudes for HDT plateau #3 ($A_{max} \approx 23\% - 30\%$) are clearly greater than those at HDT plateau #1 ($A_{max} \approx 17\% - 21\%$). This is expected to be due to the lower freestream turbulence levels measured at the later plateau, as less disturbances from the environment are contributing towards the destabilization of the boundary layer.

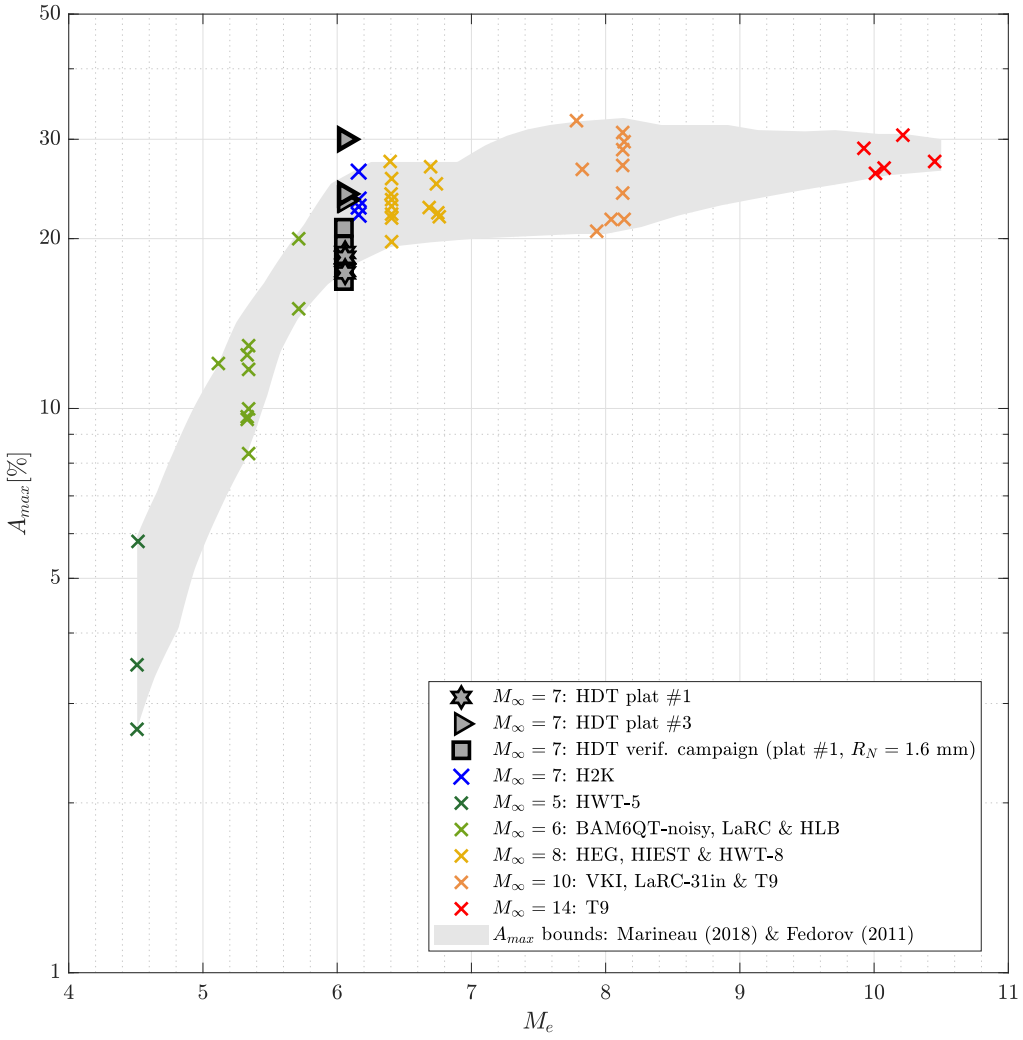


Figure 6.16: Comparison of the HDT maximum second mode amplitude to conventional wind tunnel results collated by Marineau et al. [54] and Fedorov [95].

6.3 T4 Stalker tunnel: low T_w/T_0, $\alpha = 0°$

Boundary layer instability measurements are obtained using the $R_N = 1.55$ mm nosepiece, for the front segment of the RST 7° cone model. Results are presented at a sweep of Reynolds number and for multiple T_w/T_0 distributions. The facility conditions are calculated using ESTCj [62], assuming chemical and temperature equilibrium at the relatively low enthalpies targeted in this campaign [204]. Section 3.3 provides further information about the T4 Stalker Tunnel. An overview of the facility conditions is given in Table 6.2.

The nominal condition for this research is the high Reynolds number condition with a constant T_W/T_0. Boundary layer instability results are presented for the T4 nominal condition, before assessing the effect of wall temperature distributions and facility Reynolds numbers. All non flow representative transient events were removed from the dataset, using the method described in Section 3.7.2.

Parameter	Nominal condition (High Re)	Mid Re	Low Re
P_0 (MPa)	34.3	27.1	18.4
T_0 (K)	2220	2370	2440
H_0 ($MJkg^{-1}$)	2.3	2.5	2.6
M_∞	7.1	7.0	7.0
$Re_{unit,\infty}$ ($\times 10^6$)	11.0	8.2	5.3
T_w/T_0	0.13 - 0.19	0.12 - 0.18	0.12 - 0.18
Segment duration (ms)	1	1	1
Diaphragm thickness (mm)	4	3	2

Table 6.2: T4 condition for $\alpha = 0°$ results. The quoted facility values are the average of all shots at each condition.

6.3.1 T4 Nominal condition: $Re_{unit} = 11 \times 10^6$ /m, T_w/T_0 const.

A progression of continuous wavelet scalogram results for successive PCB132 sensors is presented in Figure 6.17. No wavelets are resolvable in the upstream gauges ($Re_x \approx 1.3 \times 10^6$). For the final two sensor locations ($Re_x \geq 2.7 \times 10^6$), the wavelet coefficient power increases and the packets occur more frequently in the test-time. The potential disturbance is observed at relatively high frequencies ($f \approx 700 - 900$ kHz) and at relatively small wavelet coefficient powers (max. power ≈ 0.2) when compared to the HDT results ($f \approx 200 - 300$ kHz, max. power ≈ 0.7). It is therefore possible that the high frequency wavelet content represents the early stage of second mode growth.

Power spectral density results are shown in Figure 6.18, comparing Welch's method to the CWT method. For the PSD using Welch's method, the fluctuation data for four repeated shots have been concatenated to increase the segment length. The peak observed at 300 kHz for each gauge is the PCB132 sensor resonance. A peak is resolvable at $f \approx 725 - 790$ kHz in the power spectra for the two downstream sensors, $Re_x \geq 2.6 \times 10^6$. The peak increases in amplitude and decreases in frequency, potentially indicating the modal growth of a disturbance. There is no sign of broadband power increase or decay to turbulence. This may suggest that further disturbance growth would be expected. The PSD results agree with the observations made in the wavelet scalograms.

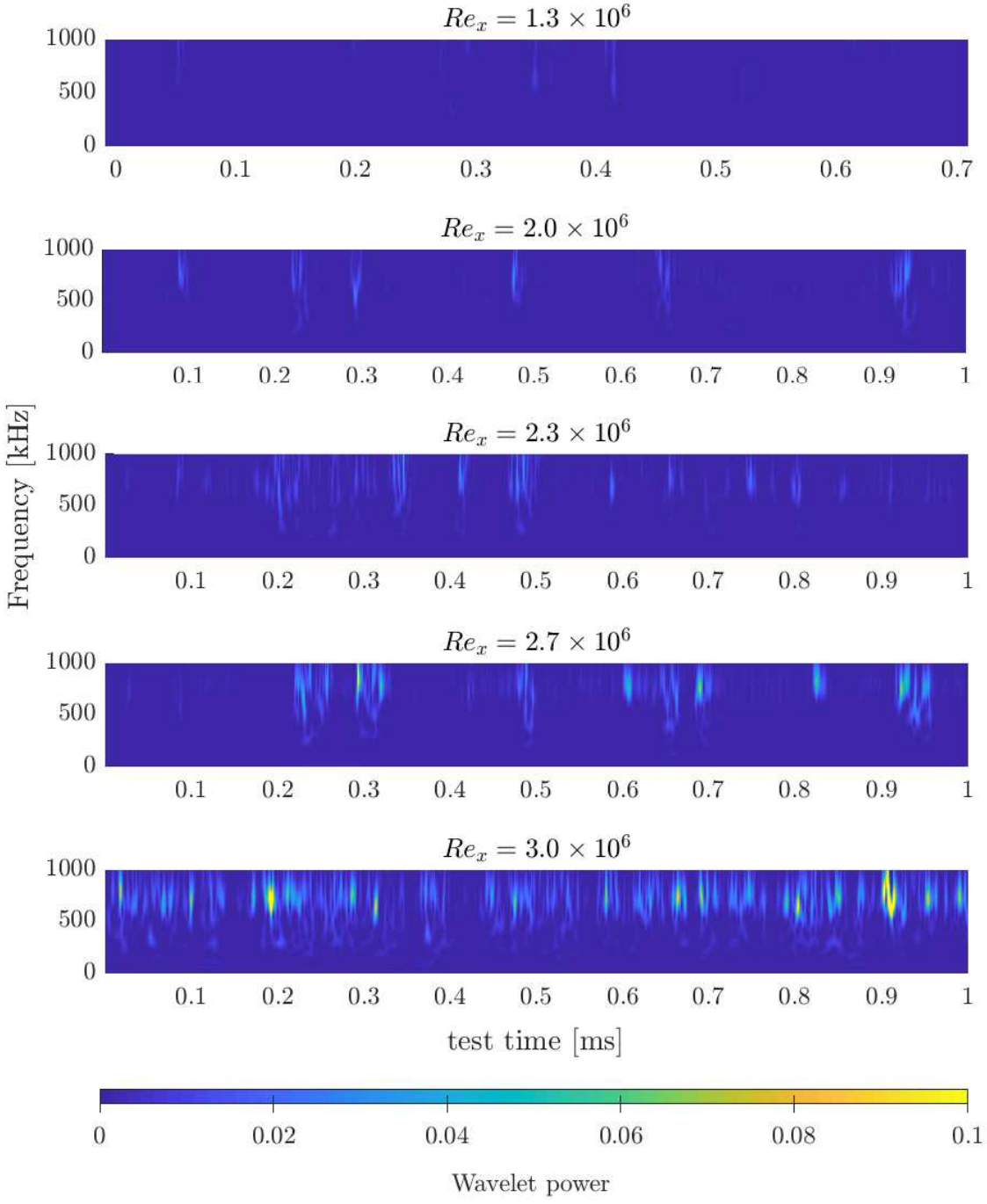


Figure 6.17: Power scalograms using the continuous wavelet transform for the T4 Nominal condition: $M_\infty = 7.1$, $Re_{unit,\infty} = 11.9 \times 10^6$ /m, $T_w/T_0 = 0.13$, $\alpha = 0°$, $R_N = 1.55$ mm. The scalograms bounds are consistent, ranging from 0 to 0.1.

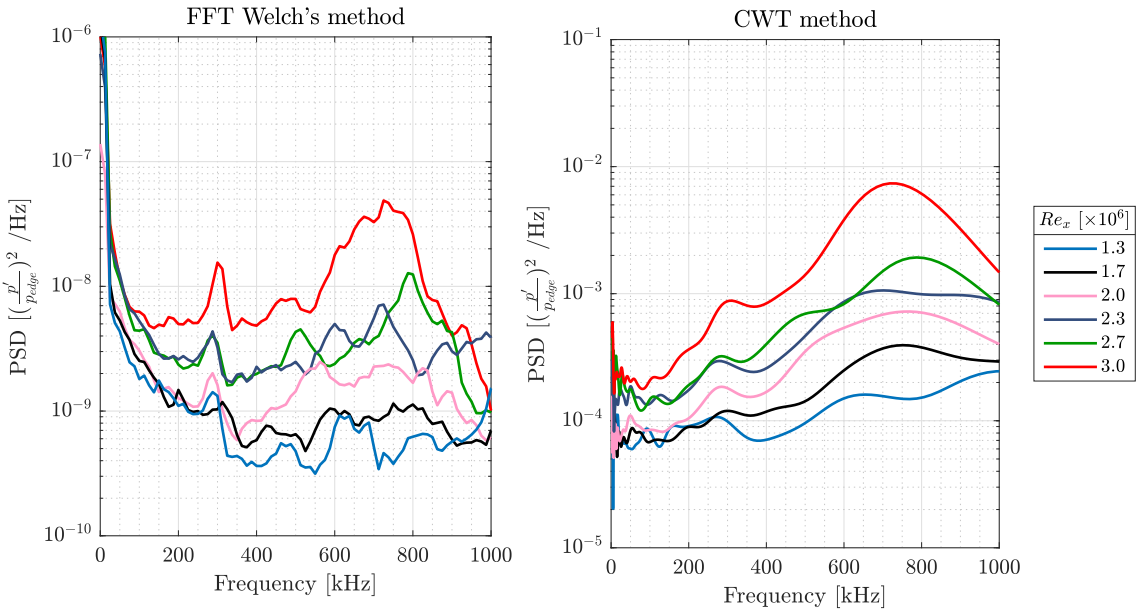


Figure 6.18: Surface pressure fluctuation power spectral density using the continuous wavelet transform and fast Fourier transforms, for the T4 nominal condition: $M_\infty = 7.1$, $Re_{unit,\infty} = 11.9 \times 10^6$ /m, $T_w/T_0 = 0.13$, $\alpha = 0°$, $R_N = 1.55$ mm. The Welch PSD is calculated using the fluctuation data for four repeated shots.

The integrated PSD for the T4 nominal condition is shown in Figure 6.19. The standard deviation is calculated from four shots at repeated conditions. The PSD is integrated about the central disturbance frequency (f_c) for the final two sensors. For $Re_x \leq 2.3 \times 10^6$, no clear peak is observed in the power spectra. A disturbance frequency of $f_c = 850$ kHz is assumed for these upstream sensors, as this is slightly larger than the frequency of the first disturbance observed ($f_c \approx 800$ kHz at $Re_x = 2.7 \times 10^6$). Circle markers are used for sensors where this assumption has been made.

The amplitude clearly increases as a function of Re_x, up to a maximum of $A_{max} = 8.1\%$ at $Re_x = 3.0 \times 10^6$. Measurements collated by Marineau et al. suggest that the maximum second mode amplitude before breakdown is in the order of $A_{max} = 20\% - 30\%$ [54]. If the observed peak is a second mode, the relatively low T4 A_{max} value indicates that only the early stages of growth has been captured.

The growth rate is different over the earlier portion of the cone, as the gradient noticeably increases once a peak in the PSD is first observed at $Re_x = 2.7 \times 10^6$. This may indicate that the assumed central frequency for integration purposes ($f_c = 850$ kHz) is not accurate. The PSE calculated growth rate[4] ($\alpha = dN/dR$) is compared to the exponential fit of second mode amplitudes ($d = dA/dR$) in Figure 6.19. The PSE-Chem growth rate, α, was calculated assuming a linear N-factor envelope over the range of Re_x covered in the T4 test campaign ($N = \alpha R + b$, see Figure 6.25). The experimental growth rate was calculated from the final two sensors[5].

The experimental growth rate for the final two sensors agrees with the PSE-Chem value, to within 5%. This suggests that the final two gauges may represent the beginning of the modal growth of the second mode. Due to the lack of sensors used to form the experimental best fit, it is clear that measurements further downstream are required to establish confidence in this result, and to generate meaningful N factor results.

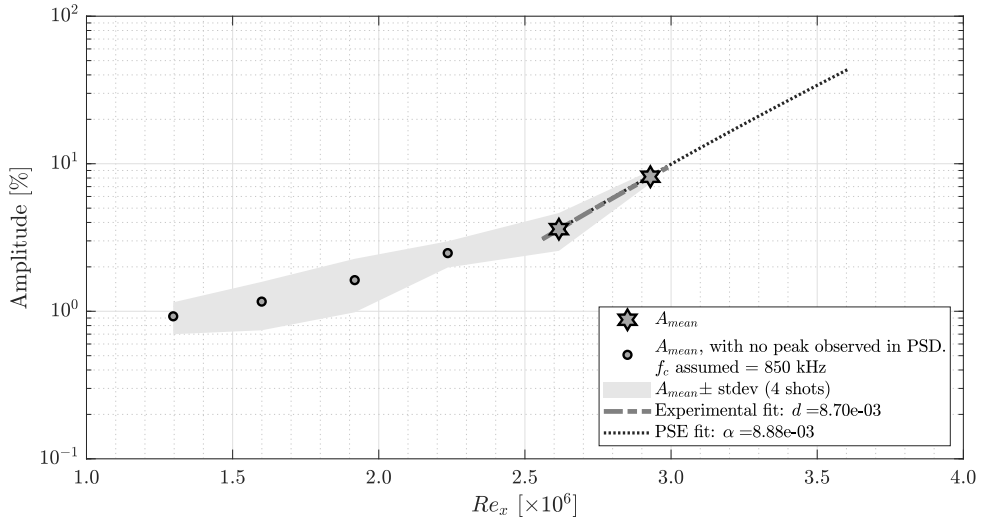


Figure 6.19: Mean integrated PSD amplitude for the T4 nominal condition: $M_\infty = 7.1$, $Re_{unit,\infty} = 11.9 \times 10^6$ /m, $T_w/T_0 = 0.13$, $\alpha = 0°$, $R_N = 1.55$ mm.

[4]See Section 2.3.2 for information about the PSE-Chem setup and assumptions made for the T4 computations. The Reynolds number is calculated using Sutherland's law for viscosity, and is therefore consistent with the T4 experiments.

[5]Both data points represent the average of eight measurements (four shots, with two separate sensors at a given location)

The peak frequencies observed at the final two sensor locations in the T4 experiments are compared to PSE-Chem computations, as well as the estimated frequency using Howarth's approximation [84]. Comparisons are not made for earlier sensors, as no clear peaks in the PSD were observed. Results are shown in Figure 6.20. The agreement between the experimentally measured peak frequency and Howarth's approximation is within 5%.

However, a large discrepancy exists ($> 30\%$) between the PSE-Chem computed disturbance frequency, and those that were measured in the experiments. The PCB132 sensors are not able to measure frequencies above 1 MHz, so if the dominant disturbance did exist at these high frequencies it would not have been resolved. The origin of the horizontal part of the predicted frequency between $Re_x = 0.2 - 1.1 \times 10^6$ is also unknown, though may be due to non-amplified disturbances when $N < 0$. Work is currently ongoing to resolve this discrepancy.

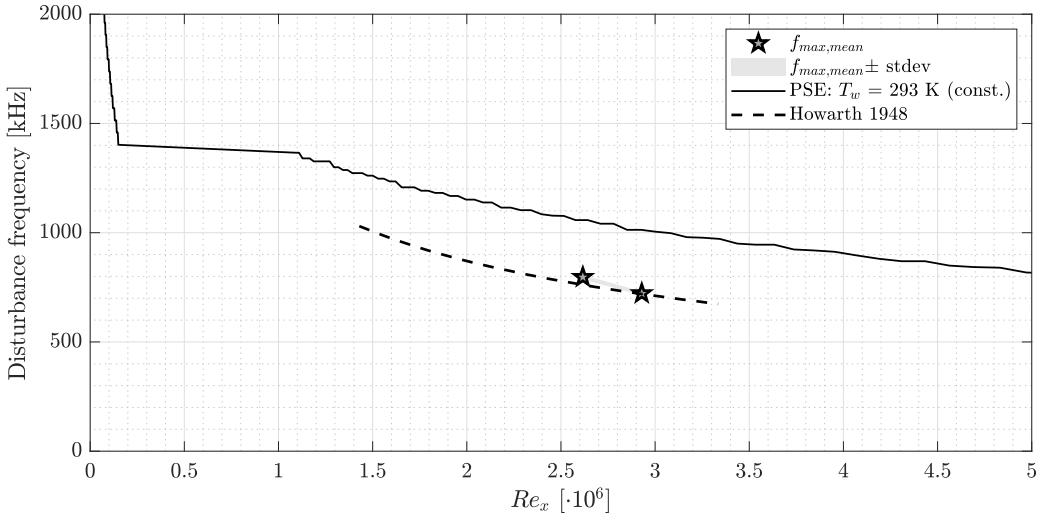


Figure 6.20: PSE-computed disturbance frequencies compared to Howarth's approximation [84] and the peak PSD frequencies measured in HDT.

6.3.2 Effect of T_w/T_0 distributions

The effect of wall temperature distributions is investigated. The wavelet scalogram and PSD is presented for the most downstream gauge ($x = 257$ mm), as it consistently had the greatest disturbance amplitude at the nominal condition. The RST 7° cone model nosepiece was heated to multiple wall-temperatures using the DC powered heater cartridge. The tested wall-temperature distributions ranged from 300 K $\leq T_w \leq$ 390 K at P = 10 W, and 300 K $\leq T_w \leq$ 425 K at P = 15 W. These distributions can be found in Figure 3.14, with details about the calibration process in Section 3.5.

Figure 6.21 shows the CWT scalogram results for the most downstream sensor for multiple wall-temperature distributions. Wave packets are visible at similar frequencies ($f \approx 700 - 900$ kHz) and amplitudes for all three temperature profiles. The high wall-temperature distribution ($T_w/T_0 = 0.13-0.19$, P = 15 W) results seem to show less frequent wave packets over the test time, and at smaller magnitudes. On the other hand, the medium wall-temperature distribution ($T_w/T_0 = 0.13-0.17$, P = 10 W) shows wave packets that are more unstable than the nominal case. These wavelet observations are consistent with the PSD results, shown in Figure 6.22, and the integrated PSD amplitude results, shown in Figure 6.23. Differences observed for the three wall-temperature distributions are therefore inconclusive and expected to be within the shot-to-shot uncertainty.

Discussion

If the observed peaks represent a second mode, linear stability theory suggests that it should be stabilized when the wall-to-total temperature ratio is increased [17] (see Section 2.7.5). There are multiple reasons why this may not have been observed in the T4 experiments:

1. It is possible that wall-heating occurred too far upstream. The wall-temperature reached $T_w \approx 425$ K at the nosepiece, however the wall had returned to

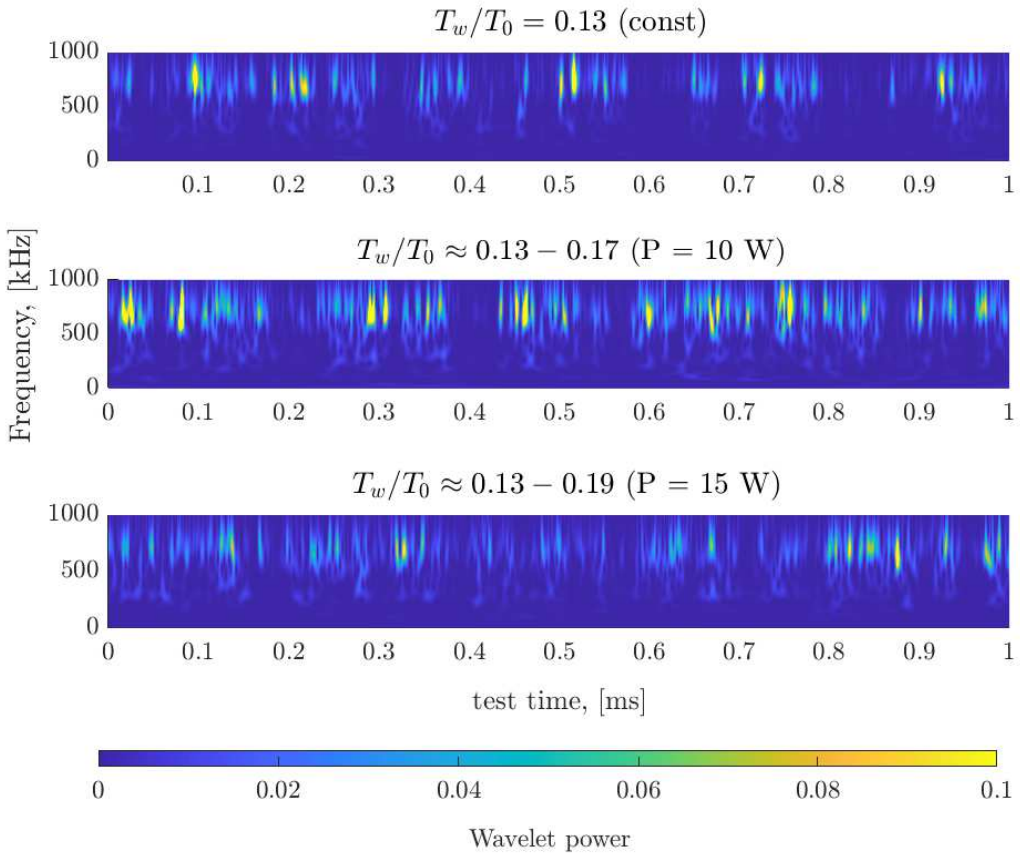


Figure 6.21: Effect of T_w/T_0 distribution on wavelet scalograms: $M_\infty = 7.1$, $Re_{unit,\infty} = 11.0 \times 10^6$ /m, $T_w/T_0 = 0.13 - 0.19$, $Re_x = 3.0 \times 10^6$, $\alpha = 0°$, $R_N = 1.55$ mm.

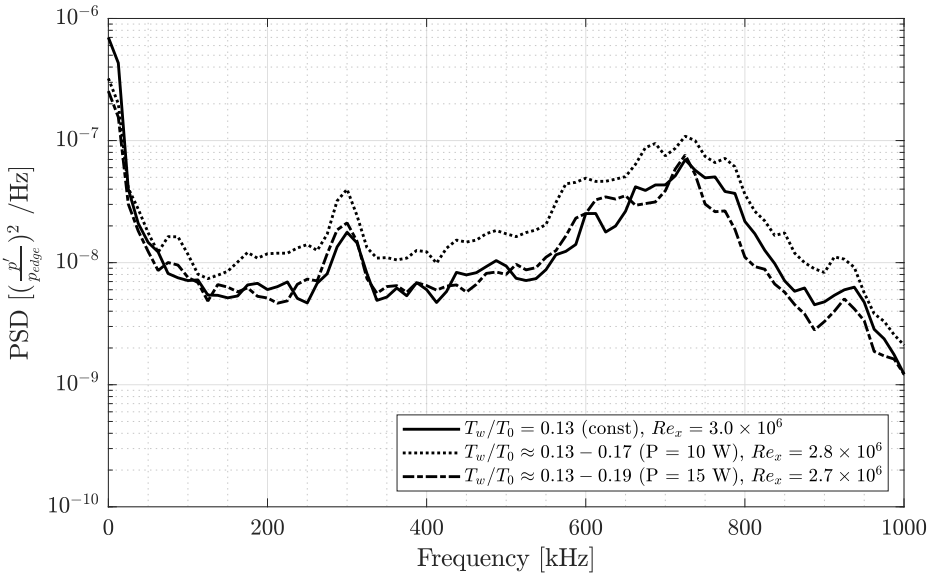


Figure 6.22: Effect of T_w/T_0 distribution on power spectral density (calculated using Welch's method): $M_\infty = 7.1$, $Re_{unit,\infty} = 11.0 \times 10^6$ /m, $T_w/T_0 = 0.13 - 0.19$, $\alpha = 0°$, $R_N = 1.55$ mm.

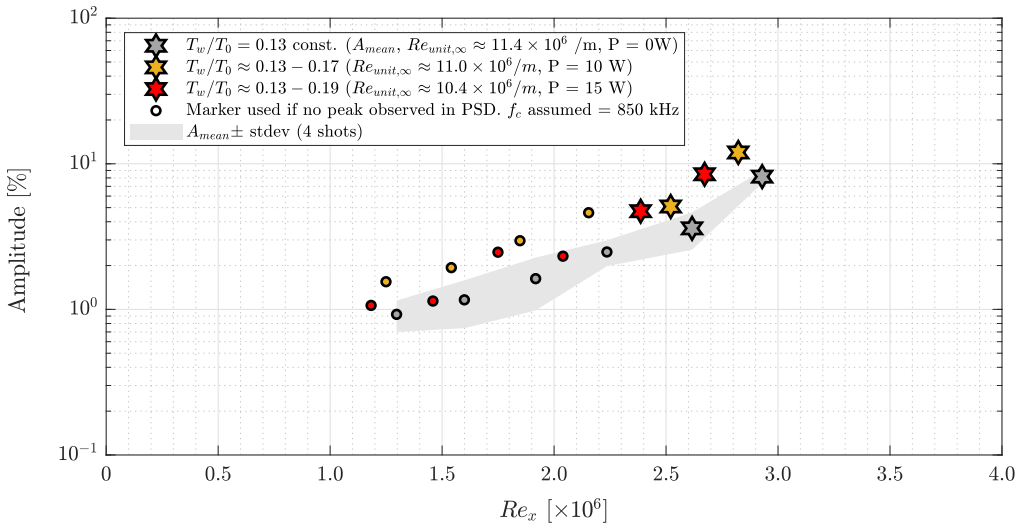


Figure 6.23: Effect of T_w/T_0 distribution on integrated PSD amplitude: $M_\infty = 7.1$, $Re_{unit,\infty} = 11.0 \times 10^6$ /m, $T_w/T_0 = 0.13 - 0.19$, $\alpha = 0°$, $R_N = 1.55$ mm. The circle markers indicate sensors where no peak was observed in the PSD ($f_c = 850$ kHz assumed).

$T_w \approx 320$ K at the sensor where a peak in the PSD was first observed ($x = 240$ mm). This suggests that the wall-heating may have affected the laminar boundary layer before disturbances are present, rather than the growth of the second mode instability itself. A schematic to illustrate this is shown in Figure 6.24.

2. The range of wall-to-total temperature ratios covered using the heater cartridge was 0.13 - 0.19. It is possible that this range was insufficient to observe clear stabilization of a second mode. This theory is supported by the PSE-Chem N-factor envelopes for each wall-temperature distribution, shown in Figure 6.25. The deviation in computed N-factor begins at $Re_x \approx 3.6 \times 10^6$, which is slightly downstream of the final sensor location ($Re_x = 3 \times 10^6$). It should also be noted that the transition results obtained by Sanator et al. did not observe any trends over this T_w/T_0 range [205], whereas the destabilization observed in the Stetson experiments occurred over the range $T_w/T_0 = 0.42 - 0.84$.

3. The peak observed may not be a second mode disturbance, and as such, would not necessarily be expected to change as a function of T_w/T_0.

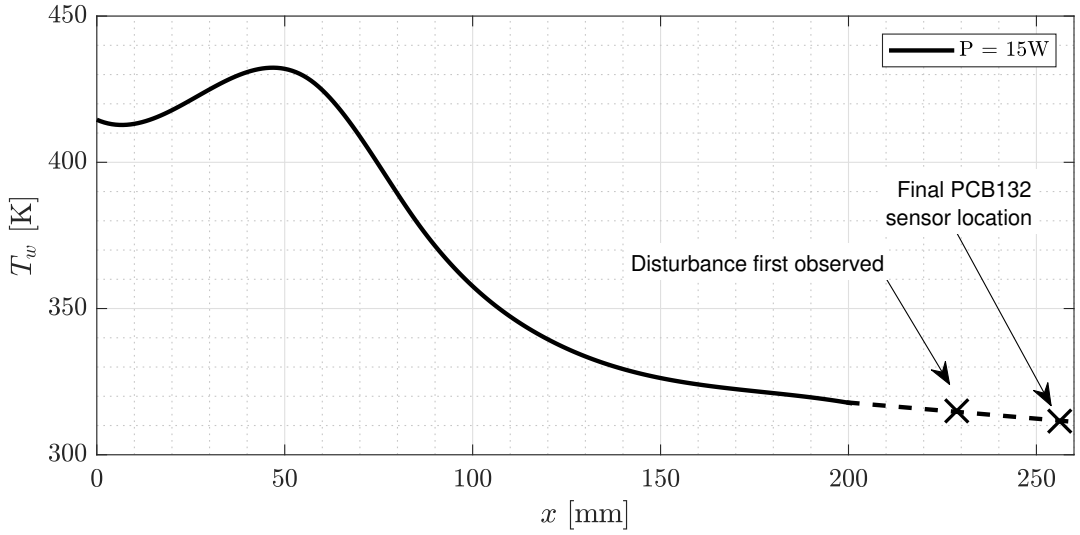


Figure 6.24: Wall temperature distribution for $P = 15$ W, including the location of the first observed peak in the PSD. $M_\infty = 7.1$, $Re_{unit,\infty} = 11.0 \times 10^6$ /m, $T_w/T_0 = 0.13 - 0.19$, $\alpha = 0°$, $R_N = 1.55$ mm.

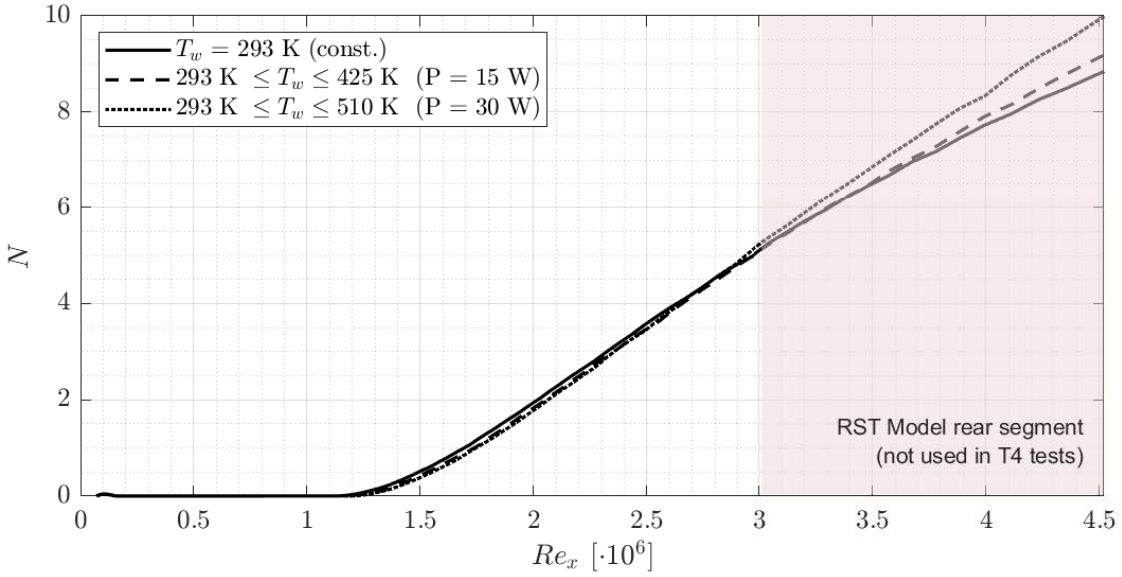


Figure 6.25: PSE-computed critical N-factor envelope for T4 nominal condition using multiple wall-temperature distributions. $M_\infty = 7.1$, $Re_{unit,\infty} = 11.9 \times 10^6$ /m, $T_w/T_0 = 0.14 - 0.19$, $R_N = 1.55$ mm.

6.3.3 Effect of Re_{unit}

The effect of facility Reynolds number is investigated. The CWT scalogram and PSD results are presented for the most downstream gauge ($x = 257$ mm). The PSD increases in amplitude with $Re_{unit,\infty}$, suggesting that the boundary layer is less stable at higher Re_x (i.e. when $Re_{unit,\infty}$ is increased at a certain location).

The peak frequency does not clearly shift as a function of $Re_{unit,\infty}$, as would be expected. For example, the anticipated disturbance frequencies can be estimated using the boundary layer thickness approximation proposed by Howarth [84], described in Section 2.5.2. The values for the High Re #, Mid Re #, and Low Re # conditions are $f_c = 740$ kHz, 640 kHz, and 540 kHz respectively. The High Re # frequency agrees very well with the peak observed in the PSD (discrepancy $< 3\%$) as shown in Figure 6.20, however the progressive decrease in disturbance frequency with $Re_{unit,\infty}$ is not apparent.

The integrated amplitudes are shown for each facility condition in Figure 6.28. In the low Re_x limit, the amplitudes tend to an amplitude of $\approx 1\%$. At $Re_{unit,\infty} = 8.1 \times 10^6$ /m, the disturbance growth occurred earlier than at the nominal condition. This is surprising, as the dataset may be expected to collapse onto a single curve for a given nose radius. One possible explanation is that the freestream noise levels were higher at the lower facility Reynolds number, and that this may have contributed to the destabilization of the boundary layer. This trend has been observed using a 7° half angle cone in the HIEST shock tunnel at Mach 8, with a similar enthalpy to T4 ($H_0 \approx 2 - 3$ MJkg^{-1}, see Section 6.3.4). The results collated by Marineau et al. also show the same trend for multiple other conventional tunnels at various flow conditions (e.g. HLB & LaRC-20in at Mach 6, T9 and HWT-14 at Mach 14) [54].

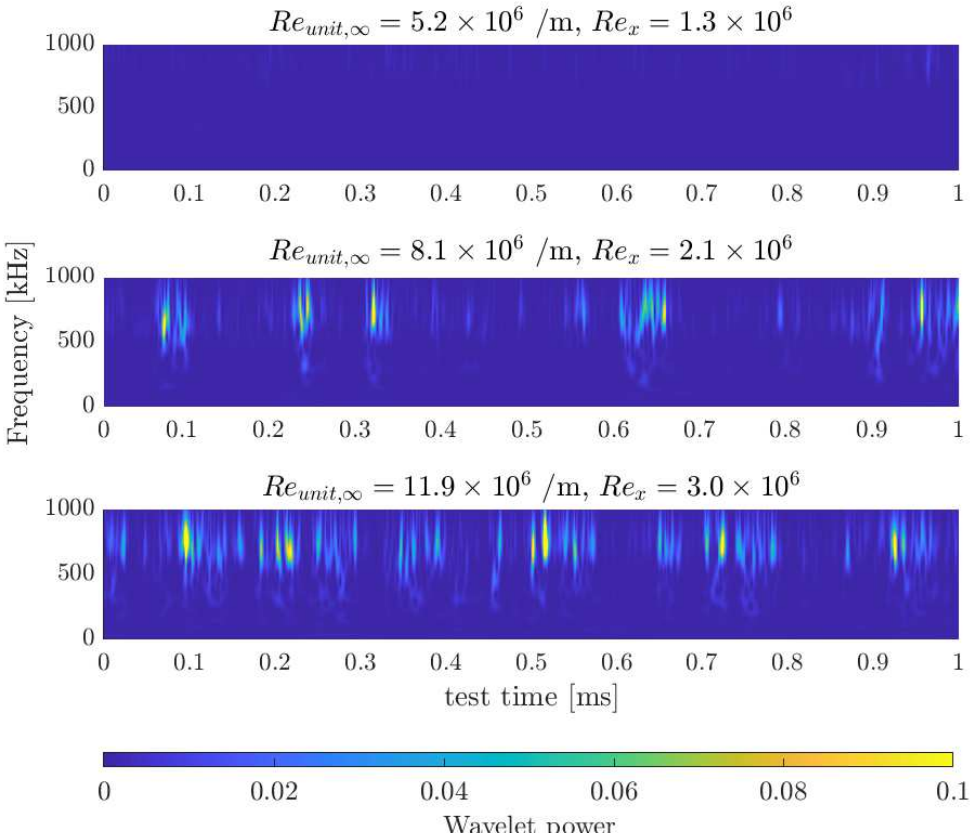


Figure 6.26: Effect of $Re_{unit,\infty}$ on wavelet scalograms: $M_\infty = 7.1$, $Re_{unit,\infty} = 5.2 - 11.9 \times 10^6$ /m, $T_w/T_0 = 0.13$, $\alpha = 0°$, $R_N = 1.55$ mm.

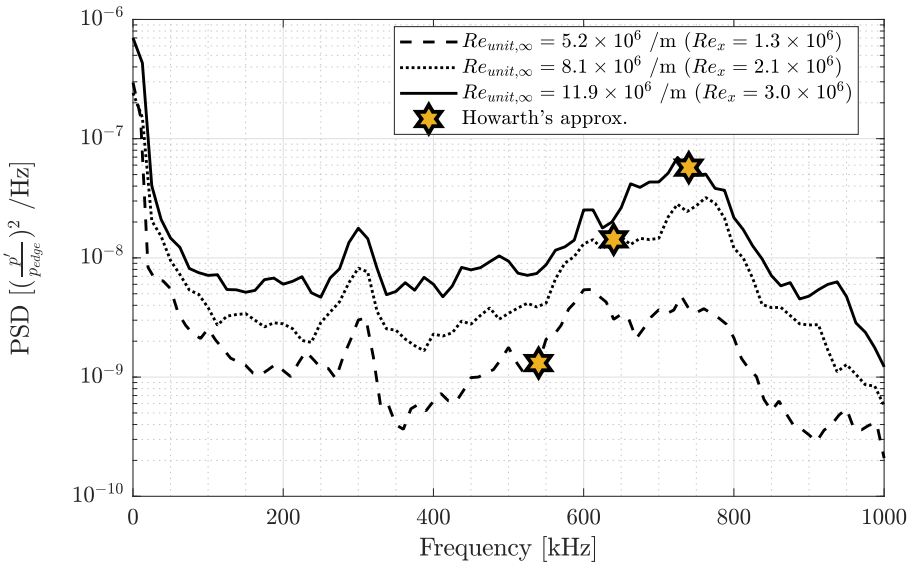


Figure 6.27: Effect of $Re_{unit,\infty}$ on power spectral density (calculated using Welch's method): $M_\infty = 7.1$, $Re_{unit,\infty} = 5.2 - 11.9 \times 10^6$ /m, $T_w/T_0 = 0.13$, $\alpha = 0°$, $R_N = 1.55$ mm. The gold markers illustrate the peak frequency predicted by Howarth's approximation [84].

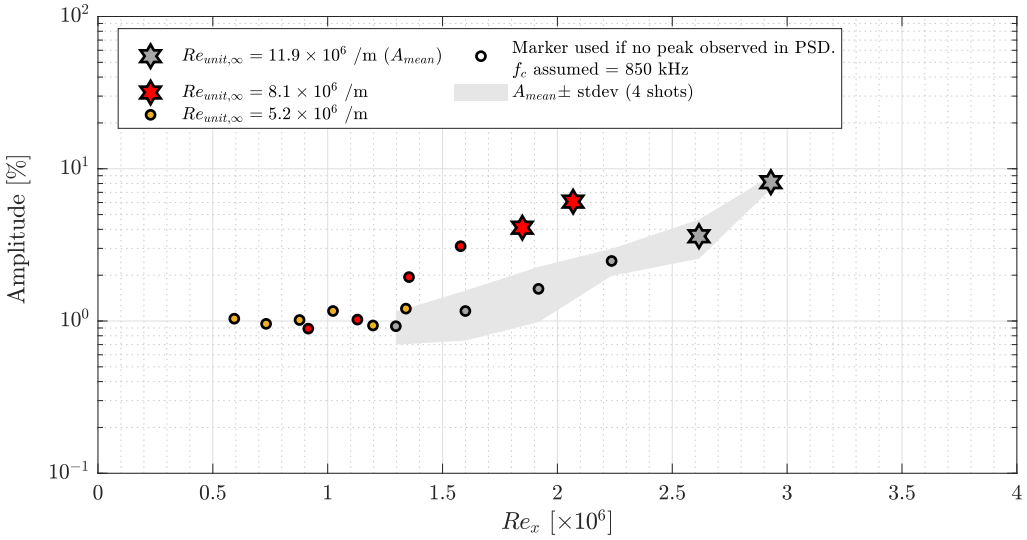


Figure 6.28: Effect of $Re_{unit,\infty}$ on integrated PSD amplitude: $M_\infty = 7.1$, $Re_{unit,\infty} = 5.2 - 11.9 \times 10^6$ /m, $T_w/T_0 = 0.13$, $\alpha = 0°$, $R_N = 1.55$ mm. The circle markers indicate sensors where no peak in the power spectra was observed ($f_c = 850$ kHz assumed).

6.3.4 T4 comparison to HEG and HIEST shock tunnels

Figure 6.29 compares the T4 integrated PSD amplitudes at three facility Reynolds numbers ($Re_{unit,\infty} = 5.3, 8.1, 11.4 \times 10^6$ /m), to measurements obtained in the HEG and HIEST shock tunnels [54]. The HEG and HIEST 7° cone models both have a nose radius of 2.5 mm, and a length of 1.1 m and 1.0 m respectively. The stagnation enthalpy is approximately constant at 3 MJ/kg in both facilities, and the facility Reynolds numbers are specified in the legend ($Re_{unit,\infty} = 1.5 - 4.8 \times 10^6$ /m).

The HEG and HIEST results reach a maximum second mode amplitude at $A_{max} \approx 20$ - 30%, whereas the maximum integrated amplitude measured in T4 was 8.1% (decay to turbulence was not observed in T4). For the HIEST results, the increase in disturbance amplitude occurs earlier as the facility Reynolds number is decreased from $Re_{unit,\infty} = 4.8 \times 10^6$ /m to $Re_{unit,\infty} = 3.3 \times 10^6$ /m. A similar trend is observed in the T4 results, when comparing the $Re_{unit,\infty} = 8.1 \times 10^6$ /m results to $Re_{unit,\infty} = 11.5 \times 10^6$ /m. Marineau et al. suggest that this may be due to increased freestream disturbance levels at lower facility $Re_{unit,\infty}$.

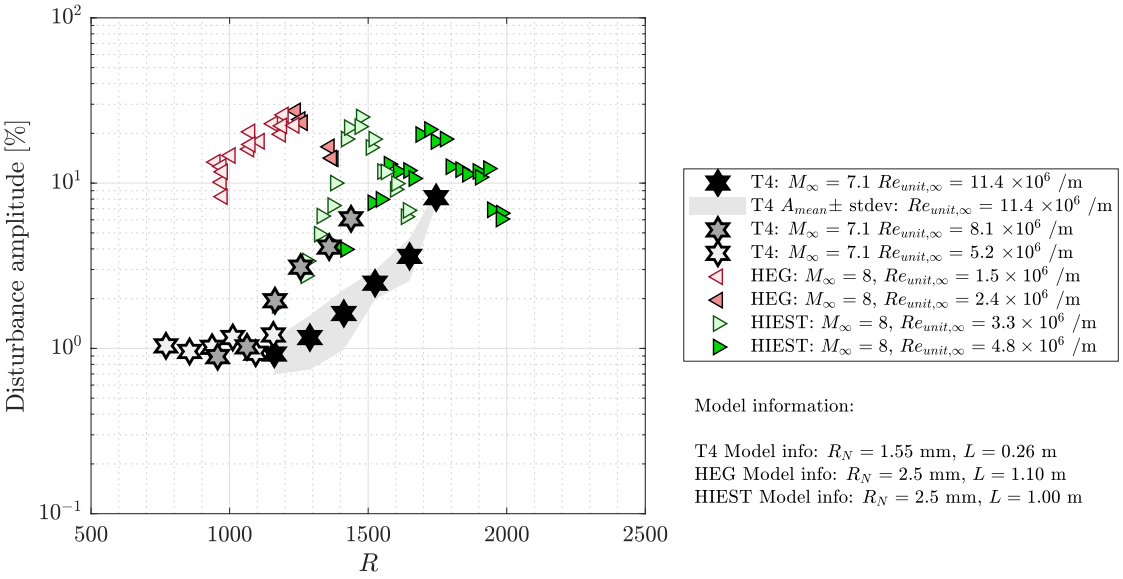


Figure 6.29: Comparison of the integrated PSD amplitudes between T4 and HEG and HIEST [54].

6.3.5 T4 comparison to HDT

The T4 power spectral density results are compared to results from the HDT verification campaign (Chapter 5) in Figure 6.30. The HDT campaign also used an $R_N = 1.6$ mm nosepiece, and results are presented for sensors at similar Re_x. In the power spectra results for both facilities, sensors in the range $Re_x \approx 2.3 - 3.0 \times 10^6$ show early stages of a peak increasing in amplitude. The peak is at significantly higher frequencies in the T4 tests due to the higher enthalpy conditions[6]. The T4 power spectra increases in magnitude at lower frequencies when progressing from $Re_x = 2.6 \times 10^6$ to $Re_x = 3.0 \times 10^6$. Typically, the disturbance energy is expected to be concentrated within a small frequency band, as shown in the HDT progression.

If the T4 high frequency peak does correspond to the second mode disturbance, this result suggests that the lower wall-to-total temperature ratio in T4 has not caused the second mode to be observed further upstream (both show an initial increase at $Re_x \approx 2.5 \times 10^6$). However, it is difficult to conclude whether the second

[6]Larger u_e and smaller δ, where $f \approx u_e/(2\delta)$

mode has been destabilized at lower T_w/T_0 for three reasons. Firstly, the high-frequency peak in the T4 tests has not been confirmed as a second mode disturbance. Secondly, the freestream disturbance environment in T4 must be quantified and compared to that of HDT. Finally, the maximum second mode amplitude location must be compared, as it is possible that differences in the freestream disturbance environment could cause the boundary layer to decay at lower amplitudes and further upstream. Additional measurements and analysis is therefore required to make meaningful comparisons to the T4 dataset.

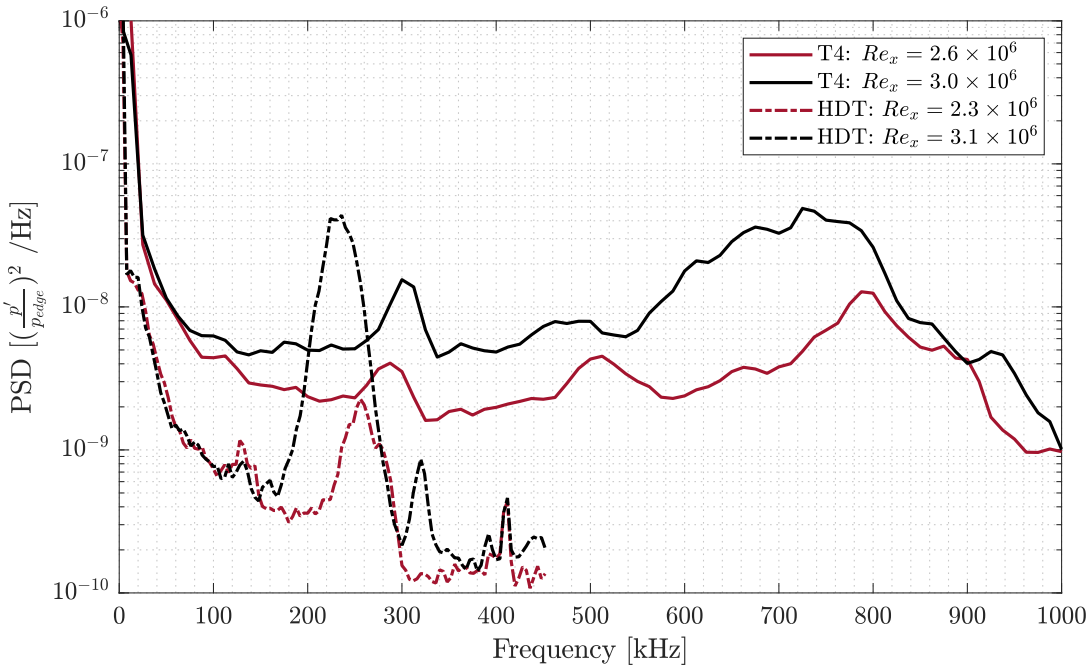


Figure 6.30: Comparison of the power spectral density results for similar gauges in T4 and HDT. The T4 condition is: $M_\infty = 7.1$, $Re_{unit,\infty} = 11.4 \times 10^6$ /m, $T_w/T_0 = 0.13$. The HDT condition is: $M_\infty = 7.0$, $Re_{unit,\infty} = 8.4 \times 10^6$ /m, $T_w/T_0 = 0.56$. The PSD for the HDT condition is plotted up to 450 kHz, as higher frequencies are affected by the noise floor.

6.4 Non-dimensional frequency comparison

The disturbance frequency is normalised so that comparisons can be made between multiple facilities and freestream conditions. The dimensionless frequency, F, was proposed by Stetson et al. [94] and provided in Equation 2.9 of Section 2.5.4. For convenience, it is reproduced here:

$$F = \frac{2\pi f}{u_\infty Re_{unit,\infty}} \tag{6.3}$$

Where f is the disturbance frequency, u_∞ is the freestream velocity, and $Re_{unit,\infty}$ is the facility unit Reynolds number. Marineau et al. applied this frequency scaling to investigate the effect of Reynolds number on the PSE-Chem computed non-dimensional frequency for conditions in HWT-8 using a sharp cone (see Figure 2 in Ref. [54]). They noted that the most unstable second-mode frequency can be expressed as

$$F = \frac{g}{R^h} \tag{6.4}$$

where g and h are constants, R is the stability Reynolds number ($R = \sqrt{Re_x}$) and typically $h \approx 1$ [54].

Figure 6.31 shows the HDT and T4 disturbance frequencies normalised using the same method. These measurements are compared to the PSE-Chem disturbance frequencies, the estimated frequencies using Howarth's boundary layer thickness approximation [84], and the result presented by Marineau et al. for the HWT-8 facility using a sharp cone [54]. The agreement is good between both facilities and the Marineau sharp-cone trend. The maximum discrepancy is 14% for the T4 $Re_x = 2.6 \times 10^6$ sensor, however the HDT measurements agree within 5%. The disagreement with the T4 PSE-Chem computation is substantial ($> 30\%$) and is the focus of ongoing work.

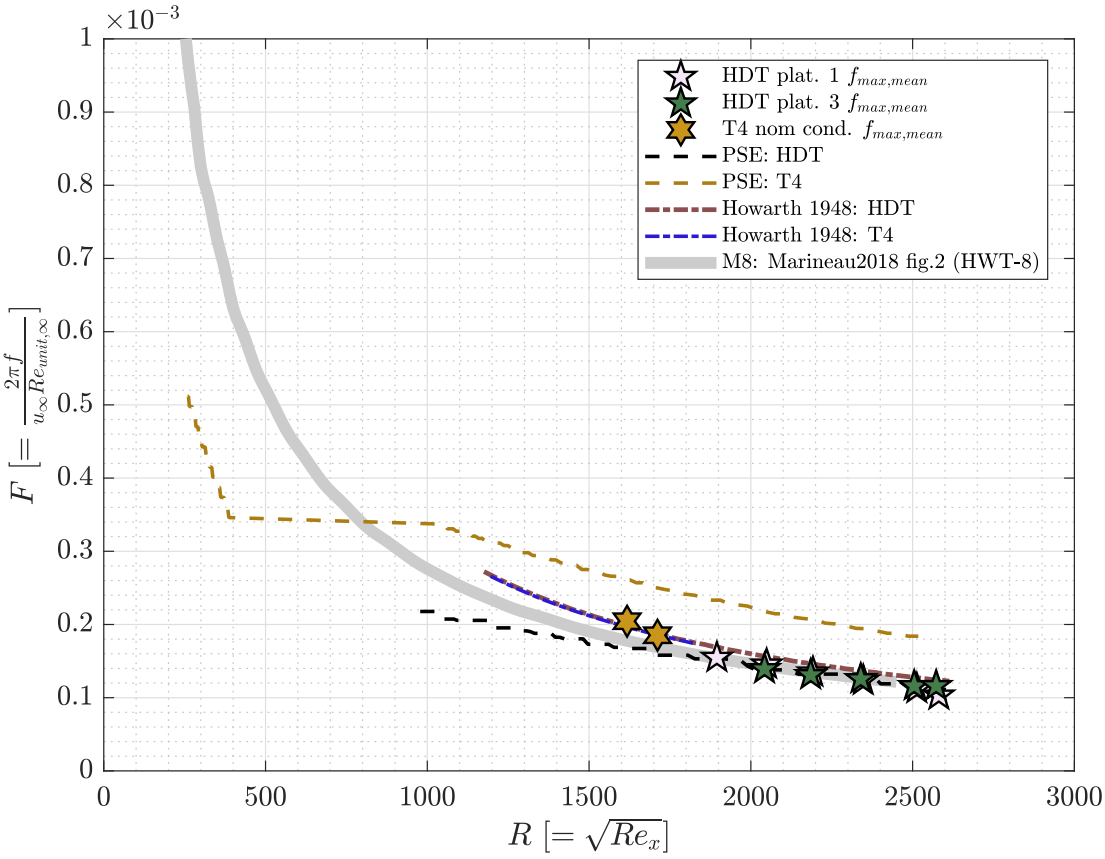


Figure 6.31: Comparison of the non-dimensional frequency, F. Measurements in HDT and T4 are compared to PSE-Chem computations, the estimated frequency using the Howarth boundary layer thickness approximation, and the result presented by Marineau et al. for the HWT-8 facility using a sharp cone [54].

7

Boundary layer instabilities at angle of attack

Boundary layer instability measurements are presented for the High Density tunnel at Mach 7, $Re_{unit,\infty} = 5.92 - 12.31 \times 10^6$ /m, $T_w/T_0 = 0.64$, $\alpha = 5° - 13°$, and Noise = 0.44% - 1.49%. A brief overview of the HIFiRE-1 flight test is provided, as the HDT measurements are compared to this dataset wherever possible. The HDT 7° cone model is used with its $R_N = 1.25$ mm nosepiece. At these angles of attack, the crossflow instability is expected to play a role in the transition process for azimuths around the cone. The second mode instability is expected to dominate along the windward ray, as no circumferential velocity component exists within the boundary layer.

The HDT transition front results are presented at the various angles of attack and scaled $Re_{unit,\infty}$ observed during the HIFiRE-1 descent stage of flight. A particular focus has been given to the HIFiRE-1 high frequency pressure measurements. The transition onset criteria used in flight and the HDT results are described. The HDT results are then compared to some of the key observations from flight, such as the windward transition, leeward transition, and the general shape of the transition front.

The boundary layer instabilities are then investigated for a finer resolution of azimuths at $Re_{unit,\infty} = 12.3 \times 10^6$ /m, $\alpha = 8°$. This condition corresponds to the scaled $Re_{unit,\infty}$ and nominal angle of attack for the final transition observed in flight. To investigate the effect of freestream disturbances, instability measurements are finally compared between HDT plateau #1 and #3. All of the power spectral density results presented in this chapter are calculated using Welch's fast Fourier transform (described in Section 3.7.1).

7.1 HIFiRE-1 flight test

The Hypersonic International Flight Research Experimentation (HIFiRE) program was a hypersonic flight test program executed by the Air Force Research Laboratory (AFRL) and the Australian Defence Science and Technology Organisation (DSTO) [206, 207]. The primary objective of the first flight test was to measure aerothermal phenomena in hypersonic flight, by investigating boundary layer transition on a 7-degree half angle axisymmetric cone with a nose bluntness of 2.5 mm radius[1]. The descent phase of flight provided a wealth of transition data at Mach 7 and relatively high angles of attack ($\alpha \approx 6° - 13°$). Results and reviews of the flight test can be found in [26, 27, 28, 29, 30, 31, 32, 33, 34]. A very brief overview of transition observations in the flight test was also provided in Section 2.7.4. Some of the key transition results are reviewed here for convenience.

Summary of transition observations

Figure 7.1 shows the transition front measured in the descent stage of flight, as detected by high frequency Kulite pressure sensors (PHBW1-3) and a Vatell Corporation thin-film thermopile heat transfer gauge (HT3). The figure has been reproduced using data from Figure 25 in Ref. [32] (also shown in Figure 2.17). This Re_x-ϕ map is formulated using measurements from the entire transition process,

[1] Details of the design of the vehicle and its construction can be found in [208, 27].

and therefore consists of data at varying angle of attack and Re_{unit}. Some key features of the transition process are annotated as follows [32]:

1. The earliest transition was observed on the leeward ray at $M_\infty = 7$, $Re_{x,tr} = 3.1 \times 10^6$, and $\alpha = 13°$.

2. The transition along the windward ray was observed at $M_\infty = 7$, $Re_{x,tr} = 4.7 \times 10^6$, and $\alpha = 9°$.

3. The latest transition was observed on azimuths $\phi = 30°$, $280°$, at $M_\infty = 7$, $Re_{x,tr} \approx 6.0 \times 10^6$ and $\alpha = 5°$.

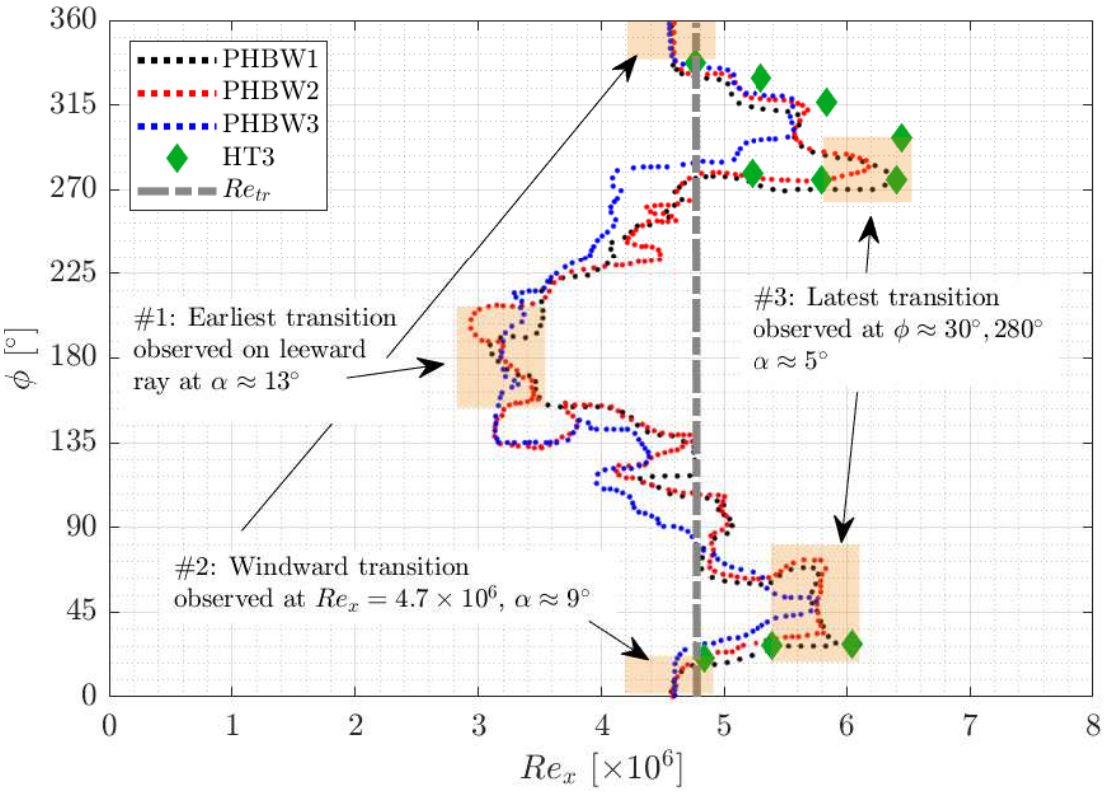


Figure 7.1: HIFiRE-1 descent transition map. Data is extracted from Figure 25 in [32]. PHBW1 - PHBW3 are measurements from high frequency Kulite pressure transducers in flight. HT3 is a high frequency Vatell heat transfer gauge, and the dot-dashed line given by Re_{tr} is the low-frequency transition measured by a Medtherm coaxial gauge in flight.

7.1.1 Flight test overview

The HIFiRE-1 flight test took place in March 2010 in Woomera, Australia. It was a largely successful flight test; however, an anomaly in the exoatmospheric pointing manoeuvre resulted in much higher re-entry angles of attack than initially anticipated. The angle of attack at transition onset was $13 \pm 3°$, and this reduced to $8 \pm 3°$ as the boundary layer became fully turbulent across all azimuths [27, 32, 34]. During this time, the freestream Reynolds number increased from 2.0×10^6 to 8.0×10^6 per meter, whilst the freestream Mach number steadily increased from 6.8 to 7.0 [32][2]. The wall-to-total temperature ratio was less than 0.19 during transition [31].

The payload was spinning throughout the descent transition. The maximum spin rate observed during re-entry was 4 Hz, which is equivalent to 4ms^{-1} at the downstream end of the cone [32]. Stanfield et al. note that this tangential velocity is less than 0.2% of the freestream velocity ($u_\infty = 2090\text{ms}^{-1}$ at maximum spin rate), and the fluid dynamics is therefore unlikely to have any effect on transition [32]. Stanfield et al. also cite wind-tunnel tests by Buchanan et al. in AEDC Tunnel B at $M_\infty = 5$ and 8, where they compared transition data on a spinning cone to a stationary cone at angles of attack up to $\alpha = 6°$ [209]. The heat transfer data showed no skewing of the boundary-layer transition front, with spin rates up to 6000 degrees per second (16.7 Hz roll rate) investigated [209].

The combination of payload spinning and changes in angle of attack complicated the analysis of the flight data. Surface pressure measurements showed clear crests and troughs, making it possible to assign azimuths to times for the windward and leeward rays respectively [32]. With the spin rate assumed to be constant over one

[2]Ref. [26, 27] provide information about the reconstruction of freestream conditions using the best-estimated trajectory (BET), best-estimated atmosphere (BEA), and vehicle attitude estimate. For information about how the angle of attack was calculated from low bandwidth surface pressure traces and computations, see Ref. [31] and Ref. [32].

revolution, the times were interpolated for the other angular rotations [27, 31, 32, 33].

7.1.2 Instrumentation

The HIFiRE-1 vehicle was instrumented with various low-bandwidth and high-bandwidth transducers. Type-T Medtherm dual thermocouples (TLBW) were used to measure the wall temperatures. The frequencies of the low-bandwidth heat transfer and thermocouple gauges were too low to resolve the three-dimensional transition front for each spin[3]. Vatell thin-film thermopile heat transfer gauges (HT) were able to resolve high frequency transition information (f = 0 - 2kHz), for azimuths where heating was sufficiently high [32].

Kulite low-bandwidth pressure transducers (PLBW) provided low-frequency pressure measurements. These were used to determine the model angle of attack, and for the normalization of the high frequency pressure signals. High bandwidth Kulite pressure transducers (PHBW1-3) were able to resolve the transition front as the vehicle was spinning during descent. The spin therefore provided a sweep in results at a fine resolution of azimuths for a given freestream condition and angle of attack. The high frequency kulite pressure transducers are able to sample up to 60 kHz. The HDT measurements are compared to the transition front detected using these sensors.

A periodic signal was observed at low frequencies in the PHBW signals. The frequency of this signal was too low to be the second mode or travelling crossflow instability, however it had similar rms magnitudes to the higher-frequency content [32]. Separating the signal into two frequency bands made it possible to distinguish between both types of fluctuations. For detailed information about the periodic disturbance, consult Section VI b) in Ref. [32].

[3]The average transition Reynolds number is shown by the Re_{tr} dashed line in Figure 7.1, where it reassuringly lies on the average Re_x of the higher-frequency content.

7.1.3 Pressure fluctuation transition onset criterion

To summarize the content in the signal, the rms of the high frequency pressure fluctuations (PHBW1-PHBW3) was calculated and normalized by the mean surface pressure (PLBW). The normalized rms surface pressure contours were determined by computing the area underneath the autospectral density function over a low and high frequency band [32]. The first frequency band isolates the periodic disturbances (f = 100 Hz - 1 kHz), whilst the second band considered the high frequency disturbances (f = 4 - 30 kHz). Surface pressure contours of the periodic disturbance and high frequency transition front are shown for PHBW1 in Figure 7.2 a) and b) respectively.

The initial rise of the high frequency surface pressure rms contours was used to define the transition front in flight. The resultant transition front is illustrated by the black line in Figure 7.2 b), for PHBW1. The threshold rms magnitude required for transition onset is not clear, though it must be small (for example, consider azimuths $\phi = 60° - 110°$ and $\phi = 250° - 280°$). The PHBW-determined transition front agreed well with the high frequency heat transfer results, denoted by the red diamonds of HT3 (see Ref. [32] for HT-detected transition information).

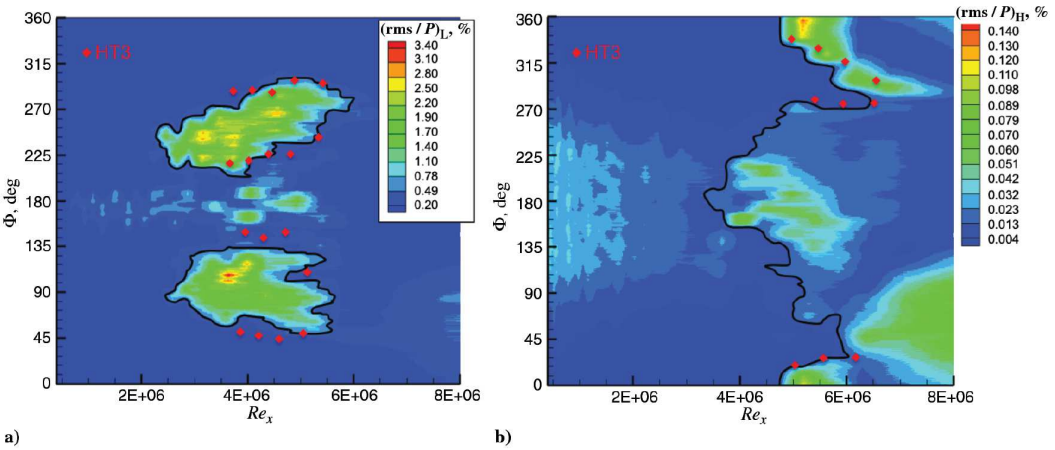


Figure 7.2: Contour maps of rms pressure fluctuations from a high frequency Kulite pressure transducer as measured in flight (PHBW1). Taken from Figure 18 in Ref. [32]. The black line shows the transition front as measured using PHBW sensors. The transition onset is defined by the initial rise in normalized high frequency rms. Red diamonds show the transition locations measured using the Vatell thin-film thermopile heat transfer gauges. [31, 32]

7.2 HDT conditions overview

Transition was observed in the HIFiRE-1 descent phase of flight over a range of freestream Reynolds numbers ($2 - 8 \times 10^6$ /m) and angles of attack ($5° - 13°$). A campaign was undertaken in the Oxford HDT to match the angles of attack and scaled $Re_{unit,\infty}$ observed in flight. The progression of facility conditions is referred to as HDT Conditions 1-3. These conditions correspond to targeted flight times of: t = 482.0, 483.0, and 484.3 seconds respectively. Figure 7.3 illustrates the HDT sweep in angles of attack and Reynolds number, when compared to the HIFiRE-1 trajectory (as calculated in [26, 32, 31]). The facility flow conditions for these three cases are then presented in Table 7.1.

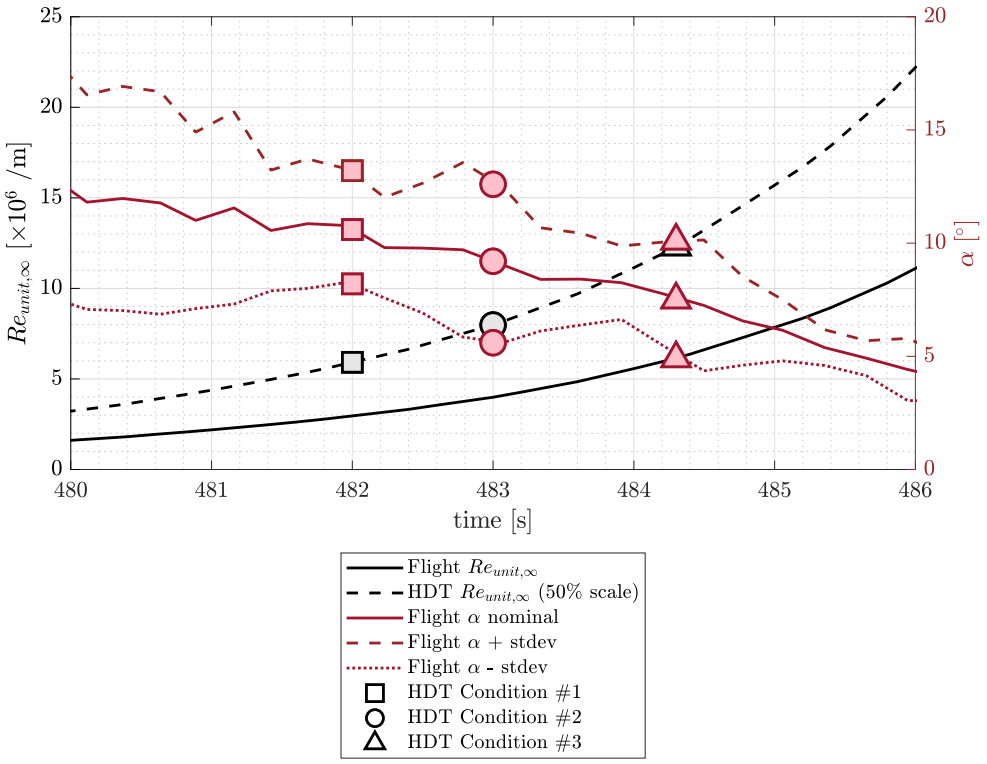


Figure 7.3: Illustration of HDT test conditions, when compared to the HIFiRE-1 flight descent trajectory [26, 31, 32]

HDT Condition	1	2	3
HIFiRE-1 flight time (s)	482	483	484.3
HDT facility plateau	3	3	3
P_0 (kPa)	960	1298	2021
T_0 (K)	458	458	458
$Re_{unit,\infty}(\times 10^6/m)$	5.9	8.0	12.3
M_∞	7.0	7.0	7.0
T_w/T_0	0.64	0.64	0.64
α_{low} (°)	7	6	5
α_{nominal} (°)	10	9	8
α_{high} (°)	13	12	10
Noise (%) (total)	0.44	0.44	0.44

Table 7.1: HDT facility nominal conditions for mapping the time, angle of attack, and $Re_{unit,\infty}$ during the HIFiRE-1 descent transition phase of flight. The scaled conditions are for the HDT 7° cone model with its $R_N = 1.25$ mm nosepiece.

7.3 Static cone pressures at angle of attack

The pressure fluctuation measurements are normalised by the static cone pressures[4]. For cones at angle of attack, the static pressure is expected to vary for azimuths around the cone. This variation is measured using Kulite XTEL-140(M) sensors at $x = 451$ - 480 mm. Measurements were taken at fourteen separate azimuthal angles (ϕ) for HDT Condition 3 at $\alpha = 8°$. At other conditions and angles of attack, the static pressure was measured at four or five azimuths.

Figure 7.4 compares the Kulite pressures to Cheng's correlation [202, 203] as a function of cone azimuth. Both results show a higher pressure towards the windward ray, which is expected due to the stronger shock lying closer to the model surface. The tail-off in pressure towards the leeward ray is also quite similar for both methods. Cheng's correlation consistently over-predicts the pressure on the leeward ray for

[4]The same method for normalising the pressure fluctuations was done at $\alpha = 0°$ in Section 6.1.

the high angle-of-attack bound. This is most likely due to the boundary layer separation at these high angles of attack.

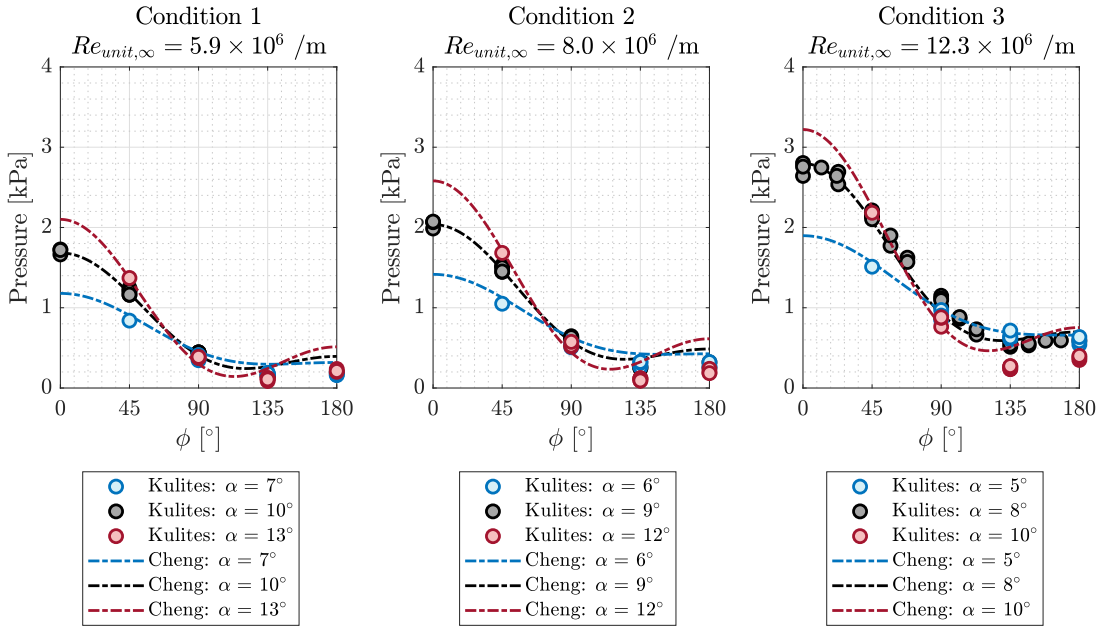


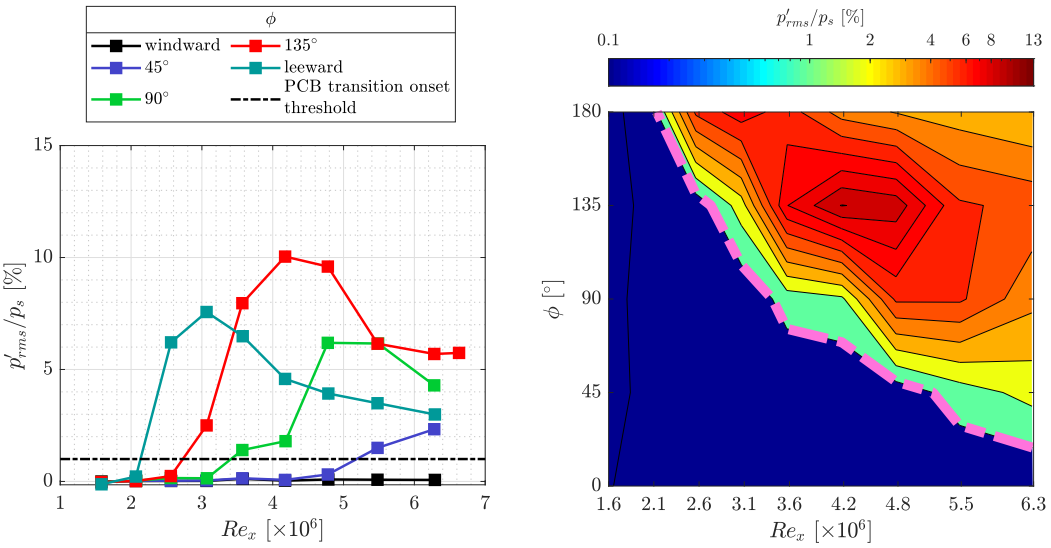
Figure 7.4: Cone surface pressure as a function of azimuth for HDT Conditions 1, 2, and 3. Kulite pressures are compared to those calculated using Cheng's correlation [202, 203].

The pressure fluctuation results for the following subsections are therefore normalised by the average Kulite measurement for each azimuth. For azimuths that do not have static pressure measurements, the value from Cheng's correlation at that particular azimuth has been used. This substitution is only required on the windward ray for the low and high angle-of-attack bounds, where Cheng's correlation seems to be able to more accurately predict the static pressure.

7.4 Pressure fluctuation transition onset criterion

The initial rise of the rms pressure fluctuation contours was used to define the transition front in the HDT experiments. A low-frequency disturbance and a high frequency disturbance were observed in the normalised power spectral density results. The low-frequency disturbance amplitudes are calculated by integrating the normalised PSD over a frequency band of 11 - 80 kHz, whereas the high frequency disturbance amplitude used a frequency band of 100 - 600 kHz.

The amplitudes for each disturbance are presented as individual $Re_x - \phi$ contours. An example is given for the high frequency band of HDT Condition 3, with the model pitched at $\alpha = 8°$. Figure 7.5a shows the integrated PSD result for $\phi = 0°$, 45°, 90°, 135°, and 180°. The same dataset is then presented as a $Re_x - \phi$ map in Figure 7.5b. A PCB-detected transition onset threshold of 1% is used to identify the location that the fluctuations clearly rise above the laminar baseline levels. This threshold is illustrated by the black dashed line in Figure 7.5a, and the resultant transition front is illustrated by the pink dashed line in Figure 7.5b. The contour limits for the $Re_x - \phi$ maps are 0.1% to 13% for all HDT results presented in this chapter.



(a) Integrated PSD with transition onset threshold.

(b) $Re_x - \phi$ contour with transition front (pink).

Figure 7.5: HDT criterion for PCB detected transition onset. The criterion is applied to the result at HDT condition 3 for the model at $\alpha = 8°$.

7.4.1 Comparison to HIFiRE-1 criterion: similarities and discrepancies

Some of the key similarities between both methods are:

1. The transition onset criteria is defined as the initial rise of the rms pressure fluctuation contours, with the onset threshold being slightly above the laminar baseline.

2. The pressure fluctuations are normalised by the surface pressure at each azimuth.

3. The HDT rms calculation should be equivalent to the area under the auto-spectral density over a specified frequency band, as calculated for the flight results.

Some of the differences that exist between the methods include:

1. The integrated frequency bands used to summarised the disturbance front are different. The PCB132s are able to resolve higher frequencies than the 30 kHz maximum from the Kulites in flight, making it possible to track the growth of high frequency disturbances.

2. The $Re_x - \phi$ map resolution is significantly greater in the flight results. In ground experiments, measurements are taken for an array of sensors at discrete x locations and an individual facility Reynolds number (i.e. $Re_{x,i} = Re_{unit,\infty} \times x_i$). In the HIFiRE-1 flight test, the sensors experience a naturally increasing unit Reynolds number as the vehicle continues in time. This results in a very fine resolution of $Re_{unit,\infty}$, and therefore Re_x. The payload spinning also allowed measurements to be taken at a fine resolution of azimuths for each Re_x condition (see Ref. [32]).

3. The HDT $Re_x - \phi$ maps are presented using a logarithmic colour scale. It is important to note that the transition onset results are unchanged by the scale used. This logarithmic scale was chosen as it identifies a laminar (dark blue) and unstable (red) region clearly.

4. Even though both criteria define transition onset as being the initial rise of the rms pressure fluctuations, the threshold magnitudes may be slightly different. This would result in a small systematic error between both transition fronts.

7.5 HIFiRE-1 descent: sweep in Re_{unit} & angle of attack in the Oxford HDT

Results are presented for the high frequency band (100 - 600 kHz) at each of the scaled HIFiRE-1 descent conditions: HDT condition 1, 2, and 3. A matrix of contour results is presented in Figure 7.6. The rows correspond to each angle of attack bound, and the columns correspond to HDT condition #1 - #3. The differences in the measured axial Reynolds numbers are due to changes in facility freestream Reynolds numbers for each condition (i.e. $Re_x = Re_{unit,\infty} \times x_{PCB}$). Results are processed for HDT plateau #3, where a noise value of 0.44% was measured. The freestream turbulence levels may decrease as the facility Re_{unit} increases, however this variation was not investigated.

7.5.1 General observations

For all test conditions, the presence of instabilities moves progressively upstream when moving along azimuths from the windward ray to the leeward ray. This trend agrees with results from the verification campaign (Section 5.5) and other experiments completed in similar cold-flow hypersonic facilities. The windward boundary layer is much thinner at angle of attack, and is clearly stabilized when compared to the $\alpha = 0°$ results (see Section 6.2.2). The leeward boundary layer transition shifts to lower Reynolds numbers, and is most likely separated at these high angles of attack [32, 143].

Table 7.2 summarizes the disturbance onset for each angle of attack in HDT condition 3. The extracted transition onset lines are then shown in Figure 7.7. The leeward and $\phi = 135°$ transition onset locations don't seem to be affected by angle of attack within these bounds ($Re_{x,tr} \approx 2.0 - 2.3$). This contrasts with the instabilities present along the windward ray, which are stabilized when the angle of attack is increased from $\alpha = 5°$ to 8°.

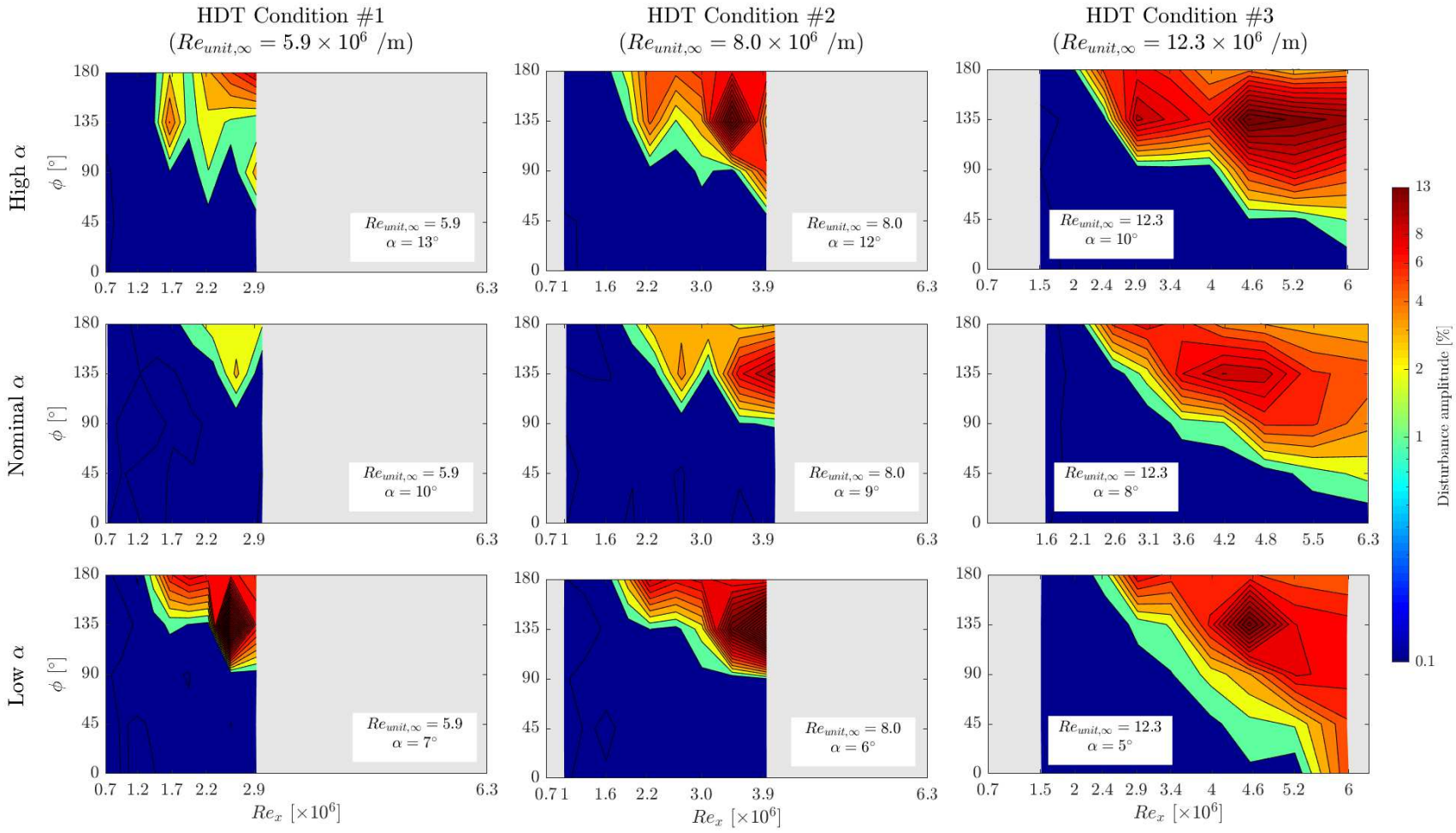


Figure 7.6: Integrated surface power spectra for HIFiRE-1 descent conditions, sweeping through both $Re_{unit,\infty}$ (i.e. time) and the uncertainty in angle of attack, α. The power spectra has been calculating using Welch's FFT method, and integrated between f = 100 - 600 kHz.

Angle of attack effects: HDT Condition 3					
Angle of attack (°)	$Re_x(\times 10^6)$				
	$\phi = 180°$	$\phi = 135°$	$\phi = 90°$	$\phi = 45°$	$\phi = 0°$
5	2.3	2.8	3.4	4.1	5.2
8	2.1	2.6	3.6	4.8	> 6.3
10	2.0	2.4	2.9-4.0	4.5	> 6.0

Table 7.2: Effect of angle of attack on disturbance amplitude for HDT Condition 3. The PSD integration bounds are $f = 100 - 600$ kHz. Re_x values correspond to the onset of the increase in disturbance amplitudes above laminar baseline levels, as described in Section 7.4.

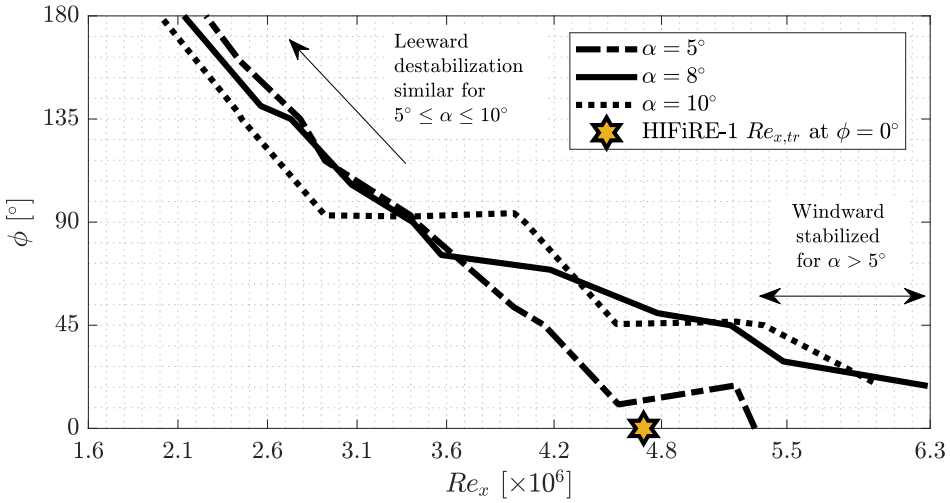


Figure 7.7: Transition onset lines for HDT condition #3 over the sweep in angles of attack: $5° \leq \alpha \leq 10°$. The figure has been annotated to show key features, including the HIFiRE-1 windward transition observed at $Re_{x,tr} = 4.7 \times 10^6$. The onset criteria is described in Section 7.4.

7.5.2 Comparisons to HIFiRE-1 flight observations

Earlier stages of flight (low $Re_{unit,\infty}$, high α)

Transition was initially observed along the leeward azimuth at the earlier stages of flight, where the angles of attack were highest and the freestream Re_{unit} was still relatively low. The lowest flight transition Reynolds number was at $Re_x = 3.1 \times 10^6 \pm 1.9 \times 10^5$, with the vehicle pitched at $\alpha = 13 \pm 3°$ [32].

When considering the high angle of attack bound for HDT Condition 1 and 2, it is clear that instabilities are detected on the leeward ray first. The high angle of attack bound for HDT Condition 1 was at $\alpha = 13°$, with sensors measuring up to $Re_x = 2.9 \times 10^6$. The first observed increase in the leeward power spectra contours is at $Re_x \approx 1.5 \times 10^6$ (see Figure 7.6). The HDT leeward transition therefore occurs significantly earlier than flight, with a discrepancy of $Re_x \approx 1.5 \times 10^6$. The earlier transition is expected to be due to the higher freestream turbulence levels in HDT than flight. Wall-cooling is expected to stabilize the stationary crossflow instability[5] [210], so this may also contribute to the discrepancy observed.

Later stages of flight (high $Re_{unit,\infty}$, low α)

The transition on the windward ray in flight occurred at $Re_x = 4.7 \times 10^6 \pm 2.9 \times 10^5$ and $\alpha = 9 \pm 3°$. For HDT Condition 3, the windward transition Reynolds number is larger than flight ($Re_x \geq 5.3 \times 10^6$) for each iteration of angle of attack: $\alpha = 5°$ - $10°$. A similar result was observed in post-flight tests conducted in DLR's H2K facility [36, 37], where they also observed windward transition at higher Re_x than flight.

The indented front observed in flight was not present for any of the three HDT Conditions, irrespective of the angle of attack bound. The sensor resolution was quite

[5] Computations by Gosse et al. have suggested that wall cooling stabilizes the crossflow instability by reducing the boundary layer thickness and percentage crossflow [210].

poor in both the axial and azimuthal coordinates for this descent sweep, however for each condition the $\phi = 45°$ ray is clearly more unstable than the windward ray. HDT results are presented at a finer resolution of azimuths in Section 7.6 ($\alpha = 8°$, $Re_{unit,\infty} = 12.31 \times 10^6$ /m), with the disturbance front compared to flight.

The lack of indented front and the higher $Re_{x,tr}$ along the windward ray has been attributed to the destabilizing effect of wall-cooling on the second mode instability along the windward ray, and the possible stabilization of the crossflow instability on the shoulder of the cone at lower T_w/T_0 [210]. It has been assumed that the combined effect of second mode destabilization and crossflow stabilization has a greater influence in the transition process than the differences in freestream turbulence levels between flight and conventional wind tunnels. The results from the HDT experiments support this hypothesis.

7.6 HDT Condition 3: $Re_{unit,\infty} = 12.3 \times 10^6$ /m, $\alpha = 8°$

Results are presented at a finer resolution of azimuths for HDT Condition #3 and the nominal angle of attack. This corresponds to: $M_\infty = 7.0$, $Re_{unit,\infty} = 12.3 \times 10^6$ /m, $T_w/T_0 = 0.64$, $\alpha = 8°$, and a post-shock noise level of 0.44%. Results are then compared to HDT facility plateau #1, to investigate the effect of an increase in freestream disturbances.

The automated traverse was used to measure instabilities at a finer resolution of azimuths between the windward and the leeward ray. This provides additional information about the three dimensional disturbance front at high angles of attack, and allows a more detailed comparison to be made with the flight results. The model-fixed sensor azimuth locations are at $\varphi = 0°$, 90°, 180° and 270°. The sensor azimuths relative to the incoming flow are changed by decreasing the traverse angle of attack (α), and increasing the traverse angle of yaw (β). Table 7.3 summarizes

the traverse α and β combinations used to achieve the nominal flight $\alpha_{effective} = 8°$, along with the resultant sensor azimuth locations (relative to incoming flow).

#	$\alpha_{effective}$ (°)	α (°)	β (°)	ϕ_{PCB132} (°)	ϕ_{HT} (°)
1	8.0	8.0	0.0	0, 45, 90, 135, 180	0, 45, 90
3	8.0	7.8	1.6	33, 57, 123, 147	12, 78
2	8.0	7.4	3.1	23, 67, 113, 157	22, 112

Table 7.3: Combinations of traverse α and β used to get instability and heat transfer data at a finer resolution of azimuths.

7.6.1 $Re_x - \phi$ map and transition front

Figure 7.8 shows the rms pressure fluctuation contour results, as a function of azimuth around the cone. Results are presented for both frequency bands: $f = 11 - 80$ kHz and $f = 100 - 600$ kHz. The heat-transfer detected transition is plotted on the $Re_x - \phi$ map as green diamonds, whereas the green arrow plotted on the windward ray indicates that transition onset was not observed. The transition onset lines have been extracted from the rms pressure fluctuation contours, and are compared to the HIFiRE-1 flight transition front in Figure 7.9.

The transition front becomes unstable when shifting from the windward meridian to the leeward meridian. This trend is observed for both disturbances and the heat transfer detected onset location. The HT-detected destabilization occurs between $\phi = 0°$ - $13°$ and then $\phi = 45°$ - $67°$. The PCB-detected transition front shows an immediate and continuous destabilization when departing from the windward ray. The transition onset results once again reiterate that the indented transition front was not detected in the HDT measurements.

7.6.2 Disturbance characteristics

The power spectral densities and integrated amplitudes for all sensors at each azimuth are presented in Appendix D. A suspected travelling crossflow peak was

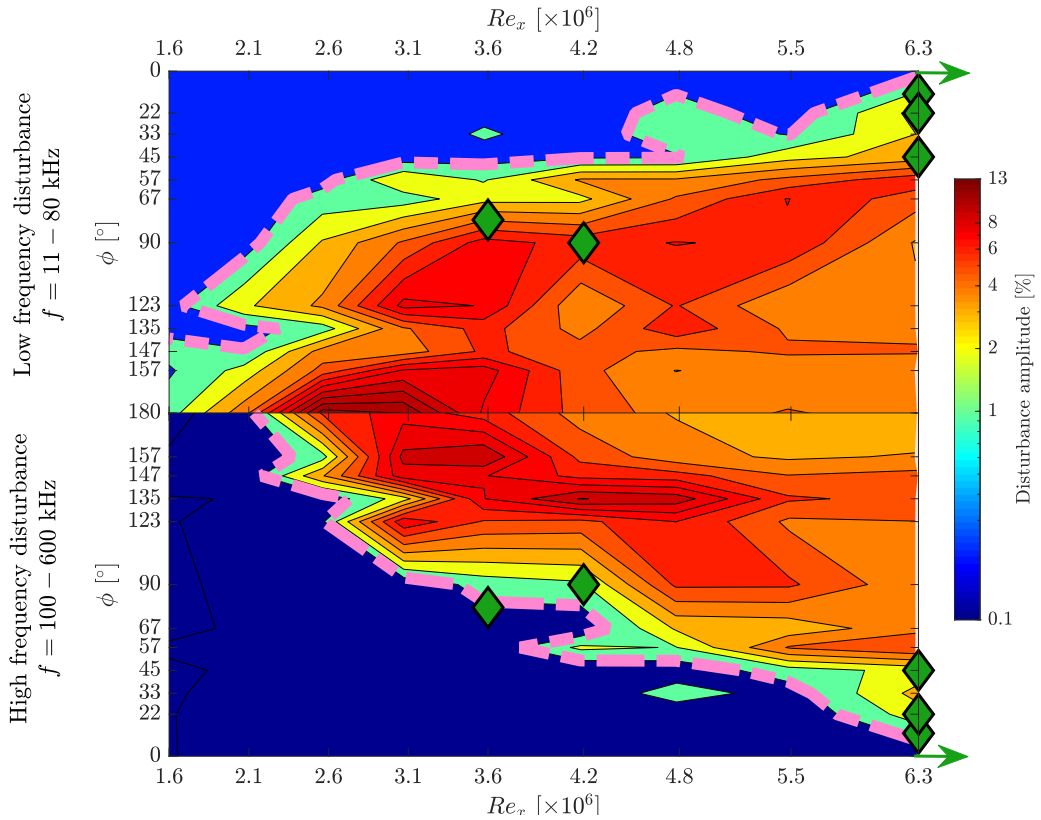


Figure 7.8: Contour plots of rms surface pressure fluctuation for two frequency bands, corresponding to a suspected travelling crossflow instability and a stationary crossflow / second mode instability. The pink dashed line corresponds to the PCB-detected transition front. The frequency bands are $f = 11 - 80$ kHz and $f = 100 - 500$ kHz. The green diamonds correspond to the thin-film gauge heat transfer detected onset. The green arrow at $\phi = 0°$ indicates that all sensors lied on the laminar baseline along the windward ray.

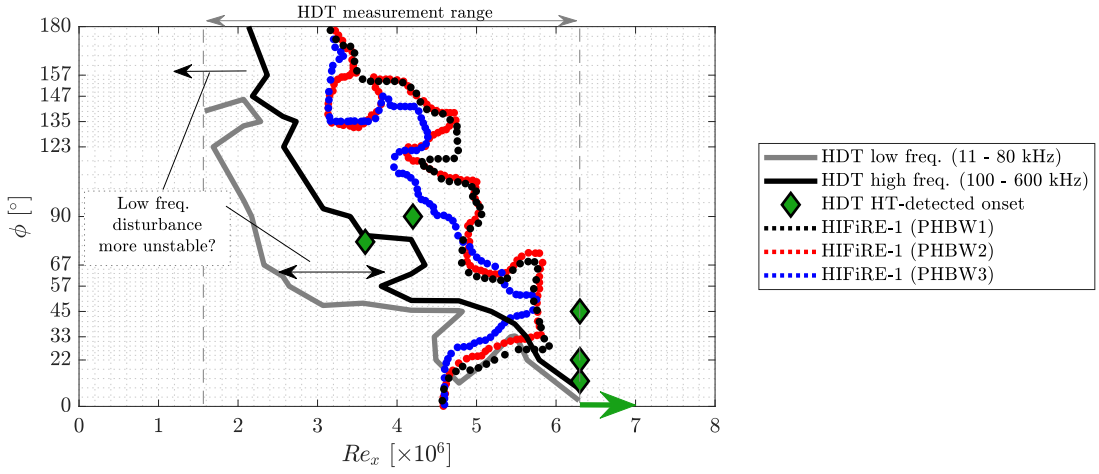
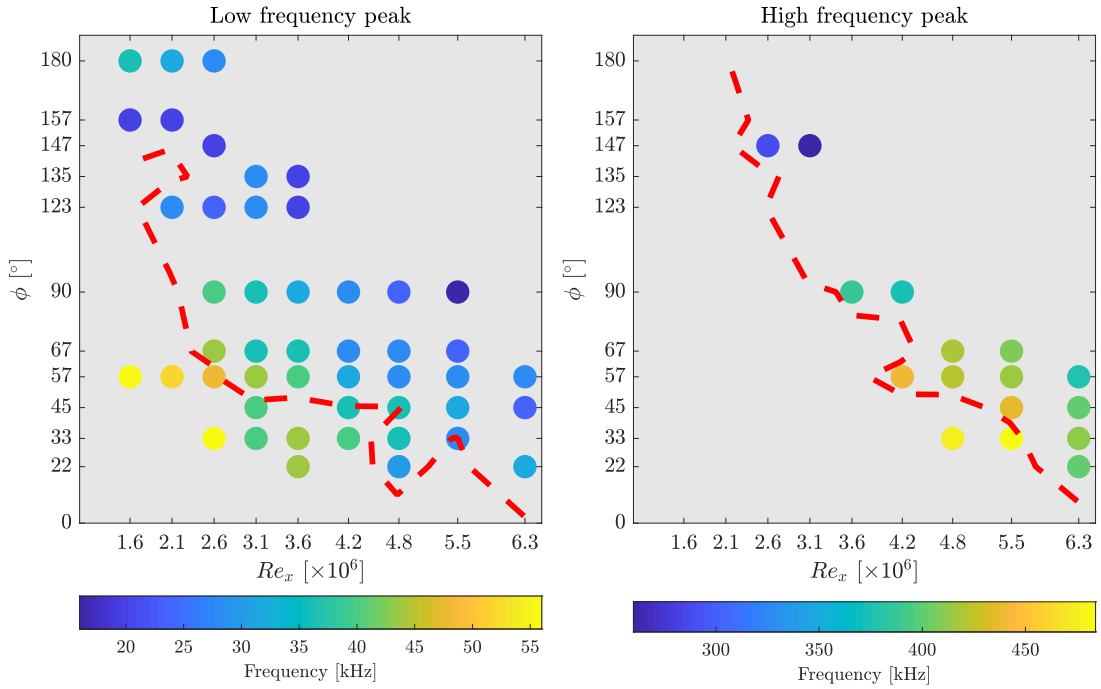


Figure 7.9: Transition front comparison between HDT and HIFiRE-1 flight. The green arrow indicates that HT-detected transition onset was not observed along the windward ray in HDT.

observed between $\phi = 22°$ - $180°$ and $Re_x = 1.6 - 5.5 \times 10^6$. A high frequency peak was observed between $\phi = 22°$ - $147°$, and $Re_x = 2.6 - 6.3 \times 10^6$. The high frequency peak is believed to correspond to the second mode instability or the secondary instability of stationary crossflow vortices.

Figure 7.10 shows the locations where peak frequencies were clearly observed, with the marker colors corresponding to the peak frequency at the particular location. The red dashed line shows the PCB-detected transition front from Figure 7.9. The first disturbance peaks are observed further upstream when approaching the leeward ray. The first observed peak agrees quite well with the transition onset extracted from the rms contours. The peak frequencies generally decrease at larger azimuths and Re_x, most likely due to the thickening of the boundary layer.



(a) Suspected travelling crossflow instability.

(b) Suspected second mode or stationary crossflow instability

Figure 7.10: Locations of sensors that showed clear low frequency or high frequency peaks in the PSD. The marker colours are used to identify the frequency at each particular location. The red dashed line shows the PCB-detected transition front, extracted from the rms contours.

Figure 7.11 shows an example of the power spectral density and rms amplitude results for multiple sensors along the $\phi = 90°$ array[6]. The results are annotated to identify multiple disturbance characteristics, with the accompanying discussion below. It should be noted that these sensors are not on the same flow streamline, as the streamlines will curve towards the leeward ray as they progress downstream.

(a) *Higher baseline rms magnitudes in the low frequency contour*

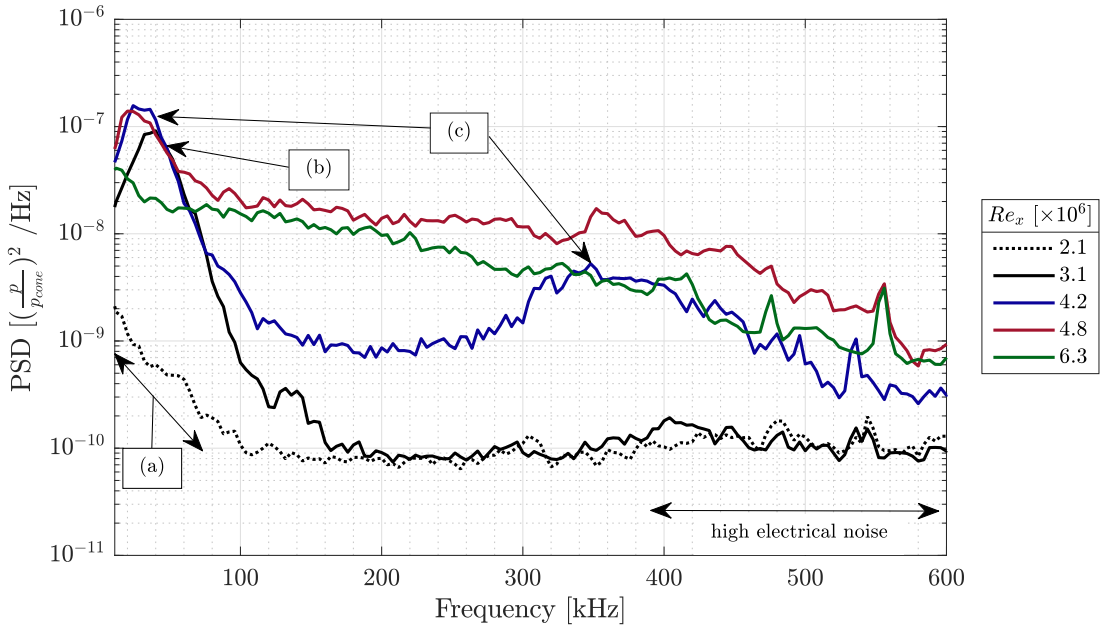
The $Re_x = 2.1 \times 10^6$ sensor is an example where no disturbances are identifiable, and the boundary layer is assumed to be completely stable. The magnitude of the PSD is larger over the lower frequency range (11 - 80 kHz), as shown by the "(a)" annotation in Figure 7.11a. This is the cause for the higher baseline rms values observed in the stable regions of the low frequency contours (i.e. the lighter blue in Figure 7.8). The baseline rms values are investigated further in Section 7.6.3.

(b) *Which disturbance exists furthest upstream?*

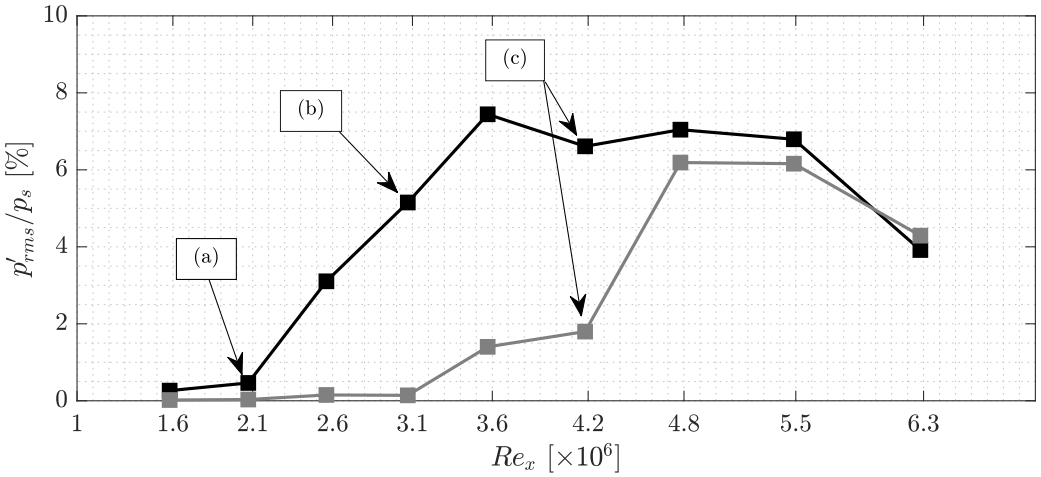
The HDT transition onset result suggests that the low-frequency disturbance exists furthest upstream for azimuths $\phi = 45°$ - $123°$, and $\phi \geq 147°$. The low-frequency disturbance peaks are also consistently observed at lower Re_x for each azimuth in Figure 7.10. The $Re_x = 3.1 \times 10^6$ sensor shows an example where a low frequency disturbance is detected at $f \approx 40$ kHz, with no peak observed at higher frequencies (see annotation "(b)"). Possible explanations are outlined as follows:

(i) The stationary crossflow vortices are growing alongside the suspected travelling crossflow instability, and the vortices have not saturated. The increase in vortex amplitude is not necessarily identifiable in the spectra, as the high frequency peak is expected to correspond to the rapid growth of secondary instabilities after the crossflow vortices have saturated (or the second mode instability).

[6]The $\phi = 90°$ azimuth has been chosen as sensors show multiple stages of the transition process.



(a) Power spectral density (various Re_x, $\phi = 90°$)



(b) RMS of normalised pressure fluctuations ($\phi = 90°$)

Figure 7.11: Examples of power spectral density and RMS amplitudes of pressure fluctuations. Results are presented for sensors along the $\phi = 90°$ array. The figure is annotated to illustrate the various stages of disturbance growth, as described in the text.

(ii) It is possible that the high electrical noise levels have disguised the initial growth of the high frequency disturbance.

(iii) The travelling crossflow instability may truly exist further upstream of the high frequency disturbance.

(c) *The low frequency and high frequency disturbance are able to coexist*
The $Re_x = 4.2 \times 10^6$ sensor illustrates an example with multiple clear peaks (see annotation "(c)" in Figure 7.11). The low frequency disturbance has a peak at 32 kHz, whereas the high frequency disturbance has a peak at ≈ 370 kHz. This result provides evidence that the suspected travelling crossflow instability is able to coexist with the high frequency stationary crossflow instability or second mode. The presence of two peaks may also indicate that there is a non-linear interaction between the travelling and stationary modes. This would imply that the boundary layer destabilization can not be solely attributed to one instability at this particular location.

Edelman et al. investigated the rapid growth of the secondary instability of stationary crossflow vortices [211]. The difference between the first increase in rms amplitude and the location of maximum rms amplitude was less than $Re_x = 1 \times 10^6$ [211]. If the high frequency peak observed in HDT does correspond to the secondary instability of the stationary crossflow vortices, it may also undergo rapid growth and cause the boundary layer to decay before the travelling mode saturates. Evidence of this may be visible in the $Re_x = 4.8 \times 10^6$ sensor. The low frequency peak is still visible at f = 24 kHz, whereas at all other frequencies the spectra seems to be turbulent. Further work is therefore required to isolate the role of each instability for various areas on the cone.

7.6.3 Effect of higher freestream disturbance levels: comparison to HDT plateau #1

Pressure fluctuation contour results are presented for HDT plateau #1, to investigate the effect of higher freestream disturbances. The plateau #1 freestream conditions are $M_\infty = 7.0$, $Re_{unit,\infty} = 12.3 \times 10^6$ /m, $T_w/T_0 = 0.58$, and noise $\approx 1.49\%$. The Reynolds number and Mach number are therefore matched to the condition previously presented, whereas the post-shock fluctuation levels have increased from $\approx 0.44\%$ to $\approx 1.49\%$ (see Section 4.3). Figure 7.12 shows the comparison of rms contours for both the low frequency and high frequency bands.

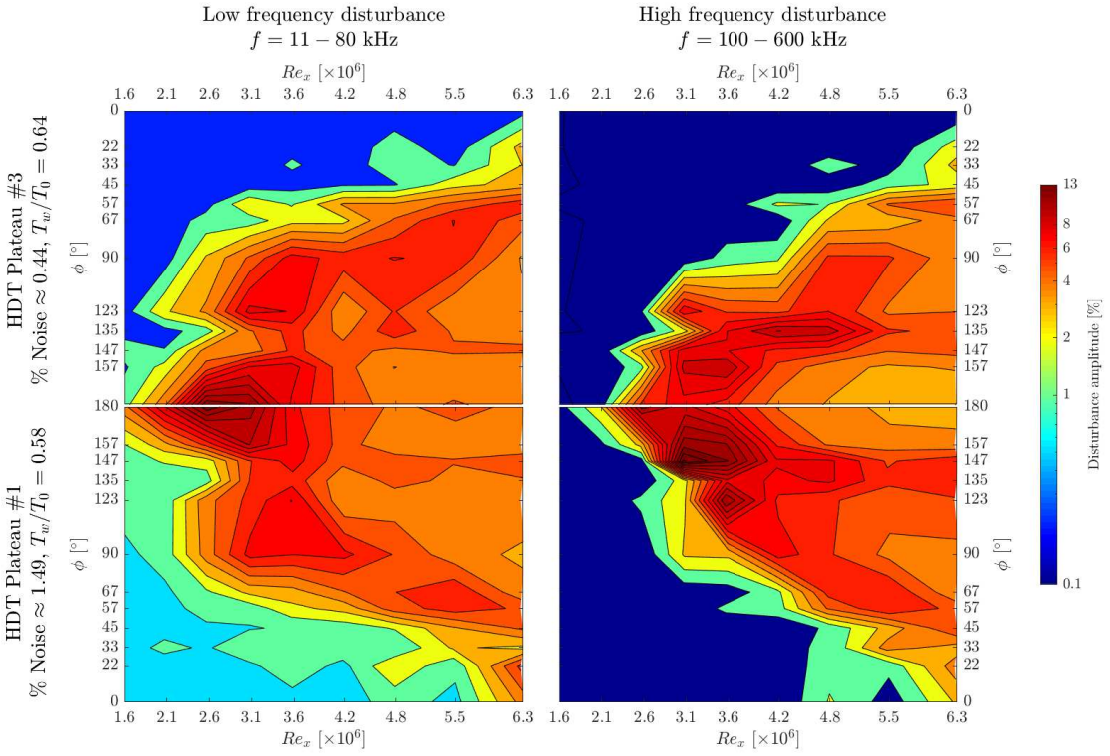


Figure 7.12: Comparison of rms pressure fluctuation contours for HDT plateau #1 and HDT plateau #3, with results presented for both frequency bands. The HDT plateau #1 condition is: $Re_{unit,\infty} = 12.3$, $M_\infty = 7.0$, $T_w/T_0 \approx 0.58$, noise $\approx 1.49\%$. The HDT plateau #3 condition is: $Re_{unit,\infty} = 12.3$, $M_\infty = 7.0$, $T_w/T_0 \approx 0.64$, noise $\approx 0.44\%$.

The transition fronts are extracted from the rms contours using the same criterion, with results shown in Figure 7.13. The shape of the disturbance front looks quite similar when the freestream disturbances have increased, indicating

that the dominant mechanisms leading to transition have not changed[7]. The transition onset location at $\phi = 45°$ - $180°$ is quite similar for both freestream disturbance environments, however there is a noticeable difference when approaching the windward ray. The "staggered" shape of the transition onset line along the windward ray may be a concern, as it would be expected to destabilize directly when progressing downstream[8]. It is difficult to draw many conclusions without investigating the individual disturbances and the frequency content of the power spectra.

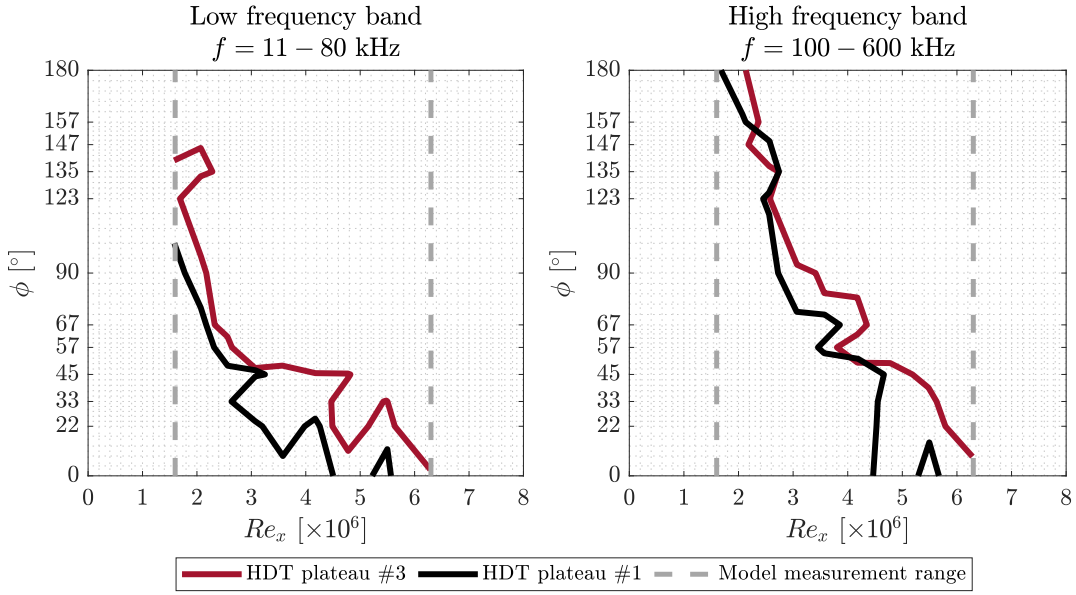


Figure 7.13: Effect of increased freestream disturbances on the PCB-detected transition onset. Results from HDT plateau #1 (noise $\approx 1.49\%$) are compared to HDT plateau #3 (noise $\approx 0.44\%$), with the Reynolds number and Mach number otherwise matched.

Low frequency and high frequency peaks are observed in the power spectra for plateau #1. This suggests that the suspected travelling crossflow instability and stationary crossflow instability (or second mode) are also present in the higher freestream noise environment. The PSDs for sensors along the $\phi = 90°$ array at

[7] If the environmental disturbances are significant, the modal path to transition may be bypassed. The matched shape and similar power spectra features indicates that this is not the case when comparing to HDT plateau #1

[8] The windward ray is the only azimuth that also tracks the flow streamline, and so this is a fair assumption.

both freestream disturbance levels are compared in Figure 7.14. The power spectra have been annotated to describe the nature of the destabilization for each sensor. These results provide evidence that both the high and low frequency boundary layer disturbances are destabilized as a function of an increase in freestream disturbance, even if the PCB-detected transition onset location did not vary significantly.

Results presented at $\alpha = 0°$ also showed minimal variation in the PCB-detected transition onset location when the freestream disturbances was increased (see Section 6.2.3). For the $\alpha = 0°$ results, it was the maximum disturbance amplitude and therefore the critical N factor which was most affected. The maximum disturbance amplitude before decay was smaller and occurred further upstream in HDT plateau #1, resulting in a lower critical N factor. Future work will investigate if the same trend is observed for the three-dimensional instabilities.

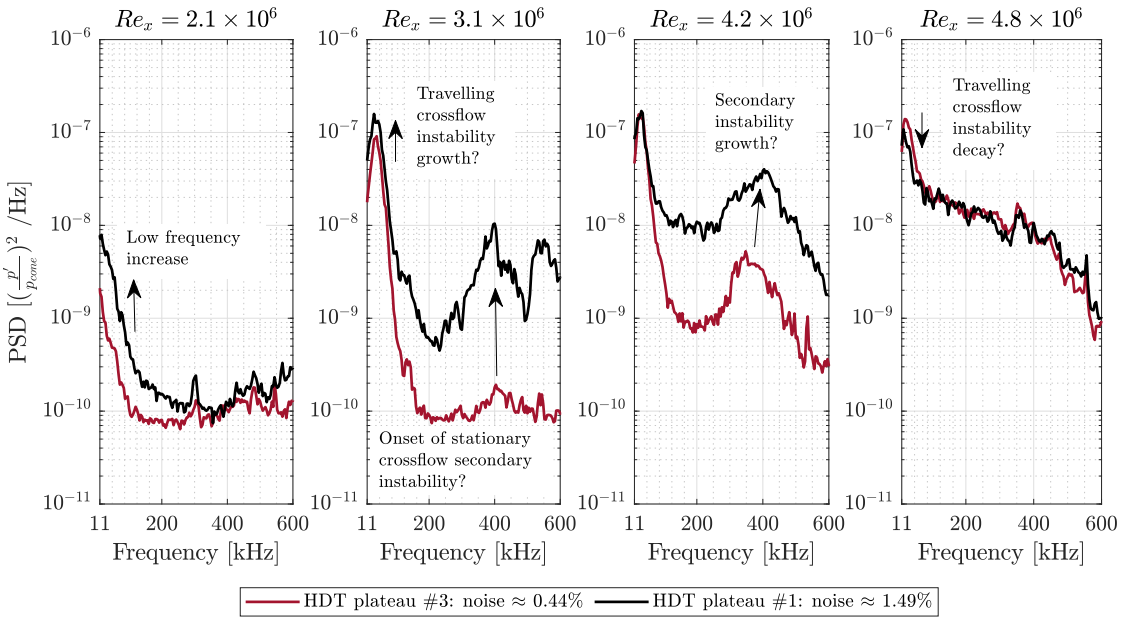


Figure 7.14: Effect of increased freestream disturbances on multiple sensors along the $\phi = 90°$ array. Results from HDT plateau #1 (noise ≈ 1.49%) are compared to HDT plateau #3 (noise ≈ 0.44%), with the Reynolds number and Mach number otherwise matched.

The laminar rms magnitude has increased for the low frequency disturbance, as shown by the lighter blue colour in the upstream section of Figure 7.12. This result suggests that the increase in post-shock freestream fluctuations causes the baseline rms content to also increase. The result is only identifiable in the low frequency band for multiple reasons. Firstly, the majority of the freestream disturbances are expected to exist at frequencies below 100 kHz (the drop-off can be approximated by $\sim f^{-3.5}$ at high frequencies [120]). Secondly, the PSD has a greater signal magnitude when compare to the electrical noise floor in the low frequency band. This makes it easier to identify small changes in the baseline fluctuation levels. The baseline rms increase is shown for $Re_x = 2.1 \times 10^6$, $\phi = 45°$ in Figure 7.15. The hexagram markers illustrate the location of the sensor on the low frequency rms contours.

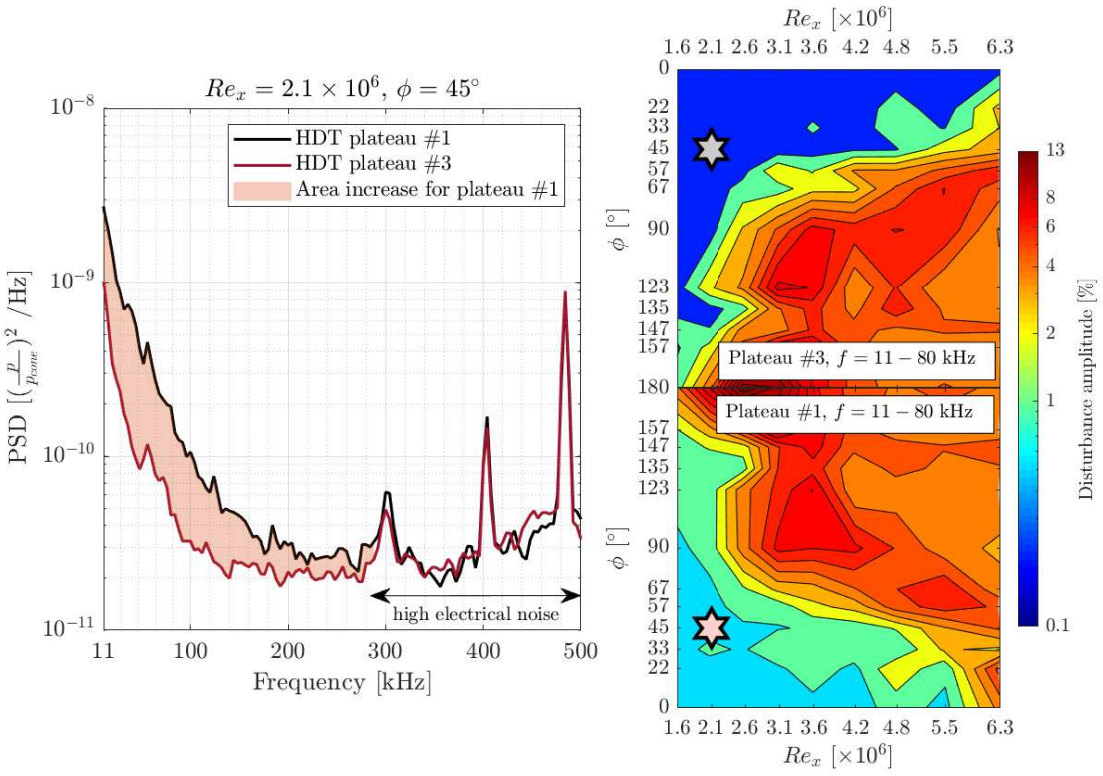


Figure 7.15: Effect of HDT facility plateau on laminar pressure fluctuation PSD. The sensor is at $Re_x = 2.6 \times 10^6$, $\phi = 45°$, as illustrated by the hexagram markers in the accompanying rms magnitude contours (both for low frequency band).

8

Conclusions and Future Work

8.1 Conclusions

8.1.1 Commissioning of the Oxford HDT

This research represents the first experiments in the newly-commissioned High Density Tunnel. Significant efforts were therefore made to characterise the HDT freestream post-shock fluctuation levels using its Mach 7 nozzle, and to compare instability results and processing methodologies with a similar dataset from DLR's H2K facility.

Post-shock freestream fluctuation levels were characterised for the Mach 7 conditions presented in this research. The effect of HDT facility plateau and distance from nozzle centreline were both investigated. The HDT plateau #1 post-shock fluctuations agreed with the lower bound of the conventional tunnel results collated by Duan et al. [120]. The HDT plateau #3 results were at significantly lower fluctuation levels, and were limited by the electrical noise floor at $f \geq 500$ kHz. The centreline RMS noise values were 1.49% in plateau #1, and 0.44% in plateau #3. The discrepancy between the plateaus is due to the unsteady compression from the facility settling chamber when using the Mach 7 nozzle. The post-shock fluctuations increased by several orders of magnitude for sensors outside the HDT coreflow, as expected.

The excellent agreement of instability measurements with DLR's H2K facility, and to PSE-Chem stability computations at $\alpha = 0°$, indicated that the HDT can be trusted for boundary layer transition studies. At $\alpha = 0°$, the second mode instability dominated transition in both facilities. The maximum second mode amplitude was observed one gauge further upstream in the HDT facility. This is possibly due to higher freestream disturbance levels in HDT plateau #1 than the H2K condition. Both datasets showed good agreement with PSE-Chem computations (frequencies within 11%), and the HDT second mode frequencies agreed with

Howarth's approximation within 13%.

Instability measurements were also compared at angles of attack up to $\alpha = 12°$. Both facilities observed stabilization along the windward ray and destabilization towards the leeward ray, when compared to the $\alpha = 0°$ results. The power spectral density results were comparable at all azimuths, indicating that the transition mechanisms are the same at high angles of attack. The destabilization towards the leeward ray was very similar at all angles of attack ($3° \leq \alpha \leq 12°$), whereas the HDT windward transition was observed upstream of H2K. The windward discrepancy may indicate that only second mode dominated transition is observed earlier in the HDT.

8.1.2 Transition at $\alpha = 0°$

Second mode dominated transition was investigated at $\alpha = 0°$ in the Oxford HDT and The University of Queensland's T4 Stalker Tunnel. The effect of an increase in freestream disturbances was examined at high wall-to-total temperature ratios in the HDT, whereas the T4 experiments investigated multiple wall-to-total temperature ratio distributions and facility Reynolds numbers at flight-representative enthalpies.

Oxford HDT: effect of an increase in freestream disturbances

Results were presented using multiple facility plateaus to assess whether the increase in freestream fluctuations also translated to changes in second mode dominated transition. The facility flow conditions were: $M_\infty = 7$, $Re_{unit,\infty} = 12.3 \times 10^6$ /m, and a nosepiece radius of $R_N = 1.25$ mm was used. Results from both plateaus were compared to PSE-Chem computations, and N factors were calculated using the method proposed by Marineau [54].

A decrease in freestream fluctuations resulted in a delay in the breakdown of the second mode (A_{max} observed at $Re_x = 4.8 \times 10^6$ to $Re_x = 6.6 \times 10^6$), an increase in the critical N factor ($N_{crit} = 7.2$ to 9.4), and it allowed the second mode to reach larger amplitudes before decaying ($A_{max} = 17\%$ - 19% to 23% - 30%). These trends are in agreement with the results collated by Marineau et al. [54].

The disturbance frequencies and growth rates showed excellent agreement with the PSE-Chem computations, within 5% and 3% respectively. Likewise, even though Howarth's approximation consistently over-predicted the disturbance frequencies, the discrepancy was always less than 8%.

The critical N factor result for HDT plateau #1 ($N_{crit} = 7.2$) is within the bounds of sharp cone results obtained in multiple conventional wind tunnels with similar post-shock Pitot fluctuation spectra ($N_{crit} \approx 6 - 8$ observed in HLB and LaRC at Mach 6, and HWT-8 at Mach 8). The higher critical N factor for HDT plateau #3 ($N_{crit} = 9.4$) is due to the lower freestream fluctuations that were measured. The effect of small nose bluntness on the magnitude of the critical N factor was not investigated and must be acknowledged as a potential source of uncertainty.

T4 Stalker Tunnel: effect of wall-to-total temperature ratio and facility $Re_{unit,\infty}$

Boundary layer instability measurements were obtained over a range of facility Reynolds numbers ($Re_{unit,\infty} \approx 5.3 - 11.4 \times 10^6$ /m) and multiple wall-to-total temperature ratio distributions ($T_w/T_0 = 0.12 - 0.19$) in the T4 Stalker Tunnel at Mach 7 and flight total enthalpy ($H_0 \approx 2.5$ MJkg^{-1}).

The nominal condition was $M_\infty = 7.1$, $Re_{unit,\infty} = 11.4 \times 10^6$ /m, $T_w/T_0 = 0.13$. A peak in the PSD was observed at the two most downstream gauges ($Re_x = 2.6$ and $Re_x = 3.0$) at a frequency of $f \approx 725 - 790$ kHz. The peak frequency agreed

with estimates using Howarth's boundary layer thickness approximation and the non-dimensionalised frequency relationship proposed by Marineau et al. [54, 94] ($F = g/R^h$) to within 14%. There was a large discrepancy when compared to frequencies predicted by the PSE-Chem package ($> 30\%$), and this is the focus of ongoing work. The wavelet coefficient of the continuous wavelet transform increased in amplitude at the downstream locations, and the suspected wave packets occurred more frequently within the test time. A maximum integrated PSD amplitude of 8% was calculated. If the observed peak does correspond to the second mode, this result suggests that only the early stages of growth were captured[1]. This would not be particularly surprising, due to the short model (maximum $Re_x = 3.0 \times 10^6$) and the stabilizing effect of nose bluntness ($R_N = 1.6$ mm).

Three wall temperature distributions were tested using the nosetip heater cartridge. Results were inconclusive and the variation is expected to be within the shot-to-shot uncertainty. It is assumed that second mode stabilization was not observed due to insufficient wall temperatures being reached (i.e. $T_w/T_0 > 0.19$ is required), and possibly that the wall-heating occurred too far upstream. Results were presented at three facility Reynolds numbers: $Re_{unit,\infty} = 5.3$, 8.2, and 11.4 $\times 10^6$ /m. The peak frequency did not decrease as a function of $Re_{unit,\infty}$, as would be expected for the second mode disturbance. The integrated PSD results suggested that disturbance growth is observed further upstream at $Re_{unit,\infty} = 8.2 \times 10^6$ /m than at the nominal condition ($Re_{unit,\infty} = 11.4 \times 10^6$ /m). This trend has been observed in similar facilities, and may be due to an increase in freestream disturbance levels when the T4 facility Reynolds number is decreased.

8.1.3 Transition at high angles of attack

Boundary layer instability measurements were presented at $M_\infty = 7$, $Re_{unit,\infty} = 5.9 - 12.3 \times 10^6$ /m, $T_w/T_0 = 0.59 - 0.64$, and $\alpha = 5°$ - 13°. A sweep in Reynolds

[1] A maximum second mode amplitude of $\approx 20\%$ would be expected for an edge Mach number of ≈ 6.2 [54]

numbers and angles of attack using HDT plateau #3 allowed a more accurate comparison to the HIFiRE-1 flight transition results. Measurements were then presented for a fine resolution of azimuths at $\alpha = 8°$, with results compared between plateaus to investigate any effects of increasing freestream disturbance levels.

Comparison to HIFiRE-1 flight: sweep in Reynolds number and angles of attack

For all test conditions and angles of attack, the presence of instabilities moved upstream when progressing from the windward ray to the leeward ray. The leeward transition was observed earlier in HDT when compared to the HIFiRE-1 flight, with a discrepancy of $Re_x \approx 1.5 \times 10^6$ at $\alpha = 13°$. This discrepancy can be attributed to the higher freestream disturbance levels in HDT.

The transition on the windward ray in flight occurred at $Re_{x,tr} = 4.7 \times 10^6$ and $\alpha = 9°$ [32]. The HDT windward transition occurred later than flight ($Re_{x,tr} \geq 5.3$) at each iteration of angle of attack: $\alpha = 5°$ - $10°$. The discrepancy is believed to be due to the destabilizing effect of wall-cooling on the second mode instability in flight, which is expected to dominate along the windward ray. This assumes that the wall-cooling destabilization plays a more significant role in the transition process than the differences in freestream disturbance levels. The windward destabilization in flight is also expected to be the cause of the stable indented front that is observed between $\phi = 20° - 60°$. This feature was not observed in any HDT transition front results.

Disturbance characteristics at $\alpha = 8°$

Disturbance characteristics at $\alpha = 8°$ were investigated at a higher resolution of azimuths. A peak was observed at low frequencies, $f \approx 20 - 45$ kHz, and was assumed to correspond to the travelling crossflow instability. A second peak was observed at high frequencies, typically $f \approx 250 - 500$ kHz, and was assumed to

correspond to the secondary instabilities of stationary crossflow vortices or the second mode instability. For the high frequency peak, it was not possible to distinguish between the second mode and the stationary crossflow instability.

The suspected travelling crossflow peak was observed between $\phi = 22°$ - 180°, and $Re_x = 1.6 - 5.5 \times 10^6$. The high frequency peak was observed between $\phi = 22°$ - 147°, and $Re_x = 2.6 - 6.3 \times 10^6$. The disturbance peaks were observed further upstream when approaching the leeward ray. The peak frequencies also decreased at larger azimuths and Re_x, as would be expected due to the thickening boundary layer. These trends were observed for both the low and high frequency disturbance.

The suspected travelling crossflow instability was observed to coexist with the high frequency instability, likely to be the stationary crossflow mode. The travelling crossflow mode was frequently detected upstream of the high-frequency peak, and it had a larger integrated PSD amplitude at multiple locations (otherwise they matched quite closely). This did not necessarily suggest that transition is dominated by the travelling mode at these cone locations in the HDT. It is possible that the stationary crossflow vortices were growing in amplitude alongside the travelling mode, as the increase in vortex amplitude is not necessarily identifiable in the pressure fluctuation power spectra results. On multiple occasions, the PSD also showed a turbulent profile at high frequencies, whereas a low frequency travelling crossflow peak was still visible. This observation may indicate that the secondary instabilities of stationary crossflow vortices have actually destabilized the boundary layer at multiple locations.

Measurements were compared to the higher freestream disturbance environment of HDT plateau #1. The increase in freestream fluctuations caused the low frequency laminar PSD to increase. This is suspected to be due to the low frequency overlap with the freestream disturbance content, as measured in the post-shock Pitot pressure fluctuations. Both the low frequency and high frequency disturbances were also destabilized when the freestream disturbances increased.

8.2 Future work

Further work is required to completely characterise the freestream disturbances and boundary layer instabilities presented in this research. Suggestions are discussed below, however this list is by no means exhaustive.

Freestream disturbance characterisation in the HDT

The effect of Reynolds number was not investigated in this research. Future tests should therefore investigate the post-shock fluctuations at multiple conditions. The freestream fluctuations are expected to decrease when $Re_{unit,\infty}$ increases. It would be interesting to see whether this is observed in the HDT, and to what extent for each plateau.

Further work is required to make meaningful comparisons to Chaudhry's DNS results [197] (current results are presented in Appendix C). Firstly, it would be beneficial to compare the measured PSD ratios to DNS-simulations of the HDT Pitot probe geometries and flow conditions. The flow disturbance angle is still expected to play a significant role, however a more accurate simulation comparison would eliminate a lot of the other differences that currently exist (Mach number, shock standoff, etc.). A similar dataset using multiple cap geometries also exists for the HDT Mach 5 nozzle. This data should be processed and compared to a representative DNS-simulation to investigate the role of Mach number.

Finally, efforts are currently ongoing within the Oxford hypersonics group to develop Focused Laser Differential Interferometry (FLDI) capabilities. This would make it possible to measure the fluctuations in the freestream and calculate the transfer function directly.

Boundary layer instability results: $\alpha = 0°$

The HDT measurements can be processed to gain additional insight into the second mode instability. The bicoherence should be calculated to ensure that the peaks in the PSD are statistically significant. It may also be possible to calculate the wave speeds using the cross-correlations of successive PCB132 sensors. These results should be compared to observations using Focused Schlieren, to completely characterise the second mode disturbance in the HDT (for example, Refs. [78, 79, 80, 212, 213] have done this successfully). In future experiments, measurements should be taken using a perfectly sharp nosetip to enable comparisons to results in the literature and Pate's correlation.

The T4 instability measurements should be compared to the downstream thin film heat transfer results (separation between sensors $\approx$ 200 mm). The downstream heat transfer measurements may provide some insight into the instability observations made upstream. If future tests are conducted, the conditions and model must be prepared so that second mode destabilization is also observed. This may involve a sharp nosepiece, higher $Re_{unit,\infty}$, and particularly a longer model. The maximum disturbance amplitude and breakdown to turbulence should be captured, to be truly confident in the current dataset and enable comparisons to stability codes. The discrepancy between the measured frequency and the PSE-Chem predicted frequency must also be resolved.

Boundary layer instability results at high angles of attack

Further work is required to improve the understanding of instabilities at high angles of attack. In the first case, results should be presented along an approximate streamline path rather than along model-fixed azimuths. This will inevitably still be approximate due to the resolution of the sensors in the HDT model. Results presented by the Purdue group have also shown that instability spectra varies when measuring the crest or trough of individual vortices [115, 112, 114, 211, 99,

100]. Nevertheless, it is believed that presenting the progression of PSDs along an approximate flow streamline may provide a physical insight into the instability development and breakdown. Figure 8.1 shows an example of the computed streamlines using parameters from Cheng's correlation [202, 203].

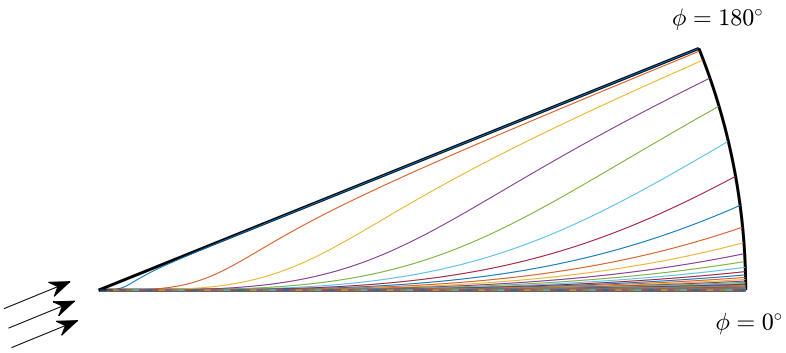


Figure 8.1: Computed streamlines around a sharp cone at $\alpha = 8°$. Parameters computed using Cheng's correlations [202, 203] for the nominal condition: $M_\infty = 7.0$, $Re_{unit,\infty} = 12.3 \times 10^6$ /m, $T_w/T_0 = 0.64$.

The continuous wavelet transform should be calculated to investigate the disturbance behaviour as a function of time, rather than purely a summary from the entire test-time interval. The bicoherence for sensors along a particular streamline path should also be calculated to ensure that the progression of the observed disturbances is actually statistically significant. Modifications to the cone are required to track the wave speeds and angles, as the resolution of the PCB132 sensors is not adequate to track the development of individual disturbances. This would be worthwhile doing in any future campaigns.

Finally, the critical N factors for individual disturbances should be calculated for various approximate streamlines around the cone. This would provide insight into the critical N factor for different instabilities before breakdown. Work must be done to find a suitable initial amplitude (A_0) for the N factor calculations, as PSE-Chem computations are currently not available at high angles of attack. Future tests should also investigate the instabilities and transition front using a sharp nosepiece, so that results can be compared to more datasets presented in the literature.

Appendices

A

Oxford 7° Cone Models: instrumentation locations and roughness characterization

This appendix details the instrumentation locations and roughness characteristics for the HDT 7° Cone Model and the RST 7° Cone Model. Additional details about the HDT 7° Cone Model and RST 7° Cone Model can be found in Section 3.4.1 and Section 3.4.2, respectively.

A.1 HDT 7° Cone Model

Instrumentation

The HDT 7° Cone Model was instrumented with pressure sensors (Kulite XTEL-140M and PCB132A31) and heat transfer gauges (thin-film [168] and diamond calorimeter [169]). The instrumentation locations are presented in Table A.1, where axial locations are from the apex of a theoretically-sharp nosetip. These locations were chosen to match post-flight experiments undertaken in DLR's H2K facility in 2014 [36, 35].

		Pressure				Heat transfer	
	sharp apex	PCB132		Kulite		Thin-film/Diamond	
	x (mm)	Name	$\varphi(°)$	Name	$\varphi(°)$	Name	$\varphi(°)$
front segment	139.8	PCB1A PCB1C	0 180	-		-	
	180.5	PCB2B PCB2D	90 270	-		-	
	219.5	PCB3A PCB3C	0 180	-		-	
	260.5	PCB4B PCB4D	90 270	-		-	
rear segment	301.5	PCB5A PCB5C	0 180	-		TFG1	225
	350.5	PCB6B PCB6D	90 270	-		TFG2 DHTG1	225 45
	399.5	PCB7A PCB7C	0 180	-		TFG3	225
	427.7	-		Kulite1	0	-	
	456.5	PCB8B PCB8D -	90 270	Kulite2 Kulite4 Kulite5	0 45 315	TFG4	225
	485.7	-		Kulite3	0	-	
	521.5	PCB9A PCB9C	0 180	-		TFG5 DHTG2	225 45
	549.9	PCB10B	90	-		TFG6	225

Table A.1: Instrumentation locations in the HDT 7° Cone Model. 'x' is the axial distance from the apex of a theoretically-sharp nosepiece to the gauge.

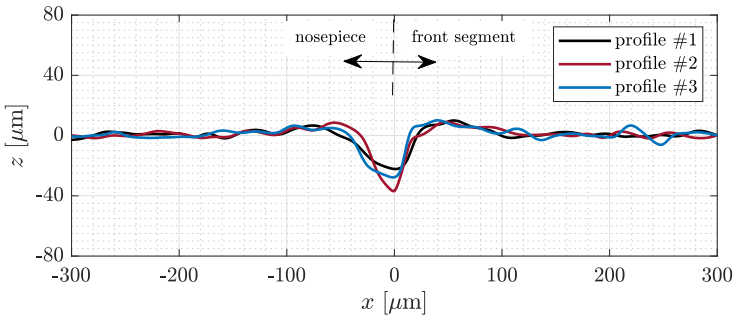
Roughness characterization

The surface roughness was determined using an Alicona InfiniteFocus camera. The camera allows for complete 3D surface analysis, providing high-resolution roughness measurements over a targeted area. The roughness was characterised at each segment (nosetip, front & rear). Multiple profiles were taken for each roughness targeted area. The average roughness (R_a) and rms roughness (R_q) for the profiles are summarised in Table A.2. The mean and standard deviation roughness values are calculated from multiple profiles (at least three).

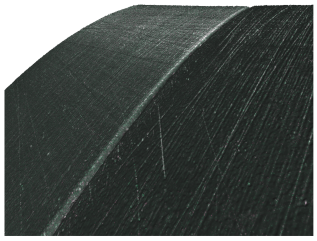
HDT model part	Material	R_a (μm)		R_q (μm)	
		mean	std	mean	std
Nosepiece	EN36B (hardened)	1.73	0.24	2.26	0.26
Front segment	EN36B (hardened)	1.78	0.07	2.28	0.09
Rear segment	Aluminium 7375	0.88	0.15	1.10	0.19
PCB sensor	-	2.53	-	3.06	-

Table A.2: HDT 7° Cone Model roughness information. R_a is the average roughness of the profile, and R_q is the rms roughness of the profile. The mean and standard deviation (std) of multiple profiles are presented. Only one profile was taken for the PCB sensor, so no standard deviation is calculated.

The Alicona InfiniteFocus camera was used to characterise the step between the nosepiece and the front segment, as well as the step that would be expected for a PCB132 sensor. Figure A.1 shows the results for the junction between the nosepiece and the front segment, with Figure A.2 showing the results for the artificial PCB132 sensor. For each result, three representative profiles are plotted along with an image of the area from which the profiles were generated. For the junction, the peak-to-peak step seems to be in the order of $\approx 30\mu$m. For the artificial PCB132 sensors, the peak-to-peak step is in the order of $\approx 60\mu$m.

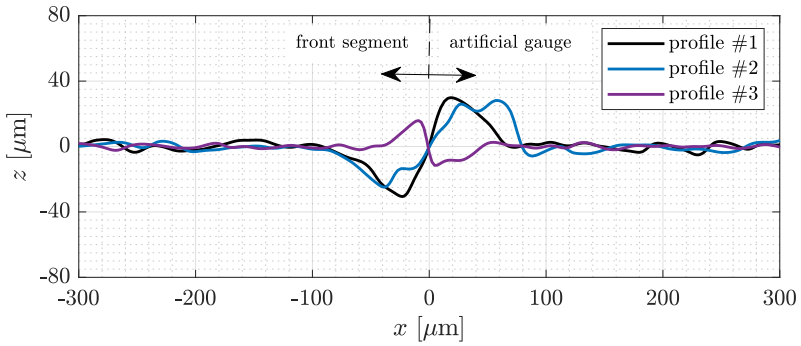


(a) Roughness profiles

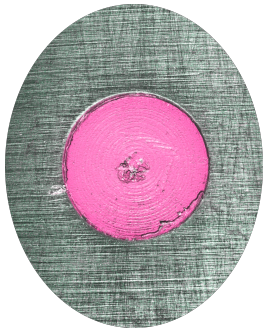


(b) Camera image

Figure A.1: Roughness characterisation for the junction between the front segment and the nosepiece.



(a) Roughness profiles



(b) Camera image

Figure A.2: Roughness characterisation for an artificial PCB132 sensor inside the HDT 7° cone model.

A.2 RST 7° Cone Model

Instrumentation

The RST 7° Cone Model was instrumented with pressure sensors (Kulite XCEL-152 and PCB132A31) and heat transfer gauges (thin-film and diamond calorimeter). The instrumentation locations are presented in Table A.3, where axial locations are from the apex of a theoretically-sharp nosetip. These instrumentation locations are scaled down from the HDT 7° Cone Model, with the scaling factor equal to the ratio of the cone model lengths.

Roughness characterization

The surface roughness for the RST 7° cone model is summarised in Table A.2. The average roughness (R_a) and rms roughness (R_q) are provided for the nosepiece, front segment and the rear segment, with the quoted values being the mean and standard deviation of multiple measurement profiles (at least three). The values presented for the PCB132 sensor and the neoprene tubing are for one profile, so no standard deviation values are provided.

The camera was used to characterise the typical discontinuity for a PCB132 sensor inside the neoprene housing. Figure A.3 shows the results for multiple profiles, illustrating the step between the model and the neoprene as well as the discontinuity between the neoprene and the sensor itself. Profile #3 has a significantly larger step than the others, with a peak-to-peak step of $\approx 200\mu$m. A discontinuity of this magnitude is definitely a concern, as this may be in the order of 10% of the boundary layer thickness[1]. The location of the neoprene-to-PCB step is also different for profile #2. The reason for this is unknown, though it may be that the gauge has compressed the neoprene sleeve in one direction more than the other. Figure A.3b is an image of the area from which the profiles were generated.

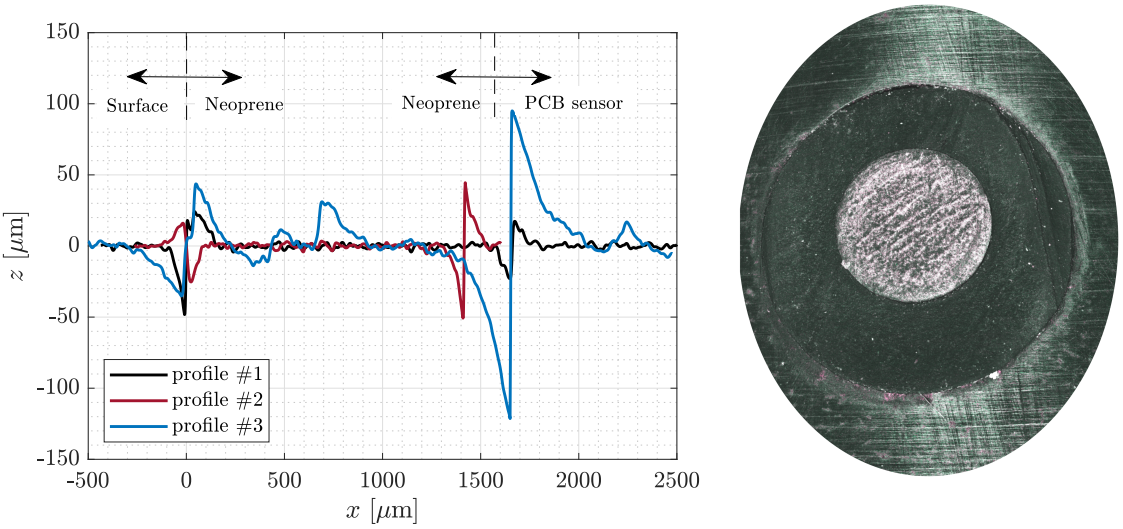
[1]To minimize the surface discontinuities, the neoprene tubing was cut only after it was fixed into the cone. It was cut using a flexible blade in a single motion, with the blade able to bend around the curvature of the cone surface.

	sharp apex x (mm)	Pressure PCB132 Name	φ(°)	Pressure Kulite Name	φ(°)	Heat transfer Thin-film/Diamond Name	φ(°)
front segment	124.6	PCB1A	0	-		-	
	151.1	PCB2A	0	-		-	
		PCB2C	180				
	179.0	PCB3B	90	-		TFG1	0
		PCB3D	270			DHTG1	180
	206.9	PCB4A	0	-		TFG2	90
		PCB4C	180			DHTG2	270
	240.2	PCB5B	90	-		TFG3	0
		PCB5D	270			DHTG3	180
	267.6	PCB6A	0	-		TFG4	90
		PCB6C	180			DHTG4	270
rear segment	311.3	PCB7B	90	-		TFG5	0
		PCB7D	270			DHTG5	180
	326.3	-		-		TFG6	90
	341.1	-		-		TFG7	90
	355.8	PCB8A	0	Kulite1	45	TFG8	90
		PCB8C	180	Kulite2	225	DHTG6	270
		PCB8E	315	-		-	
	378.0	-		-		TFG9	90

Table A.3: Instrumentation locations in the RST 7° Cone Model. 'x' is the axial distance from the apex of a theoretically-sharp nosepiece to the gauge.

HDT model part	Material	R_a (μm) mean	std	R_q (μm) mean	std
Nosepiece	EN36B (hardened)	1.73	0.24	2.26	0.26
Front segment	EN36B (hardened)	1.78	0.07	2.28	0.09
Rear segment	EN24T	1.81	0.10	2.88	0.29
PCB sensor	-	2.53	-	3.06	-
Neoprene housing	Neoprene 6705	1.44	-	1.83	-

Table A.4: HDT 7° Cone Model roughness information. R_a is the average roughness of the profile, and R_q is the rms roughness of the profile. The mean and standard deviation (std) of multiple profiles are presented. Only one profile was taken for the PCB sensor roughness and the Neoprene sleeve roughness.



(a) Roughness profiles **(b)** Camera image

Figure A.3: Roughness characterisation for a PCB132 sensor housed inside neoprene tubing for the RST 7° cone model.

B

HDT P_{fill} calculation: pressure loss across the plug valve

This appendix details the correlations used to calculate the required barrel fill pressure for a targeted condition at Mach 7.

The experimenter uses the total temperature history and viscosity model to calculate what supply pressure is needed for the chosen test time plateau. The plug valve pressure loss has therefore been characterised so that the experimenter can determine what P_{fill} is required to reach the targeted stagnation pressure for the designated facility plateau. The relationship between P_{fill} and P_0 for each facility plateau is shown in Figure B.1, with the linear relationships given in Equations B.1 - B.4.

Plateau #1: $$P_{fill} = 1.0528 \times P_{0,\text{plat.1}} + 14.226 \quad \text{(B.1)}$$

Plateau #2: $$P_{fill} = 1.1395 \times P_{0,\text{plat.2}} + 8.880 \quad \text{(B.2)}$$

Plateau #3: $$P_{fill} = 1.2142 \times P_{0,\text{plat.3}} + 29.231 \quad \text{(B.3)}$$

Plateau #4: $$P_{fill} = 1.3115 \times P_{0,\text{plat.4}} + 1.1711 \quad \text{(B.4)}$$

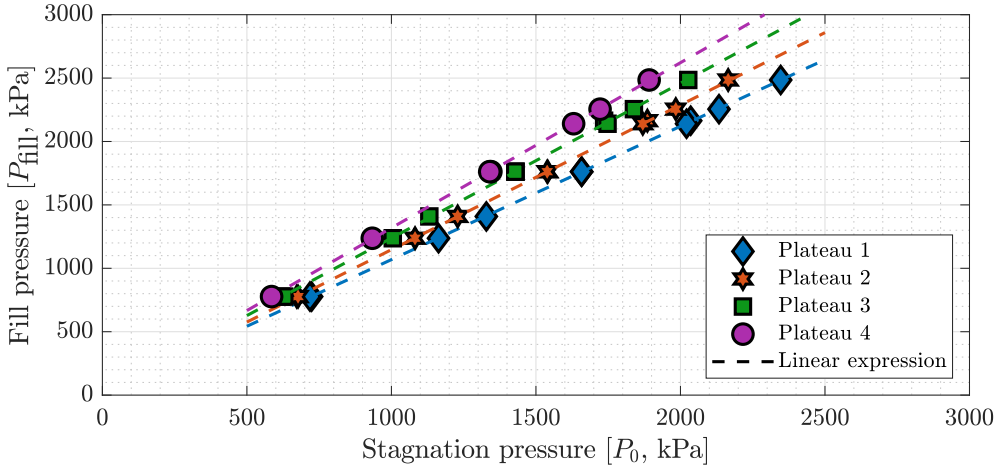


Figure B.1: HDT facility required P_{fill} as a function of targeted supply pressures over multiple facility plateaus. The dashed line is the linear relationship used for the Mach 7 nozzle ($T_{fill} \approx 500$ K), as described in Equations B.1 - B.4.

C

Freestream Disturbance Characterization: Frequency-dependent PSD ratio between probes

This appendix details ongoing work that compares freestream post-shock Pitot pressure fluctuations using multiple probe geometries to DNS simulations [197]. The ultimate objective is to back out the pre-shock freestream disturbance environment. The motivation and method is briefly described below, before presenting the comparisons to HDT measurements.

Chaudhry et al. use DNS to calculate the transfer function, $\chi(f)$, for freestream acoustic disturbances that propagate at between 100° to 130° relative to the bulk flow [197]. Experiments using Pitot probes are only able to measure the post-shock power spectra, $\mathrm{PSD_t}$. Chaudhry et al. take the ratio of transfer functions for multiple probe geometries to cancel the freestream disturbance term, PSD_∞, as shown in Equation C.2 [214, 215, 197]. $\mathrm{R}_{a,b}$ is the frequency-dependent ratio between probes a and b. It can be determined experimentally using post-shock PSDs from different probes, or computationally from the DNS of the two probes.

The freestream disturbances are then known from the input of the DNS.

$$\chi_t(f) = \frac{\mathrm{PSD_t}}{\mathrm{PSD_\infty}} \tag{C.1}$$

$$\mathrm{R}_{a,b} = \frac{\chi_a}{\chi_b} = \frac{\mathrm{PSD}_a}{\mathrm{PSD}_b} \tag{C.2}$$

DNS results show that the transfer function is substantially affected by the incident angle of acoustic disturbances [197], and by the Pitot probe geometry itself [215]. Chaudhry et al. suggest that the resonant frequency and amplitude of the transfer function decreases as the disturbance angle decreases [197]. Simulations were compared to measurements taken in Purdue University's BAM6QT facility at Mach 6. Kulite XCE-062-15A pressure sensors were used in multiple probe geometries ($r_{\text{no-sleeve}} = 0.83$ mm, $r_{\text{small}} = 1.50$ mm, $r_{\text{medium}} = 3.00$ mm, $r_{\text{large}} = 3.60$ mm). Figure C.1 shows PSD-ratio results for the $\frac{\mathrm{PSD_{large}}}{\mathrm{PSD_{small}}}$ case, compared to Chaudhry's DNS-simulations (taken from Figure 10d in Ref. [197]).

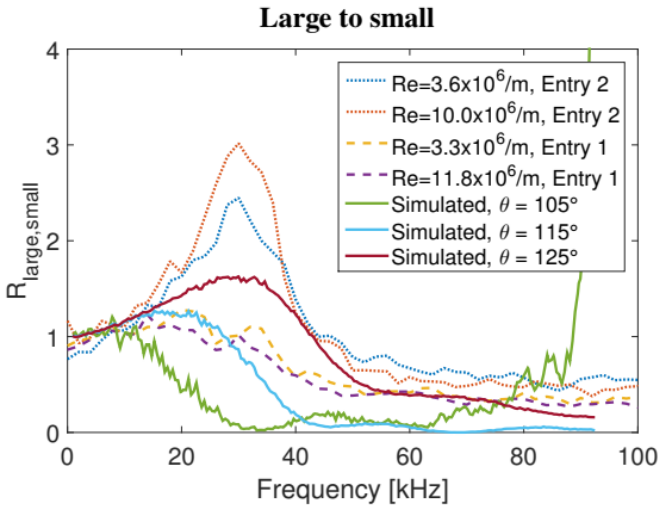


Figure C.1: Comparison of Purdue measured PSD ratio and Chaudhry's DNS computations. Taken from Figure 10d in Ref. [197]. Geometries are: $r_{\text{Purdue,large}} = 3.60$ mm, and $r_{\text{Purdue,small}} = 1.50$ mm.

Duan et al. performed DNS simulations of the turbulent boundary layer along the nozzle wall, and found that the disturbance angle propagated at $\theta = 111°$ - 120° relative to the flow direction [216]. It should be noted that these nozzle DNS

freestream conditions were at Mach 6. Duan et al. found that as the Mach number increases, the free-stream acoustic fluctuations have shallower orientation of wave fronts relative to the flow direction [216]. The HDT Mach 7 freestream disturbances would therefore be expected to propagate at lower θ. Chaudhry et al. also suggest that the incident angle can be estimated by $\theta = 90° + \arcsin(\frac{1}{M})$, where $\arcsin(\frac{1}{M})$ represents the Mach angle. This would result in an incident angle of $\theta = 98.2°$ for the HDT Mach 7 freestream.

C.1 HDT cap geometry PSD rebuild & R results

The Pitot probes in the Oxford Rake have threads so that multiple cap sizes can be tested. Key dimensions for the "small" (no-cap), "medium", and "large" Pitot geometries are given in Table C.1. The shock standoff distance is calculated from simulations using Eilmer4[1].

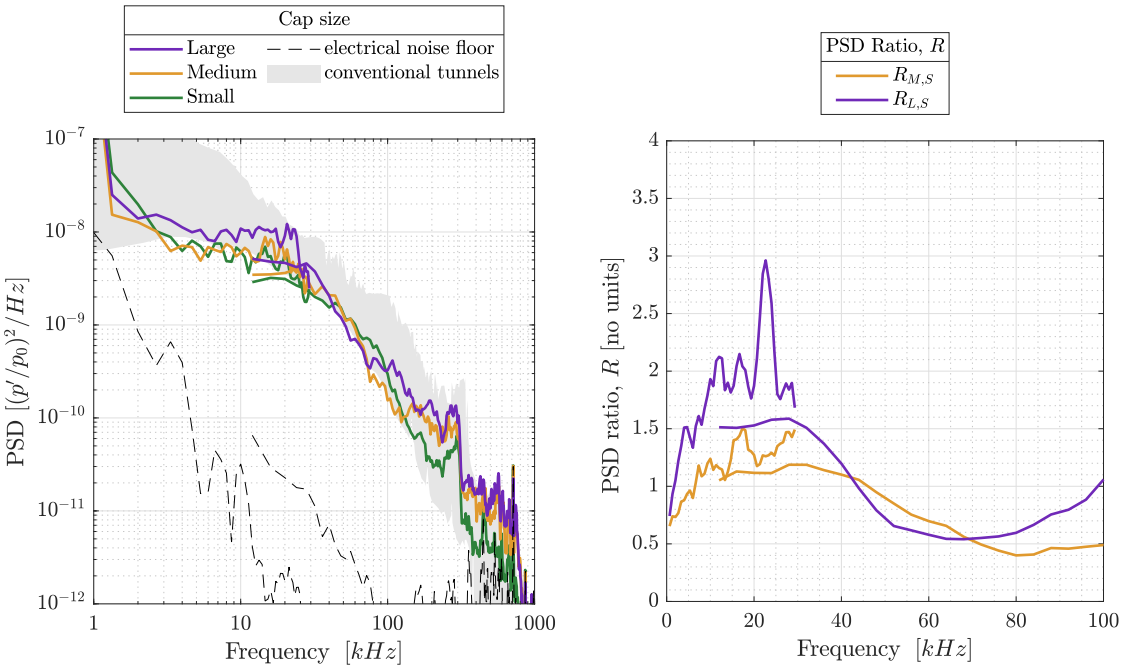
Probe name	Total radius (r_{tot}, mm)	Fillet radius (mm)	Shock standoff (Δ, mm)
Small (no cap)	3.18	1.00	1.28
Medium	4.78	1.00	2.10
Large	6.36	1.00	2.91

Table C.1: Pitot probe details for multiple cap sizes. The probe geometry is consistent for PCB and Kulite sensors.

The PSD ratio (R) is calculated for two cases: $R_{\mathrm{M,S}} = \frac{\mathrm{PSD_M}}{\mathrm{PSD_S}}$, and $R_{\mathrm{L,S}} = \frac{\mathrm{PSD_L}}{\mathrm{PSD_S}}$. The ratio is sensitive to errors in the individual PSDs. For this reason, the calculation of R is best done using two geometries with sufficiently different power spectra. For the HDT experiments, this is achieved using the three cap geometries: $r_{\mathrm{small}} = 3.18$ mm ("small" or "S"), $r_{\mathrm{medium}} = 4.78$ mm ("medium" or "M") and $r_{\mathrm{large}} = 6.36$ mm ("large" or "L").

[1]The axisymmetric simulation is steady state with viscous terms included, and a perfect gas assumed.

The effect of probe geometry on PSD rebuild is presented in Figure C.2a. These are the individual PSDs that are used to generate the PSD ratios, R, shown in Figure C.2b. Results are presented for facility plateau #1, and for the Pitot probe located on the nozzle centreline[2]. Results are only shown for facility plateau #1 due to the superior signal to electrical noise ratio.



(a) PSD rebuild **(b)** PSD ratio, R

Figure C.2: Effect of Pitot probe geometry on post-shock pressure fluctuations for the HDT Mach 7 nozzle plateau #1. Results are shown for Pitot probe located on the nozzle centreline.

C.2 Low frequency results: 1 kHz ≤ f < 100 kHz

The PSD rebuild is clearly dependent on cap geometry. The small geometry PSD is at a lower magnitude than the larger geometries over most frequencies, resulting in $R > 1$. The PSD ratio tends to have a peak value of $R \approx 1 - 2$ at $f \approx 30$ kHz,

[2]Results have been processed for other radial distances. At first glance, the trends seem to be consistent for each coreflow location. For the purpose of this research, only the centreline result is discussed.

and steadily decreases to $R \approx 0.25 - 0.5$ at $f \approx 70 - 100$ kHz. A similar decay is observed in the DNS simulations and Purdue measurements, as shown in Figure C.1 [197]. Chaudhry et al. showed that the decay in the transfer function ratio is more dependent on the angle that the flow disturbances propagate than the differences in probe geometries [197].

Figure C.3 shows the HDT centreline results superimposed onto the Chaudhry DNS simulations for their closest geometry case, $S_{large,small}$ [197]. It should be noted that the geometries used for this case are still not particularly close to the ones used in the HDT campaign[3], despite both experiments having $r_{large}/r_{small} \approx 2$. The HDT results seem to agree quite well with the DNS simulations with freestream disturbances at $\theta_{\text{dist.}} = 125°$. For both sets of results, a peak in the ratio is observed at $f \approx 20 - 30$ kHz. The ratio then decays until $f \approx 80$ kHz. The 120° disturbance angle is slightly larger than the range predicted by Duan et al. ($\theta = 100° - 120°$) [216]. The results don't agree with the $\theta = 105°$ simulation, which is the closest case to the $\theta = 98°$ incident angle that was predicted when using $\theta = 90° + \arcsin(\frac{1}{M})$.

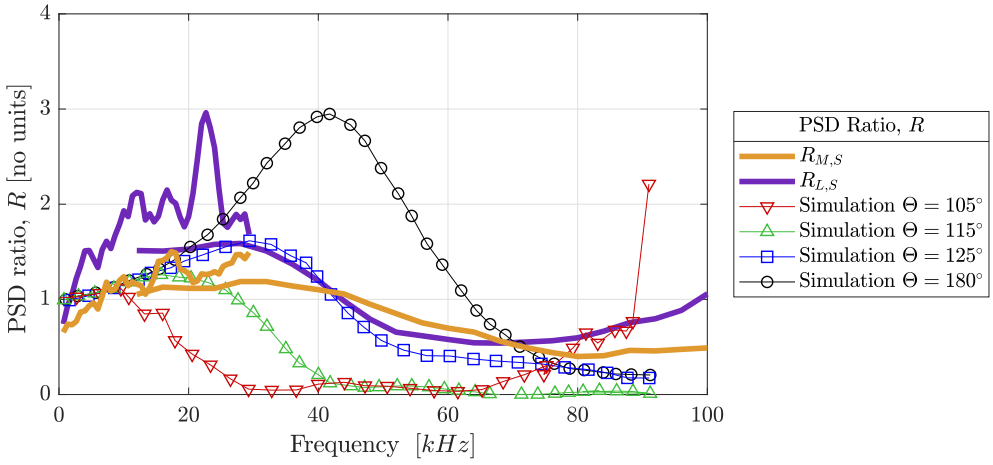


Figure C.3: Comparison of PSD ratio R to DNS simulations from Chaudhry et al. (for the Purdue probe geometry and flow conditions, taken from Fig 9d in Ref. [197]). HDT conditions are $M_\infty = 7.0$, $Re_{unit,\infty} = 10.7 \times 10^6$ /m. Gauge location is on centreline, $r_{large} = 6.36$ mm and $r_{small} = 3.18$ mm.

[3]DNS/Purdue have $r_{large} = 3.60$ mm and $r_{small} = 1.50$ mm with sharp corners, whilst HDT have $r_{large} = 6.36$ mm and $r_{small} = 3.18$ mm with a fillet radius of 1 mm

Low frequency limit

Chaudhry et al. found that the transfer function at the low-frequency limit is independent of geometry [197]. Physically, Chaudhry explained that the length scale of the disturbance increases as the frequency decreases, and that the disturbance length is expected to be larger than the Pitot probe in the low frequency limit. The measured PSD is therefore expected to be the same for each Pitot geometry, so should tend to $R = 1$ as seen in the Chaudhry DNS results. The low frequency experimental PSD-ratios are at $\approx 0.7 - 0.8$. The reason for the small discrepancy unknown.

PSD ratio drop-off frequency

The peak frequency and amplitude decreased with disturbance angle in the DNS simulations [197]. This has been attributed to phase interference of disturbances reflecting between the Pitot probe face and the shock. Chaudhry et al. equated the freestream spanwise wavelength with the transducer diameter to propose an interference frequency, f_{pi}, described by

$$f_{pi} = \frac{\bar{u}\cos\theta + \bar{c}}{2r_{tra}\sin\theta} \tag{C.3}$$

Where $\bar{u}$ is the average streamwise velocity, θ is the disturbance angle, $\bar{c}$ is the average speed of sound, and r_{tra} is the Pitot probe transducer radius. This interference frequency was found to correlate well with the drop-off in transfer function. As R is the ratio of two transfer functions, the dropoff in R should correlate reasonably well with the interference frequency for the larger geometry, as this tails off at the lowest frequency[4]. When using the HDT conditions ($M = 7.0$, $T_\infty = 49$ K) and large/medium probe geometries ($r_{large} = 6.36$ mm, $r_{med} = 4.77$ mm), a disturbance frequency magnitude of $f_{pi,large} = 3.2 - 4.1 \times 10^4$ Hz and $f_{pi,med} = 4.2 - 5.4 \times 10^4$ Hz is calculated for assumed disturbance angles of $\theta = 120°$

[4]For example, compare the drop-off frequency of Figure 8 to those of Figure 9 in Ref.[197]

$-125°$. This agrees quite well with the drop-off frequency observed experimentally in Figure C.3.

C.3 High frequency results: $f \geq 100$ kHz

Chaudhry et al. have observed smaller-amplitude secondary resonances in the transfer function at higher frequencies [215]. An example is shown in Figure C.4 for Purdue's BAM6QT probe at $M_\infty = 6$, $T_0 = 500$ K, with flow-parallel disturbances assumed (taken from Figure 7 in Ref. [215]). The resonant mechanism is an acoustic disturbance reflecting between the shock and Pitot probe face. They noted that the valleys in the transfer function corresponded to destructive interference of the acoustic disturbances. These valleys correlated with multiples of the standoff frequency,

$$f_\Delta = \frac{\sqrt{\gamma R T_0}}{2\Delta} \tag{C.4}$$

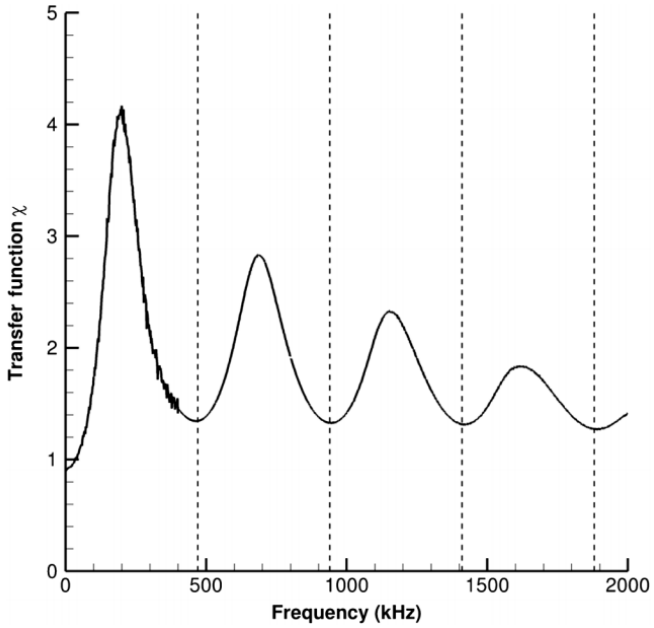


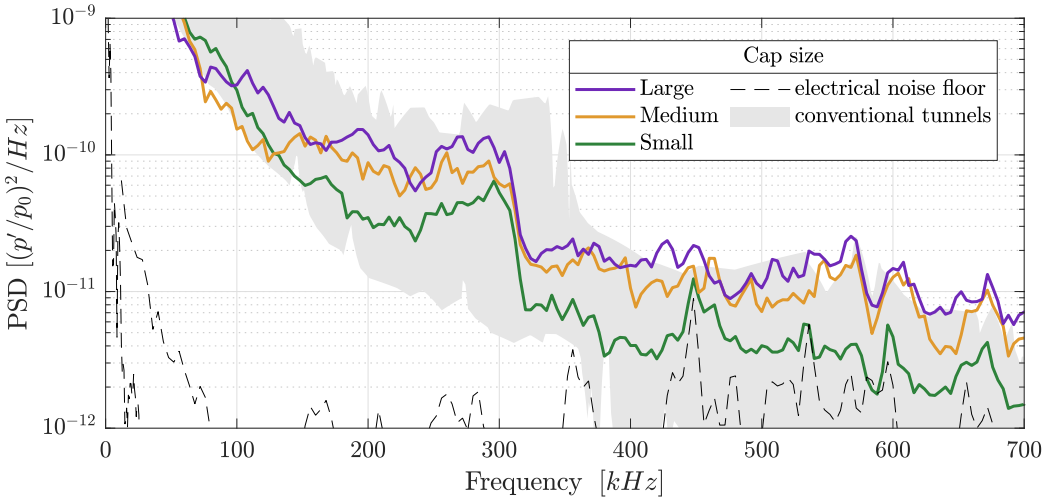
Figure C.4: Transfer function for the BAM6QT probe, $M_\infty = 6$, $T_0 = 500$ K. Taken from Figure 7 in Ref. [215]. The dashed lines correspond to integer multiples of the standoff frequency, f_Δ.

A similar high-frequency peak and valley structure may therefore be present at high frequencies in the HDT experimental data. Figure C.5 shows the centreline PSD rebuild and ratio results, with a focus on the high frequency content. The electronic noise floor corrupts the flow PSD from $f \approx 500 - 700$ kHz, as shown in Figure C.5a. For this reason, the PSD ratio result is only shown up to ≈ 700 kHz, and even some of the features above $f \approx 450$ kHz need to be treated with caution. Multiples of the standoff frequency for the large Pitot probe are included as dashed lines. This result may show evidence of valleys in the large Pitot geometry transfer function, however the result is inconclusive for multiple reasons. These are detailed below.

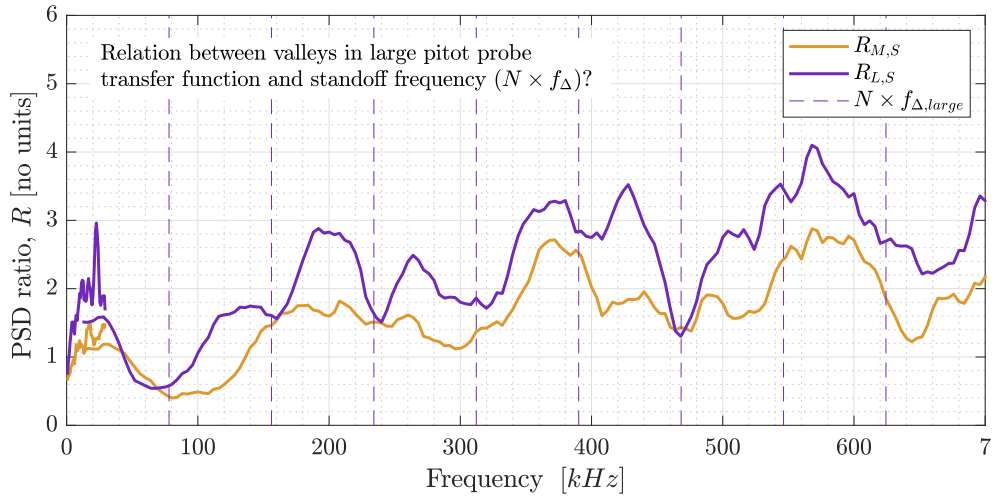
1. The result presented in Figure C.4 is for flow-parallel disturbances. Chaudhry's recent work has indicated that the transfer function resonance changes significantly with disturbance angle, as it shifts to lower frequencies and smaller amplitudes. The frequency of the higher resonances would therefore be expected change when the flow-parallel assumption is relaxed, as the disturbance resonance is no longer a two-dimensional problem.

2. If the transfer function valleys are observed at the standoff frequency for angled disturbances, these valleys will be difficult to identify in the PSD ratio, R. The peaks and valleys for each gauge will be out of phase, due to the differences in shock standoff distance (Δ) for the Pitot geometries. It will therefore be difficult to identify features in the ratio of two PSD results with valleys that are out-of-phase.

3. The frequencies that are of interest overlap with the high-frequencies where PCB132 sensors have shown non-uniform sensitivity. The sensitivity variation must not be mistaken as flow features (for example, the feature at $f = 300$ kHz in Figure C.5a is sensor resonance).



(a) high frequency PSD



(b) high frequency PSD ratio

Figure C.5: PSD rebuild and ratio results ($R_{L,S}$ and $R_{M,S}$) with a focus on the higher frequency PCB132 measurements. Results are for the centreline Pitot probe.

D

HDT boundary layer instability measurements at each azimuth: $Re_{unit,\infty} = 12.3 \times 10^6$ /m, $\alpha = 8°$

This appendix provides details of the power spectral density and rms fluctuation amplitudes for each of the azimuths presented in the high angle of attack results in Section 7.6. Results are presented at a fine resolution of azimuths: $\phi = 0°$, 22°, 33°, 45°, 57°, 67°, 90°, 123°, 135°, 147°, 157°, and 180°. The fluctuations are normalised by the cone surface pressure at the specific azimuth. The rms amplitudes are calculated by integrating the PSD over two frequency bands. The lower frequency band corresponds to 11 - 80 kHz, where a peak is believed to represent the travelling crossflow instability. The higher frequency band corresponds to 100 - 600 kHz, and is believed to correspond to the stationary crossflow instability or second mode instability. The PSD results and subsequent rms amplitudes are presented for each azimuth below.

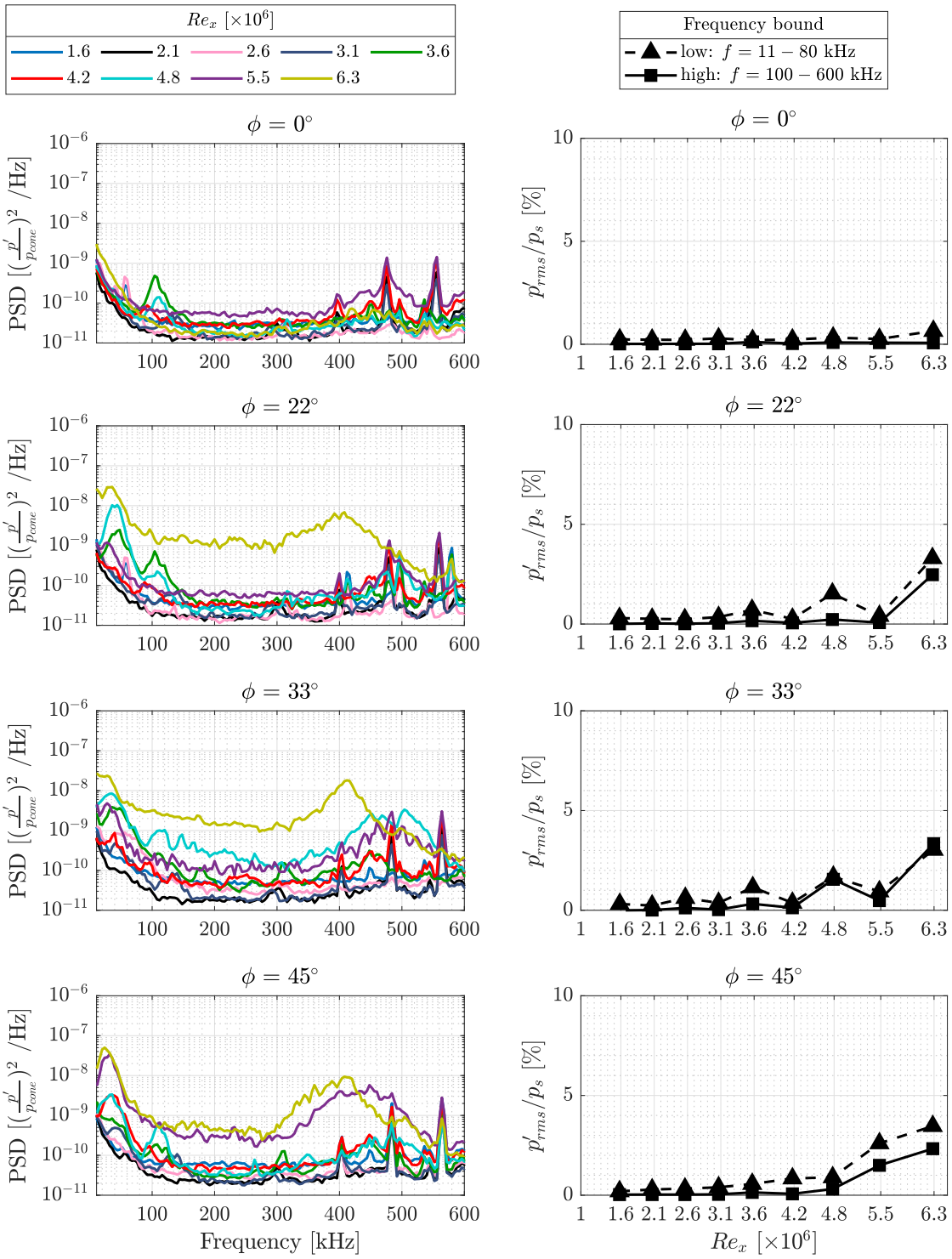


Figure D.1: HDT Condition 3: $M_\infty = 7.0$, $Re_{unit,\infty} = 12.3 \times 10^6$ /m, $\alpha = 8°$, $T_w/T_0 = 0.64$. Progression of surface pressure power spectra and integrated power content (f = 11 - 80 kHz and f = 100 - 600 kHz) as a function of azimuth around the model

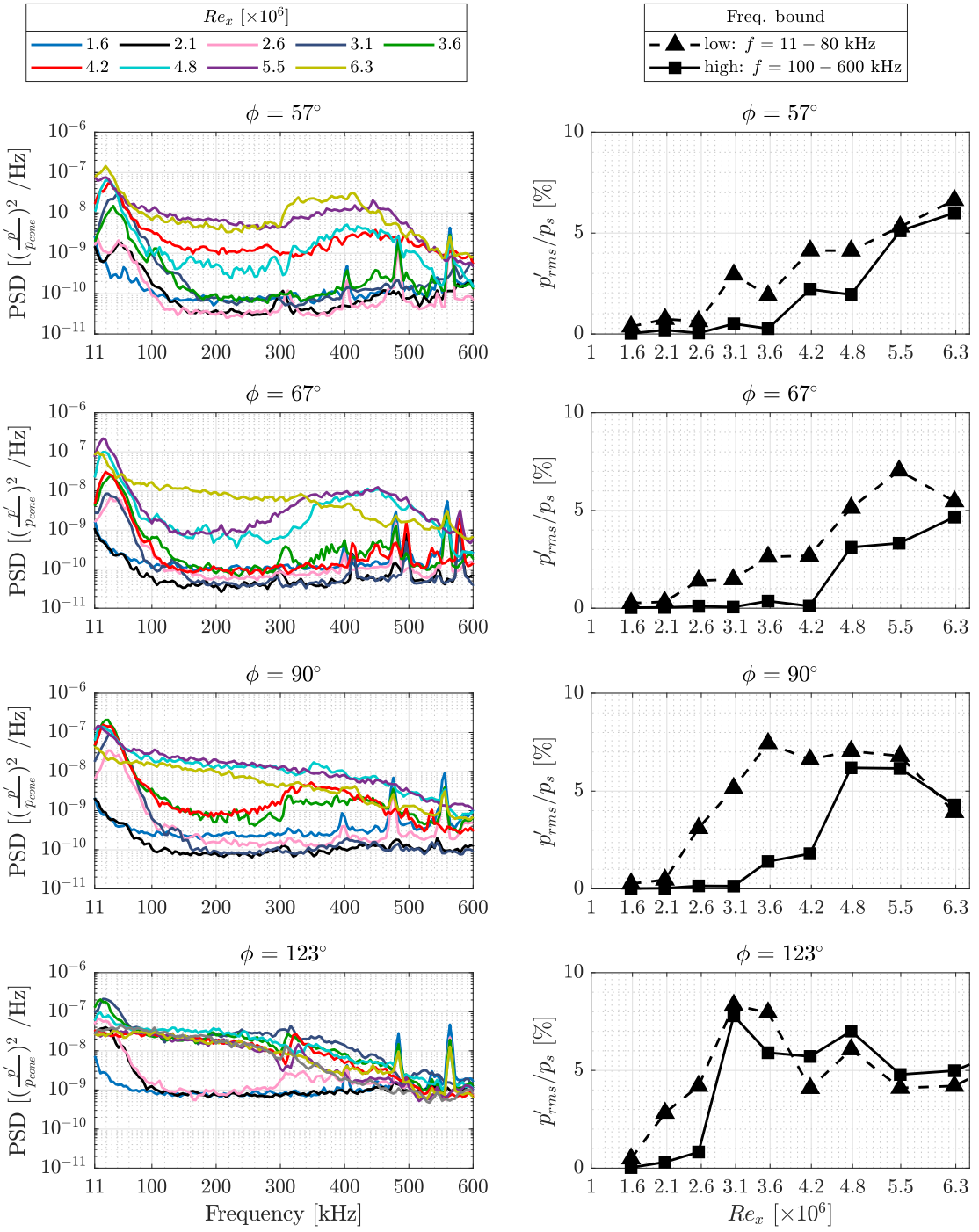


Figure D.1: HDT Condition 3: $M_\infty = 7.0$, $Re_{unit,\infty} = 12.3 \times 10^6$ /m, $\alpha = 8°$, $T_w/T_0 = 0.64$. Progression of surface pressure power spectra and integrated power content (f = 11 - 80 kHz and f = 100 - 600 kHz) as a function of azimuth around the model (continued)

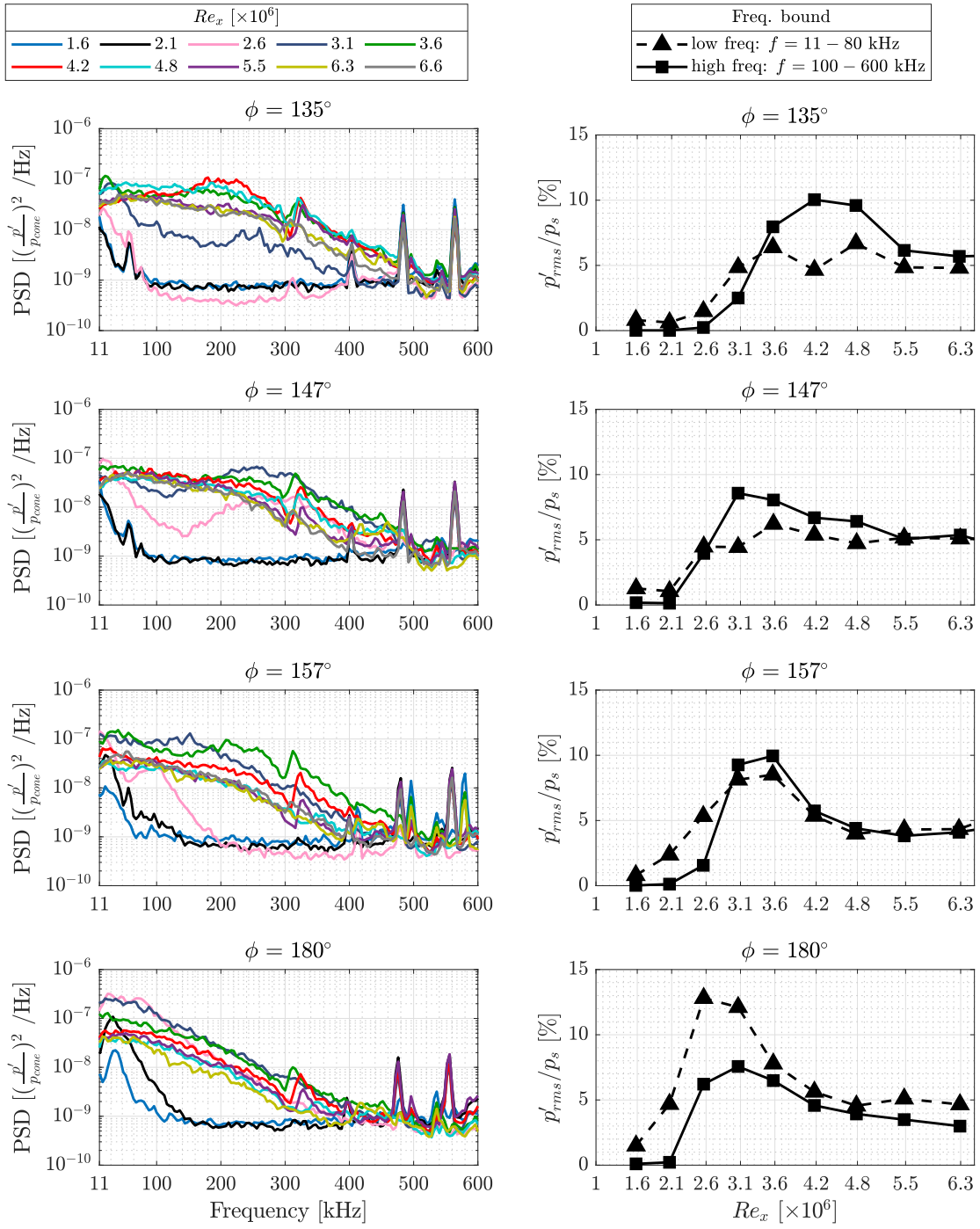


Figure D.1: HDT Condition 3: $M_\infty = 7.0$, $Re_{unit,\infty} = 12.3 \times 10^6$ /m, $\alpha = 8°$, $T_w/T_0 = 0.64$. Progression of surface pressure power spectra and integrated power content (f = 11 - 80 kHz and f = 100 - 600 kHz) as a function of azimuth around the model (continued)

References

[1] A. Martellucci, L. Chaump, D. Rogers, et al. "Experimental Determination of the Aeroacoustic Environment about a Slender Cone". In: *AIAA Journal* 11.5 (May 1973), pp. 635–642. ISSN: 0001-1452. DOI: 10.2514/3.50503.

[2] R. Johnson, M. Macourek, and H. Saunders. "Boundary layer acoustic measurements in transitional and turbulent flow at M infinity equals 4.0". In: Aerodynamic Testing Conference. American Institute of Aeronautics and Astronautics, Apr. 1969. DOI: 10.2514/6.1969-344.

[3] S. R. Pate and M. D. Brown. *Acoustic Measurements in Supersonic Transitional Boundary Layers*. AEDC-TR-69-182. Oct. 1969.

[4] J. M. Cassanto and D. A. Rogers. "An Experiment to Determine Nose Tip Transition with Fluctuating Pressure Measurements". In: *AIAA Journal* 13.10 (Oct. 1975), pp. 1257–1258. ISSN: 0001-1452. DOI: 10.2514/3.60533.

[5] S. P. Schneider. "Hypersonic laminar–turbulent transition on circular cones and scramjet forebodies". In: *Progress in Aerospace Sciences* 40.1 (2004), pp. 1 –50. ISSN: 0376-0421.

[6] T. C. Lin. "Influence of laminar boundary-layer transition on entry vehicle designs". In: *Journal of Spacecraft and Rockets* 45.2 (2008), pp. 165–175.

[7] H. L. Reed, E. Perez, J. Kuehl, et al. "Verification and validation issues in hypersonic stability and transition prediction". In: *Journal of Spacecraft and Rockets* 52.1 (2014), pp. 29–37.

[8] S. A. Berry, A. H. Auslender, A. D. Dilley, et al. "Hypersonic boundary-layer trip development for Hyper-X". In: *Journal of spacecraft and Rockets* 38.6 (2001), pp. 853–864.

[9] M. P. Borg and S. P. Schneider. "Effect of freestream noise on roughness-induced transition for the X-51A forebody". In: *Journal of Spacecraft and Rockets* 45.6 (2008), pp. 1106–1116.

[10] E. Reshotko. "Is Retheta/Me a Meaningful Transition Criterion?" In: *AIAA journal* 45.7 (2007), pp. 1441–1443.

[11] A. M. O. Smith. "Transition, pressure gradient and stability theory". In: *Douglas Aircraft Co., Report ES 26388* (1956).

[12] J. Van Ingen. "A suggested semi-empirical method for the calculation of the boundary layer transition region". In: *Technische Hogeschool Delft, Vliegtuigbouwkunde, Rapport VTH-74* (1956).

[13] J. van Ingen. "The eN Method for Transition Prediction. Historical Review of Work at TU Delft". In: Fluid Dynamics and Co-located Conferences 0. American Institute of Aeronautics and Astronautics, Apr. 2008. DOI: 10.2514/6.2008-3830.

[14] H. H. Hamilton, D. R. Millman, and R. B. Greendyke. "Finite-difference solution for laminar or turbulent boundary layer flow over axisymmetric bodies with ideal gas, CF4, or equilibrium air chemistry". In: (1992).

[15] U. S. D. S. B. T. F. on the National Aerospace Plane. *Report of the Defense Science Board Task Force on the National Aerospace Plane (NASP)*. Office of the Under Secretary of Defense for Acquisition, 1988.

[16] K. Stetson and R. Kimmel. "On hypersonic boundary-layer stability". In: Aerospace Sciences Meetings. American Institute of Aeronautics and Astronautics, Jan. 1992. DOI: 10.2514/6.1992-737.

[17] L. M. Mack. *Special Course on Stability and Transition of Laminar Flow*. Tech. rep. California Institute of Technology, 1984.

[18] A. Fedorov. "Transition and Stability of High-Speed Boundary Layers". In: *Annual Review of Fluid Mechanics* 43.1 (2011), pp. 79–95. DOI: 10.1146/annurev-fluid-122109-160750.

[19] H. L. Reed and W. S. Saric. "Stability of three-dimensional boundary layers". In: *Annual Review of Fluid Mechanics* 21.1 (1989), pp. 235–284.

[20] W. S. Saric, H. L. Reed, and E. B. White. "Stability and Transition of Three-Dimensional Boundary Layers". In: *Annual Review of Fluid Mechanics* 35.1 (2003), pp. 413–440. DOI: 10.1146/annurev.fluid.35.101101.161045.

[21] W. Saric and H. Reed. "Crossflow instabilities-theory & technology". In: *41st Aerospace Sciences Meeting and Exhibit*. 2003, p. 771.

[22] T. S. Kocian, A. Moyes, H. L. Reed, et al. "Hypersonic Crossflow Instability". In: AIAA SciTech Forum. American Institute of Aeronautics and Astronautics, Jan. 2018. DOI: 10.2514/6.2018-0061.

[23] W. S. Saric. "Görtler vortices". In: *Annual Review of Fluid Mechanics* 26.1 (1994), pp. 379–409.

[24] F. M. White and I. Corfield. *Viscous fluid flow*. Vol. 3. McGraw-Hill New York, 2006.

[25] S. P. Schneider. "Flight Data for Boundary-Layer Transition at Hypersonic and Supersonic Speeds". In: *Journal of Spacecraft and Rockets* 36.1 (Jan. 1999), pp. 8–20. ISSN: 0022-4650. DOI: 10.2514/2.3428.

[26] D. Adamczak, R. Kimmel, T. D. S. T. O. A. V. D. t.-B., et al. "HIFiRE-1 Flight Trajectory Estimation and Initial Experimental Results". In: International Space Planes and Hypersonic Systems and Technologies Conferences. American Institute of Aeronautics and Astronautics, Apr. 2011. DOI: 10.2514/6.2011-2358.

[27] R. Kimmel, D. Adamczak, A. Paull, et al. "HIFiRE-1 Preliminary Aerothermodynamic Measurements". In: Fluid Dynamics and Co-located Conferences. American Institute of Aeronautics and Astronautics, June 2011. DOI: 10.2514/6.2011-3413.

[28] R. Kimmel, D. Adamczak, S. Stanfield, et al. "HIFiRE-1 Boundary Layer Transition Measurements". In: *28th Congress of the International Council of the Aeronautical Sciences*. ICAS, 2012.

[29] R. Kimmel and D. Adamczak. "HIFiRE-1 Background and Lessons Learned". In: Aerospace Sciences Meetings. American Institute of Aeronautics and Astronautics, Jan. 2012. DOI: 10.2514/6.2012-1088.

[30] S. Stanfield, R. Kimmel, and D. Adamczak. "HIFiRE-1 Data Analysis: Boundary Layer Transition Experiment During Reentry". In: Aerospace Sciences Meetings. American Institute of Aeronautics and Astronautics, Jan. 2012. DOI: 10.2514/6.2012-1087.

[31] R. L. Kimmel, D. Adamczak, M. Borg, et al. *HIFiRE-1 and HIFiRE-5 Test Results*. Tech. rep. February 2014.

[32] S. A. Stanfield, R. L. Kimmel, D. Adamczak, et al. "Boundary-Layer Transition Experiment During Reentry of HIFiRE-1". In: *Journal of Spacecraft and Rockets* 52.3 (May 2015), pp. 637–649. ISSN: 0022-4650. DOI: 10.2514/1.a33197.

[33] R. L. Kimmel, D. W. Adamczak, M. P. Borg, et al. "HIFiRE-1 and -5 Flight and Ground Tests". In: AIAA SciTech Forum. American Institute of Aeronautics and Astronautics, Jan. 2018. DOI: 10.2514/6.2018-0056.

[34] R. L. Kimmel, D. W. Adamczak, M. P. Borg, et al. "First and Fifth Hypersonic International Flight Research Experimentation's Flight and Ground Tests". In: *Journal of Spacecraft and Rockets* (Nov. 2018), pp. 1–11. ISSN: 0022-4650. DOI: 10.2514/1.a34287.

[35] S. Willems, A. Guelhan, T. J. Juliano, et al. "Laminar to turbulent transition on the HIFiRE-1 cone at Mach 7 and high angle of attack". In: AIAA SciTech Forum. American Institute of Aeronautics and Astronautics, Jan. 2014. DOI: 10.2514/6.2014-0428.

[36] T. J. Juliano, R. L. Kimmel, S. Willems, et al. "HIFiRE-1 Surface Pressure Fluctuations from High Reynolds, High Angle Ground Test". In: AIAA SciTech Forum. American Institute of Aeronautics and Astronautics, Jan. 2014. DOI: 10.2514/6.2014-0429.

[37] T. J. Juliano, R. L. Kimmel, S. Willems, et al. "HIFiRE-1 Boundary-Layer Transition: Ground Test Results and Stability Analysis". In: AIAA SciTech Forum. American Institute of Aeronautics and Astronautics, Jan. 2015. DOI: 10.2514/6.2015-1736.

[38] M. V. Morkovin. "Bypass transition to turbulence and research desiderata". In: (1985).

[39] E. Reshotko. "Transient growth: a factor in bypass transition". In: *Physics of Fluids* 13.5 (2001), pp. 1067–1075.

[40] M. Choudhari and P. Fischer. "Roughness induced transient growth: nonlinear effects". In: *IUTAM Symposium on Laminar-Turbulent Transition*. Ed. by R. Govindarajan. Dordrecht: Springer Netherlands, 2006, pp. 237–242. ISBN: 978-1-4020-4159-4.

[41] E. Reshotko, A. Leidy, F. Siddiqui, et al. "Characterizing the Transient Growth Mechanism on a Hypersonic Blunt Body at a High Angle of Attack". In: AIAA AVIATION Forum 0. American Institute of Aeronautics and Astronautics, Apr. 2016. DOI: 10.2514/6.2016-3951.

[42] P. Paredes, M. M. Choudhari, and F. Li. "Blunt-body paradox and transient growth on a hypersonic spherical forebody". In: *Phys. Rev. Fluids* 2 (5 2017), p. 053903. DOI: 10.1103/PhysRevFluids.2.053903.

[43] P. Paredes, M. M. Choudhari, and F. Li. "Nonlinear Transient Growth and Boundary Layer Transition". In: AIAA AVIATION Forum 0. American Institute of Aeronautics and Astronautics, Apr. 2019. DOI: 10.2514/6.2016-3956.

[44] P. Paredes, M. M. Choudhari, and F. Li. "Blunt-Body Paradox and Improved Application of Transient-Growth Framework". In: *AIAA Journal* 56.7 (Apr. 2019), pp. 2604–2614. ISSN: 0001-1452. DOI: 10.2514/1.j056678.

[45] M. Morkovin. "Transition in open flow systems-a reassessment". In: *Bull. Am. Phys. Soc.* 39 (1994), p. 1882.

[46] W. S. Saric, H. L. Reed, and E. J. Kerschen. "Boundary-layer receptivity to freestream disturbances". In: *Annual Review of Fluid Mechanics* 34.1 (2002), pp. 291–319. DOI: 10.1146/annurev.fluid.34.082701.161921.

[47] M. V. Morkovin. *Critical evaluation of transition from laminar to turbulent shear layers with emphasis on hypersonically traveling bodies*. Tech. rep. MARTIN MARIETTA CORP BALTIMORE MD RESEARCH INST FOR ADVANCED STUDIES, 1969.

[48] M. T. Landahl. "A note on an algebraic instability of inviscid parallel shear flows". In: *Journal of Fluid Mechanics* 98.2 (1980), 243–251. DOI: 10.1017/S0022112080000122.

[49] E. Reshotko. "Disturbances in a laminar boundary layer due to distributed surface roughness". In: *Turbulence and Chaotic Phenomena in Fluids*. Ed. by T. Tatsumi. 1984, pp. 39–46.

[50] E. Reshotko. "Boundary layer instability, transition and control". In: Aerospace Sciences Meetings 0. American Institute of Aeronautics and Astronautics, Apr. 1994. DOI: 10.2514/6.1994-1.

[51] L. Mack. "The inviscid stability of the compressible laminar boundary layer". In: *Space Programs Summary* 37 (1963), pp. 297–312.

[52] T. Herbert. "Parabolized stability equations". In: *Annual Review of Fluid Mechanics* 29.1 (1997), pp. 245–283.

[53] H. Johnson and G. Candler. "Hypersonic boundary layer stability analysis using PSE-Chem". In: *35th AIAA Fluid Dynamics Conference and Exhibit*. 2005, p. 5023.

[54] E. C. Marineau, G. Grossir, A. Wagner, et al. "Compilation and Analysis of Second Mode Amplitudes on Sharp Cones in Hypersonic Wind Tunnels". In: AIAA SciTech Forum 0. American Institute of Aeronautics and Astronautics, Dec. 2018. DOI: 10.2514/6.2018-0349.

[55] N. Jaffe, T. Okamura, and A. Smith. "Determination of spatial amplification factors and their applicationto predicting transition". In: *Aiaa Journal* 8.2 (1970), pp. 301–308.

[56] M. R. Malik. "Hypersonic flight transition data analysis using parabolized stability equations with chemistry effects". In: *Journal of Spacecraft and Rockets* 40.3 (2003), pp. 332–344.

[57] J. S. Jewell and R. L. Kimmel. "Boundary-Layer Stability Analysis for Stetson's Mach 6 Blunt-Cone Experiments". In: *Journal of Spacecraft and Rockets* 54.1 (Oct. 2017), pp. 258–265. DOI: 10.2514/1.a33619.

[58] J. S. Jewell, R. E. Kennedy, S. J. Laurence, et al. "Transition on a Variable Bluntness 7-Degree Cone at High Reynolds Number". In: *2018 AIAA Aerospace Sciences Meeting*. 2018, p. 1822.

[59] M. J. Wright, G. V. Candler, and D. Bose. "Data-parallel line relaxation method for the Navier-Stokes equations". In: *AIAA journal* 36.9 (1998), pp. 1603–1609.

[60] H. B. Johnson. "Thermochemical Interactions in Hypersonic Boundary Layer Stability". PhD thesis. Minneapolis, MN: University of Minnesota, 2000.

[61] H. B. Johnson, T. G. Seipp, and G. V. Candler. "Numerical study of hypersonic reacting boundary layer transition on cones". In: *Physics of Fluids* 10 (1998), pp. 2676–2685. DOI: 10.1063/1.869781.

[62] P. Jacobs, R. Gollan, D. Potter, et al. "Estimation of high-enthalpy flow conditions for simple shock and expansion processes using the ESTCj program and library". In: (2014).

[63] A. Fedorov. "Instability of the entropy layer on a blunt plate in supersonic gas flow". In: *Journal of applied mechanics and technical physics* 31.5 (1990), pp. 722–728.

[64] V. Lysenko. "Influence of the entropy layer on the stability of a supersonic shock layer and transition of the laminar boundary layer to turbulence". In: *Journal of Applied Mechanics and Technical Physics* 31.6 (1990), pp. 868–873.

[65] K. Stetson, E. Thompson, J. Donaldson, et al. "Laminar boundary layer stability experiments on a cone at Mach 8. II- Blunt cone". In: *American Institute of Aeronautics and Astronautics, Aerospace Sciences Meeting, 22 nd, Reno, NV*. 1984.

[66] G. Dietz, S. Mählmann, and S. Hein. "Entropy-Layer Instabilities in Plane Supersonic Flow". In: *New Results in Numerical and Experimental Fluid Mechanics II*. Springer, 1999, pp. 108–115.

[67] R. Greenwood and S. P. Schneider. "Measurements of Entropy-Layer instabilities over a Cone-Ogive-Cylinder in a Mach-6 Quiet Tunnel". In: AIAA SciTech Forum 0. American Institute of Aeronautics and Astronautics, Apr. 2019. DOI: 10.2514/6.2019-0627.

[68] H. G. Hornung and P. Lemieux. "Shock layer instability near the Newtonian limit of hypervelocity flows". In: *Physics of Fluids* 13.8 (2001), pp. 2394–2402. DOI: 10.1063/1.1383591.

[69] H. L. Reed, W. S. Saric, and D. Arnal. "Linear stability theory applied to boundary layers". In: *Annual review of fluid mechanics* 28.1 (1996), pp. 389–428.

[70] S. J. Laurence, A. Wagner, K. Hannemann, et al. "Time-Resolved Visualization of Instability Waves in a Hypersonic Boundary Layer". In: *AIAA Journal* 50.1 (Jan. 2012), pp. 243–246. ISSN: 0001-1452. DOI: 10.2514/1.j051112.

[71] S. J. Laurence, A. Wagner, and K. Hannemann. "Schlieren-based techniques for investigating instability development and transition in a hypersonic boundary layer". In: *Experiments in Fluids* 55.8 (2014), p. 1782. ISSN: 1432-1114. DOI: 10.1007/s00348-014-1782-9.

[72] L. Mack. "The inviscid stability of the compressible laminar boundary layer: part II". In: *Space Programs Summary* 4 (1964), p. 165.

[73] L. Mack. "The stability of the compressible laminar boundary layer according to a direct numerical solution(Stability of compressible laminar boundary layer according to direct numerical solution)". In: *1965.* (1965), pp. 329–362.

[74] L. M. Mack. "Linear stability theory and the problem of supersonic boundary-layer transition". In: *AIAA journal* 13.3 (1975), pp. 278–289.

[75] L. M. Mack. "On the inviscid acoustic-mode instability of supersonic shear flows". In: *Theoretical and Computational Fluid Dynamics* 2.2 (1990), pp. 97–123.

[76] S. J. Laurence, A. Wagner, H. Ozawa, et al. "Visualization of Hypersonic Boundary-Layer Transition on a Slender Cone (Invited)". In: AIAA AVIATION Forum. American Institute of Aeronautics and Astronautics, June 2014. DOI: 10.2514/6.2014-3110.

[77] J. S. Jewell. *Boundary-layer transition on a slender cone in hypervelocity flow with real gas effects*. California Institute of Technology, 2014.

[78] G. Grossir, F. Pinna, G. Bonucci, et al. "Hypersonic Boundary Layer Transition on a 7 Degree Half-Angle Cone at Mach 10". In: AIAA AVIATION Forum. American Institute of Aeronautics and Astronautics, June 2014. DOI: 10.2514/6.2014-2779.

[79] G. Grossir. "Longshot Hypersonic Wind Tunnel Flow Characterization and Boundary Layer Stability Investigations". PhD thesis. von Karman Institute for Fluid Dynamics, 2015.

[80] A. Wagner. "Passive Hypersonic Boundary Layer Transition Control Using Ultrasonically Absorptive Carbon-Carbon Ceramic with Random Microstructure". PhD thesis. Oct. 2014. DOI: 10.13140/RG.2.1.4246.8968.

[81] R. L. Kimmel, A. Demetriades, and J. C. Donaldson. "Space-time correlation measurements in a hypersonic transitional boundary layer". In: *AIAA journal* 34.12 (1996), pp. 2484–2489.

[82] E. K. Jagde, R. E. Kennedy, S. J. Laurence, et al. "Visualizations of Boundary-Layer Transition on a Sharp Cone at Mach 6". In: *AIAA Aviation 2019 Forum*. 2019, p. 3080.

[83] S. Raghunath and D. J. Mee. "A semi-empirical expression to estimate the most-amplified frequencies of second-mode instabilities in hypersonic transitional flows". manuscript in preparation.

[84] L. Howarth. "Concerning the effect of compressibility on lam inar boundary layers and their separation". In: *Proceedings of the Royal Society of London. Series A. Mathematical and Physical Sciences* 194.1036 (1948), pp. 16–42.

[85] G. I. Taylor and J. Maccoll. "The air pressure on a cone moving at high speeds.—II". In: *Proceedings of the Royal Society of London. Series A, Containing Papers of a Mathematical and Physical Character* 139.838 (1933), pp. 298–311.

[86] K. Stewartson. *The theory of laminar boundary layers in compressible fluids*. Clarendon Press Oxford, 1964.

[87] S. Mallinson, S. Gai, and N. Mudford. "The boundary layer on a flat plate in hypervelocity flow". In: *The Aeronautical Journal* 100.994 (1996), pp. 135–141.

[88] J. Kendall. "Wind tunnel experiments relating to supersonic and hypersonic boundary-layer transition". In: *Aiaa Journal* 13.3 (1975), pp. 290–299.

[89] K. Stetson, E. Thompson, J. Donaldson, et al. "Laminar boundary layer stability experiments on a cone at Mach 8. I - Sharp cone". In: Fluid Dynamics and Co-located Conferences 0. American Institute of Aeronautics and Astronautics, Apr. 1983. DOI: 10.2514/6.1983-1761.

[90] K. Fujii. "Experiment of the two-dimensional roughness effect on hypersonic boundary-layer transition". In: *Journal of Spacecraft and Rockets* 43.4 (2006), pp. 731–738.

[91] N. Parziale, J. Shepherd, and H. Hornung. "Differential interferometric measurement of instability in a hypervelocity boundary layer". In: *AIAA journal* 51.3 (2012), pp. 750–754.

[92] R. E. Kennedy, S. J. Laurence, M. S. Smith, et al. "Investigation of the second-mode instability at Mach 14 using calibrated schlieren". In: *Journal of Fluid Mechanics* 845 (2018).

[93] E. C. Marineau, G. C. Morraru, and D. Daniel. "Sharp Cone Boundary-Layer Transition and Stability at Mach 14". In: *55th AIAA Aerospace Sciences Meeting*. DOI: 10.2514/6.2017-0766. eprint: https://arc.aiaa.org/doi/pdf/10.2514/6.2017-0766.

[94] K. Stetson. "Nosetip bluntness effects on cone frustum boundary layer transition in hypersonic flow". In: Fluid Dynamics and Co-located Conferences. American Institute of Aeronautics and Astronautics, July 1983. DOI: 10.2514/6.1983-1763.

[95] A. Fedorov and M. Kozlov. "Receptivity of high-speed boundary layer to solid particulates". In: *6th AIAA Theoretical Fluid Mechanics Conference*. 2011.

[96] H Reed and W Saric. "Supersonic laminar flow control on swept wings using distributed roughness". In: *40th AIAA Aerospace Sciences Meeting & Exhibit*. 2002, p. 147.

[97] H Deyhle and H Bippes. "Disturbance growth in an unstable three-dimensional boundary layer and its dependence on environmental conditions". In: *Journal of Fluid Mechanics* 316 (1996), pp. 73–113.

[98] S. A. Craig and W. S. Saric. "Crossflow instability in a hypersonic boundary layer". In: *Journal of Fluid Mechanics* 808 (2016), pp. 224–244. ISSN: 0022-1120. DOI: 10.1017/jfm.2016.643.

[99] J. B. Edelman and S. P. Schneider. "Secondary Instabilities of Hypersonic Stationary Crossflow Waves". In: *AIAA Journal* 56.1 (Jan. 2018), pp. 182–192. ISSN: 0001-1452. DOI: 10.2514/1.j056028.

[100] J. Edelman and S. P. Schneider. "Using Discrete and Distributed Roughness to Generate Stationary Crossflow Waves in a Mach 6 Quiet Tunnel". In: *AIAA Aviation 2019 Forum*. 2019, p. 2968.

[101] L. Lees and C. C. Lin. "Investigation of the stability of the laminar boundary layer". In: (1946).

[102] N. B. Oliviero, T. S. Kocian, A. Moyes, et al. "EPIC: NPSE analysis of hypersonic crossflow instability on yawed straight circular cone". In: *45th AIAA Fluid Dynamics Conference*. 2015, p. 2772.

[103] R. Radeztsky Jr, M. Reibert, and W. Saric. *Effect of micron-sized roughness on transition in sweptwing flows*. 1992.

[104] M. Reibert, W. Saric, R. Carrillo Jr, et al. "Experiments in nonlinear saturation of stationary crossflow vortices in a swept-wing boundary layer". In: *34th Aerospace Sciences Meeting and Exhibit*. 1996, p. 184.

[105] R. B. Carrillo Jr, M. S. Reibert, and W. S. Saric. "Distributed-roughness effects on stability and transition in swept-wing boundary layers". In: (1997).

[106] E. B. White and W. S. Saric. "Secondary instability of crossflow vortices". In: *Journal of Fluid Mechanics* 525 (2005), 275–308. DOI: 10.1017/S002211200400268X.

[107] M. R. Malik, F. Li, M. M. Choudhari, et al. "Secondary instability of crossflow vortices and swept-wing boundary-layer transition". In: *Journal of Fluid Mechanics* 399 (1999), pp. 85–115.

[108] Y Kohama. "Some expectation on the mechanism of cross-flow instability in a swept wing flow". In: *Acta mechanica* 66.1-4 (1987), pp. 21–38.

[109] M. Malik, F Li, and C.-L. Chang. "Nonlinear crossflow disturbances and secondary instabilities in swept-wing boundary layers". In: *IUTAM Symposium on Nonlinear Instability and Transition in Three-Dimensional Boundary Layers*. Springer. 1996, pp. 257–266.

[110] S. A. Craig and W. S. Saric. "Crossflow Instability on a Yawed Cone at Mach 6". In: *Procedia IUTAM* 14 (Jan. 2015), pp. 15–25. ISSN: 2210-9838.

[111] S. A. Craig and W. S. Saric. "Experimental study of crossflow instability on a Mach 6 yawed cone". In: *45th AIAA Fluid Dynamics Conference*. 2015, p. 2774.

[112] C. Ward, R. Henderson, and S. P. Schneider. "Secondary Instability of Stationary Crossflow Vortices on an Inclined Cone at Mach 6". In: AIAA AVIATION Forum. American Institute of Aeronautics and Astronautics, June 2015. DOI: 10.2514/6.2015-2773.

[113] B. C. Chynoweth, C. Ward, and S. P. Schneider. "Measuring Transition and Instabilities in a Mach 6 Hypersonic Quiet Wind Tunnel". In: AIAA AVIATION Forum. American Institute of Aeronautics and Astronautics, June 2014. DOI: 10.2514/6.2014-2643.

[114] R. Henderson. "Crossflow Transition at Mach 6 on a Cone at Low Angles of Attack". MA thesis. Purdue University, 2014.

[115] C. Ward. "Crossflow Instability and Transition on a Circular Cone at Angle of Attack in a Mach-6 Quiet Tunnel". MA thesis. Purdue University, 2014.

[116] J. B. Edelman. "Secondary instabilitied of hypersonic stationary crossflow waves". Master's Thesis. Purdue University, 2016.

[117] C. J. Sweeney, B. C. Chynoweth, J. Edelman, et al. "Instability and Transition Experiments in the Boeing/AFOSR Mach-6 Quiet Tunnel". In: AIAA SciTech Forum. American Institute of Aeronautics and Astronautics, Jan. 2016. DOI: 10.2514/6.2016-0355.

[118] H. Bippes. "Basic experiments on transition in three-dimensional boundary layers dominated by crossflow instability". In: *Progress in Aerospace Sciences* 35.4 (1999), pp. 363 –412. ISSN: 0376-0421. DOI: https://doi.org/10.1016/S0376-0421(99)00002-0.

[119] M. P. Borg, R. L. Kimmel, and S. Stanfield. "Traveling Crossflow Instability for the HIFiRE-5 Elliptic Cone". In: *Journal of Spacecraft and Rockets* 52.3 (May 2015), pp. 664–673. ISSN: 0022-4650. DOI: 10.2514/1.a33145.

[120] L. Duan, M. M. Choudhari, A. Chou, et al. "Characterization of freestream disturbances in conventional hypersonic wind tunnels". In: *2018 AIAA aerospace sciences meeting*. 2018, p. 0347.

[121] T. Corke, A. Arndt, E. Matlis, et al. "Control of stationary cross-flow modes in a Mach 6 boundary layer using patterned roughness". In: *Journal of Fluid Mechanics* 856 (2018), pp. 822–849.

[122] F. Muñoz, D. Heitmann, and R. Radespiel. "Instability modes in boundary layers of an inclined cone at Mach 6". In: *Journal of Spacecraft and Rockets* 51.2 (2014), pp. 442–454.

[123] J. Kuehl, E. Perez, and H. Reed. "JoKHeR: NPSE Simulations of Hypersonic Crossflow Instability". In: Aerospace Sciences Meetings 0. American Institute of Aeronautics and Astronautics, Aug. 2012. DOI: 10.2514/6.2012-921.

[124] C. A. Ward. "Crossflow instability and transition on a circular cone at angle of attack in a Mach-6 quiet tunnel". PhD thesis. 2014.

[125] S. P. Schneider. "Effects of High-Speed Tunnel Noise on Laminar-Turbulent Transition". In: *Journal of Spacecraft and Rockets* 38.3 (Apr. 2001), pp. 323–333. ISSN: 0022-4650. DOI: 10.2514/2.3705.

[126] S. P. Schneider. "Development of Hypersonic Quiet Tunnels". In: *Journal of Spacecraft and Rockets* 45.4 (July 2008), pp. 641–664. ISSN: 0022-4650. DOI: 10.2514/1.34489.

[127] S. R. Pate. *Dominance of radiated aerodynamic noise on boundary layer transition in supersonic-hypersonic wind tunnels*. Tech. rep. 1978.

[128] P. C. STAINBACK. "Hypersonic boundary-layer transition in the presence of wind-tunnel noise." In: *AIAA Journal* 9.12 (1971), pp. 2475–2476.

[129] M. Holden. "Experimental studies of the effects of asymmetric transition on the aerothermal characteristics of hypersonic blunted slender cones". In: Aerospace Sciences Meetings. American Institute of Aeronautics and Astronautics, Jan. 1985. DOI: 10.2514/6.1985-325.

[130] B. Graber, E. Softley, and R. E. Zempel. "Experimental observation of transition of the hypersonic boundary layer." In: *AIAA Journal* 7.2 (1969), pp. 257–263.

[131] E. C. Marineau, G. C. Moraru, D. R. Lewis, et al. "Mach 10 Boundary Layer Transition Experiments on Sharp and Blunted Cones (Invited)". In: AIAA AVIATION Forum. American Institute of Aeronautics and Astronautics, June 2014. DOI: 10.2514/6.2014-3108.

[132] P. C. Stainback, R. D. Wagner, F. K. Owen, et al. *Experimental studies of hypersonic boundary-layer transition and effects of wind-tunnel disturbances.* Tech. rep. 1974.

[133] F. K. Owen, C. C. Horstman, P. C. Stainback, et al. "Comparison of Wind Tunnel Transition and Freestream Disturbance Measurements". In: *AIAA Journal* 13.3 (Mar. 1975), pp. 266–269. ISSN: 0001-1452. DOI: 10.2514/3.49691.

[134] P Krogmann. "An experimental study of boundary layer transition on a slender cone at Mach 5". In: *In AGARD Laminar-Turbulent Transition 12 p (SEE N78-14316 05-34).* 1977.

[135] C. F.J., M. R. Malik, and I. E. Beckwith. "Boundary-layer transition on a cone and flat plate at Mach 3.5". In: *AIAA Journal* 27.6 (June 1989), pp. 687–693. ISSN: 0001-1452. DOI: 10.2514/3.10166.

[136] P. Paredes, M. M. Choudhari, F. Li, et al. "Nose-Tip Bluntness Effects on Transition at Hypersonic Speeds". In: *Journal of Spacecraft and Rockets* 56.2 (Mar. 2019), pp. 369–387. ISSN: 0022-4650. DOI: 10.2514/1.a34277.

[137] E Softley. "Boundary layer transition on hypersonic blunt, slender cones". In: *2nd Fluid and Plasma Dynamics Conference.* 1969, p. 705.

[138] E. Swanson and S. Schneider. "Boundary-layer transition on cones at angle of attack in a Mach-6 quiet tunnel". In: *48th AIAA Aerospace Sciences Meeting Including the New Horizons Forum and Aerospace Exposition.* 2008, p. 1062.

[139] J. Muir. and A. Trujillo. "Experimental investigation of the effects of nose bluntness, free-stream unit Reynolds number, and angle of attack on cone boundary layer transition at a Mach number of 6". In: Aerospace Sciences Meetings. American Institute of Aeronautics and Astronautics, Jan. 1972. DOI: 10.2514/6.1972-216.

[140] E. C. Marineau, G. C. Moraru, D. R. Lewis, et al. "Investigation of Mach 10 Boundary Layer Stability of Sharp Cones at Angle-of-Attack, Part 1: Experiments". In: AIAA SciTech Forum. American Institute of Aeronautics and Astronautics, Jan. 2015. DOI: 10.2514/6.2015-1737.

[141] M. Holden, D. Bower, and K. Chadwick. "Measurements of boundary layer transition on cones at angle of attack for Mach numbers from 11 to 13". In: Fluid Dynamics and Co-located Conferences. American Institute of Aeronautics and Astronautics, June 1995. DOI: 10.2514/6.1995-2294.

[142] K. F. Stetson. *Hypersonic boundary layer transition experiments.* Tech. rep. AIR FORCE WRIGHT AERONAUTICAL LABS WRIGHT-PATTERSON AFB OH, 1980.

[143] K. F. Stetson. "Mach 6 Experiments of Transition on a Cone at Angle of Attack". In: *Journal of Spacecraft and Rockets* 19.5 (Sept. 1982), pp. 397–403. ISSN: 0022-4650. DOI: 10.2514/3.62276.

[144] L. E. Sakell. "An experimental investigation of boundary layer transition over three axially symmetric bodies at Mach 6". PhD thesis. Ph. D. dissertation, New York University, New York, 1972.

[145] V. DiCristina. "Three-dimensional laminar boundary-layer transition on a sharp 8 degcone at Mach 10". In: *AIAA Journal* 8.5 (May 1970), pp. 852–856. ISSN: 0001-1452. DOI: 10.2514/3.5777.

[146] K. Stetson, E. Thompson, J. Donaldson, et al. "Laminar boundary layer stability experiments on a cone at Mach 8. III - Sharp cone at angle of attack". In: Aerospace Sciences Meetings. American Institute of Aeronautics and Astronautics, Jan. 1985. DOI: 10.2514/6.1985-492.

[147] G. H. Rushton and K. F. Stetson. "Shock tunnel investigation of boundary-layer transition at M equals 5.5." In: *AIAA Journal* 5.5 (May 1967), pp. 899–906. ISSN: 0001-1452. DOI: 10.2514/3.4098.

[148] T. Horvath, S. Berry, B. Hollis, et al. "Boundary Layer Transition on Slender Cones in Conventional and Low Disturbance Mach 6 Wind Tunnels". In: Fluid Dynamics and Co-located Conferences 0. American Institute of Aeronautics and Astronautics, Sept. 2002. DOI: 10.2514/6.2002-2743.

[149] L. M. Mack. "Effect of cooling on boundary-layer stability at Mach number 3". In: *Instabilities and Turbulence in Engineering Flows*. Springer, 1993, pp. 175–188.

[150] A. Demetriades. "Hypersonic viscous flow over a slender cone. III-Laminar instability and transition". In: *7th Fluid and PlasmaDynamics Conference*. 1974, p. 535.

[151] K. Stetson, E. Thompson, J. Donaldson, et al. "Laminar boundary layer stability experiments on a cone at Mach 8. V - Tests with a cooled model". In: Fluid Dynamics and Co-located Conferences. American Institute of Aeronautics and Astronautics, June 1989. DOI: 10.2514/6.1989-1895.

[152] V. I. Lysenko and A. A. Maslov. "The effect of cooling on supersonic boundary-layer stability". In: *Journal of Fluid Mechanics* 147 (1984), pp. 39–52.

[153] J. L. Potter. "Review of the influence of cooled walls on boundary-layer transition". In: *AIAA Journal* 18.8 (1980), pp. 1010–1012.

[154] E. V. Driest. "Experiments on boundary-layer transition at supersonic speeds". In: *Journal of the Aeronautical Sciences* 24.12 (1957), pp. 885–899.

[155] J. DeCarlo, R. Sanator, and D. Torrillo. "Hypersonic boundary-layer transition data for a cold-wall slender cone". In: *AIAA Journal* 3.4 (1965), pp. 758–760.

[156] P. E. Everhart and H. H. Hamilton. "Experimental investigation of boundary-layer transition on a cooled 7.5 deg total-angle cone at Mach 10". In: (1967).

[157] D. M. Bushnell. "Hypersonic Ground Test Requirements". In: Progress in Astronautics and Aeronautics. American Institute of Aeronautics and Astronautics, Jan. 2002, pp. 1–15. DOI: 10.2514/5.9781600866678.0001.0015.

[158] "Principles of Hypersonic Test Facility Development". In: Progress in Astronautics and Aeronautics. American Institute of Aeronautics and Astronautics, Jan. 2002, pp. 17–27. DOI: 10.2514/5.9781600866678.0017.0027.

[159] D. Wise. "Experimental Investigation of a Three Dimensional Scramjet Engine at Hypervelocity Conditions". PhD thesis. The University of Queensland, 2014.

[160] M. McGilvray, L. J. Doherty, A. J. Neely, et al. "The Oxford High Density Tunnel". In: International Space Planes and Hypersonic Systems and Technologies Conferences. American Institute of Aeronautics and Astronautics, July 2015. DOI: 10.2514/6.2015-3548.

[161] P. S. T.V. Jones and M. Westby. "Recent Enhancement to the DRA Shock Tunnel". In: *Conference, Wind tunnels and wind tunnel test techniques.* Southampton, Sept. 1992, pp. 30.1–30.14.

[162] M. Robinson, S. Rowan, J Odam, et al. "T4 Free Piston Shock Tunnel Operator's Manual Version 2.0". In: *Fuel* 2 (2015), p. 11.

[163] L. J. Doherty. "An experimental investigation of an airframe integrated three-dimensional scramjet engine at a Mach 10 flight condition". PhD thesis. The University of Queensland, 2014.

[164] R. Stalker, A Paull, D. Mee, et al. "Scramjets and shock tunnels—the Queensland experience". In: *Progress in Aerospace Sciences* 41.6 (2005), pp. 471–513.

[165] D. Gildfind, R. Morgan, M McGilvray, et al. "Free-piston driver optimisation for simulation of high Mach number scramjet flow conditions". In: *Shock Waves* 21.6 (2011), p. 559.

[166] R. Stalker. "A study of the free-piston shock tunnel." In: *AIAA Journal* 5.12 (1967), pp. 2160–2165.

[167] Y He and R. Morgan. "Transition of compressible high enthalpy boundary layer flow over a flat plate". In: *The Aeronautical Journal* 98.972 (1994), pp. 25–34.

[168] M Hayne. "The Manufacture and Mounting of Thin Film Gauges for Heat Transfer". In: *Univ. of Queensland, Dept. of Mechanical Engineering SID-61-275, St. Lucia, Australia* (2003).

[169] R. T. Penty Geraets, M. McGilvray, L. Doherty, et al. "Development of a Fast-Response Calorimeter Gauge for Hypersonic Ground Testing". In: AIAA AVIATION Forum. American Institute of Aeronautics and Astronautics, June 2017. DOI: 10.2514/6.2017-3238.

[170] T. Wadhams. personal communication. Oct. 2016.

[171] D. J. Wise and M. K. Smart. "Roughness-Induced Transition of Hypervelocity Boundary Layers". In: *Journal of Spacecraft and Rockets* 51.3 (May 2014), pp. 847–854. ISSN: 0022-4650. DOI: 10.2514/1.a32674.

[172] C. G. Miller III. "Comparison of thin-film resistance heat-transfer gages with thin-skin transient calorimeter gages in conventional hypersonic wind tunnels". In: (1981).

[173] D. L. Schultz and T. Jones. *Heat-transfer measurements in short-duration hypersonic facilities.* Tech. rep. ADVISORY GROUP FOR AEROSPACE RESEARCH and DEVELOPMENT PARIS (FRANCE), 1973.

[174] M. Collins, K. Chana, and T. Povey. "New technique for the fabrication of miniature thin film heat flux gauges". In: *Measurement Science and Technology* 26.2, 025303 (Feb. 2015), p. 025303. DOI: 10.1088/0957-0233/26/2/025303.

[175] R. Anthony, M. Oldfield, T. Jones, et al. "Development of high-density arrays of thin film heat transfer gauges". In: *JSME Thermal Engineering Joint Conference, San Diego, CA, No. AJTE99-6159.* 1999.

[176] M. L. Oldfield. "Impulse Response Processing of Transient Heat Transfer Gauge Signals". In: *Journal of Turbomachinery* 130.2 (Mar. 2008), pp. 021023–021023–9. ISSN: 0889-504X. DOI: 10.1115/1.2752188.

[177] E. R. van Driest. "Turbulent Boundary Layer in Compressible Fluids". In: *Journal of Spacecraft and Rockets* 40.6 (Nov. 1951), pp. 1012–1028. ISSN: 0022-4650. DOI: 10.2514/2.7048.

[178] D. C. Berridge and S. P. Schneider. "Calibration of PCB-132 sensors in a shock tube". MA thesis. Purdue University, 2012.

[179] D. Ort and J. J. Dosch. "Influence of Mountiing on the Accuracy of Piezoelectric Pressure Measurements for Hypersonic Boundary Layer Transition". In: AIAA SciTech Forum. American Institute of Aeronautics and Astronautics, Jan. 2019. DOI: 10.2514/6.2019-2292.

[180] P. Welch. "The use of fast Fourier transform for the estimation of power spectra: a method based on time averaging over short, modified periodograms". In: *IEEE Transactions on audio and electroacoustics* 15.2 (1967), pp. 70–73.

[181] A. Teolis and J. J. Benedetto. *Computational signal processing with wavelets*. Vol. 182. Springer, 1998.

[182] A. Wagner, M. Kuhn, J. M. Schramm, et al. "Experiments on passive hypersonic boundary layer control using ultrasonically absorptive carbon–carbon material with random microstructure". In: *Experiments in Fluids* 54.10 (2013), p. 1606.

[183] D. Berridge, K. Casper, S. Rufer, et al. "Measurements and Computations of Second-Mode Instability Waves in Several Hypersonic Wind Tunnels". In: *40th Fluid Dynamics Conference and Exhibit*. 2010, p. 5002.

[184] N. Chokani. "Wavelet analysis of a hypersonic laminar boundary layer flow". In: *38th Aerospace Sciences Meeting and Exhibit*. 2000, p. 535.

[185] L. Aguiar-Conraria and M. J. Soares. "The continuous wavelet transform: moving beyond uni-and bivariate analysis". In: *Journal of Economic Surveys* 28.2 (2014), pp. 344–375.

[186] C. Liner. "An overview of wavelet transform concepts and applications". In: *University of Houston* (2010), pp. 1–17.

[187] T. Hermann, M. McGilvray, C. Hambidge, et al. "Total Temperature Measurements in the Oxford High Density Tunnel". In: *ESA FAR 2019 Conference*. 2019.

[188] T. Robarge and S. Schneider. "Laminar boundary-layer instabilities on hypersonic cones: Computations for benchmark experiments". In: *35th AIAA Fluid Dynamics Conference and Exhibit*. 2005, p. 5024.

[189] F. Keyes. "A summary of viscosity and heat-conduction data for He, A, H2, O2, CO, CO2, H2O, and air". In: *Transactions of the ASME* 73 (1951), pp. 589–596.

[190] C. Roy and F. Blottner. "Review and Assessment of Turbulence Models for Hypersonic Flows: 2D/Asymmetric Cases". In: Aerospace Sciences Meetings. American Institute of Aeronautics and Astronautics, Jan. 2006. DOI: 10.2514/6.2006-713. URL: https://doi.org/10.2514/6.2006-713.

[191] L. S. Kovasznay. "Turbulence in supersonic flow". In: *Journal of the Aeronautical Sciences* 20.10 (1953), pp. 657–674.

[192] D. Masutti, E. Spinosa, O. Chazot, et al. “Disturbance level characterization of a hypersonic blowdown facility”. In: *AIAA journal* 50.12 (2012), pp. 2720–2730.

[193] J. Wu, P. Zamre, and R. Radespiel. “Flow quality experiment in a tandem nozzle wind tunnel at Mach 3”. In: *Experiments in Fluids* 56.1 (2015), p. 20.

[194] T. Schilden, W. Schröder, S. R. C. Ali, et al. “Analysis of acoustic and entropy disturbances in a hypersonic wind tunnel”. In: *Physics of Fluids* 28.5 (2016), p. 056104. DOI: 10.1063/1.4948435.

[195] F. Munoz, J. Wu, R. Radespiel, et al. “Freestream Disturbances Characterization in Ludwieg Tubes at Mach 6”. In: AIAA SciTech Forum. American Institute of Aeronautics and Astronautics, Jan. 2019. DOI: 10.2514/6.2019-0878.

[196] L. Duan, G. L. Nicholson, J. Huang, et al. “Direct Numerical Simulation of Nozzle-Wall Pressure Fluctuations in a Mach 8 Wind Tunnel”. In: AIAA SciTech Forum. American Institute of Aeronautics and Astronautics, Jan. 2019. DOI: 10.2514/6.2019-0874.

[197] R. S. Chaudhry, G. V. Candler, K. A. Gray, et al. “Computations of Measured Pitot-Probe Spectra using Angled Freestream Disturbances and Comparisons to Experiments”. In: AIAA SciTech Forum. American Institute of Aeronautics and Astronautics, Jan. 2019. DOI: 10.2514/6.2019-2149.

[198] A. Bounitch, D. Lewis, and J. Lafferty. “Improved Measurements of "Tunnel Noise" Pressure Fluctuations in the AEDC Hypervelocity Wind Tunnel No. 9”. In: Aerospace Sciences Meetings. American Institute of Aeronautics and Astronautics, Jan. 2011. DOI: 10.2514/6.2011-1200.

[199] S. Wylie, L. Doherty, and M. McGilvray. “Commissioning of the Oxford High Density Tunnel (HDT) for Boundary Layer Stability Measurements at Mach 7”. In: AIAA Aviation Forum. American Institute of Aeronautics and Astronautics, June 2018.

[200] S. Willems. personal communication. Feb. 2018.

[201] C. R. Alba, H. B. Johnson, M. D. Bartkowicz, et al. “Boundary-layer stability calculations for the HIFiRE-1 transition experiment”. In: *Journal of Spacecraft and Rockets* 45.6 (2008), pp. 1125–1133.

[202] H. Cheng. “Hypersonic flows past a yawed circular cone and other pointed bodies”. In: *Journal of Fluid Mechanics* 12.2 (1962), pp. 169–191.

[203] I. G. Sapunkov. “Hypersonic flow past a circular cone at an angle of attack”. In: *Journal of Applied Mathematics and Mechanics* 27.5 (1963), pp. 1422–1436.

[204] D. J. Mee. personal communication. 2019.

[205] J. DeCarlo, R. Sanator, and D. Torrillo. “Hypersonic boundary-layer transition data for a cold-wall slender cone”. In: *AIAA Journal* 3.4 (1965), pp. 758–760.

[206] D. Dolvin. “Hypersonic International Flight Research and Experimentation (HIFiRE) Fundamental Science and Technology Development Strategy”. In: International Space Planes and Hypersonic Systems and Technologies Conferences. American Institute of Aeronautics and Astronautics, Apr. 2008. DOI: 10.2514/6.2008-2581.

[207] D. Dolvin. "Hypersonic International Flight Research and Experimentation Technology Development and Flight Certification Strategy". In: International Space Planes and Hypersonic Systems and Technologies Conferences. American Institute of Aeronautics and Astronautics, Oct. 2009. DOI: 10.2514/6.2009-7228.

[208] R. Kimmel. "Aerothermal Design for the HIFiRE Flight Vehicle". In: Fluid Dynamics and Co-located Conferences. American Institute of Aeronautics and Astronautics, June 2008. DOI: 10.2514/6.2008-4034.

[209] T. Buchanan, L. Jenke, and M. Chaney. *Dynamic Force Measurements and Boundary-Layer Transition Mapping on a Spinning 9-deg Cone With and Without Mass Addition at Mach Numbers 5 and 8*. Tech. rep. ARO INC ARNOLD AFS TN, 1978.

[210] R. Gosse and R. Kimmel. "CFD Study of Three-Dimensional Hypersonic Laminar Boundary Layer Transition on a Mach 8 Elliptic Cone". In: Fluid Dynamics and Co-located Conferences. American Institute of Aeronautics and Astronautics, June 2009. DOI: 10.2514/6.2009-4053.

[211] J. Edelman, K. M. Casper, J. Henfling, et al. "Crossflow Transition on a Pitched Cone at Mach 8". In: *47th AIAA Fluid Dynamics Conference*. 2017, p. 4299.

[212] J. S. Jewell, R. E. Kennedy, S. J. Laurence, et al. "Transition on a Variable Bluntness 7-Degree Cone at High Reynolds Number". In: AIAA SciTech Forum. American Institute of Aeronautics and Astronautics, Jan. 2018. DOI: 10.2514/6.2018-1822.

[213] R. E. Kennedy, E. K. Jagde, S. J. Laurence, et al. "Visualizations of Hypersonic Boundary-Layer Transition on a Variable Bluntness Cone". In: *AIAA Aviation 2019 Forum*. 2019, p. 3079.

[214] R. S. Chaudhry and G. V. Candler. "Recovery of freestream disturbance spectrum from stagnation pressure spectrum for hypersonic pitot probes". In: *54th AIAA Aerospace Sciences Meeting, 2016*. American Institute of Aeronautics and Astronautics Inc, AIAA. 2016.

[215] R. S. Chaudhry and G. V. Candler. "Computing measured spectra from hypersonic pitot probes with flow-parallel freestream disturbances". In: *AIAA Journal* (2017), pp. 4155–4166.

[216] L. Duan, M. M. Choudhari, and C. Zhang. "Pressure fluctuations induced by a hypersonic turbulent boundary layer". In: *Journal of Fluid Mechanics* 804 (2016), pp. 578–607.